Ultrafast Magnetization Dynamics in Ferromagnetic Thin Films, Heterostructures & Nanostructures

Thesis submitted for the degree of

Doctor of Philosophy (Science)

In

Physics (Experimental)

By

Sucheta Mondal

Department of Physics

Jadavpur University

2019

CERTIFICATE FROM THE SUPERVISOR

This is to certify that the thesis entitled "**Ultrafast Magnetization Dynamics in Ferromagnetic Thin Films, Heterostructures & Nanostructures**" submitted by **Smt. Sucheta Mondal** who got her name registered on 26th April, 2016 for the award of Ph. D. (Science) degree of Jadavpur University, is absolutely based upon her own work under the supervision of **Prof. Anjan Barman** and that neither this thesis nor any part of it has been submitted for either any degree / diploma or any other academic award anywhere before.

Anjan Barman 23/7/19

(Signature of the Supervisor date with official seal)

Dr. Anjan Barman, Ph.D.
Senior Professor & Associate Dean (Faculty)
Dept. of Condensed Matter Physics and Material Sciences
S. N. Bose National Centre for Basic Sciences
Block-JD, Sector-III, Salt Lake, Kolkata-700106, India

To the Nation…

Abstract

Generation and manipulation of various nanoscale spin textures, spin waves and spin current have gain huge impetus due to their potential applications in high-density media for data storing, spin-based transistors, logic, reconfigurable magnonic waveguides for energy-efficient transmission of signals, switching devices, neuromorphic computation, etc. This doctoral research is based on the study of high frequency spin dynamics from femtosecond to nanosecond time scales in ferromagnetic systems of reduced dimensions ranging from thin films to patterned nanostructures. The study involves exploitation of several external stimuli, such as, laser fluence, spin current, and surface acoustic wave induced strain for modulation of ultrafast magnetization dynamics in ferromagnetic thin films, heterostructures and nanostructures. The experiments have been performed using custom-built space- and time-resolved magneto-optical Kerr effect (TR-MOKE) magnetometry. The experimental results have been modeled by using analytical theories and numerical micromagnetic simulations. The study of laser fluence-dependent ultrafast magnetization dynamics in $Ni_{80}Fe_{20}$ thin films having different thicknesses has been carried away by using TR-MOKE magnetometry based on amplified laser system. The effect of increasing system temperature to Curie temperature ratio on various dynamical entities, such as, ultrafast demagnetization time, remagnetization time, Gilbert damping, precessional frequency and temporal chirping is comprehensively studied. The precessional magnetization dynamics in $Gd_{10}Fe_{90}$ thin films of different thicknesses is explored by varying the magnitude and orientation of the bias magnetic field from nearly in-plane to nearly out-of-plane direction of the thin film surface. The precessional frequency and effective damping in this system are found to be strongly correlated with the development of weak out-of-plane anisotropy when the film thickness increases. We have further investigated the femtosecond laser induced collective precessional dynamics in two-dimensional nanodot arrays by TR-MOKE microscopy with varying lattice properties. We have observed a transition from a strongly collective to a completely isolated magnetization dynamics via various weakly collective dynamics by systematically increasing the inter-dot separation in nanodot arrays having hexagonal, honeycomb and octagonal lattice symmetries. The effect of anisotropic dipolar interaction between the nanodots arranged in octagonal and honeycomb lattices is demonstrated from their

time-resolved precessional dynamics. Experimental generation of hybrid magneto-dynamical modes in a single magnetostrictive Co nanomagnet grown on piezoelectric substrate (PMN-PT) has also been demonstrated. Laser induced surface acoustic wave gives rise to the periodic strain anisotropy at the interface and due to Villari effect, magneto-elastic modulation of magnetization dynamics is evidenced within the nanomagnet. The spin-wave modes are composed of both the periodic strain- and laser-induced spin precession. We then demonstrate an all-optical detection of spin-Hall effect in Sub/W(t)/$Co_{20}Fe_{60}B_{20}$(3 nm)/SiO_2(2 nm) heterostructures with varying the thickness (t) of W. Exploiting TR-MOKE microscopy we study the modulation of Gilbert damping of the adjacent $Co_{20}Fe_{60}B_{20}$ layer induced by the spin current induced spin torque from the W layer. The damping modulation is significantly high for the heterostructures having β-W and its nonmonotonic decrease across the β-W to α-W phase transition regime with increasing W-thickness is correlated with the resistivity change. The charge current to spin current conversion efficiency, *i.e*. spin-Hall angle for W is also estimated. The experimental and numerical results presented in this thesis may find applications in energy efficient magnetic data storage and memory technology as well as on-chip GHz frequency communication devices.

List of Publications

Included in this thesis

1. Transition from Strongly Collective to Completely Isolated Ultrafast Magnetization Dynamics in Two-Dimensional Hexagonal Arrays of Nanodots with Varying Inter-dot Separation; **S. Mondal**, S. Choudhury, S. Barman, Y. Otani, and A. Barman, *RSC Advances* **6**, 110393 (2016).
2. All-optical Detection of the Spin Hall Angle in W/CoFeB/SiO_2 Heterostructures by Varying Tungsten Layer Thickness; **S. Mondal**, S. Choudhury, N. Jha, A. Ganguly, J. Sinha, and A. Barman, *Physical Review B* **96**, 054414 (2017).
3. Influence of Anisotropic Dipolar Interaction on the Spin Dynamics of $Ni_{80}Fe_{20}$ Nanodot Arrays Arranged in Honeycomb and Octagonal Lattices; **S. Mondal**, S. Barman, S. Choudhury, Y. Otani, and A. Barman, *Journal of Magnetism and Magnetic Materials* **458**, 95 (2018).
4. Laser Controlled Spin Dynamics of Ferromagnetic Thin Film from Femtosecond to Nanosecond Time scale; **S. Mondal** and A. Barman, *Physical Review Applied* **10**, 054037 (2018).
5. Hybrid Magneto-dynamical Modes in a Single Magnetostrictive Nanomagnet on a Piezoelectric Substrate; **S. Mondal**, M. A. Abeed, K. Dutta, A. De, S. Sahoo, A. Barman, and S. Bandyopadhyay, *ACS Applied Material & Interfaces* **10**, 43970 (2018).
6. Role of Magnetic Anisotropy on the Ultrafast Magnetization Dynamics of Gd-Fe Thin Films with Different Thicknesses; **S. Mondal**, A. Talapatra, J. Arout Chelvane, J. R. Mohanty, and A. Barman (Submitted).

Not included in this thesis

7. Influence of Thickness Dependent Structural Evolution on Ultrafast Magnetization Dynamics in $Co_{2.0}Fe_{0.4}Mn_{0.6}Si$ Heusler Alloy Thin Films; S. Pan, **S. Mondal**, T. Seki, K. Takanashi, and A. Barman, *Physical Review B* **94**, 184417 (2016).
8. Enhanced Amplification and Fan-Out Operation in an All-Magnetic Transistor; S. Barman, S. Saha, **S. Mondal**, D. Kumar, and A. Barman, *Scientific Reports* **6**, 33360 (2016).

9. Investigation of Magnetization Dynamics in Two-dimensional $Ni_{80}Fe_{20}$ Diatomic Nanodot Arrays; A. De, **S. Mondal**, C. Banerjee, A. K. Chaurasiya, R. Mandal, Y. Otani, R. K. Mitra, and A. Barman, *Journal of Physics D: Applied Physics* **50**, 385002 (2017).
10. Ultrafast Magnetization Dynamics in a Nanoscale Three-Dimensional Cobalt Tetrapod Structure; S. Sahoo, **S. Mondal**, G. Williams, A. May, S. Ladak, and A. Barman, *Nanoscale* **10**, 9981 (2018).
11. Field Controlled Ultrafast Magnetization Dynamics in Two-dimensional Nanoscale Ferromagnetic Antidot Arrays; A. De, **S. Mondal**, S. Sahoo, S. Barman, Y. Otani, R. K. Mitra, and A. Barman, *Beilstein Journal of Nanotechnology* **9**, 1123 (2018).
12. All Optical Detection of Picosecond Spin-wave Dynamics in Two-dimensional Annular Antidot Lattice; N. Porwal, **S. Mondal**, S. Choudhury, A. De, J. Sinha, A. Barman, and P. K. Datta, *Journal of Physics D: Applied Physics* **51**, 055004 (2018).
13. Shape Dependent High Frequency Spin-Wave Dynamics in Nanoscale Magnonic Crystal; A. De, **S. Mondal**, S. Choudhury, S. Sahoo, S. Majumder, Y. Otani, and A. Barman, *Journal of Magnetism and Magnetic Materials* **487**, 165263 (2019).
14. All Optical Detection of Spin Transparency by Spin Pumping in β-Ta/CoFeB Thin Films; S. N. Panda, **S. Mondal**, J. Sinha, S. Choudhury, and A. Barman, *Science Advances* **5**, eaav7200 (2019).
15. Tunability of Domain Structure and Magnonic Spectra in Antidot Arrays of Heusler alloy; S. Mallick, **S. Mondal**, T. Seki, S. Sahoo, T. Forrest, F. Maccherozzi, A. Barman, K. Takanashi, and S. Bedanta (accepted in *Physical Review Applied,* 2019).
16. All Optical Study of Angle Dependent Mode Conversion and Mode Hopping in 2D Annular Antidot Lattice; N. Porwal, A. De, **S. Mondal**, K. Dutta, S. Choudhury, J. Sinha, A. Barman, and P. K. Datta (accepted in *Scientific Reports,* 2019).
17. Tri-State Buffer: Magnetic Vortex Transistor Based Logic Devices; **S. Mondal**, S. Barman, and A. Barman (submitted).
18. Edge Localization of Spin Waves in Antidot Multilayers eith Perpendicular Magnetic Anisotropy; S. Pan, **S. Mondal**, M. Zelent, R. Szwierz, S. Pal, O. Hellwig, M. Krawczyk, and A. Barman (submitted).
19. Observation of Band Narrowing and Mode Conversion in Two-dimensional Binary Magnonic Crystal; N. Porwal, K. Dutta, **S. Mondal**, S. Choudhury, J. Sinha, A. Barman, and P. K. Datta (submitted).

Book Chapters

1. Precessional Magnetization Dynamics and Spin Waves in 3D Ferromagnetic Nanostructures, S. Mondal, S. Sahoo, and **A. Barman,** in *Three-Dimensional magnonics: Layered Micro- and Nano-Structures*, Ed. G. Gubbiotti, Pan Stanford Publishing (ISBN 9789814800730-CAT#K426145).
2. Tunable picosecond magnetization dynamics in ferromagnetic nanostructures, S. Choudhury, S. Mondal, A. De and **A. Barman**, *21st century Nanoscience: A Handbook*, Ed. Klaus Sattler, Taylor & Francis Books, Inc. (accepted).

Acknowledgement

Since beginning of this five years' journey, I started working without any expectation. Unexpectedly, I was blessed with many things. Most importantly, I received 'appreciation' from my supervisor, Prof. Anjan Barman. He taught me each and every detail of the lab culture, way of planning new experiments, harnessing new ideas, analyzing data and to present those in extremely scientific manner. While working with him I feel that an experimentalist should always keep the mind and intuitions open for new challenges. His positive approach made me aware of the fact that hurdles can be crossed by only knowledge and perseverance. There is no shortcut to this journey. Starting from personal life to professional life, he has always been supportive and caring. I would like to thank him for his continuous effort to fashion out a 'motivated researcher' from an 'obedient student'. I would like to thank Dr. Saswati Barman from bottom of my heart for her constant guidance while working in various projects. It was great opportunity for me to learn several things from her including LLG simulator.

I would like to thank my seniors who implemented work ethics within me from the very beginning. Dr. Susmita Saha and Dr. Semanti Pal, taught me how to build up lab habits, how to search literatures, how to patiently face the challenges during difficult experiments. They trained me with the optical alignment from the scratch. Dr. Chandrima Banerjee, helped me a lot in learning various useful software, performing simulations, explaining experimental results. They have been exceedingly loving and caring. I would like to thank Dr. Bivas Rana, Dr. Ruma Mandal, Dr. Bipul Kumar Mahato, Dr. Debanjan Polley, Dr. Kallol Mukherjee and Dr. Arnab Ganguly for providing me really fruitful suggestions during my research. I would like to acknowledge Dr. Dheeraj Kumar for developing DotMag code and helping us in understanding the 'spin waves' better. Dr. Jaivardhan Sinha is the person who guided me wholeheartedly in configuring experiments and preparing the manuscripts every time I felt lack of confidence. He is a very humble person and his delicacy is something that I would like to adopt for me. Dr. Dipak Kumar Das, Dr. Rakhi Acharyya and Dr. Sumona Sinha were always there as my well-wishers. Being a part of a big experimental group I got opportunity to work with a lot of my juniors, named specifically, Avinash, Kartik, Sourav, Sudip, Panda, Koustuv, Sayantan, Arundhati, Amrit, Anuj, and Pratap. They all love me. Undoubtedly, they are

my best companion ever. My friends, Santanu, Anulekha and Samiran, who share the same time line in the lab, also shared many colorful memories which I will cherish forever. I express my love to all those juniors who joined here as project students.

I would like to acknowledge our collaborators, Prof. Maciej Krawcyk from Poland for giving me the opportunity to visit his group and to continue the collaboration. I would also like to thank Prof. Y. Otani (from Riken, Japan), Prof. O. Hellwig (Germany), Prof. K. Takanashi, Tohoku, Japan), Dr. Subhankar Bedanta (from NISER, Bhubaneswar, India), Prof. P. K. Datta (IIT Kharagpur, India) and Dr. Jyoti Mohanti (IIT Hyderabad, India) for providing us with the samples in which we explored exciting physical phenomena. I pay my sincere gratitude to Prof. S. Bandhyopadhyay (Virginia, USA) whose knowledge and wisdom mesmerized us while working with him in our lab.

I would like to express my gratitude to all the colleagues in this campus. I acknowledge the help and support from the academic section and technical cell of our Centre for smoothly carrying out my research. I acknowledge DST, Govt. of India, for Inspire fellowship. I thank S. N. Bose Centre for giving me the opportunity to pursue research with great facilities and amenities in the campus.

A short paragraph cannot be sufficient for describing the contribution of my friends and family members. Still I thank my parents (Mr. Subrata Kumar Mondal and Mrs. Karabi Mondal), my sister (Ms. Subarna Mondal) and my grandparents from bottom of my heart for making my life easier so that I can concentrate more on my studies. My friends, Ankita Konar, Ankita Datta, Ankita Sarkar, Ankita Mahajan, Monalisa Halder, Puspita Ray and Sneha Paul have been exceedingly supportive. I would like to thank Mr. Sauradip Mukherjee for his intensive care since our childhood. Irrespective of the situation, he kept pushing me continuously towards my dream. Last but not the least I personally feel that I would have never been inclined towards research, if my teachers were not there since early stage of my life. This thesis is a tribute to all of them.

Sucheta Mondal

S. N. Bose National Centre for Basic Sciences,

Salt Lake, Kolkata, India.

List of Abbreviations

AFM: Atomic force microscope

AHE: Anomalous Hall effect

AOS: All optical switching

AO-HDS: All optical helicity dependent switching

BLS: Brillouin light scattering

CPA: Chirped pulse amplification

CW: Continuous wave

DC: Direct current

DE: Damon–Eshbach

DLT: Damping like torque

DMI: Dzyaloshinskii Moriya interaction

DPSS: Diode pumped solid state

DW: Domain wall

EBL: Electron beam lithography

EDX: Energy dispersive X-ray spectroscopy

FDM: Finite difference method

FEM: Finite element method

FLT: Field like toque

FM: Ferromagnet

FMR: Ferromagnetic resonance

fs: Femtosecond

FWHM: Full width at half maxima

GMR: Giant magnetoresistance

GPU: Graphical processing unit

GVD: Group velocity dispersion

HAMR: Heat assisted magnetic recording

HM: Heavy metal

IFE: Inverse Faraday effect

IP: In-plane

IR: Infra-red

(I)SHE: (Inverse) spin Hall effect

LCP: Left circularly polarized

LLG: Landau-Lifshitz-Gilbert

MC: Magnonic crystal

MFM: Magnetic force microscope

MO: Microscope objective

MOD: Modulation of damping

MOKE: Magneto-optical Kerr effect

MRAM: Magnetoresistive random access memory

MSBVW: Magnetostatic backward volume wave

MSFVM: Magnetostatic forward volume mode

MSSW: Magnetostatic surface wave

MTJ: Magnetic tunnel junction

NA: Numerical aperture

NLSV: Nonlocal spin valve

NM: Nonmetal

OBD: Optical bridge detector

OOMMF: Object oriented micromagnetic framework

OOP: Out-of-plane

PBS: Polarizing beam splitter

ps: Picosecond

PSSW: Perpendicular standing spin waves

PZT: Piezoelectric transducer

QHE: Quantum Hall effect

RCP: Right circularly polarized

RE-TM: Rare earth-transition metal

RF: Radio frequency

RGA: Regenerative amplifier

RR: Retro-reflector

RT: Room temperature

SEM: Scanning electron microscope

SDG: Synchronized delay generator

SHA: Spin Hall angle

SHE: Spin Hall effect

SHE-ST: Spin Hall effect generated spin torque

SHG: Second harmonic generation

SOC: Spin orbit coupling

STNO: Spin-torque nano oscillator

STT: Spin transfer torque

SW: Spin wave

TMR: Tunnel magnetoresistance

TR-MOKE: Time-resolved magneto-optical Kerr effect

TEM: Transmission electron microscope

UV: Ultraviolet

VSM: Vibrating sample magnetometer

VPUF: Verdi pumped ultrafast laser

XMCD: X-ray magnetic circular dichroism

XRD: X-ray diffraction

List of Figures

Contents

Chapter 1

1 Introduction

'Spin' is one of the most fundamental quantum numbers for any particle. It is very much associated with the magnetization of the magnetic elements. Spin alone or with charge can be harnessed for storing and processing information. During last few decades this close association has caused revolutionary growth in the 'Information Technology'. Starting from read head of magnetic recording media, nonvolatile magnetic random access memory to ultramodern robotics technology, the charge-spin association undoubtedly plays a key role. In magnetic memory devices magnetization state is switched by external magnetic field to achieve stable 'up' and 'down' configuration which in turn can store a 'bit', the smallest unit of data in a computer. A vigorous effort has been made by the scientists to explore a smart way to manipulate a spin and exploit the interaction between spin current and magnetic moment. The growing demand of 'storing more information within less space' has increased the quest to study the static and dynamic properties of nanoscale magnetic systems, such as ultrathin films, heterostructures and patterned magnetic media. One important aspect of magnetization dynamics is spin-waves (SWs) and quanta of SWs known as 'magnons'. This leads to the development of the vast field of 'Nanomagnetism' with its young sub-brunch known as 'Magnonics'. If a ferromagnetic medium is artificially pattered in a way that the magnetic properties exhibit periodic modulation in space, similar to photonic or sonic crystals and acts as a medium of propagation of SWs (magnons), then it can be termed as a magnonic crystal (MC). The physical phenomena associated with magnetization dynamics in these nanomagnetic systems are extremely fascinating. On the other hand, the development of spin-based analogues of charge-based devices has emerged as a very important field of study, named as 'spintronics'. An important aspect of this field is the spin-charge conversion in low dimensional systems.

1.1 Magnetization Switching

In the following sections, we discuss some of the recent advancements in the fields of spintronics and spin dynamics.

1.1.1 All-Optical Switching

Magnetic field can be sensed by the magnetization easily and application of magnetic field on static magnetization can control its direction. In case of time varying magnetization, it is found that if this field exerts a torque on the magnetization then the mechanism of precessional switching can switch the magnetization faster [1-4]. Still these deterministic switching is not enough to meet the growing demand of faster switching speed of the devices. Researchers thus continued their hunt for various emerging mechanisms, including all-optical switching (AOS) [5], strain induced switching [6] and spin current induced switching [7]. Earlier experiments on laser-induced ultrafast demagnetization [8] and spin reorientation showed new pathway to exploit [9] ultrafast lasers for manipulating magnetization in the time scales of a picosecond to femtosecond. Sub-pico second laser pulse was used by Kimel *et al.* to excite the spin dynamics non-thermally and coherent control over the magnetization was achieved by way of the inverse Faraday effect (IFE) [10]. It was demonstrated that electric field of light can act as an effective magnetic field directed along the wave vector of the light. Thus, lights with right and left circular polarization should act as magnetic fields with opposite sign. They showed that in $DyFeO_3$, which is a rare-earth orthoferrite, circularly polarized pump pulses of opposite helicities excite magnetization precession with opposite phases. This ignited huge research interest in the field of ultrafast opto-magnetism. The aim was complete reversal of the magnetization by optically induced field pulses. In 2007, Stanciu *et al.* experimentally demonstrated a method for compact all-optical recording of magnetic bits [5]. They used a circularly polarized laser beam to scan across a ferromagnetic sample while simultaneously altering the helicity of the beam. The main two factors responsible for magnetization switching was laser induced heating and a circularly polarized light acting as effective magnetic field. The former process energizes the spin system into a demagnetized and transient ferromagnetic state [11], and latter is consequence of IFE [12]. This magnetization reversal phenomenon namely all-optical helicity dependent switching (AO-HDS) was then observed for multilayered synthetic ferrimagnets [13]. Later, it was evidenced that switching is a consequence of angular momentum transfer between the sublattices in ferrimagnet [14]. After Lambert *et al.* reported AO-HDS in ferromagnetic Co/Pt multilayers and partial switching in FePt granular films [15], the debate about the origin of AO-HDS began to intensify. They proposed that IFE can lead

to AO-HDS when the system temperature approaches the Curie temperature within very short time scale. A material with low Curie temperature is desirable for AO-HDS. For creating a favorable condition for AOS role of magnetic damping is also inadvertent. Moreover, researchers have observed the effect of optical spin transfer torque (consisting of field like and damping like torque components) along with IFE [16]. Thus, several mechanisms were proposed to explain the magnetization reversal due to application of ultrafast laser and the field began to expand.

It is pertinent to mention here that, not only reversing the magnetization direction but also femtosecond laser can modulate several static and dynamic properties of the magnetic materials. The coercivity and anisotropy of the ferromagnetic thin films can also be modified by laser fluence, which show application potential in heat assisted magnetic recording (HAMR) technology [17]. Recent reports reveal that precessional frequency and damping can be modulated noticeably due to application of fluence in optical excitation technique and the process is reversible [18-20]. All these studies stipulate the necessity for unification of ultrafast magnetic processes in magnetic thin films and its control over a broad time scale for enabling the integration of those processes in a single device and simultaneous use one effect to control another.

1.1.2 Strain Induced Switching

Nanomagnetic logic and memory applications require switching of magnetization with high efficiency. For example, in modern spin transfer torque magnetic random access memory (STT-MRAM), 'writing' of a bit is accomplished by switching the magnetization of the free layer (a soft nanomagnet) by a spin transfer torque (STT) generated from a spin-polarized current [21,22]. Application of spin polarized current to write bits in nonvolatile magnetic memory has become an effective approach because it promises to reduce the unnecessary power consumption in the system in comparison to existing electronic memory devices, including conventional MRAM devices. The 'reading' is done by measuring the magnetoresistance of two opposite orientation of free layer magnetization with respect to the fixed layer. In order to commercialize any magnetic tunnel junction (MTJ)-based device prototypes, it is very important to achieve extremely high ratio between the rate of success and number of attempts made to switch the magnetization. Recently, it is claimed that the strain mediated switching [23,24] could be a more efficient approach than the STT-based switching which

passively consumes more energy than it is required to operate even an electronic transistor. Strain mediated switching can be achieved in magnetostrictive ferromagnet (FM) and piezoelectric nonmagnet (NM) based heterostructures. In case of magneto-elastically coupled nanomagnet fabricated on top of piezoelectric substrate, electric field is applied in the substrate which produces highly localized in-plane (IP) compressive strain (due to d_{31} coupling) and out-of-plane (OOP) tensile strain (due to d_{33} coupling). This mechanical strain gets coupled to the magnetization of the nanomagnet due to Villari effect [25] which drives the switching [23]. This entire process involves three types of energy dissipations: internal energy, mechanical energy (stress×strain×volume of magnet) and electrical energy (capacitance×voltage^2) [26]. These energies are found to be in tens of aJ order [27]. Despite of being energy efficient this technique is not used in MRAM because it has certain drawbacks. First of all, the nanomagnets cannot always be flipped by 180°, which is necessary. In case of 90° rotation, the probability of writing and storing of data is 50%. The magnetization can flip in either side following the shape anisotropy axis of the nanostructure. At room temperature, geometrical defects, such as voids in the nanostructures will exacerbate switching failures [28]. Later, researchers have applied a trick to overcome these problems by employing two step switching process. Two pairs of electrodes fabricated in diagonally opposite position around the nanomagnet can apply sequential voltage leading towards a complete 180° switching of the magnetization. This strain mediated scheme has larger cell foot print and is not suitable for high density data storage application [6]. On the other hand, it is necessary to explore the speed limit for strain mediated switching process. Interestingly, the coupling between strain induced switching and SW dynamics in nanostructures can give rise to intriguing hybrid magnetodynamical modes in the nanomagnet, with characteristic frequencies of in the range of high GHz frequency. This indicates that in magnetoelastic nano-oscillators strain can affect magnetization in time scales much smaller than 1 ns, which will be advantageous of increasing the speed of the magnetoelectric devices.

1.1.3 Spin Current Induced Switching

The discovery of spin current [29-31] ignited huge research interest for designing various prototypes of spin-based devices as a reliable substitution of charge-based devices. It is pertinent to mention here that the demonstration of the giant magneto resistance (GMR) effect is one of the most remarkable successes of spintronics [32,33].

The first commercial product based on GMR was a magnetic field sensor released in 1994 [34]. In 1997, the first GMR read head for reading data stored in magnetic hard disks was released by IBM [35]. GMR-based read heads replaced earlier read heads based on the anisotropic magnetoresistance effect. Today, GMR based read heads are frequently found in laptop or desktop computers, and other consumer electronic devices. In the 21st century, tunneling magnetoresistance (TMR)-based read heads started to replace GMR based read heads. The typical TMR device is essentially a thin insulating layer sandwiched between two ferromagnetic contacts [36]. Later, the current driven magnetic domain wall (DW) movement in racetrack memory [37], spin-current-driven spin-torque nano-oscillator (STNO) [38] and various other inventions added new dimensions to the spintronics research. However, the device performances still rely on the application of charge current in the active terminals followed by passive usage of spin current for further manipulation. Though lesser power is required in comparison to the charge-based devices, those cannot completely get rid of the bottleneck of Joule heating. The celebrated Moore's law (published in 1965) foreseen the doubling of device density on a single chip in every 18^{th} months [39]. To maintain the ever-growing demand of storing data by the society, it is very important to exercise control over the miniaturization and energy dissipation by the device. However, the following example can shed light on the difficulties of designing ultra-high density storage device. If a chip (similar to Pentium IV) consists of 10^8 transistors per cm^2 and each spinFET consumes 20μW power, then the entire chip will consume about 20 kW/cm^2 power [31]. This is exceptionally higher than a commercially available Si-based chip at present. Thus, the size of spinFET and also the whole device cannot be reduced due to this energy threshold. Later, a more radical branch of spintronics was developed as 'single spin' spintronics. Here, a single electron subjected to magnetic field does not move in real space however its polarization can be switched in two opposite states - 'up spin' and 'down spin'. This two spin states are manipulated for storing data in the form of binary digits '0' and '1'. This requires no active participation of charge current, hence involves no Joule heating. A manifestation of such progressive idea is single spin logic [31]. However, the Boolean formalism cannot be realized unless two or more spins start to interact. Consequently, the exploitation of Qbits in quantum computation has become a matter of immense research interest worldwide.

The idea of utilizing the pure spin current is a major breakthrough, which promises revolutionary development in the energy-efficient data-storage technology [40]. It is well known that use of charge current and spin-polarized current involves flow of charge and ensuing Joule heating leading towards unwanted power loss. This puts a limit towards miniaturization of the magnetic recording devices, which is a setback for the ever-growing demand of data to be used and stored by the society in the coming days. Various approaches have been explored relentlessly to overcome this hurdle. Most celebrated one is the generation and exploitation of pure spin current, which is dissipationless and compatible with the length and time scales associated with nanotechnology. For efficient use of pure spin current in a circuit, one needs a source (spin battery), a conductor, a detector and an external manipulator, and researchers in this field have been working intensely in developing various components of a spintronic device. The idea of 'spin battery' was surfaced early of this century where pure spin current from the precessing spins within a ferromagnet was injected into a nonmagnetic conductor due to the spin bias developed in the system [41]. Several mechanisms have been proposed for the creation of pure spin current, such as, spin pumping (the mechanism believed to be responsible for operating 'spin battery') [42-44], Rashba effect [45-47], inverse Rashba-Edelstein effect [48], spin Hall effect (SHE) [49-52], inverse SHE [53] and various spin-caloric effects (which rely upon the coupling of heat transport with spintronics: spin Seebeck effect, spin Peltier effect, spin Nernst effect) [54-56] etc. However, this spin-charge conversion cannot be directly measured in real space and time, and passive mechanisms have been generally used to quantify this conversion efficiency. Consequently, the idea of exploiting 'spin-current meter' has become popular [57]. SHE is an efficient and well-studied method for generation of pure spin current, and to quantify its spin-charge conversion efficiency an important parameter, namely, spin Hall angle (SHA), has been coined. During last two decades, this effect has been studied in a series of materials. Apart from semiconductors [58], metal [59], transition metal [60], transition metal oxide [61], topological insulators etc. have become excellent materials for the efficient generation of pure spin current. Pt, Ta and W are the popular HMs, which are being studied extensively these days because of their high SOC strength [57,60,62,63]. It is observed that W and Ta have larger SHA with opposite sign compared to that of Pt. Moreover, W and Ta are cheaper materials than Pt, show less tendency towards developing perpendicular magnetic anisotropy and exhibit

interesting structural evolution from β- to α-phase with film thickness, which may further affect the SHA. Among these different structural phases, β is higher resistive phase with distorted tetragonal crystal structure with stronger SOC. However, stability of this phase also depends upon the deposition conditions. The SHE generated spin torque (SHE-ST) induced switching has been established to be more efficient than the conventional STT in MTJ [7,21]. The so called spin-orbit fields (or torques), generally originates from exchange of the angular momentum between crystal lattice and magnetic moment, which makes it possible to switch the magnetization of a ferromagnetic layer. Thus, a new subfield of spintronics has grown known as 'Spin-orbitronics' [64], which aims the development of new generation spin-based data recording and processing technology utilizing the effect of SOC. In HM/FM (or AFM) heterostructures the current-induced torques are generally originated from the SOC within the bulk of the HM or at the interface [65,66]. There can be two types of torque acting simultaneously on the magnetization of the adjacent FM layer: a damping-like torque (DLT) and a field-like torque (FLT). However, their effective magnitudes within the heterostructure depend upon several factors, namely relative contribution from SHE and Rashba effect which vary with layer thickness [65], quality of interface in terms of the spin-mixing conductance, spin-flip probability and interfacial spin transparency [67], and electronic properties (such as charge conductivity) [68]. There are many sophisticated techniques available for experimental detection of spin-Hall-generated spin current, such as, non-local spin valve (NLSV) technique [69], second harmonic generation [70], spin-torque ferromagnetic resonance (ST-FMR) [7,71], inverse spin-Hall effect measurement, static magneto-optical Kerr effect (MOKE) [72], etc. However the value of SHA reported from various techniques are found to vary by a factor of 20. For example, in case of Pt, the reported values vary in the range of 0.0037 to 0.08 [52]. There are several factors involved as experimental artifacts in different techniques. One of those is most importantly, the interfacial transparency. During the detection, the HM layer act as 'spin-sink' to the adjacent FMs. When the spin current is generated in the HM layer, the effective torque exerted in the FM layer modulates the damping and the extent of modulation can be reduced if the HM/FM interface is not fully transparent. Thus, the magnitude of spin torque extracted without considering the spin-mixing conductance, spin transparency and other interfacial effects, may contain large error. Naturally, overlooking of spin transparency may lead to an incomplete determination of

intrinsic SHA. Despite of having plethora of work reported on the generation and manipulation of pure spin current, quantification of SHA and extent of modulation of damping (MOD) are still a matter of huge debate. Development of an all-optical detection technique based on time-resolved MOKE (TR-MOKE) magnetometry for unambiguous determination of SHA and MOD in HM/FM heterostructures may lead to a solution of this problem [73,74]. All-optical method does not suffer from the effect of defects and inhomogeneities due to the large area averaging. Moreover, magnetization damping can be extracted directly from time-resolved precession data, which is more advantageous than other available techniques.

1.1.4 Nanomagnetism and Magnonics

Nanostructured magnetic materials offer several new functionalities, which could not have been achieved from their bulk counterparts [75,76]. Currently broad range of real-world applications of nanostructured materials are available and continuously emerging, exploiting many of these functionalities. High density media for data storing [77], spin-based transistors [78], nanomagnet logic [79], reconfigurable waveguide for energy-efficient transmission of signal [80], switching of nanomagnet for nonvolatile memory application [6,81], spin-Hall nano-oscillators (SHNO) [82], nanobiomedicines [83], and neuromorphic computation [84] are just a few examples of those devices which are proposed to be designed in submicron to atomic length scales. SW-based systems can offer excellent scalability, which are not accessible in electromagnetic wavebased system (*e.g.* photonic crystal) [85]. Additionally, it promises low energy consumption and high data processing rate. These exciting opportunities fueled an upsurge in the research interest during last two decades and enormous efforts have been made to develop advanced fabrication procedures and new state of the art characterization techniques for studying the static and dynamic properties of nanostructured magnetic materials. This journey began with patterning a thin ferromagnetic film with a certain periodicity or preparing chemically grown assembly of micro and nanostructures in mono-dimension. Stripes [86-88], waveguides [89,90], nanowires [91,92], chains of nanoparticles [93], MCs with unidirectional periodic modulation of magnetic properties are the members of this one-dimensional (1D) nanostructure family [94,95]. Those exhibit some exciting phenomena such as, SW propagation along with transmission and reflection from the artificial boundaries, magnonic band formation with partial band gap, etc. However, researchers soon

realized that an extension to another dimension may provide more control points for creation of stop bands for propagating SWs, processing and storing of information within lesser space, etc. Most of these features originate from the competition between short-range exchange coupling, long-rage dipolar coupling and magnetic anisotropy. Initially lattice of bubble domains inside a ferromagnetic film was considered as two-dimensional (2D) structuring which was also used in the primary stage of magnetic recording. Bit-patterned media (BPM) was developed that utilize the patterned 2D arrays of magnetic bits, which rely on data storage by switching the magnetic field [96]. Further progress in fabrication techniques facilitates the construction and investigation of magnetization dynamics of nanodot arrays [97], nanohole arrays (or antidot array) [98,99], MC [100-103], spin-ice structures [104], magnetic solitons [105] and skyrmion lattices [106,107].

Based on the structural features MCs can be broadly categorized into three classes: a), nanodots [108,109] b) antidots [110-113] and c) nano-composites including multicomponent materials and structures [114-118]. Initially works on these structures were limited to studying their precessional frequency and damping leading towards possible applications in magnetic storage and memory. With the emergence of magnonics in last one decade, a plethora of study in probing their SW dynamics, including magnon band structures, band gaps and propagation characteristics have been made. Further, multiphysics aspects of excitation and control of such structures using spin torque, voltage and other external stimuli are at the nascent stage. The nature of SW is governed by the internal fields as well as the dipolar and multipolar interactions in MC. In case of dot lattice, the SW can exhibit collective as well as non-collective behavior while tuning the dipolar interactions. Importantly studies of spin dynamics of 2D lattices of nanodots by varying the shape and size of the dots [108,119,120] as well as the lattice parameters, [109,121-124] have been conducted by using TR-MOKE magnetometry, FMR technique and Brillouin light scattering (BLS) technique.

Aiming towards the construction of ultra-high density data storage and memory devices with advanced functionalities, researchers have started to explore several new spin textures in the third dimension (3D) of a nanomagnetic system. The idea of breaking mono-domain formalism along the thickness of existing 2D nanostructures and

designing of 3D objects in micro and nanoscale gives birth to a new subfield as '3D nanomagnetism' [125,126].

1.2 Objectives of the Thesis

The study of ultrafast magnetization dynamics from femtosecond to nanosecond time scales is the bedrock of this thesis. The objective can be broadly described as follows: effect of laser fluence, magnetic anisotropy, nanostructuring, magneto-elastic coupling and spin-Hall-generated pure spin current on the ultrafast magnetization dynamics of ferromagnetic systems. The studied systems are classified as follows:

(1) Ultrafast magnetization dynamics in ferromagnetic thin films

A. Effect of laser fluence on modulation of magnetization dynamics of ferromagnetic thin films: Chapter 4 describes the study of pump fluence-dependent ultrafast magnetization dynamics in $Ni_{80}Fe_{20}$ thin films having different thicknesses. The effect of increasing system temperature to Curie temperature ratio on various dynamical entities, such as, ultrafast demagnetization time, remagnetization time, Gilbert damping, and precessional frequency, is comprehensively studied.

B. Role of magnetic anisotropy on modifying the magnetization dynamics in rare earth-transition metal system: Chapter 5 describes the study of precessional magnetization dynamics in Gd-Fe thin films of different thicknesses by varying the magnitude and orientation of the bias magnetic field from nearly IP to nearly OOP direction of the film plane. The precessional frequency and effective damping in this system are found to be strongly correlated with the development of OOP anisotropy when the film thickness increases.

(2) Spin-wave dynamics in ferromagnetic nanostructures

A. Investigation and control of spin waves by varying lattice properties in two-dimensional magnonic crystals made of nanodot arrays: In chapter 6 and 7, we investigate the femtosecond laser induced collective precessional dynamics in $Ni_{80}Fe_{20}$ nanodot arrays arranged in different lattices by TR-MOKE microscope. Here, we demonstrate a transition from a strongly collective to a completely isolated spin dynamics via several weakly collective dynamics by varying the inter-dot separation of circular nanodots of 100-nm-diameter arranged in hexagonal, honeycomb and

octagonal lattices. Further, the comparison of configurational magnetic anisotropy originating from anisotropic dipolar interaction between the nanodots arranged in octagonal and honeycomb lattice is investigated quantitatively.

B. Strain induced modulation in spin-wave dynamics of a single magnetostrictive nanomagnet: In chapter 8, experimental demonstration of generation of hybrid magneto-dynamical modes are presented for a single magnetostrictive Co nanomagnet grown on a piezoelectric substrate (PMN-PT). Laser induced surface acoustic wave (SAW) gives rise to the periodic strain anisotropy in the nanomagnet due to Villari effect and magneto-elastic modulation of precessional dynamics is evidenced. The magnetodynamical modes are reproduced by micromagnetic simulations and the spatial profiles of the modes reveal new types of hybrid modes composed of both the SAW and spin precession inside the nanomagnets.

(3) Precessional dynamics in nonmagnet/ferromagnet heterostructures

A. Spin-Hall-generated spin torque induced modulation of Gilbert damping: In chapter 9, we demonstrate an all-optical detection of spin-Hall effect (SHE) in Sub/W(t)/$Co_{20}Fe_{60}B_{20}$(3 nm)/SiO_2(2 nm) heterostructures with varying the thickness (t) of W. Exploiting TR-MOKE microscopy we study the modulation of Gilbert damping of the adjacent CoFeB layer induced by the spin-current-induced spin torque from the W layer. The damping modulation is significantly high, and it is correlated with the resistivity change across the β-W to α-W phase transition regime with increasing W-thickness. The charge current to spin current conversion efficiency (SHA) for W is also explored.

References

1. T. Gerrits, H. A. M. van den Berg, J. Hohlfeld, L. Bär, and T. Rasing, Nature **418**, 509 (2002).
2. T. M. Crawford, P. Kabos, and T. J. Silva, Appl. Phys. Lett. **76**, 2113 (2000).
3. M. Bauer, R. Lopusnik, J. Fassbender, B. Hillebrands, and H. Dotsch, IEEE Trans. Magn. **36**, 2764 (2000).
4. A. Barman, V. V. Kruglyak, R. J. Hicken, J. Scott, and M. Rahman, J. Appl. Phys. **97**, 10A710 (2005).

5. C. D. Stanciu, F. Hansteen, A. V. Kimel, A. Kirilyuk, A. Tsukamoto, A. Itoh, and T. Rasing, Phys. Rev. Lett. **99**, 047601 (2007).
6. A. K. Biswas, H. Ahmad, J. Atulasimha, and S. Bandyopadhyay, Nano Lett. **17**, 3478 (2017).
7. L. Liu, C.-F. Pai, Y. Li, H. W. Tseng, D. C. Ralph, and R. A. Buhrman, Science **336**, 555 (2012).
8. E. Beaurepaire, J. C. Merle, A. Daunois, and J. Y. Bigot, Phys. Rev. Lett. **76**, 4250 (1996).
9. A. V. Kimel, A. Kirilyuk, A. Tsvetkov, R. V. Pisarev, and Th. Rasing, Nature 429, 850-853 (2004).
10. A. V. Kimel, A. Kirilyuk, P. A. Usachev, R. V. Pisarev, A. M. Balbashov, and T. Rasing, Nature **435**, 655 (2005).
11. I. Radu, K. Vahaplar, C. Stamm, T. Kachel, N. Pontius, H. A. Dürr, T. A. Ostler, J. Barker, R. F. L. Evans, R. W. Chantrell, A. Tsukamoto, A. Itoh, A. Kirilyuk, T. Rasing, and A. V. Kimel, Nature **472**, 205 (2011).
12. T. D. Cornelissen, R. Córdoba, and B. Koopmans, Appl. Phys. Lett. **108**, 142405 (2016).
13. A. Kirilyuk, A. V. Kimel, and T. Rasing, Rep. Prog. Phys. **76**, 026501 (2013).
14. A. R. Khorsand, M. Savoini, A. Kirilyuk, A. V. Kimel, A. Tsukamoto, A. Itoh, and T. Rasing, Phys. Rev. Lett. **108**, 127205 (2012).
15. C. H. Lambert, S. Mangin, B. S. D. C. S. Varaprasad, Y. K. Takahashi, M. Hehn, M. Cinchetti, G. Malinowski, K. Hono, Y. Fainman, M. Aeschlimann, and E. E. Fullerton, Science **345**, 1337 (2014).
16. G.-M. Choi, A. Schleife, and D. G. Cahill, Nat. Commun. **8**, 15085 (2017).
17. W. Peng, Y.-T. Hsia, K. Sendur, and T. McDaniel, Tribol. Int. **38**, 588 (2005).
18. S. Mizukami, H. Abe, D. Watanabe, M. Oogane, Y. Ando, and T. Miyazaki, Appl. Phys. Express **1**, 121301 (2008).
19. B. Liu, X. Ruan, Z. Wu, H. Tu, J. Du, J. Wu, X. Lu, L. He, R. Zhang, and Y. Xu, Appl. Phys. Lett. **109**, 042401 (2016).
20. S. Mondal and A. Barman, Phys. Rev. Appl. **10**, 054037 (2018).
21. D. C. Ralph and M. D. Stiles, J. Magn. Magn. Mater. **320**, 1190 (2008).
22. S. Parkin, J. Xin, C. Kaiser, A. Panchula, K. Roche, and M. Samant, Proceedings of the IEEE **91**, 661 (2003).

23. A. K. Biswas, S. Bandyopadhyay, and J. Atulasimha, Appl. Phys. Lett. **103**, 232401 (2013).
24. J. Cui, J. L. Hockel, P. K. Nordeen, D. M. Pisani, C. Y. Liang, G. P. Carman, and C. S. Lynch, Appl. Phys. Lett. **103**, 232905 (2013).
25. A. H. Morrish, *in The Physical Principles of Magnetism*, (Wiley, New York, 1965), p. 545.
26. J. L. Drobitch, M. A. Abeed, and S. Bandyopadhyay, Jpn. J. Appl. Phys. **56**, 100309 (2017).
27. K. Roy, S. Bandyopadhyay, and J. Atulasimha, J. Appl. Phys. **112**, 023914 (2012).
28. M. A. Abeed, J. Atulasimha, and S. Bandyopadhyay, J. Phys. Condens. Matter. **30**, 394001 (2018).
29. S. Takahashi and S. Maekawa, Sci. Technol. Adv. Mater. **9**, 014105 (2008).
30. T. Shinjo (Ed.), *Nanomagnetism and Spintronics* (Elsevier B.V., Amsterdam, The Netherlands, 2009).
31. S. Bandyopadhyay and M. Cahay, *Introduction to Spintronics* (Boca Raton: CRC Press, 2008).
32. M. N. Baibich, J. M. Broto, A. Fert, F. N. Van Dau, F. Petroff, P. Etienne, G. Creuzet, A. Friederich, and J. Chazelas, Phys. Rev. Lett. **61**, 2472 (1988).
33. G. Binasch, P. Grunberg, F. Saurenbach, and W. Zinn, Phys. Rev. B 39, 4828 (1989).
34. J. Daughton, J. Brown, E. Chen, R. Beech, A. Pohm, and W. Kude, IEEE Trans. Magn. **30**, 4608 (1994).
35. G. A. Prinz, Science **282**, 1660 (1998).
36. J. S. Moodera, L. R. Kinder, T. M. Wong, and R. Meservey, Phys. Rev.Lett. **74**, 3273 (1995).
37. S. S. P. Parkin, M. Hayashi, and L. Thomas, Science **320**, 190 (2008).
38. S. Kaka, M. R. Pufall, W. H. Rippard, T. J. Silva, S. E. Russek, and J. A. Katine, Nature **437**, 389 (2005).
39. G. E. Moore, Electronics **38** (1965).
40. A. Hoffmann, Phys. Status Solidi C **4**, 4236 (2007).
41. A. Brataas, Y. Tserkovnyak, G. E. W. Bauer, and B. I. Halperin, Phys. Rev. B **66**, 060404 (2002).
42. P. Sharma, Science **307**, 531 (2005).
43. Y. Tserkovnyak, A. Brataas, and G. E. W. Bauer, Phys. Rev. Lett. **88**, 117601 (2002).

44. Y. Tserkovnyak, A. Brataas, and G. E. W. Bauer, Phys. Rev. B **66**, 224403 (2002).
45. Y. A. Bychkov and E. I. Rashba, JETP Letters **39**, 78 (1984).
46. J. C. R. Sánchez, L. Vila, G. Desfonds, S. Gambarelli, J. P. Attané, J. M. De Teresa, C. Magén, and A. Fert, Nat. Commun. **4**, 2944 (2013).
47. I. Mihai Miron, G. Gaudin, S. Auffret, B. Rodmacq, A. Schuhl, S. Pizzini, J. Vogel, and P. Gambardella, Nat. Mater. **9**, 230 (2010).
48. K. Shen, G. Vignale, and R. Raimondi, Phys. Rev. Lett. **112**, 096601 (2014).
49. M. I. Dyakonov and V. I. Perel, Phys. Lett. A **35**, 459 (1971).
50. J. E. Hirsch, Phys. Rev. Lett. **83**, 1834 (1999).
51. A. Hoffmann, IEEE Trans. Magn. **49**, 10 (2013).
52. R. A. Buhrman, L. Liu, and D. C. Ralph, arXiv:1111.3702 (2012).
53. E. Saitoh, M. Ueda, H. Miyajima, and G. Tatara, Appl. Phys. Lett. **88**, 182509 (2006).
54. K. Uchida, S. Takahashi, K. Harii, J. Ieda, W. Koshibae, K. Ando, S. Maekawa, and E. Saitoh, Nature **455**, 778 (2008).
55. J. Flipse, F. L. Bakker, A. Slachter, F. K. Dejene, and B. J. van Wees, Nat. Nanotechnol. **7**, 166 (2012).
56. S. Meyer, Y. T. Chen, S. Wimmer, M. Althammer, T. Wimmer, R. Schlitz, S. Geprägs, H. Huebl, D. Ködderitzsch, H. Ebert, G. E. W. Bauer, R. Gross, and S. T. B. Goennenwein, Nat. Mater. **16**, 977 (2017).
57. K. Ando, S. Takahashi, K. Harii, K. Sasage, J. Ieda, S. Maekawa, and E. Saitoh, Phys. Rev. Lett. **101**, 036601 (2008).
58. Y. K. Kato, R. C. Myers, A. C. Gossard, and D. D. Awschalom, Science **306**, 1910 (2004).
59. S. O. Valenzuela and M. Tinkham, Nature **442**, 176 (2006).
60. T. Kimura, Y. Otani, T. Sato, S. Takahashi, and S. Maekawa, Phys. Rev. Lett. **98**, 156601 (2007).
61. K.-U. Demasius, T. Phung, W. Zhang, B. P. Hughes, S.-H. Yang, A. Kellock, W. Han, A. Pushp, and S. S. P. Parkin, Nat. Commun. **7**, 10644 (2016).
62. E. Sagasta, Y. Omori, S. Vélez, R. Llopis, C. Tollan, A. Chuvilin, L. E. Hueso, M. Gradhand, Y. Otani, and F. Casanova, Phys. Rev. B **98**, 060410 (2018).
63. C. Zhang, S. Fukami, K. Watanabe, A. Ohkawara, S. DuttaGupta, H. Sato, F. Matsukura, and H. Ohno, Appl. Phys. Lett. **109**, 192405 (2016).

64. A. Soumyanarayanan, N. Reyren, A. Fert, and C. Panagopoulos, Nature **539**, 509 (2016).
65. P. M. Haney, H.-W. Lee, K.-J. Lee, A. Manchon, and M. D. Stiles, Phys. Rev. B **87**, 174411 (2013).
66. W. Zhang, M. B. Jungfleisch, W. Jiang, J. E. Pearson, A. Hoffmann, F. Freimuth, and Y. Mokrousov, Phys. Rev. Lett. **113**, 196602 (2014).
67. W. Zhang, W. Han, X. Jiang, S.-H. Yang, and S. S. P. Parkin, Nat. Phys. **11**, 496 (2015).
68. E. Sagasta, Y. Omori, M. Isasa, M. Gradhand, L. E. Hueso, Y. Niimi, Y. Otani, and F.Casanova, Phys. Rev. B **94**, 060412 (2016).
69. F. J. Jedema, A. T. Filip, and B. J. van Wees, Nature **410**, 345 (2001).
70. L. K. Werake and H. Zhao, Nat. Phys. **6**, 875 (2010).
71. A. Ganguly, K. Kondou, H. Sukegawa, S. Mitani, S. Kasai, Y. Niimi, Y. Otani, and A. Barman, Appl. Phys. Lett. **104**, 072405 (2014).
72. M. Montazeri, P. Upadhyaya, M. C. Onbasli, G. Yu, K. L. Wong, M. Lang, Y. Fan, X. Li, P. Khalili Amiri, R. N. Schwartz, C. A. Ross, and K. L. Wang, Nat. Commun. **6**, 8958 (2015).
73. A. Ganguly, R. M. Rowan-Robinson, A. Haldar, S. Jaiswal, J. Sinha, A. T. Hindmarch, D. A. Atkinson, and A. Barman, Appl. Phys. Lett. **105**, 112409 (2014).
74. S. Mondal, S. Choudhury, N. Jha, A. Ganguly, J. Sinha, and A. Barman, Phys. Rev. B **96**, 054414 (2017).
75. S. D. Bader, Rev. Mod. Phys. **78**, 1 (2006).
76. R. Skomski, J. Phys. Condens. Matter. **15**, R841 (2003).
77. T. Thomson, G. Hu, and B. D. Terris, Phys. Rev. Lett. **96**, 257204 (2006).
78. D. E. Nikonov and G. I. Bourianoff, IEEE Trans. Nanotechnol. **4**, 206 (2005).
79. A. Imre, G. Csaba, L. Ji, A. Orlov, G. H. Bernstein, and W. Porod, Science **311**, 205 (2006).
80. A. Haldar, D. Kumar, and A. O. Adeyeye, Nat. Nanotechnol. **11**, 437 (2016).
81. D. Bhowmik, L. You, and S. Salahuddin, Nat. Nanotechnol. **9**, 59 (2013).
82. V. E. Demidov, S. Urazhdin, H. Ulrichs, V. Tiberkevich, A. Slavin, D. Baither, G. Schmitz, and S. O. Demokritov, Nat. Mater. **11**, 1028 (2012).
83. S. C. McBain, H. H. P. Yiu, and J. Dobson, Int. J. Nanomed. **3**, 169 (2008).
84. S. Lequeux, J. Sampaio, V. Cros, K. Yakushiji, A. Fukushima, R. Matsumoto, H. Kubota, S. Yuasa, and J. Grollier, Sci. Rep. **6**, 31510 (2016).

85. E. Yablonovitch, Phys. Rev. Lett. **58**, 2059 (1987).
86. S. Tacchi, M. Madami, G. Gubbiotti, G. Carlotti, S. Goolaup, A. O. Adeyeye, N. Singh, and M. P. Kostylev, Phys. Rev. B **82**, 184408 (2010).
87. Z. K. Wang, V. L. Zhang, H. S. Lim, S. C. Ng, M. H. Kuok, S. Jain, and A. O. Adeyeye, ACS Nano **4**, 643 (2010).
88. S. Saha, S. Barman, Y. Otani, and A. Barman, Nanoscale **7**, 18312 (2015).
89. V. E. Demidov, M. P. Kostylev, K. Rott, P. Krzysteczko, G. Reiss, and S. O. Demokritov, Appl. Phys. Lett. **95**, 112509 (2009).
90. A. V. Chumak, P. Pirro, A. A. Serga, M. P. Kostylev, R. L. Stamps, H. Schultheiss, K. Vogt, S. J. Hermsdoerfer, B. Laegel, P. A. Beck, and B. Hillebrands, Appl. Phys. Lett. **95**, 262508 (2009).
91. G. Gubbiotti, S. Tacchi, G. Carlotti, P. Vavassori, N. Singh, S. Goolaup, A. O. Adeyeye, A. Stashkevich, and M. Kostylev, Phys. Rev. B **72**, 224413 (2005).
92. O. Dmytriiev, U. A. S. Al-Jarah, P. Gangmei, V. V. Kruglyak, R. J. Hicken, B. K. Mahato, B. Rana, M. Agrawal, A. Barman, M. Mátéfi-Tempfli, L. Piraux, and S. Mátéfi-Tempfli, Phys. Rev. B **87**, 174429 (2013).
93. M. Agrawal, B. Rana, and A. Barman, J. Phys. Chem. C **114**, 11115 (2010).
94. M. Kostylev, P. Schrader, R. L. Stamps, G. Gubbiotti, G. Carlotti, A. O. Adeyeye, S. Goolaup, and N. Singh, Appl. Phys. Lett. **92**, 132504 (2008).
95. S. A. Nikitov, P. Tailhades, and C. S. Tsai, J. Magn. Magn. Mater. **236**, 320 (2001).
96. T. R. Albrecht, H. Arora, V. Ayanoor-Vitikkate, J. Beaujour, D. Bedau, D. Berman, A. L. Bogdanov, Y. Chapuis, J. Cushen, E. E. Dobisz, G. Doerk, H. Gao, M. Grobis, B. Gurney, W. Hanson, O. Hellwig, T. Hirano, P. Jubert, D. Kercher, J. Lille, Z. Liu, C. M. Mate, Y. Obukhov, K. C. Patel, K. Rubin, R. Ruiz, M. Schabes, L. Wan, D. Weller, T. Wu, and E. Yang, IEEE Trans. Magn. **51**, 1 (2015).
97. S. Jung, B. Watkins, L. DeLong, J. B. Ketterson, and V. Chandrasekhar, Phys. Rev. B **66**, 132401 (2002).
98. S. Neusser, B. Botters, and D. Grundler, Phys. Rev. B **78**, 054406 (2008).
99. S. Neusser, B. Botters, M. Becherer, D. Schmitt-Landsiedel, and D. Grundler, Appl. Phys. Lett. **93**, 122501 (2008).
100. B. Lenk, H. Ulrichs, F. Garbs, and M. Münzenberg, Phys. Rep. **507**, 107 (2011).
101. V. V. Kruglyak, S. O. Demokritov, and D. Grundler, J. Phys. D Appl. Phys. **43**, 260301 (2010).

102. S. Neusser and D. Grundler, Adv. Mater. **21**, 2927 (2009).
103. M. Krawczyk and D. Grundler, J. Phys. Condens. Matter. **26**, 123202 (2014).
104. R. F. Wang, C. Nisoli, R. S. Freitas, J. Li, W. McConville, B. J. Cooley, M. S. Lund, N. Samarth, C. Leighton, V. H. Crespi, and P. Schiffer, Nature **446**, 102 (2007).
105. A. Fernández-Pacheco, D. Petit, R. Mansell, R. Lavrijsen, J. H. Lee, and R. P. Cowburn, Phys. Rev. B **86**, 104422 (2012).
106. D. A. Gilbert, B. B. Maranville, A. L. Balk, B. J. Kirby, P. Fischer, D. T. Pierce, J. Unguris, J. A. Borchers, and K. Liu, Nat. Commun. **6**, 8462 (2015).
107. S. Heinze, K. von Bergmann, M. Menzel, J. Brede, A. Kubetzka, R. Wiesendanger, G. Bihlmayer, and S. Blügel, Nat. Phys. **7**, 713 (2011).
108. B. Rana, D. Kumar, S. Barman, S. Pal, Y. Fukuma, Y. Otani, and A. Barman, ACS Nano **5**, 9559 (2011).
109. S. Saha, R. Mandal, S. Barman, D. Kumar, B. Rana, Y. Fukuma, S. Sugimoto, Y. Otani, and A. Barman, Adv. Funct. Mater. **23**, 2378 (2013).
110. R. Mandal, S. Saha, D. Kumar, S. Barman, S. Pal, K. Das, A. K. Raychaudhuri, Y. Fukuma, Y. Otani, and A. Barman, ACS Nano **6**, 3397 (2012).
111. S. Pal, J. W. Klos, K. Das, O. Hellwig, P. Gruszecki, M. Krawczyk, and A. Barman, Appl. Phys. Lett. **105**, 162408 (2014).
112. S. Choudhury, S. Majumder, S. Barman, Y. Otani, and A. Barman, Phys. Rev. Appl. **10**, 064044 (2018).
113. A. De, S. Mondal, S. Sahoo, S. Barman, Y. Otani, R. K. Mitra, and A. Barman, Beilstein J. Nanotechnol. **9**, 1123 (2018).
114. S. Choudhury, S. Saha, R. Mandal, S. Barman, Y. Otani, and A. Barman, ACS Appl. Mater. Interfaces **8**, 18339 (2016).
115. S. Saha, S. Barman, J. Ding, A. O. Adeyeye, and A. Barman, Appl. Phys. Lett. **102**, 242409 (2013).
116. N. Porwal, S. Mondal, S. Choudhury, A. De, J. Sinha, A. Barman, and P. K. Datta, J. Phys. D Appl. Phys. **51**, 055004 (2018).
117. S. Choudhury, S. Barman, Y. Otani, and A. Barman, ACS Nano **11**, 8814 (2017).
118. A. De, S. Mondal, C. Banerjee, A. K. Chaurasiya, R. Mandal, Y. Otani, R. K. Mitra, and A. Barman, J. Phys. D Appl. Phys. **50**, 385002 (2017).
119. B. K. Mahato, B. Rana, D. Kumar, S. Barman, S. Sugimoto, Y. Otani, and A. Barman, Appl. Phys. Lett. **105**, 012406 (2014).

120. K. Adhikari, S. Barman, R. Mandal, Y. Otani, and A. Barman, Phys. Rev. Appl. **10**, 044010 (2018).
121. B. Rana, S. Pal, S. Barman, Y. Fukuma, Y. Otani, and A. Barman, Appl. Phys. Exp. **4**, 113003 (2011).
122. S. Mondal, S. Choudhury, S. Barman, Y. Otani, and A. Barman, RSC Adv. **6**, 110393 (2016).
123. S. Mondal, S. Barman, S. Choudhury, Y. Otani, and A. Barman, J. Magn. Magn. Mater. **458**, 95 (2018).
124. S. Tacchi, M. Madami, G. Gubbiotti, G. Carlotti, H. Tanigawa, T. Ono, and M. P. Kostylev, Phys. Rev. B **82**, 024401 (2010).
125. S. Sahoo, S. Mondal, G. Williams, A. May, S. Ladak, and A. Barman, Nanoscale **10**, 9981 (2018).
126. A. Fernández-Pacheco, R. Streubel, O. Fruchart, R. Hertel, P. Fischer, and R. P. Cowburn, Nat. Commun. **8**, 15756 (2017).

Chapter 2

2 Theoretical Background

2.1 Introduction

The fundamental theories of magnetism have been developed by a large of group of scientists working persistently for few centuries building up in-depth understanding of the correlation between basic magnetism, electricity and optics. In magnetism, materials were classified into five main classes: ferromagnet, ferrimagnet, antiferromagnet, diamagnet and paramagnet. Magnetic domain theory was developed by Weiss in 1906 which demonstrates that a large number of atomic magnetic moments are aligned parallel in each domain inside a ferromagnetic system [1,2]. His theory suggests that ferromagnet and ferrimagnet have spontaneous magnetization which makes them distinct from other materials. The interplay between the internal magnetic energies plays extremely crucial role in determining their magnetic properties. The origin of these energies is solely microscopic and is quantum mechanical in nature. In 1929, Heisenberg proposed the theory of 'Heisenberg exchange' in magnetic system based on Pauli's principle [3]. Initially, simpler pictures were depicted to realize the magnetic domain formation, magnetic reversal and other properties based on macroscopic model. Later, with the introduction of nanomagnetism, the scenario becomes different. Many new and essentially unique properties were found within confined magnetic systems, which differ a lot from their bulk counterparts. Magnetization reversal could not be described by only coherent and incoherent rotation but shows curling, buckling, fanning, cork-screw modes, quasi-single-domains nature depending upon the length scale and minimization of magnetic energies. The Stoner-Wohlfarth model for single domain system ignored any spatial nonuniformity in the system, which becomes essential to be considered for realistic magnetic nanostructures [4].

The time-dependent evolution of magnetization or the magnetization dynamics in such systems becomes further intriguing. In 1935, Landau and Lifshitz proposed an equation describing the magnetization precession. In presence of effective magnetic field magnetization can survive any external perturbation by exhibiting a precessional

motion to reach to its equilibrium state [5]. Interestingly, ferromagnetic resonance was observed by Griffith in 1946 [6]. Kittel derived a formula to model the relationship between precessional frequency and magnetic field in a ferromagnetic system, which has close similarity with Larmor precession in atomic level [7]. Gilbert introduced a damping term in the equation derived by Landau and Lifshitz, to realistically describe the natural energy dissipation during magnetization motion [8]. Further, these simplified models for uniformly magnetized system were reconstructed and approximated in presence of several external factors, such as, development of nonuniform spin textures due to spatial confinement, magnetic anisotropy, large perturbation field, opening of additional energy dissipation channels, application of spin torques, coupling between magnetic and nonmagnetic modes.

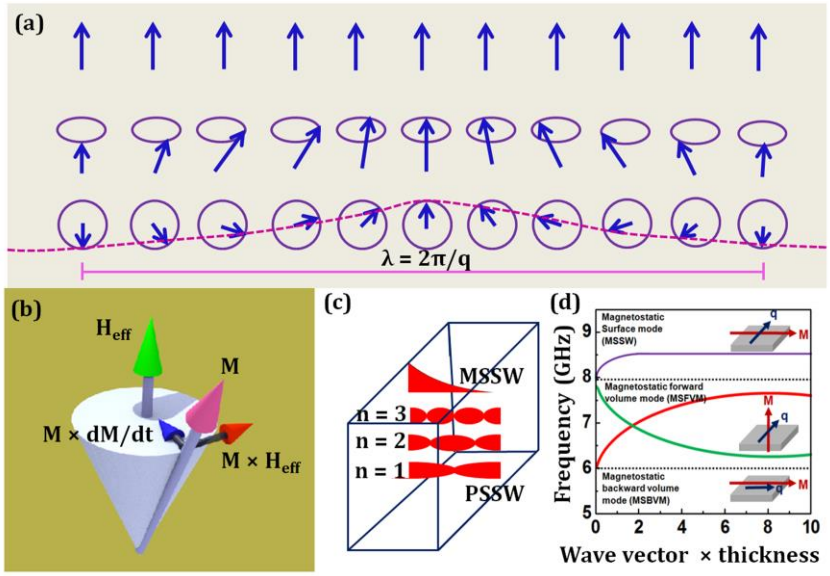

Figure 2.1: (a) Semiclassical representation of spin wave (SW) in a ferromagnet: the ground state, chain of precessing magnetic moments and the SW (top view). (b) Motion of the magnetization around the effective magnetic field. Schematics of (c) perpendicular standing SW mode (PSSW) and magnetostatic surface SW mode (MSSW) within ferromagnetic thin film. (d) The dispersion relation for different types of magnetostatic SWs modes.

The phenomena related to magnetization dynamics can be classified based on their characteristic time scales. The fastest process is the fundamental exchange interaction occurring within about 10 fs. The spin-orbit coupling (SOC) and related phenomena occur in the time scale of 10 fs - 1 ps. The laser-induced ultrafast demagnetization takes place within few hundreds of fs. The fast remagnetization covers the time span of 1-10 ps which is followed by the slow remagnetization, precession and damping over ps to ns time scale. The relatively slower processes are vortex core gyration, core switching

(time scale few tens of ns) and domain wall motion (time scale few ns to μs time scale) (as shown in Fig. 2.1).

In this chapter, the background theories for understanding the fundamental static and dynamic magnetic phenomena appeared at different length and time scales are discussed.

2.2 Magnetic Energy

In application of any external perturbation a magnetic system respond according to effects of several magnetic energies present in the system [8,9].

2.2.1 Zeeman Energy

In a magnetic system having volume V, the interaction of magnetization ($\boldsymbol{M}$) to external magnetic field $\boldsymbol{H}$ is described by the Zeeman energy:

$$E_Z = -\int_V \boldsymbol{M}.\boldsymbol{H}\, dv \tag{2.1}$$

Here dv is the volume element and this equation states that when $\boldsymbol{M}$ and $\boldsymbol{H}$ are parallel to each other the energy minimum.

2.2.2 Exchange Energy

Exchange interaction between the neighbouring spins is responsible for strong and long range magnetic order. It is Columbic in nature and can be described only from quantum mechanical point of view. Heisenberg exchange Hamiltonian can be expressed as [3]:

$$H_{ex} = -2J_e \sum_j \boldsymbol{S}_i.\boldsymbol{S}_j \tag{2.2}$$

Here $\boldsymbol{S}$ is the spin operator and J_e is the isotropic exchange integral. In the continuum model the exchange energy can be expressed as [10]:

$$E_{ex} = A\int_V (\nabla m)^2\, dv \tag{2.3}$$

m is magnetic moment and A is the exchange constant,

$$A = \frac{2J_eS^2}{a} \tag{2.4}$$

here a is the lattice constant. Apart from this direct exchange, there are systems with indirect exchange, *e.g.* (1) Ruderman–Kittel–Kasuya–Yosida (RKKY) exchange, where

the metallic ions are coupled via itinerant electrons [11], (2) super-exchange, where the exchange is mediated via different non-magnetic ions [3], (3) anisotropic exchange interaction (also known as Dzyaloshinskii-Moriya interaction or DM interaction) [3], where the spin orbit interaction plays a major role and often leads to canting of spins by small angle.

2.2.3 Dipolar Energy

For 3d transition metal the magnetization distribution is almost spherical in the atomic level and the energy between two dipoles can be expressed as [12]:

$$E_{dip} = \frac{\mu_B^2}{2} \sum_{i \neq j} \frac{1}{r_{ij}^3} \left(\boldsymbol{m}_i . \boldsymbol{m}_j - 3 \frac{(\boldsymbol{m}_i . \boldsymbol{r}_{ij})(\boldsymbol{m}_j . \boldsymbol{r}_{ij})}{r_{ij}^5} \right) \tag{2.5}$$

here μ_B, $\boldsymbol{m}_i$ and $\boldsymbol{r}_{ij}$ are Bohr magneton, magnetic dipolar moment and distance between two dipoles respectively. This energy plays an important role in a number of phenomena such as formation of domains, demagnetizing field and spin waves (SWs) in the long wavelength regime.

2.3 Magnetic Anisotropy

Sometimes, in magnetic systems there are some preferential directions along which it is easier to magnetize the sample. Those directions are called easy axes and this effect is known as magnetic anisotropy [12].

2.3.1 Magnetocrystalline Anisotropy

In some materials, spatial arrangement of electrons in the orbitals is closely associated with the crystallographic structure. The SOC plays a vital role in assigning certain crystallographic directions along which the material exhibit magnetocrystalline anisotropy. The anisotropic energy in cubic structure can be expressed as [12]:

$$E_{cryst} = K_0 + K_1(\alpha_1^2\alpha_2^2 + \alpha_2^2\alpha_3^2 + \alpha_3^2\alpha_1^2) + K_1\alpha_1^2\alpha_2^2\alpha_3^2 + \cdots \tag{2.6}$$

The anisotropic energy in hcp structure can be expressed as:

$$E_{cryst} = K_0 + K_1(sin^2\theta) + K_2(sin^4\theta) + (K_3 + K_3'cos6\phi)sin^6\theta + \cdots \tag{2.7}$$

Here K_0, K_1, K_2, K_3, K'_3 are anisotropy constants. α_1, α_2 and α_3 are the three components of magnetization direction. θ (ϕ) is the angle between a (c) axes with magnetization vector in the hcp structure. This kind of anisotropy is generally a material property.

2.3.2 Shape Anisotropy

In confined magnetic structures, the shape of the elements can generate some preferential directions for the magnetization to align in order to achieve minimum energy configuration. This shape anisotropy can be described by the energy expression given below which results from the dominant demagnetizing effect or the dipolar interaction in the micro and nanostructures [9,12]:

$$E_{shape} = -\frac{1}{2}\int_V \boldsymbol{M}.\boldsymbol{H}_d dv \tag{2.8}$$

For example, in case of an ellipsoid,

$$\boldsymbol{H}_d = -4\pi \boldsymbol{D}.\boldsymbol{M}_V \tag{2.9}$$

where, $\boldsymbol{M}_V$ is the bulk value of magnetization, $\boldsymbol{D}$ is the demagnetizing tensor.

$$\mathrm{tr}\boldsymbol{D} = 1 \tag{2.10}$$

Thus the shape anisotropy energy per unit volume is,

$$G^V_{shape} = -2\pi \boldsymbol{M}_V.\boldsymbol{D}.\boldsymbol{M}_V \tag{2.11}$$

2.3.3 Surface and Interface Anisotropy

The broken symmetry at surfaces and interfaces of magnetic thin films and multilayers often induces an effective anisotropy in the system. In a ferromagnetic thin film, the anisotropy energy per unit volume can be expressed as [13]:

$$E_{ani} = K^{eff} \sin^2\theta \tag{2.12}$$

$$K^{eff} = K_v^{eff} + \frac{2K_s^{eff}}{d} \tag{2.13}$$

where d is the thickness, K_v^{eff} is the effective volume anisotropy constant involving the magneto-crystalline terms as well as the demagnetizing term. K_s^{eff} is the effective surface or interface anisotropy constant. There are competing volume and surface anisotropies where the latter exhibits an inverse dependence on the thickness d of the system and preferably orients the magnetization of the sample towards out of plane. Surface (or interfacial) roughness modifies the magnetocrystalline surface anisotropy by breaking the symmetry near the atoms located at that plane.

2.3.4 Strain Induced Anisotropy

If there is a change in the dimensions of a specimen when its magnetization is varied - that is known as magnetostriction. The magnetoelastic interaction also causes the

inverse effect, *i.e.* application of a stress changes the magnetization, which is called the Villari effect. In presence of stress generated in magnetic nanostructure via Villari effect or lattice mismatch at the interface [3], the free energy can be expressed as:

$$F = F_K + F_{EL} + F_{ME} \tag{2.14}$$

where the three terms correspond to anisotropy energy, elastic energy and magnetoelastic energy. The amount of strain generated in terms of length elongation or contraction will be:

$$\frac{\delta l}{l} = \frac{3}{2}\,\lambda_s\,(cos^2\theta - \frac{1}{3}) \tag{2.15}$$

where λ_s is the isotropic magnetostriction and θ is the angle between spontaneous magnetization and direction of length contraction or elongation. If σ is the stress applied then energy expression becomes:

$$F_\sigma = -\sigma \int d\left(\frac{\delta l}{l}\right) = -\frac{3}{2}\,\sigma\lambda_s\,cos^2\theta \tag{2.16}$$

2.3.5 Perpendicular Magnetic Anisotropy

Due to the following reasons magnetization in nanostructures may inclined towards out-of-plane (OOP) exhibiting perpendicular magnetic anisotropy (PMA): reduced coordination symmetry, altered electronic structure, localized epitaxial strain at the interface, electronic band-structure interactions and competition between several magnetic energies present in the system [11].

2.4 Magnetization Dynamics

In presence of an external magnetic field, the magnetic moments of a magnetic material experience a torque which induces precessional motion about the direction of the external field. In addition, the moments try to align themselves along the external field to minimize the Zeeman energy (Fig. 2.1). Effectively, they execute a damped spiral motion about the field direction, which is referred to as precessional magnetization dynamics. The net behavior of dynamic magnetization is phenomenologically illustrated by the Landau-Lifshitz-Gilbert (LLG) equation of motion. As previously mentioned, the LLG equation is a torque equation which was first introduced by Landau and Lifshitz [5], and later Gilbert modified it by inserting a Gilbert damping term [8].

From a semi-classical approach, it can be described that spin angular momentum operator $\boldsymbol{S}$ experiences a torque associated with an electron spin:

$$\frac{d\boldsymbol{S}}{dt} = \boldsymbol{T} \tag{2.17}$$

The magnetic moment of an electron is related to the spin momentum as:

$$\boldsymbol{M} = -\gamma \boldsymbol{S} \tag{2.18}$$

Similarly, if $\boldsymbol{M}$ is placed in an effective magnetic field $\boldsymbol{H}_{\text{eff}}$, it experiences a torque given as:

$$\boldsymbol{T} = \boldsymbol{M} \times \boldsymbol{H}_{eff} \tag{2.19}$$

The discrete arrays of magnetic moments become magnetization fields in the continuum limit and the equation of motion of the magnetization becomes:

$$\frac{d\boldsymbol{M}}{dt} = -\gamma\, \boldsymbol{M} \times \boldsymbol{H}_{eff} \tag{2.20}$$

Physically, the above equation features a continuous precession which means that the system is non-dissipative. Practically the precessional amplitude decreases with time and the tip of the magnetization vector follow a spiral trajectory around the effective field. Hence, introduction of a damping term is inevitable. Landau and Lifshitz suggested a damping term and the damped LL equation reads as:

$$\frac{d\boldsymbol{M}}{dt} = -\gamma \left(\boldsymbol{M} \times \boldsymbol{H}_{eff}\right) + \frac{\lambda}{M_s^2}\ \boldsymbol{M} \times \left(\boldsymbol{M} \times \boldsymbol{H}_{eff}\right) \tag{2.21}$$

Later, Gilbert introduced another damping term into the LL equation resulting in the so called LLG equation as:

$$\frac{d\boldsymbol{M}}{dt} = -\gamma \left(\boldsymbol{M} \times \boldsymbol{H}_{eff}\right) + \frac{\alpha}{M_s} \left(\boldsymbol{M} \times \frac{d\boldsymbol{M}}{dt}\right) \tag{2.22}$$

Here, $\alpha = \frac{\lambda}{\gamma M_s}$, is Gilbert damping coefficient. γ and M_s are gyromagnetic ratio and saturation magnetization of the system.

$$\boldsymbol{H}_{eff} = \boldsymbol{H}_z + \boldsymbol{H}_d + \boldsymbol{H}_{ex} + \boldsymbol{H}_{ani} + \boldsymbol{H}_{ME} \tag{2.23}$$

H_z is the Zeeman field, H_{ex} is the exchange field and H_d represents the demagnetization field originated from the dipolar interaction of magnetic surface and volume charges.

The field H_{ani} includes different types of anisotropic fields described above and H_{ME} corresponds to magnetoelastic interaction.

2.5 Ferromagnetic Resonance and Macrospin Model

The idea of macrospin model originated from a system where all the spins exhibit uniformity and coherence, and the entire magnetic moment can be expressed by a giant spin.

If a ferromagnetic system is placed under a stable bias field and an alternating magnetic field applied orthogonal to each other, then the entire system starts precessing by absorbing power from the oscillating field. This ferromagnetic resonance occurs in much higher frequency than the Larmor precession frequency.

2.5.1 Kittel Formula

C. Kittel explicitly defined the role of demagnetizing field in the equation of motion under resonance condition [7,11]. The precessional frequency can be expressed as,

$$\omega_0 = 2\pi f = \mu_0\gamma\sqrt{[H + (N_x - N_z)M_s]\left[H + \left(N_y - N_z\right)M_s\right]} \qquad (2.24)$$

Here N_x, N_y, N_z are the demagnetizing factors which are also associated with magnetic anisotropy of the system.

For a sphere, $N_x = N_y = N_z = 1/3$.

For out-of-plane magnetized thin film, $N_x = N_y = 0$ and $N_z = 1$.

For in-plane magnetized thin film, $N_y = N_z = 0$ and $N_x = 1$.

2.5.2 Spin Waves

A ferromagnetic specimen of unit volume at absolute zero will have net magnetic moment of $M = N\mu_B$, where N is number of atom per unit volume and μ_B is Bohr magneton. Slight increase in system temperature can flip a spin from stable configuration in presence of a magnetic field. Due to the exchange coupling, the neighbouring spins also try to flip. However, the exchange energy cost associated with the reversal of one spin is reduced by spreading the disturbance over long wavelength and thereby the degree of misorientation of any two neighbouring spin is minimized. The idea of SW was introduced by Bloch [14]. The formation of SW is a fundamental

point of interest in magnetic system whose quanta is known as 'magnon' [15,16]. Similar to phonon and photon in sonic and photonic crystal respectively, magnons can carry and process signal which is already discussed before in this thesis. Having smaller wavelength at the same frequency, the usage of spin wave is more advantageous than electromagnetic wave in miniaturized devices.

Depending on the wavelength and range of interaction, SWs can be categorized in exchange dominated, dipole-exchange dominated or dipole dominated SWs. In the long wavelength regime, the phase difference between consecutive spins is rather small, and the SW energy is primarily dominated by dipolar energy and the SWs are referred to as dipole dominated or magnetostatic SWs. On the other hand, the short wavelength SWs are governed by exchange interaction and is known as exchange SWs.

In 1961, Damon and Eshbach first reported the magnetostatic or dipolar SWs [17]. If the magnetic field and the wave vector lie in film plane parallel (perpendicular) to each other, then the dipolar coupled wave is known to be magnetostatic surface wave mode (or backward volume mode). There is another type of SW mode where the propagation is along IP but the applied field is along OOP direction. This is magnetostatic forward volume mode (MSFVM). The frequency, amplitude and nature of dispersion depend on the anisptropic properties of the dipolar coupling [18]. The Damon-Eshbach (DE) mode exhibits positive dispersion which can be expressed as follows:

$$\omega_{DE} = 2\pi f_{DE} = \gamma\sqrt{[H\,(H + 4\pi M_s) + (2\pi M_s)^2(1 - e^{-2dq_{\parallel}})]} \qquad (2.25)$$

Here $q_{\parallel}$ is the in-plane wave vector and d is film thickness. Other parameters have their usual meaning. Magnetostatic backward volume waves (MSBVW) show negative dispersion which indicates that the group and phase velocities are in opposite direction. The dispersion relation is provided below,

$$\omega_{BV} = 2\pi f_{BV} = \gamma\sqrt{\left[H(H + 4\pi M_s\frac{(1 - e^{-2qd})}{qd}\right]} \qquad (2.26)$$

MSFVM posses a positive dispersion with having magnetization directed towards OOP,

$$\omega_{FV} = 2\pi f_{FV} = \gamma\sqrt{\left[(H - 4\pi M_s)(H - 4\pi M_s\frac{(1 - e^{-2qd})}{qd}\right]} \qquad (2.27)$$

There are SW modes where the dipolar interaction and exchange interaction, both are responsible to originate these modes. The SW wavelength is of the order of the exchange length. The spectrum of dipole-exchange SWs in an unlimited ferromagnetic medium is given by the Herrings-Kittel formula [19]

$$\omega_{di-ex} = 2\pi f_{di-ex} = \gamma\sqrt{\left[\left(H + \frac{2A}{M_s}q^2\right)\left(H + \frac{2A}{M_s}q^2 + 4\pi M_s sin^2\theta_q\right)\right]} \quad (2.28)$$

Here A is the exchange constant.

In a magnetic thin film with finite thickness (d) the SW spectrum is modified and the above relation can be expressed as:

$$\omega_{di-ex} = 2\pi f_{di-ex} = \gamma\sqrt{\left[\left(H + \frac{2A}{M_s}q^2\right)\left(H + \frac{2A}{M_s}q^2 + 4\pi F_{pp}(q_{\parallel}d)\right)\right]} \quad (2.29)$$

Here $q_{\parallel}$ is the continuously varying IP wave vector and F_{pp} is the matrix element of the magnetic dipole interaction.

An exchange dominated SWs can propagate across the thickness of the sample and form standing waves. Those are called the perpendicular standing SW (PSSW) modes,

$$\omega_p = 2\pi f_p = \gamma\sqrt{\left[\left(H + \frac{2A}{M_s}\left(\frac{p\pi}{d}\right)^2\right)\left(H + \frac{2A}{M_s}\left(\frac{p\pi}{d}\right)^2 + 4\pi M_s\right)\right]} \quad (2.30)$$

Here the wave vector can be written as, $q_{\perp} = \frac{p\pi}{d}$ where p is the quantum number of the SWs.

Depending upon the confinement or the feature dimension present in the nanomagnetic system, the SW can exhibit quantized or localized behavior. The formation of 'potential well' due to competition between several magnetic energies and their influence on spin precession amplitude and phase is a matter of huge interest in the nanomagnetism community. The structural confinement influences the frequency dispersion, band structure formation etc. in the nanomagnet arrays, especially in periodically patterned magnonic crystals (MCs) [15,16,20]. Similar to photonic and sonic crystal the band structure of MCs consists of several Brillouin zones. The manipulation of SW properties

can be facile by structural engineering, tuning the external bias field, or controlling the electric field, applying spin torque etc.

2.6 Ultrafast Phenomena

The time-resolved dynamics of magnetic material reveals interesting phenomena which take place in femtosecond to nanosecond time scale and have great significance from physics point of view (Fig. 2.2). These phenomena have been studied extensively, both from macroscopic and microscopic perspective, by a large number of researchers.

2.6.1 Ultrafast Demagnetization

In thermomagnetic recording before 1990s, technical applications of Curie-point writing on a ferromagnetic film was a solidifying idea [21,22]. The speed by which the ferromagnetic film can lose the magnetization and acquire it again in presence of a pulsed laser sets a fundamental limit on the data rate. It was a known fact that the laser beam hitting the sample produces a hot-electron gas which thermalizes with the lattice within a few picoseconds in magnetic as well as nonmagnetic systems. Much less was known about the interaction between the electron gas, lattice and the spin system causing reduction of magnetization due to magnon excitation. Physically such a fast magnetization change is not trivial since the optical transitions preserve the electronic spin. In the transient hot electron regime, spin populations are modified due to spin dependent electron scattering in femtosecond time scale. Due to the lack of appropriate experimental tools, the possibility of creating transient states with new magnetic properties was thus a open field worthwhile of active research. In 1996, Beaurepaire *et al.* first reported the experimentally determined time scale for ultrafast demagnetization in a Ni thin film by using optical and magneto-optical pump-probe techniques [23]. The results were described by a model including three interacting reservoirs, *i.e.* electron, spin, and lattice. Since then huge effort has been made to explore the physical origin of this phenomenon in several ferromagnetic systems. There are various theories proposed for this, however the underlying mechanisms remained a subject of intense debate till date.

2.6.1.1 Three temperature model

The pioneering work by Beaurepaire *et al.* on ultrafast demagnetization in a thin film of Ni by using magneto-optical technique [23] demonstrated the existence of femtosecond dynamics during light-matter interaction. They adopted a phenomenological model which takes into account the thermal distribution between electron, spin and lattice. This is known as the 'three temperature' model and is an extension of the well-known 'two temperature model' proposed by Anisimov on the basis of electron-lattice energy distribution [24]. After the approach of a pump pulse, the electron temperature increases rapidly followed by the same trend by the spin temperature. Within the dipole approximation, the optical transitions preserve the electronic spins. Thus the spin polarization of the emerging electronic distribution is the same as in the ground state. When scattering takes place, the majority and minority spins tend to homogenize leading to an increase of spin temperature after a finite time. This causes ultrafast demagnetization. Later, the energy dissipation from electron and spin baths to lattice bath gives rise to the fast remagnetization. The following model was used to describe

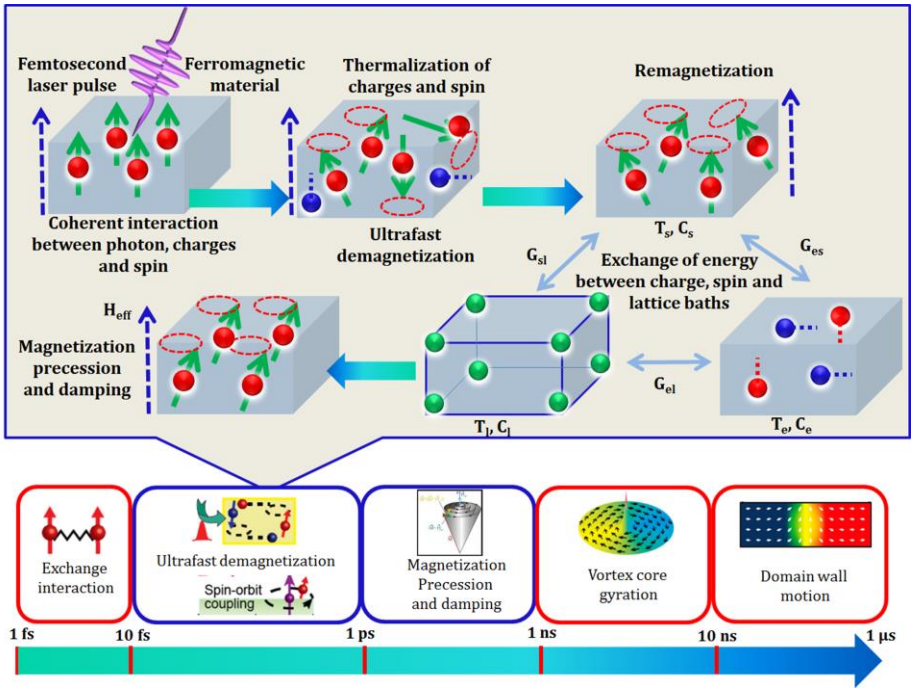

Figure 2.2: The time scale of ultrafast phenomena is shown. Schematic of ultrafast magnetization dynamics based upon 'three temperature' model is presented.

the role of the different types of interaction processes:

$$C_e(T_e)\frac{dT_e}{dt} = -G_{el}(T_e - T_l) - G_{es}(T_e - T_s) + P(t) \quad (2.31)$$

$$C_s(T_s)\frac{dT_s}{dt} = -G_{es}(T_s - T_e) - G_{sl}(T_s - T_l) \quad (2.32)$$

$$C_l(T_l)\frac{dT_l}{dt} = -G_{el}(T_l - T_e) - G_{sl}(T_l - T_s) \quad (2.33)$$

where C_e, C_s, and C_l are the electronic, spin and lattice contributions to the specific heat of the magnetic system, respectively. G_{el}, G_{es}, and G_{sl} are the electron-lattice, electron-spin, and spin-lattice interaction constants. The laser source term $P(t)$ is applied only to the electronic terms since the initial heating process occurs only in the electron bath. Solving the coupled differential equations allows for reproducing the transient reflectivity as well as magnetization dynamics profiles, but does not describe the microscopic origin of the processes involved. In 2007, Dalla Longa *et al.* derived an analytical solution based on this model to explain their experimental results. They neglected the spin specific heat and assumed an instantaneous rise of the electron temperature upon laser excitation in their work [25]. Later, this approach becomes popular and was adopted by many other groups [26].

2.6.1.2. Elliot-Yafet (EY) scattering

Immediately after the discovery of ultrafast demagnetization, a plethora of theoretical and experimental works were reported investigating the mechanism responsible for this novel phenomenon. Among those, application of Elliot-Yafet (EY) scattering mechanism gained huge interest [25,27]. In 2005, Koopmans *et al.* tried to find correlation between the ultrafast demagnetization and Gilbert damping [28]. Their work was based on the scattering mechanism proposed much earlier by Elliot and Yafet which considers the scattering between the electron and the impurity or phonon present in the system just after the arrival of pump pulse. These processes were facilitated by the SOC which transfers angular momentum between electron and lattice. Before excitation, the electron and spin baths remain in equilibrium. Immediately after the excitation, the electronic system goes in to nonequilibrium but the spin system remains unchanged. Once the phonon takes away the angular momentum from the electron, the demagnetization takes place mediated by the flipping of uncompensated

spins. Later, researcher tried to find the reason behind the fast demagnetization of transition metals (TM) and their alloys and slow demagnetization of rare earth (RE) metals. A compact differential equation based on EY scattering was used to describe the ultrafast magnetization dynamics:

$$\frac{dm}{dt} = Rm\frac{T_p}{T_c}\left[1 - \coth\left(\frac{mT_c}{T_e}\right)\right] \tag{2.34}$$

$$R \propto a_{sf}\frac{{T_c}^2}{\mu_{atomic}} \tag{2.35}$$

where a_{sf} is the spin-flip probability and if it increases then demagnetization will be faster (e.g. a_{sf} is larger for Co, Ni but smaller for Gd). R is a material-specific scaling factor for the demagnetization rate. It was predicted that if the demagnetization is governed by thermalization of electron then with increasing excitation energy demagnetization time would have decreased, which is not the real situation. In the pump-probe experiments, total number of involved photon is less, thus non-thermal processes was thought to be not responsible for ultrafast demagnetization.

2.6.1.3 Coulomb scattering (EY-like mechanism without considering phonon bath)

M. Krauβ *et al*. demonstrated the underlying mechanism of ultrafast demagnetization in ferromagnetic materials due to an EY-like mechanism which is based on electron-electron Coulomb scattering [29]. This scattering mechanism is not of quasi-elastic type. This indicates that the available phase space for transitions from the minority to themajority bands is greater than for electron-phonon scattering. The electronic distributions in the ferromagnet before excitation are assumed to be Fermi-Dirac distributions governed by the lattice temperature and band structure. The minority and majority energy dispersions are spin split resulting in a nonzero magnetization at equilibrium. Nonequilibrium electronic distributions in the bands are created due to the ultrafast optical excitation process. Deposition of energy by the pump photon forces the electrons to undergo intraband as well as interband Coulomb scattering. Assumptions about the dipole matrix elements reveal the optical excitation process cannot modify the magnetization. Thus, ultrafast demagnetization takes place when interband scattering processes between the optically energized electrons results in the

repopulation of electrons from the majority to the minority bands. The fast remagnetization occurs due to energy transfer to the lattice bath.

2.6.1.4 Relativistic quantum electrodynamic processes

Other contemporary work by Bigot *et al*. claimed the relativistic quantum electrodynamics to be responsible for occurrence of early stage phenomena in femtomagnetism [30]. There is a prominent difference between the coherent magnetic responses from the polarization free decay associated with the dephasing of the charges within very short time scale. Once the photon field of laser interacts with electrons and spins, it undergoes an angular momentum transfer process within less than ~50 fs. Later, the relaxation between electron and spin systems leads to the ultrafast demagnetization. This is an 'incoherent' process as electronic wave function is believed to loss its 'phase memory'.

Several proposed mechanisms were proposed to explain this temporal regime. However, the following points surfacing from experimental results retained the celebrated debate about the real physics behind ultrafast demagnetization,

A. Origin of THz emission associated with the process was not clearly known.

B. It was hard to find the correlation between Gilbert damping and demagnetization time.

C. Sometimes electron-magnon interaction is found to be dominant than electron-phonon interaction.

D. Nonlinear dependence and difference between the charge and spin thermalization time.

2.6.1.5 Laser induced spin-flip

A theory came up based on the *ab initio* calculations by solving many-body problem. At the very beginning of light-matter interaction, the angular momentum of light is thought to be modified. Though light does not take away the total angular momentum changed in the system, but some part of it leads to the quenching of magnetization [31,32]. Thus, light can act as an angular momentum reservoir. This theory is based on quantum mechanical approach and very hard to realize as light absorbed at each single site does

not only involve the driving optical pulse but also the emitted light from other neighboring sites. SOC is believed to have definite role in this process [33,34].

2.6.1.6 Superdiffusive spin transport

Later, a semiclassical model for femtosecond laser-induced ultrafast demagnetization governed by the spin polarized excited electron diffusion in superdiffusive regime was proposed by M. Battiatto *et al*. This model considers that energized electrons undergo transport process in ballistic and diffusive form [35]. Standard diffusive processes governed by Brownian motion are represented by the variance of the displacement of the particle distribution growing linearly with time. The electron motion of superdiffusive processes is distinct because it is time dependent and goes from a ballistic regime in short time to normal diffusive regime for long times. This furthermore emphasizes that a standard diffusion model is inappropriate to explain the electron motion on the fs time scale. In this process, the total 'first generation flux' in presence of distributed source of excited electrons is:

$$\Phi(z,t) = \int_{-\infty}^{\infty} dz_0 \int_{-\infty}^{t} dt_0 \; S^{ext}(z_0,t_0)\phi(z,t;z_0,t_0) \tag{2.36}$$

S^{ext} is the electron source term.

After obtaining the density of second and third generation electrons, the entire process can be summed up and a coupled transport equations can be derived as:

$$\frac{\partial n^{tot}}{\partial t} + \frac{n^{tot}}{\tau} = \left(-\frac{\partial}{\partial z}\hat{\phi} + \hat{I}\right)\left(\hat{S}\, n^{tot} + S^{ext}\right) \tag{2.37}$$

n^{tot} is the electron density and τ is lifetime. The main idea behind this mechanism is the passive demagnetization due to transport of spins in space experiencing multiple electronic collisions. Later, many experiments were carried out to physically prove the existence of this superdiffusive spin current [36,37].

2.6.2 Magnetic Damping

The control of damping in a magnetic system allows one to speed up the relaxation process and accelerate the approach of magnetization to equilibrium in reversal processes. This is of huge importance in magnetic recording technology. Memory pixels in MRAM must have a high damping. The fastest magnetization reversal is achieved by tuning the critical damping where the required time is about one period of precession.

Besides that, low damping materials are equally important due to their application potential in SW propagation based devices and to reduce write current in MRAM devices.

Magnetic damping can be of two types: intrinsic damping and extrinsic damping [38,39]. Intrinsic damping in a magnetic material with perfect crystal structure mainly originates from the itinerant electrons and SOC. There are several models which describe the nature of intrinsic damping in a magnetic system: s-d exchange interaction model, breathing Fermi surface model etc. Extrinsic damping of the system can be caused due to introduction of multiple energy dissipation channels during the spin precession. Phonon drag [40], eddy current [38,41], doping [42] or capping [43] with another material, injection of spin current [44], magnon-magnon scattering [45], and controlling the temperature of the system [46] are few processes which can externally modulate the damping. In optical methods, the excitation energy of the pump beam can enhance the damping by increasing electronic temperature to Curie temperature ratio [47]. Inversion symmetry breaking at the interface can lead to modification of Gilbert damping [48].

2.6.2.1 Intrinsic damping

Here we have briefly described the three main mechanism associated with intrinsic nature of damping in the magnetic system.

(A) **Spin-orbit coupling**

Spin angular momentum and orbital angular momentum can be correlated in terms of good quantum number $j_z = l_z + \sigma_z$. In ferromagnetic resonance, initially the spins get excited and transfer energy to orbital degrees of freedom, while j_z starts to precess. Electron-lattice scattering leaves the electronic orbital in low energy states and keeps altering the orbital moment, while the spin moment is unperturbed. This was explained by Kambersky in 1976 by using a SOC torque correlation model taking into account the intra-band and inter-band transitions [49]. For SOC strength (ξ), at low and high temperature, the intrinsic damping is proportional with ξ^3 and ξ^2.

(B) **Phonon-drag mechanism**

Magnon-phonon scattering is another possible mechanism for Gilbert damping. It seems to be larger in magnetostrictive magnet. Suhl *et al*. demonstrated the magnon relaxation by phonon drag. The expression for phonon Gilbert damping is given below [50];

$\alpha_{ph} = \frac{2n\gamma}{M_s}\left(\frac{B_2(1+\upsilon)}{Y}\right)^2$ where η is phonon viscosity, B_2 is magneto-elastic shear constant, Y is Youngs' modulus, and ν is Poisson ratio.

(C) **Eddy current**

Eddy current can be important for the thicker ferromagnetic films particularly which are good conductors. The mechanism behind this is: screening of electromagnetic wave by the conduction electrons. Sometimes eddy current gets associated with the rf exchange field in ferromagnetic resonance measurements and enhances the linewidth even in the absence of damping. Electrical conductivity (σ) and skin depth are two important factors, which can control the extent of this effect by the way of exchange conductivity mechanism [38,41]. The damping can be expressed as;

$$\alpha_{eddy} = \frac{(M_s\gamma)^2}{6}\left(\frac{4\pi}{c}\right)2\sigma d^2 \qquad (2.38)$$

where, c is the velocity of light, d is the film thickness, M_s is saturation magnetization and γ is the gyromagnetic ratio.

2.6.2.2 Extrinsic damping

Extrinsic effects can modify the damping of uniformly precessing spins within the magnetic systems in several ways. Presence of magnetic inhomogeneity can cause generation of large number of local resonance fields which, in turn, gives rise to other nonuniform modes causing decoherence of the uniform one. Spin current generated spin torque can modulate the damping in heterostructures with heavymetal (HM)/ferromagnet (FM) interfacing. Spin pumping is another mechanism where angular momentum transferred from the FM to HM causes enhancement of damping.

(A) **Two-magnon scatteing**

Inhomogeneous magnetic properties (such as interfacial roughness in ultra-thin films) can result in scattering of magnons. The the uniform mode can get scattered to other nonuniform modes, which is usually referred to as two-magnon scattering (TMS)

[38,51]. Conservation of energy can allow this scattering. However, due to the loss of translational invariance, momentum does not remain conserved. The number of degenerate magnons is proportional to ω^2 when microwave frequency, $\omega \rightarrow 0$, and thus, TMS eventually decreases linearly to zero with decreasing microwave frequency.

(B) **Dry friction**

During collective motion in presence of rf field a part of spin ensemble can depart from the path of uniform motion and align according to the local potential. Then it is dragged out by the exchange coupling with neighbouring magnetic moments. It causes energy loss of the uniform motion even if it is slow [38]. Thus, rf hysteresis leads to zero frequency loss and is known as dry friction. This mechanism requires large anisotropy energy with arbitrary direction. This process is more relevant for RE ions but not observed for TM.

(C) **Magnetic inhomogeneities**

Generally in ferromagnetic resonance (FMR) measurements, global excitation takes into account the effect of superposition of local resonance in case of long wavelength (small q) variation in magnetic properties [38,39]. This arises mainly due to defects in large area averaging and is different in nature from TMS. Magnetostatic contribution plays an important role in affecting the magnon-energy dispersion.

2.6.2.3 Theoretical modeling of damping

Theoretical models for extraction of damping were developed during 1970 to 1980, and these models are extremely important to describe a general picture of different damping mechanisms.

(A) **s-d exchange relaxation**

Intrinsic damping can be described in terms of SOC Hamiltonian. In presence of phonon and magnon, conduction electrons can experience incoherent scatterings. The loss of energy and momentum of localized ‘d’ electrons are mediated by itinerant ‘s’ electrons. When spin of ‘d’ electron is transferred to ‘s’ state, the ‘s’ electron-spin relaxes to lattice exhibiting a spin-flip [52]. This is possible due to presence of SOC. Classical picture of s-d relaxation depicts that, two precessing spins corresponding to ‘s’ and ‘d’ states are mutually coupled via s-d exchange field. If damping is not present, then both will

precess in phase. However, the spin mean free paths for both the electrons are different and finite. This introduces a phase lag and spins relax towards the effective field. The contribution to Gilbert damping is proportional to rate of spin-flip.

(B) **Fermi surface breathing**

In FMs the shapes of the individual layers for up and down spins of the Fermi surface are known to vary when the magnetization rotates. Thus, uniform precession of magnetization gives rise to oscillation of Fermi surface [53]. This involves the relaxation of itinerant electrons due to repopulation of the surface. The repopulation of levels shifted with respect to the chemical potential is observed as a deformation of the Fermi surface. This dissipative process takes place mostly by the more probable scattering within sub-bands of the same spin index. This process leads to overall dephasing of Fermi surface oscillation and precessing magnetization, and develops SOC dependent Gilbert like damping in the system.

2.7 Magneto-Optical Kerr Effect (MOKE)

Magneto-optic interactions may serve either for sensing the magnetic state of a medium, as for memory applications, or for modulation of the light. In 1877, Kerr observed magneto-optic effect when a reflected light changed its polarization after interacting with shiny magnetic pole piece [54]. Later Kundt observed that this effect is even enhanced in the presence of a ferromagnetic surface [55]. Magneto-optic Kerr effect (MOKE) demonstrates that when the linearly polarized light interacts with ferromagnetic material in presence of a magnetic field, polarization becomes elliptical with major axis of the ellipse rotated.

2.7.1 MOKE Geometries

Depending upon the relative orientation of magnetization vector to the sample surface and plane of incidence of light, Kerr effect can be divided into three categories (Fig. 2.3): when the magnetization lies perpendicular to the sample surface but parallel to the plane of incidence of light, then the effect is known to occur in polar geometry. If the magnetization lies in sample plane and also parallel to the plane of incidence of light, then the geometry is longitudinal geometry. These two geometries occur both for p- and s-polarized light. On the other hand, if magnetization lies in the plane of sample but perpendicular to the plane of incidence then it is called Transverse MOKE geometry and

it occurs only for p-polarized light. In transverse geometry, the reflectivity changes only when the magnetization reverses. The schematic for three geometries is presented in Fig. 2.3.

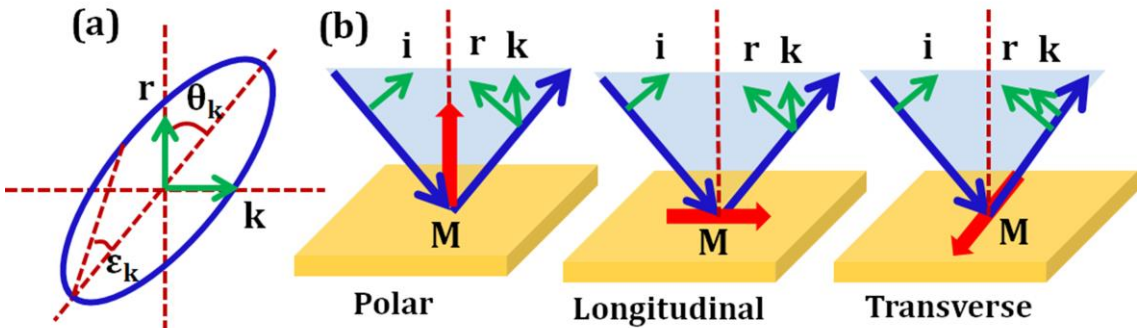

Figure 2.3: (a) Geometry of the Kerr rotation (θ_K) and Kerr ellipticity (ε_K). (b) Schematics of polar, longitudinal and transverse MOKE geometries are shown.

2. 2.7.2 Origin of Kerr effect

When light traverse through a medium, the generated electric field sets electrons into motion [56,57]. The left circularly polarized (LCP) light drives left-circular motion of electrons. Similarly, the right circularly polarized (RCP) light leads to right-circular motion. If there is no magnetic field present, the radii of these two circular motions become equal. This results in zero difference in the dielectric constants. However, in presence of the magnetic field, the electrons will feel an additional Lorentz force due to the external magnetic field. This will affect the radii of the right and left circular path. This will lead to a finite difference in the dielectric constants of both the polarized modes. The amplitude and phase of each component is altered upon reflection. So, the reflected beam do not remain linearly polarized, but becomes an elliptically polarized. This gives rise to the Kerr effect. The angle of the major axis of the polarization rotated from the linear polarization axis, is known as Kerr angle, θ_K. If r and k denote the parallel and perpendicular electric field vector components of the reflected light with respect to that of the incident light, then Kerr rotation (θ_K) and ellipticity (ε_K), which are proportional to the magnetization of the sample, can be expressed as, $\theta_K + i\epsilon_K = \frac{k}{r}$.

As Kerr effect is mainly originated from the motion of electron which couples electron spin via spin-orbit interaction according to the quantum mechanical description. The movement of electrons in presence of the electric field vector of light creates an effective magnetic field vector potential, which develops an complex interaction

between the spin and incident light. This potential can be expressed as, $\boldsymbol{s} \times \nabla \boldsymbol{V}$, $\boldsymbol{s}$ and $\nabla \boldsymbol{V}$ being the electron spin and the electric field, respectively. For ferromagnetic materials, the effect is prominent because of the unbalanced population of electron spins [56]. However, the effect is present in all materials except in nonmagnets, because of the presence of equal amount of up and down spins canceling the effect.

2.8 Spin and Spin Current

The quantum mechanical property of fundamental particles, namely 'spin' is well known. The mental picture depicts that 'spin' represents angular momentum associated with the particle during spinning about its own axis. However, this classical picture is inadequate and oversimplified to describe the quantum mechanical property.

2.8.1 Spin Polarization

In quantum mechanics 'spin' can be expressed as an operator:

$$\hat{S} = \frac{\hbar}{2}\hat{\sigma} \tag{2.39}$$

where $\hat{\sigma}$ is the Pauli spin matrix given by:

$$\hat{\sigma}_X = \begin{pmatrix} 0 & 1 \\ 1 & 0 \end{pmatrix}, \hat{\sigma}_Y = \begin{pmatrix} 0 & -i \\ i & 0 \end{pmatrix}, \hat{\sigma}_Z = \begin{pmatrix} 1 & 0 \\ 0 & -1 \end{pmatrix} \tag{2.40}$$

The wave function related to spin degree of freedom can be written as:

$$\psi\,(r,t) = a|\uparrow\rangle + b|\downarrow\rangle = \begin{pmatrix} a \\ b \end{pmatrix} \tag{2.41}$$

The probability density is:

$$\rho(r,t) = \psi^{\dagger}(r,t)\psi(r,t) = a^2 + b^2 \tag{2.42}$$

Similarly charge density can be expressed as:

$$\rho_c(r,t) = \psi^{\dagger}(r,t)\hat{Q}\psi(r,t) \tag{2.43}$$

and spin density as:

$$\rho_{\hat{S}}(r,t) = \psi^{\dagger}(r,t)\hat{S}\psi(r,t) \tag{2.44}$$

In terms of spinors, the spin charge can be described as below,

$$s(r,t) = \frac{\rho_{\hat{S}}(r,t)}{\rho(r,t)} = \varphi^{\dagger}(r,t)\hat{S}\varphi(r,t) \tag{2.45}$$

$$s(r,t) = \frac{\hbar}{2}\,\varphi^{\dagger}(r,t)\hat{\sigma}\varphi(r,t) = \frac{\hbar}{2}p(r,t) \tag{2.46}$$

The polarization vector (p) of a spin charge of electron is a real pseudovector in three-dimensional space. For an entire ensemble if the majority of spin belong to a particular state, then the beam is polarized. On the other if they are equally distributed within the states then it is unpolarized.

2.8.2 Spin Current

Now suppose in a system carrier density is n and probability densities for up and down states are a^2 and b^2, then the charge density and spin density become,

$$\rho_c = -e(a^2 + b^2) \tag{2.47}$$

$$\rho_{\hat{S}} = \frac{\hbar}{2}(a^2 - b^2) \tag{2.48}$$

$$a^2 = n_{\uparrow}, b^2 = n_{\downarrow}, a^2 + b^2 = n \tag{2.49}$$

where n is the total number of elements. Thus, if the current densities of each spin states can be described by,

$$J_{\uparrow(\downarrow)} = -en_{\uparrow(\downarrow)}v \tag{2.50}$$

Charge current density and spin current density will be,

$$J_c = \rho_c v = J_{\uparrow} + J_{\downarrow} \tag{2.51}$$

$$J_{\hat{S}} = \rho_{\hat{S}} v = -\frac{\hbar}{2e}(J_{\uparrow} - J_{\downarrow}) \tag{2.52}$$

The units of charge current and spin current are not the same. In SI system the unit of charge current is A/m^2. The unit of spin current is $\frac{\hbar}{e}A$.

When spins with opposite polarity get deflected in two opposite directions then the resultant spin imbalance is known as 'spin current'. This spin current can be categorized in to four different kinds: pure spin current, partially spin polarized current, fully spin polarized current and unpolarized current (see Fig. 2.4).

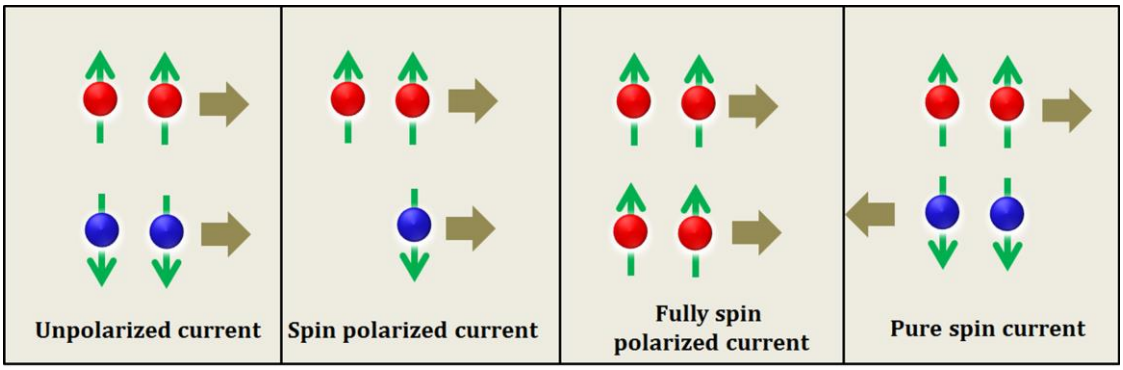

Figure 2.4: Variety of spin current: Unpolarized current, spin polarized current and pure spin current.

2.8.3 Hall Effect

E. Hall discovered this effect in 1879 [59]. This effect describes that if charge current is applied in a material in presence of a transverse magnetic field, an electric field is developed within the material perpendicular to both the applied fields. There are the following varieties of Hall effect (Fig. 2.5):

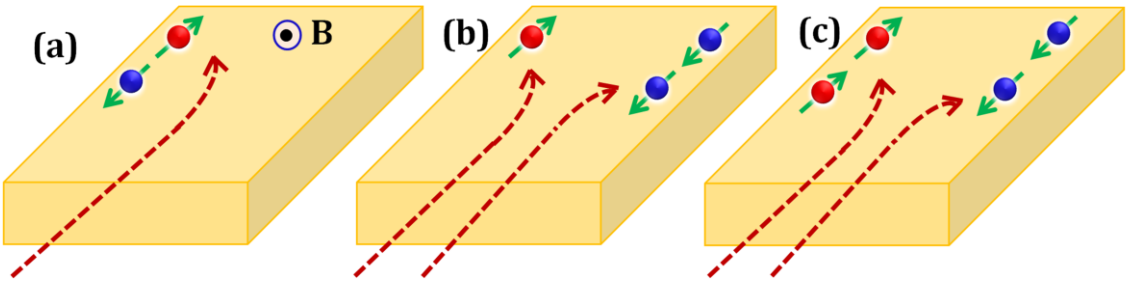

Figure 2.5: Hall geometries: (a) ordinary Hall effect, (b) anomalous Hall effect and (c) spin Hall effect.

2.8.3.1 Ordinary Hall effect

An example can describe this effect better. For a simple metal with only one type of charge carrier (*i.e.* electrons), the Hall voltage (V_H) can be estimated by using the Lorentz force. A piece of metal having dimension $L \times b \times d$, is placed in magnetic field B_y. If charge current (of electric field E) is applied along x direction then the Lorentz force acting upon the electrons is:

$$F = e\boldsymbol{E} + e(\boldsymbol{v} \times \boldsymbol{B}) \tag{2.53}$$

Now accumulation of charge in the top and bottom surface will generate a Hall voltage,

$$V_H = \boldsymbol{z}.\boldsymbol{E}_H = e(\boldsymbol{v} \times \boldsymbol{B}) = \frac{IB}{neb} \tag{2.54}$$

Where $I = nevbd$, n is number of particle, v is velocity and other symbols have usual meaning. If j is considered as applied charge current density then the Hall coefficient can be expressed as,

$$R_H = \frac{E_H}{jB} \tag{2.55}$$

In Si unit this becomes, $R_H = -\frac{1}{ne}$.

2.8.3.2 Anomalous Hall effect

In ferromagnetic system additional contribution to Hall voltage comes from the anomalous Hall effect (AHE) [60]. Here, presence of external magnetic field is not required. Due to the application of charge current spin dependent scattering leads to deviation of electrons with opposite spin polarity in opposite directions. Since the material is ferromagnet it has difference in majority and minority spin population in the bands. Thus, the number of electrons with either kinds of spin polarity accumulated after deviation will be larger than the other. This will create an additional charge imbalance, which is proportional to the magnetization of the material and is different from ordinary Hall effect. The total Hall resistance then in the material will have two contributions: $R_H = R_0B+R_AM$. Here R_0 and R_A are the ordinary and anomalous Hall coefficients. The AHE is of two types, *i.e.* intrinsic and extrinsic effects. It is worth to mention here that quantized version of intrinsic AHE is known as quantum Hall effect (QHE).

2.8.3.3 Spin Hall effect

In presence of charge current in some of the materials, the spins with opposite polarity get deflected in two opposite directions creating a spin imbalance. Without application of any external magnetic field this spin imbalance originates a spin current (J_s). This phenomenon is known as spin Hall effect [61]. As this current is transverse to the applied electric field E, then $J_s.E = 0$. There is no Joule heating associated with pure spin current as the net amount of accumulated electrons are same in either side of the material surface. There are two types of spin Hall effect: intrinsic effect is caused by Rashba spin-orbit interaction. The extrinsic effect arises from the spin dependent scattering. There are two explicit mechanisms responsible for the occurrence of extrinsic spin Hall effect:

(1) **Skew scattering mechanism**

N. F. Mott in 1929 suggested that polarized electron scatters asymmetrically due to SO coupling [62]. When as itinerant electron passes through the vicinity of electric field produced by impurity or scattering centers, $\widetilde{\boldsymbol{B}} = \boldsymbol{v} \times \boldsymbol{E}$ is felt by the electron in its own frame perpendicular to the scattering plane. Now $\boldsymbol{B}$ is inhomogeneous over space and sign changes when the electron with different polarity deflects from different sides of the impurity. The force of deflection due to Zeeman effect depends on polarity of spin.

(2) **Side jump mechanism**

When SOC is acting on a system the symmetry is low. Hence a travelling electron not necessarily retains a straight line path and either deflects with an angle θ or shifts with a path Δy after scattering [63]. This mechanism has purely quantum mechanical nature. An anomalous velocity ($\boldsymbol{v}$) of electron occurs which is spin dependent,

$$H = \frac{p^2}{2m} + eV + V_{so} \tag{2.56}$$

H is Pauli Hamiltonian in presence of spin-orbit interaction.

$$V_{so} = \frac{\hbar}{4m^2c^2}(\boldsymbol{\sigma} \times \nabla \boldsymbol{v}).\boldsymbol{P} \tag{2.57}$$

$$\boldsymbol{v} = \frac{\partial \boldsymbol{H}}{\partial \boldsymbol{P}} = \frac{\boldsymbol{P}}{m} - \frac{e\hbar}{4m^2c^2}\boldsymbol{E} \times \boldsymbol{P} \tag{2.58}$$

Here $\boldsymbol{E}$ is electric field, $\boldsymbol{\sigma}$ is the spin polarity and $\boldsymbol{P}$ is momentum vector.

2.9 Magneto-Electric Generation of Spin Wave

The emerging field of 'straintronics' deals with the 'straintronic switching' which involves rotation of magnetization of a magnetostrictive soft layer on exertion of mechanical strain produced by applying a voltage across an underlying piezoelectric layer [64]. The electric field of the charge current generates strain within the piezoelectric material, which is completely or partially transferred to the magnetostrictive soft layer and rotates its magnetization by the Villari effect. However, the manipulation of magnetization can also be achieved without application of charge current and exploiting the electric field associated with femtosecond laser. In the

following sections, we have discussed the magneto-electric generation of SW modes in a magnetostrictive nanomagnet fabricated on a piezoelectric substrate.

2.9.1 Generation of Surface Acoustic Wave in a Ferromagnetic Material

Two mechanisms can generate periodic strain in a ferromagnetic thin film/patterned array by a ultrafast femtosecond laser pulse. In the first case, for a ferromagnetic thin film grown on a piezoelectric substrate, the alternating electric field in the laser can generate a periodic (compressive and tensile) strain in the material via d_{33} and/or d_{31} coupling. In the second case, for a patterned ferromagnetic array grown on a substrate, the periodic differential thermal expansions of the two materials after shining a pulsed laser can generate periodic strain [65]. The former mechanism requires a piezoelectric substrate and the latter does not. These phenomena give rise to surface acoustic waves (SAWs) which can be probed by another pulsed laser from the variation of time resolved reflectivity.

For the case of SAW generated by electric field (E) of the laser on the piezoelectric substrate with piezoelectric coefficient d_{33}, the strain amplitude is:

$$\varepsilon = d_{33}E \tag{2.59}$$

If a nanomagnet is now patterned on the piezoelectric substrate the thermal strain in the nanomagnet due to differential thermal expansion would be approximately,:

$$\varepsilon = \xi(\alpha_{Pz} - \alpha_{FM})\Delta T \quad [\xi \ll 1] \tag{2.60}$$

where α is the thermal expansion coefficient of the materials and ΔT is the temperature rise. ξ is generally a factor much smaller than unity. For an epitaxially grown thin film on the substrate, there is a possibility of forming well-defined bonds at the interface and the above formula can be simplified as:

$$\varepsilon = (\alpha_{Pz} - \alpha_{FM})\Delta T \tag{2.61}$$

If there is substantial temperature rise due to the periodic heating by the laser pulse, then sufficient strain will be generated by the SAW.

2.9.2 Strain Induced Magnetization Dynamics of a Magnetostrictive Nanomagnet on Piezoelectric Substrate

When a nanomagnet is patterened on a piezoelectric, substrate the strain amplitude generated in the nanomagnet can be expressed by the Hooke's law, $\sigma = Y\varepsilon$, where Y is

the Young's modulus of the nanomagnet and ε is the strain amplitude generated by the SAW. The SAW will induce periodic strain anisotropy in the nanomagnet via Villari effect (application of stress can change the magnetization due to magnetoelastic interaction) if it is a magnetostrictive material. The amplitude of this anisotropy will be, $K_0 = \frac{3}{2}\chi\sigma$, where χ is magnetostriction coefficient of the nanomagnet. As the strain anisotropy is periodic in nature it can be expressed as;

$$K_1(t) = K_0[\sin(2\pi f_1 t) + \sin(2\pi f_2 t) + \cdots] \tag{2.62}$$

f_1, f_2,...are the frequencies of the polychromatic SAW. The velocity of the SAW can be determined from the following formula:

$$v = \lambda f \tag{2.63}$$

where λ is the wavelength and it depends on the distance between pinning points, *i.e.* lattice constants in case of periodically patterened nanomagnet arrays.

Now, the component of the magnetic field due to strain in the i^{th} direction is:

$$H^i_{strain}(t) = \frac{3\chi\sigma(t)m_i(t)}{\mu_0 M_s} = \frac{2K_1(t)m_i(t)}{\mu_0 M_s} \tag{2.64}$$

where m_i(t) is the i^{th} component of the normalized magnetization (spatially averaged) at time *t*. This field will simultaneously affect the effective field present in the system. Thus the magnetization dynamics in the nanomagnet in the presence of a bias magnetic field (including other interaction fields, if any) and the periodic strain due to the SAWs leads to generation of hybrid magneto-dynamical SW modes.

By employing TR-MOKE microscopy, the time-resolved Kerr rotation and reflectivity oscillations can be recorded due to the temporal variation of the intensity and polarization of light interacting with the sample. There can be additional contributions to the periodic stress from the differential thermal expansions of FM and piezoelectric material due to periodic heating by the pump laser. However, the relative contribution from this mechanism to the effective strain may differ.

References

1. P. Weiss, J. Phys. Theor. Appl. **6**, 661 (1907).
2. P. Weiss, Comptes Rendus **143**, 1136 (1906).

3. A. H. Morrish, *in The Physical Principles of Magnetism*, (Wiley, New York, 1965).
4. E. C. Stoner and E. P. Wohlfarth, *A mechanism of magnetic hysteresis in heterogeneous alloys*, philosophical transactions of the royal society of London. Ser A Math Phys Sci **240** (826) (1984), 599–642.
5. L. D. Landau and E. M. Lifshitz, Phys. Z. Sowjetunion **8**, 153 (1935).
6. J. H. E. Griffiths, Nature **158**, 670 (1946).
7. C. Kittel, Phys. Rev. **73**, 155 (1948).
8. T. L. Gilbert, IEEE Trans. Magn. **40**, 3443 (2004).
9. B. H. and and J. A. C. Bland, *Ultrathin Magnetic Structures II*. (Springer, Verlag Berlin Heidelberg, 1994).
10. A. Aharoni, *Introduction to the Theory of Ferromagnetism*. (Oxford University Press, Newyork, 2000).
11. J. M. D. Coey, *Magnetism and Magnetic Materials*. (Cambridge University Press, Cambridge, 2010).
12. P. Bruno, *Physical Origins and Theoretical Models of Magnetic Anisotropy* (Ferienkurse des Forschungszentrums Jürich, Jürich, 1993).
13. P. Bruno and J.-P. Renard, Appl. Phys. A **49**, 499 (1989).
14. F. Bloch, Z. Physik **61**, 206 (1930).
15. B. Hillebrands and K. Ounadjela (eds), *Spin Dynamics in Confined Magnetic Structures II*. (Springer, New York, 2003) pp 280–285.
16. B. Hillebrands and A. Thiaville (eds), *Spin Dynamics in Confined Magnetic Structures III*. (Springer, Berlin, 2006) pp 57-75.
17. R. W. Damon and J. R. Eshbach, J. Phys. Chem. Solids **19**, 308 (1961).
18. S. O. Demokritov, B. Hillebrands, and A. N. Slavin, Phys. Rep. **348**, 441 (2001).
19. C. Herring and C. Kittel, Phys. Rev. **81**, 869 (1951).
20. A. Barman and A. Haldar, *Time-domain study of magnetization dynamics in magnetic thin films and micro-and nanostructures.* Solid State Phys, vol **65**. (Elsevier Inc., Burlington, 2014).
21. G. L. Bona, F. Meier, G. Schönhense, and H. C. Siegmann, J. Magn. Magn. Mater. **54-57**, 809 (1986).
22. A. Vaterlaus, T. Beutler, D. Guarisco, M. Lutz, and F. Meier, Phys. Rev. B **46**, 5280 (1992).

23. E. Beaurepaire, J. C. Merle, A. Daunois, and J. Y. Bigot, Phys. Rev. Lett. **76**, 4250 (1996).
24. S. I. Anisimov, B. L. Kapeliovitch, and T. L. Perel'man, Sov. Phys. JETP **39**, 375 (1974).
25. F. Dalla Longa, J. T. Kohlhepp, W. J. M. de Jonge, and B. Koopmans, Phys. Rev. B **75**, 224431 (2007).
26. J. Walowski, G. Müller, M. Djordjevic, M. Münzenberg, M. Kläui, C. A. F. Vaz, and J. A. C. Bland, Phys. Rev. Lett. **101**, 237401 (2008).
27. B. Koopmans, G. Malinowski, F. Dalla Longa, D. Steiauf, M. Fähnle, T. Roth, M. Cinchetti, and M. Aeschlimann, Nat. Mater. **9**, 259 (2009).
28. B. Koopmans, J. J. M. Ruigrok, F. D. Longa, and W. J. M. de Jonge, Phys. Rev. Lett. **95**, 267207 (2005).
29. M. Krauß, T. Roth, S. Alebrand, D. Steil, M. Cinchetti, M. Aeschlimann, and H. C. Schneider, Phys. Rev. B **80**, 180407 (2009).
30. J.-Y. Bigot, M. Vomir, and E. Beaurepaire, Nat. Phys. **5**, 515 (2009).
31. G. P. Zhang, W. Hübner, G. Lefkidis, Y. Bai, and T. F. George, Nat. Phys. **5**, 499 (2009).
32. G. Malinowski, F. Dalla Longa, J. H. H. Rietjens, P. V. Paluskar, R. Huijink, H. J. M. Swagten, and B. Koopmans, Nat. Phys. **4**, 855 (2008).
33. G. Lefkidis, G. P. Zhang, and W. Hübner, Phys. Rev. Lett. **103**, 217401 (2009).
34. G. P. Zhang and W. Hübner, Phys. Rev. Lett. **85**, 3025 (2000).
35. M. Battiato, K. Carva, and P. M. Oppeneer, Phys. Rev. Lett. **105**, 027203 (2010).
36. B. Pfau, S. Schaffert, L. Müller, C. Gutt, A. Al-Shemmary, F. Büttner, R. Delaunay, S. Düsterer, S. Flewett, R. Frömter, J. Geilhufe, E. Guehrs, C. M. Günther, R. Hawaldar, M. Hille, N. Jaouen, A. Kobs, K. Li, J. Mohanty, H. Redlin, W. F. Schlotter, D. Stickler, R. Treusch, B. Vodungbo, M. Kläui, H. P. Oepen, J. Lüning, G. Grübel, and S. Eisebitt, Nat. Commun. **3**, 1100 (2012).
37. D. Rudolf, C. La-O-Vorakiat, M. Battiato, R. Adam, J. M. Shaw, E. Turgut, P. Maldonado, S. Mathias, P. Grychtol, H. T. Nembach, T. J. Silva, M. Aeschlimann, H. C. Kapteyn, M. M. Murnane, C. M. Schneider, and P. M. Oppeneer, Nat. Commun. **3**, 1037 (2012).
38. B. Heinrich and J. A. C. Bland, *Spin relaxation in magnetic metallic layers and multilayers. In: Bland JAC (ed) Ultrathin magnetic structures: fundamentals of nanomagnetism,* (Springer, New York, 2005).

39. A. Barman and J. Sinha, *Spin Dynamics and Damping in Ferromagnetic Thin Films and Nanostructures* (Springer Publishing AG, Switzerland, 2017).
40. B. Heinrich, J. F. Cochran, and K. Myrtle, J. Appl. Phys. **53**, 2092 (1982).
41. P. Krivosik, N. Mo, S. Kalarickal, and C. E. Patton, J. Appl. Phys. **101**, 083901 (2007).
42. J. O. Rantschler, R. D. McMichael, A. Castillo, A. J. Shapiro, W. F. Egelhoff, B. B. Maranville, D. Pulugurtha, A. P. Chen, and L. M. Connors, J. Appl. Phys. **101**, 033911 (2007).
43. Y. Tserkovnyak, A. Brataas, and G. E. W. Bauer, Phys. Rev. B **66**, 224403 (2002).
44. A. Ganguly, R. M. Rowan-Robinson, A. Haldar, S. Jaiswal, J. Sinha, A. T. Hindmarch, D. A. Atkinson, and A. Barman, Appl. Phys. Lett. **105**, 112409 (2014).
45. K. Lenz, H. Wende, W. Kuch, K. Baberschke, K. Nagy, and A. Jánossy, Phys. Rev. B **73**, 144424 (2006).
46. Y. Zhao, Q. Song, S.-H. Yang, T. Su, W. Yuan, S. S. P. Parkin, J. Shi, and W. Han, Sci. Rep. **6**, 22890 (2016).
47. S. Mondal and A. Barman, Phys. Rev. Appl. **10**, 054037 (2018).
48. E. Jué, C. K. Safeer, M. Drouard, A. Lopez, P. Balint, L. Buda-Prejbeanu, O. Boulle, S. Auffret, A. Schuhl, A. Manchon, I. M. Miron, and G. Gaudin, Nat. Mater. **15**, 272 (2015).
49. V. Kamberský, Czechoslovak Journal of Physics B **26**, 1366 (1976).
50. H. Suhl, IEEE Trans. Magn. **34**, 1834 (1998).
51. G. Woltersdorf and B. Heinrich, Phys. Rev. B **69**, 184417 (2004).
52. E. M. Kogan, E. A. Turov, and A. N. Voloshinskii, Phys. Status Solidi B **98**, 165 (1980).
53. V. Kamberský, Can. J. Phys. **48**, 2906 (1970).
54. J. Kerr, Philos. Mag. 3, 339 (1877).
55. A. Kundt, Philos. Mag. Ser. **5** 308 (1884).
56. Z. Q. Qiu and S. D. Bader, J. Magn. Magn. Mater. **200**, 664 (1999).
57. M. Freiser, IEEE Trans. Magn. **4**, 152 (1968).
58. S. Bandyopadhyay and M. Cahay, *Introduction to Spintronics.* (Boca Raton: CRC Press, 2008).
59. E. H. Hall, Am. J. Math. **2**, 287 (1879).
60. T. Jungwirth, Q. Niu, and A. H. MacDonald, Phys. Rev. Lett. **88**, 207208 (2002).
61. M. I. Dyakonov and V. I. Perel, Phys. Lett. A **35**, 459 (1971).
62. N. Mott, Proc. R. Soc. A **124**, 425 (1929).

63. S. Takahashi and S. Maekawa, Sci. Technol. Adv. Mater. **9**, 014105 (2008).

64. N. D'Souza, A. Biswas, H. Ahmad, M. Salehi-Fashami, M. M. Al-Rashid, V. Sampath, D. Bhattacharya, M. A. Abeed, J. Atulasimha, S. Bandyopadhyay, Nanotechnology **29**, 442001 (2018).

65. Y. Yahagi, B. Hartenek, S. Cabrini and H. Schmidt, Phys. Rev. B. **90**, 140405(R) (2014).

Chapter 3

3 Experimental and Numerical Methods

3.1 Introduction

Sample fabrication is an indispensible part of rapid development in the spintronics technology. The miniaturization of gadgets solely depends on the efficiency and sensitivity of on-chip device fabrication with ultra-high packing density and choice of raw materials. This demand expedites the development of various fabrication techniques for preparing samples down to nanoscale regime with high precision. The samples can be grown by following bottom-up and top-down approaches [1]. The former approach relies on chemical processes to synthesize series of nanoparticles, nanowires etc. However, using this process it is often difficult to obtain highly ordered and monodispersed structures which are essential components for device fabrication. Top-down approach is basically used to construct nanodot array, antidot array, MCs, Bi-MCs, nanostripes, quasicrystals and several other micro- and nanostructures by pattering magnetic thin films and multilayers. It is extremely important to optimize the steps of fabrication procedure to achieve high quality interfaces while involving different kinds of materials and to get very sharp edges while fabricating narrow sized elements avoiding structural distortion. Recently a combination of both top-down and bottom up techniques is being used as per convenience. In this chapter, the working principle of magnetron sputtering, electron beam (e-beam) evaporation and e-beam lithography will be discussed which have been used to grow high quality ferromagnetic thin films, ferromagnet/nonmagnet heterostructures and nanostructures.

The next challenge is to probe the static and dynamic properties of the thin fims, heterostrucrures and micro and nanostructures. The topographical and elemental quality can be studied by using scanning electron microscope (SEM), energy dispersive X-ray (EDAX), X-ray diffraction technique (XRD), atomic force microscope (AFM) etc. Study of the spin textures, magnetization and stray field distribution, developed in 2D nanostructures are conducted using magnetic force microscope (MFM) and static MOKE magnetometry etc. The well-known techniques employed to measure the magnetization dynamics in time domain, frequency domain and wave-vector domain are TR-MOKE,

FMR and BLS spectroscopy [2]. There are several other techniques based on light-mater interaction or electrical perturbation, which can excite and detect the magnetization dynamics with appreciable spatio-temporal resolution. In this chapter the features of TR-MOKE magnetometry will be discussed in detail which has been used to study the ultrafast magnetization dynamics of the samples.

Micromagnetic simulation is an efficient tool for studying a wide variety of magnetic phenomena including magnetization reversal and dynamics. Researchers have developed a series of micromagnetic simulators, such as, object oriented micromagnetic framework (OOMMF), LLG, NMAG, MuMax3, VAMPIRE, Boris etc., which are extremely efficient and useful to simulate the magnetization dynamics associated with complicated magnetic textures with convenient user interface and excellent visualization. In this chapter the overview of OOMMF [3], LLG [4] and MuMax3 [5] is demonstrated. Moreover, to extract and visualize the spin precession amplitude and phase maps of SWs a home build code DotMag [6] has been used.

3.2 Sample Preparation

Here, we give the overview of the techniques which are used to grow and fabricate the samples studied in this thesis.

3.2.1 Sputtering

In sputtering the positive ions in the plasma of an inert gas bombard a negatively charged target material, dislodge and eject neutral atoms, and deposit those on top of a substrate (see Fig. 3.1) [7]. The primary requirement is of an anode: the chamber walls, substrate, substrate holder and a cathode: the target material. The plasma of neutral gas created and stabilized within the vacuum chamber by a high voltage power supply contains atoms, ions, electrons and photons. The electrons accelerate away from the negatively charged target and produce more secondary electrons and ions in the diffused plasma by multiple collisions with the neutral atoms. Some of those secondary electrons are trapped near the surface of the target material by the applied magnetic field which causes the electrons to travel in a cyclic path (magnetron sputtering). The path of the trapped electrons is comparatively longer than the separation between the electrodes so that the electrons can continue colliding. This process is performed under high vacuum of around 10^{-7} Torr or better. The positively charge ions in plasma get

attracted towards the target and eject target atoms. Those atoms finally traverse towards the anode (mainly substrate) maintaining typical line-of-sight cosine path and deposit on top of the anode.

Sputtering technique has two major categories: dc and rf sputtering. In the former one, conductive materials are used as target. There is less probability of electrons being accumulated near the target surface causing a shielding effect. However, the problem can be major for a dielectric or electrically insulating target. Use of an alternating or radio frequency (ac or rf) power supply can avoid the problem of charge accumulation and the the deposition is continued. The plasma can be sustained by simultaneously accelerating and reversing the direction of the electrons through large distances so that they gain sufficient kinetic energy required for ionizing the sputter gas during collisions. This will be possible if the frequency of the rf field is high enough. This eliminates the need for secondary electrons from the target to sustain the plasma. Using proper electrode configuration (dc or rf), optimizing the pressure of ions with ion gauge and controlling the deposition rate monitored by a quartz crystal monitor, high quality thin films with single or multilayered thin films and heterostructures can be deposited using magnetron sputtering.

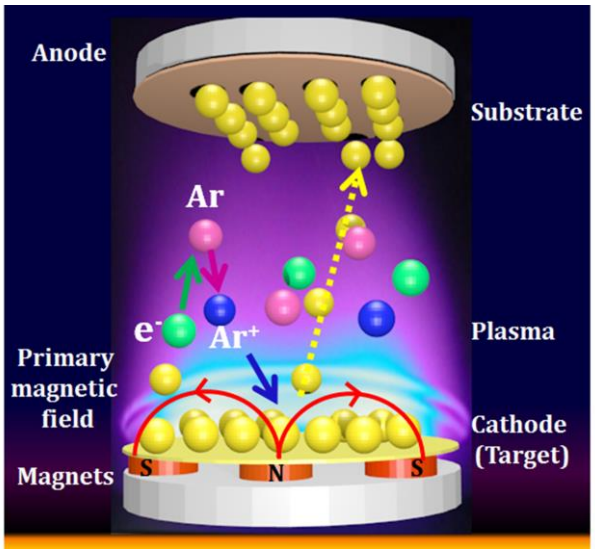

Figure 3.1: Schematic representation of the sputtering technique.

3.2.2 E-Beam Evaporation

This is a physical vapor deposition (PVD) technique, where an intense beam of electrons is generated from a filament via thermionic emission and is steered by the electric and magnetic fields towards the source material. The collision with electron beam causes heating of the source material. It vaporizes after reaching the boiling point within a vacuum environment [8]. The surface atoms having sufficient energy traverse the vacuum chamber and can be used to coat a substrate placed above the evaporating material (see Fig. 3.2). Since thermal energy is very low, the pressure in the chamber is maintained in a way so that the mean free path remain lesser than the distance between the electron beam source and the substrate. The "line of sight" arrival of material is required when masking is employed to generate a pattern in the substrate. Generally, the low arrival energy is also advantageous for sensitive substrates.

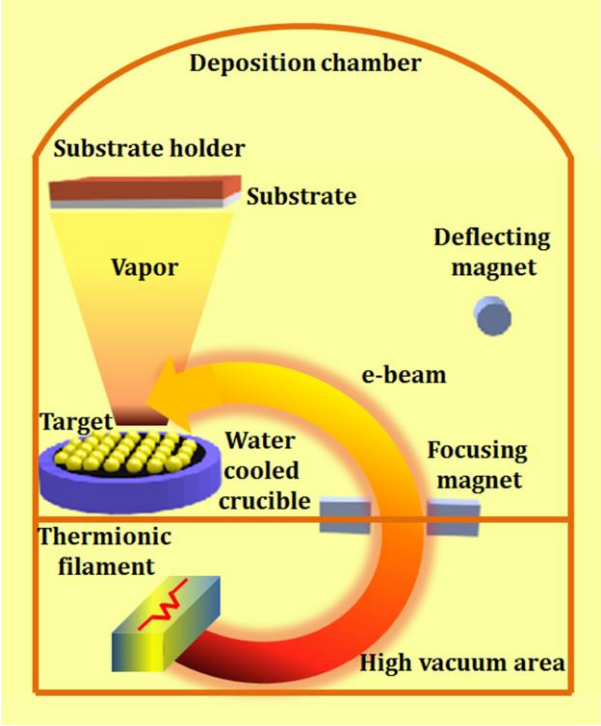

Figure 3.2: Schematic diagram of e-beam evaporation technique.

3.2.3 E-Beam Lithography

E-beam lithography (EBL) is a sophisticated technique for creating the extremely fine patterns, much smaller than that can be visualized by the naked eye or even optical microscope. The technique simply performs a scanning of electron beams across a surface covered with a resist film sensitive to those electrons. This deposits energy to make an imprint of the desired pattern in the resist [9]. The main features of this technique are,

1. It is capable of fabricating nanostructures with very high resolution down to nm scale.

2. It is a flexible technique, capable of working with a variety of materials and different patterns.

3. Being expensive and complicated it needs sophisticated handling

The higher resolution is achieved because the high energy electron beam has much shorter wavelength than light. There are few steps followed in this technique,

1. A clean substrate is spin-coated with a positive e-beam resist (bilayer methyl methacrylate (MMA)/polymethyl methacrylate (PMMA), in present case). The coating should be uniform.

2. A pattern to be developed is drawn very carefully using some commercially available design software like Auto CAD. Then the resist is exposed to focused electron beams inside an SEM through the desired pattern. Accelerated electrons are used to imprint the pattern on top of the resist.

3. The writing process in EBL is software controlled. After drawing the pattern, the resist is developed in chemical solution (methyl isobutyl ketone (MIBK) and isopropyl alcohol (IPA) solution) and then is rinsed in pure water.

4. Now the target material is deposited on top of the resist. Sometimes additional capping layer can also be deposited with the material. To remove the unexposed resist, lift off is done in acetone using ultrasonic agitation.

The schematic of the technique is shown in Fig. 3.3.

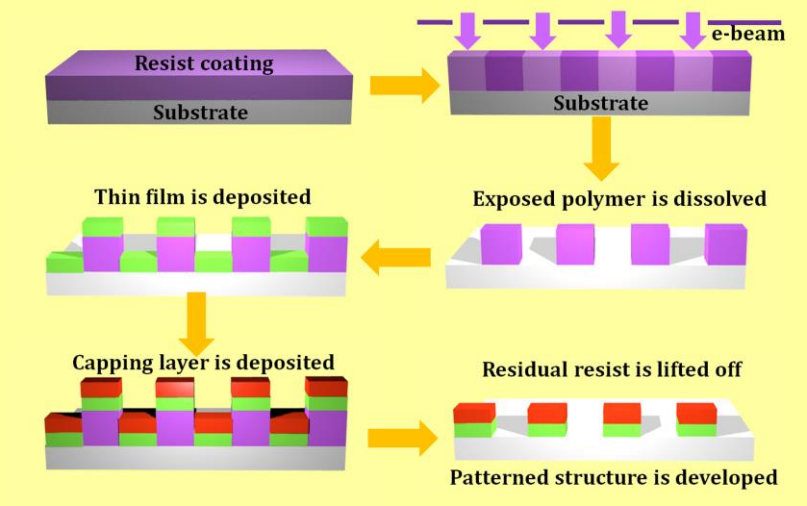

Figure 3.3: Schematic diagram of the e-beam lithography process.

3.3 Sample Characterization

Here, we will give the overview of the techniques which are used to characterize the topographical properties, elemental composition and static magnetic properties of the thin films, heterostructures and nanostructures studied in this thesis.

3.3.1 Scanning Electron Microscope

This technique is used to examine sample topographies at very high magnifications. The equipment is called the scanning electron microscope (SEM) [10]. The first SEM with a submicron probe was developed by von Ardenne. SEM magnifications can go to more than 300,000 times. SEM inspection is often used in the analyses of package cracks, bond failures, fracture surfaces, physical defects on commercial goods. Inside this equipment, a beam of electrons produced after thermionic emission is focused on a small volume of the specimen transferring energy to the spot. A pair of anodes, electromagnetic condenser lenses and scanning coils guide and focus the beam. The electron beam is swept across the area over the sample with raster scanning. These primary electrons can dislodge secondary electrons from the specimen. Those are attracted towards a positively biased detector or grid and finally are coverted into a signal. The primary electron beam also results in the emission of backscattered (or reflected) electrons which possess more energy than secondary electrons, and have a definite direction.

Not only secondary electrons or backscattered electrons, the SEM signal includes auger electrons, transmitted electrons, photons (characteristic X-rays which are used for elemental analysis and continuum X-rays), heat and visible light. By comparing the

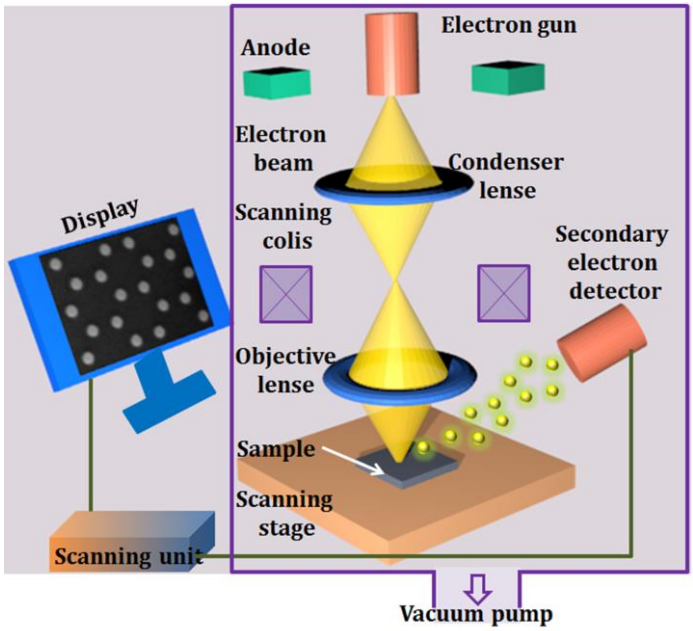

Figure 3.4: Schematic diagram of SEM technique.

intensity of secondary electrons emitted during this process to the primary electron beam, an image of the sample surface is constructed (see Fig. 3.4). We have used Model no: FEI QUANTA 200 SEM to characterize our samples.

3.3.2 Energy Dispersive X-ray Spectroscopy

An atom in ground state contains a number of electrons moving around the nucleus while arranged in discrete shells or orbits. As a high energy beam of charged particles, *i.e.* electrons, protons or X-ray, bombard the sample electrons are ejected out from an inner shell and create electron deficiency in the shell (hole). The electrons from higher energy shells then jump to the inner shell filling the hole. The difference in these two energy shells is emitted as an X-ray. Usually, a Si (or Li) detector is used as the energy dispersive spectrometer to measure the energy and number of the emitted X-rays (see Fig. 3.5). The individual elements are identified from the peak energy values of the X-rays while the relative peak intensities give the atomic percentage of the elements present in the sample.

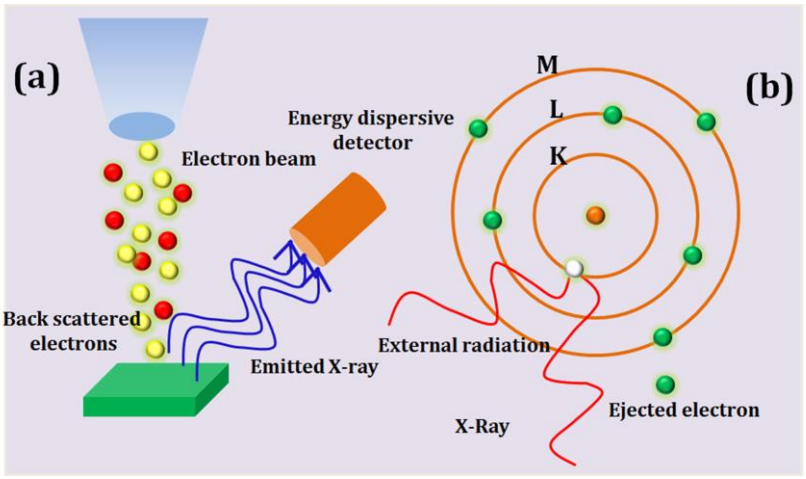

Figure 3.5: (a) Schematic diagram of EDX spectrometer. (b) Schematic of interaction of accelerated electrons with sample and emission of X-rays from the designated orbit.

3.3.3 X-ray Diffraction

Max von Laue proposed that if X-rays were waves, the wavelengths must be extremely small. Thus, the internal structure of crystalline materials can be viewed using X-rays. L. Bragg and his father W. H. Bragg discovered that diffraction could be considered as reflection from evenly spaced planes for monochromatic X-radiation [11]. If we consider a crystal as a regular array of atoms separated by a distance d, electromagnetic waves like X-rays having wavelength λ, can be scattered from those array. The scattered beams form secondary waves. Due to constructive interference they traverse to at certain directions according to the Bragg's condition: $2dsin\theta = n\lambda$, where θ is the angle of incidence and n is an integer. In practice, the incident θ is varied between a range of angles in small steps. 2θ will be the angle of the reflected beam with respect to the direction of the incident beam (see Fig. 3.6). Subsequently, the diffraction peaks are converted to d-spacing to identify the elements present in the sample with exact crystalline nature. The peak positions give direct information about the crystal plane. The X-ray tube and associated electronics produce a limited frequency range of intense X-rays. The filtering of the frequency is done by using the analysis filters, monochromators, specially tuned detectors and software.

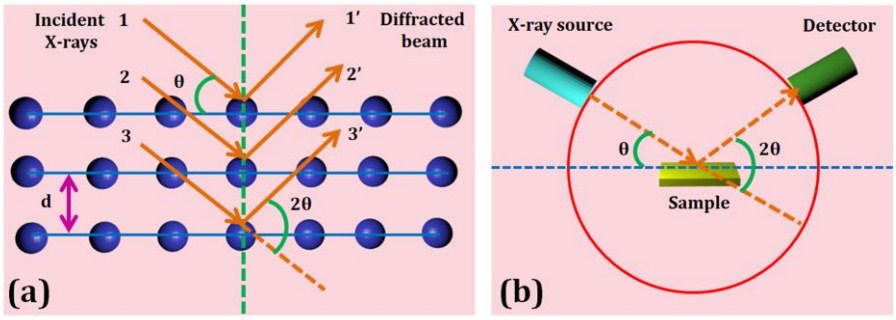

Figure 3.6: Schematic diagram of (a) X-ray diffraction process and (b) X-ray diffractometer.

3.3.4 Atomic Force Microscopy

Atomic force microscope (AFM) is a type of scanning probe microscope where a sharp probe is used to scan over a surface instead of light. With continuous development, the efficiency of this technique spatial resolution has increased significantly and a resolution down to tens of nm has been obtained [12]. The surface topography can be recorded for a wide range of materials, such as, thin films, biological membrane, polymer, semiconductor, ceramic, composite, glass etc. This technique can be exploited to study adhesion, corrosion, etching, friction and polishing of a surface as per requirement. By using this method not only one can image the surface topography but also can measure the force in nano-Newton scale.

The tip is attached to a flexible cantilever. When it approaches the sample surface it gets deflected due to effect of the intrinsic force of the sample (such as, van der Waals force, capillary forces, electrostatic forces, chemical bonding and magnetic forces) causing vibration of the cantilever. The sample is placed on a piezo-electric (PZ) controller which helps in performing the raster scan. A laser beam is pointed on top of the tip, which actually senses the deflection of the tip after being reflected and captured in a four quadrant photodiode (see Fig. 3.7). The information is acquired in terms of voltage. There is a feedback mechanism that enables the PZ scanner to keep the tip at a constant force while obtaining the height information or at constant height for obtaining the force information. Depending on the sample surface and the acting force between the probe and the sample, AFM can be operated in any one of the three modes: contact, non-contact and tapping modes.

The contact mode is generally static mode where the tip approaches in close contact with the surface maintaining a constant repulsive force between the tip and the surface. Here, low stiffness cantilevers are used to achieve a large deflection signal while keeping the interaction force within the safe limit to avoid any damage or scratch over the sample surface. In non-contact mode the tip scans over few tens of angstroms above the surface and relatively weaker force is required for the tip. The surface topography of the sample is measured by determining the change in frequency, amplitude and phase of the vibrating cantilever. The tapping mode is the most popular one. Here, the cantilever oscillates near its resonant frequency with the help of a PZ crystal. The tip is then brought close to tap the sample surface. The irregular contact between the tip and the surface causes an energy loss which is recorded and the images of topography is extracted and processed with the help of software.

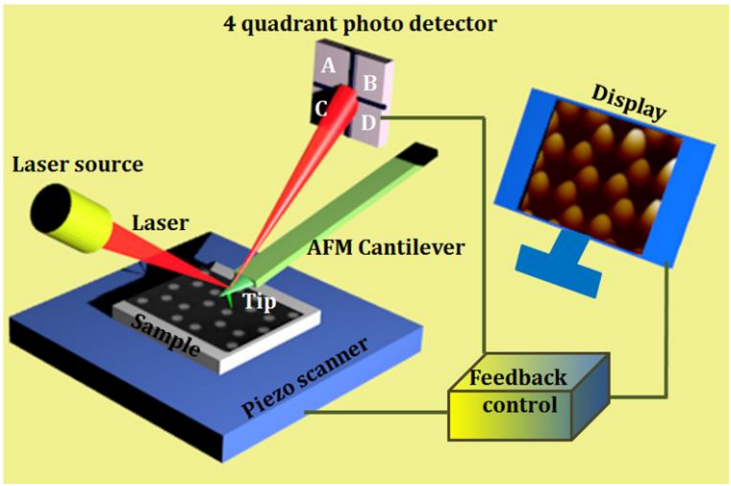

Figure 3.7: Schematic diagram of AFM technique.

3.3.5 Magnetic Force Microscopy

In magnetic force microscopy (MFM) the magnetic texture formed within a magnetic sample can be probed by studying the magnetic interactions between the tip and the sample. It is mostly associated with the AFM setup and it has two operating modes, *i.e.* static and dynamic mode. Necessarily the tip is coated with a thin magnetic layer having high coercivity for better sustainability. The tip can sense the magnetic forces along with the atomic and electrostatic forces near the surface due to the interaction between the components of stray fields. During the measurements to get a better MFM image it is

recommended to take AFM image also. Once the surface topography is recorded the tip is then lifted up and scanned again over the sample surface at that particular height to sense the out-of plane stray fields. Then the magnetic signal is obtained in terms of voltage which is extracted and processed by the software to provide information about magnetic texture.

3.3.6 Vibrating Sample Magnetometry

Magnetization of a material can be measured directly or indirectly by observing any other physical quantity. There are several methods available for the quantification of static magnetization of a magnetic material with required sensitivity, such as, inductive method, force method, magneto-optical method, electrical method etc. In inductive method voltage generated through electromagnetic induction is monitored to find the magnetic flux change in pickup coils. This, in turn, provides the change in value of magnetic induction, which can be used to find the magnetization of different materials. This method is employed in vibrating sample magnetometer (VSM), fluxgate magnetometer, vibrating coil magnetometer and extraction magnetometer etc. VSM is a very popular technique to measure the magnetic properties of thin layers and small crystals of various kinds according to the applied magnetic field and the temperature [13]. Measurement of magnetic moment as small as $\sim 10^{-5}$ emu is possible. The working principle of VSM is based on the Faraday's law. Whenever there is a change in magnetic flux through a coil with N turns, an electromotive force (E) is induced in the coil:

$$E = -NA\frac{dB}{dt} \tag{3.1}$$

A is the area of the sample and B is magnetic induction.

The following relation can describe the relation between magnetization and the induced electric field:

$$E = -NA\frac{dM}{dt} \tag{3.2}$$

as $B = \mu_0 (H+M)$.

The magnetic sample is mounted on a vertical nonmagnetic plastic/quartz rod connected to a piezoelectric transducer and is placed in a constant uniform external magnetic field (see Fig. 3.8). The transducer converts a sinusoidal electric signal

(generated by an oscillator/amplifier) into periodic vibration. As the sample is vibrated, it introduces perturbations in the external magnetic field. These perturbations are sensed by the pick-up coils. Magnetic flux piercing the coils will change the induced emf:

$$E = -mwzy_0 NN_c G\cos(\omega t) \tag{3.3}$$

where w and z are frequency and amplitude of vibration, respectively. The y_0 is distance between two pick up coils, N_c is the number of pick up coils and G is geometric factor of the sample. For particular coil geometry, the emf generated in coils will depend on several factors, *i.e.* the amplitude and frequency of vibration, external magnetic field and the magnetic moment of sample. With proper manipulation, one can deduce the value for magnetization from emf. With varying magnetic field hysteresis behavior of the sample can be measured. By varying temperature, Curie temperature, Neel temperature and compensation temperature for ferro-, antiferro- and ferromagnetic material can be determined.

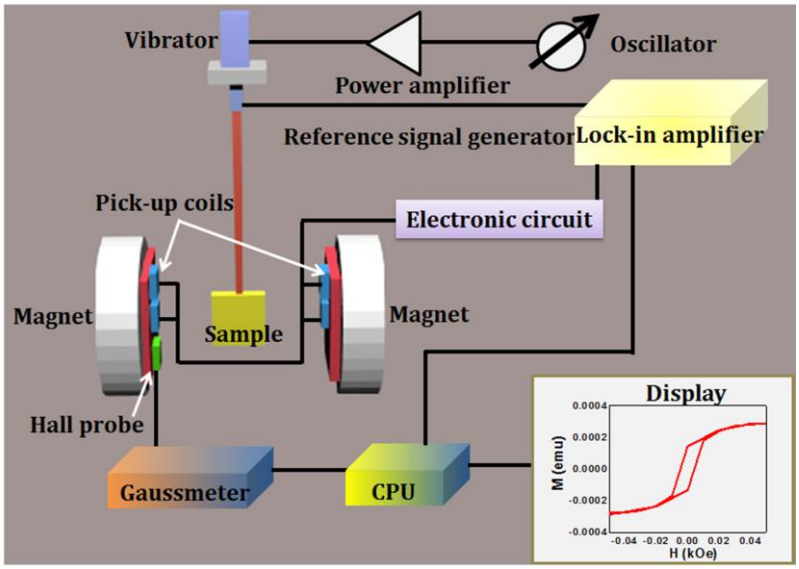

Figure 3.8: Schematic diagram of VSM.

3.3.7 Static Magneto-Optical Kerr Effect Technique

For static MOKE measurements we have adopted the longitudinal MOKE configuration [1,2]. A continuous laser beam generated from He–Ne laser of wavelength of 632.8 nm is employed to probe the magnetization. After passing through a Glan-Thompson (GT) polarizer the light becomes fully polarized and generally S polarized part is transmitted

through the optics. The beam is chopped at 2 kHz frequency by using an optical chopper. Then it is steered by a set of mirros and passed through a pair of lens arrangement. L1 (focal length: 25 mm) and L2 (focal length: 150 mm) maintain the collimation and expand the beam. The beam is incident normally at the back aperture of the microscope objective (MO1- magnification ~ 20X) by totally filling it and becomes obliquely focused on the sample to a micron-sized spot (see Fig. 3.9). The sample is mounted between two pole pieces of an electromagnet. This can provide maximum of 5 kOe field in the IP configuration. A white light is also focused on the sample via the same objective for viewing purpose. The reflected beams are collected by MO2. Later, the light is divided into two parts using a glass slide (GS2) and a fraction is sent to the CCD camera to locate the laser spot onto the sample. The other part is sent to the optical bridge detector (OBD) which can sense and distinguish the change of polarization and intensity of the laser. There is a polarized beam splitter (PBS) inside OBD which splits any light into two orthogonal components. Then a couple of photodiodes (A, B) adopt those components and convert into electrical signal. In absence of magnetic field the balanced condition (A = B) of OBD is obtained by rotating the axis of the PBS slightly away from the 45°. The calibration factor is also measured by rotating the PBS by 1° (or as per convenience) on either sides of the balanced position in the rotational scale and the dc output of the detector is the used to extract the calibration factor. In presence of magnetic field the magnetization in the sample is manipulated and the polarization of the light changes. Thus, the detector moves away from balanced condition (A ≠ B). The difference signal (A – B) is measured in a phase sensitive manner by using a lock-in amplifier. The frequency of the chopper is fed to the lock-in amplifier in order to set a reference. The output signal is converted to Kerr rotation by multiplying the calibration factor. To obtain hysteresis loop, the IP field is varied from positive to negative direction (monitored in terms of current or voltage of the power supply) and the change in magnetization is recorded using labview software.

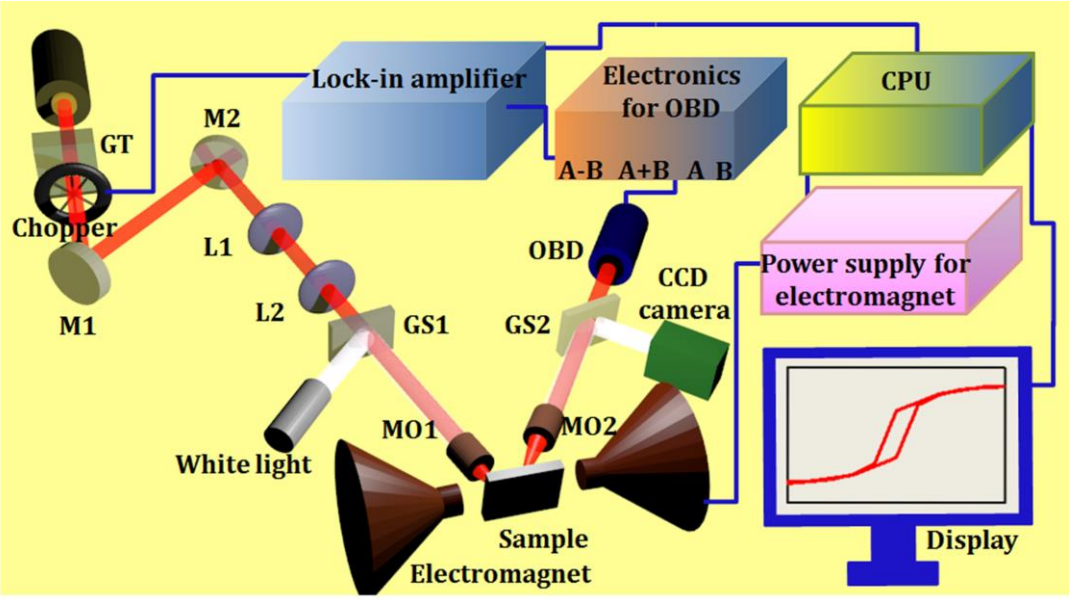

Figure 3.9: Schematic diagram of static MOKE microscope in longitudinal geometry.

3.4 Experimental Setup for Magnetization Dynamics Measurements

TR-MOKE magnetometry is a state-of-the-art technique for studying ultrafast magnetization dynamics starting from femtosecond to nanosecond time scale in which a series of phenomena, such as, ultrafast demagnetization, fast and slow remagnetzations, magnetization precession and damping occur [1, 2, 14-20]. In this section we have provided overview of the two different variants of TR-MOKE techniques based on fs oscillator and amplified laser systems.

3.4.1 Time-Resolved Magneto-Optical Kerr Effect Microscopy

Time-resolved magneto-optical Kerr effect microscope based on a fs oscillator system has three consecutive laser units: diode laser, diode pumped solid state laser (DPSS: Millennia) and Ti:sapphire femtosecond laser (Tsunami). These units have extremely complicated working principles and require vary delicate handling. The CW output from an array of diode lasers is used to pump the DPSS system which excites the laser cavity to emit IR laser. Then its frequency doubled output (green laser with wavelength of 532 nm) is fed in the fs oscillator cavity in order to pump the gain medium and finally the femtosecond laser pulse (with around 800 nm wavelength, 80 MHz repetition rate and 80 fs pulse width) is produced. Below, we will provide a brief overview of corresponding laser units.

3.4.1.1 Millennia

This unit is a specially designed high power pump laser from Newport (Sr. No.– J80 PS, Newport). It consists of two main parts: power supply unit with *FCbar* module and the X-cavity of Millennia [21]. The power supply unit with *FCbar* modules is a high power, long-lifetime 'ProLite' series fiber coupled diode laser designed for stable and efficient delivery of laser beams through the suitably designed fiber optics to the laser head inside the Millennia. Diode laser contains two *FCbar* modules forming the heart of the power supply. The extremely sophisticated fiber coupling technology provides a lot of advantages, such as, most of the power from the diode arrays are efficiently fed to the laser head without producing any significant heating and losing the stability. The bars are also field-replaceable avoiding the realignment of the cavity. These modules are operated in notably less power so that the ideal operating condition is maintained with ensuring long lifetime. Similar to all other diode lasers, these modules are attached to thermo-electric cooler (TEC) for stabilizing the temperature. Beside that, the whole unit contains microprocessor based control logic, power module and forced air-cooling unit, and hence, water-cooling is not necessary anymore. The X-cavity of Millennia contains the optical resonator, neodymium yttrium orthovanadate crystal (Nd:YVO4), guiding optics, lithium triborate (LBO) crystal, output beam telescope, electronic indicator and mechanical shutter. The pump laser from *FCbar* modules is fed to the cavity and generates infrared beam (wavelength: 1064 nm) from the Nd:YVO4 crystal. This beam is focused to the LBO crystal which produces output beam of wavelength 532 nm, by second harmonic generation. This noncritically phase matched crystal is housed in an oven that maintains the crystal at an optimum temperature. The cavity end mirrors in the frequency doubling limb has highly reflective coatings for IR and green light, and hence, the latter can be generated in reflected pass and first pass. Then the light exists through a dichroic output coupler. The whole system offers ultra-low noise of <0.04% rms in an exceptionally short cavity length. The laser head is water-cooled and filtered water is recirculated from a properly customized chiller (from Polyscience) through external tubing. The power of the output beam we use to pump the fs oscillator system is about 8 W for our system.

3.4.1.2 Tsunami

Tsunami (from Spectra-physics) delivers continuously tunable output of near-IR wavelengths ranging from 690 nm to 1080 nm with pulse width of about 80 fs [22]. The

Tsunami laser head contains the Ti:sapphire rod and the optics, such as, input coupler (IC), rod focusing mirrors, guiding mirrors, beam folding mirrors, a high reflector (HR), an output coupler (OC), dispersion control elements and tuning elements that form the resonator cavity. Ti:sapphire, a crystalline material, is the lasing medium in Tsunami. This is prepared by doping the sapphire crystal (Al_2O_3) with titanium ions (Ti^{3+}). The electronic ground state of the Ti^{3+} ion is splits into a couple of vibrationally broadened levels. Absorption transitions takes place over a wide range of wavelengths from 400 nm to 600 nm, however fluorescence transitions occur from the lower vibrational levels of excited state to the upper vibrational levels of the ground state. Although the fluorescence band spreads from wavelengths as short as 600 nm to greater than 1000 nm, the lasing action is possible only at wavelengths larger than 670 nm. This is due to the overlap between long-wavelength side of the absorption band and the short-wavelength end of the fluorescence spectrum. A high inversion density comes from having a high pump intensity and the pump illumination in a Ti:sapphire laser should be collinear with the cavity mode for a relatively long laser rod. The pump light is focused to a narrow line within the rod. Then oscillating laser mode is focused as well as overlapped within the same volume. This is known as longitudinal pumping. Further collimation and expansion is done with the output beam to maintain the normal size. A ten-fold cavity longer than that in a CW laser is necessary for the modelocked laser in order to allow it to run at repetition rate of near 80 MHz. Astigmatism in the Tsunami output beam is virtually eliminated by carefully choosing the rod length and angles of the cavity focus mirrors. However, astigmatism can still remain within the laser rod. A concave focusing mirror tuned at the proper angle introduces astigmatism in the pump beam that matches with the Tsunami cavity mode. The result is a laser with high conversion efficiency as well as appreciable beam quality. The acousto-optic modulator (AOM) offers reliable modelocked operation at laser start-up (see Fig. 3.10). It also allows the laser to operate for extended periods without shutdowns. The AOM is driven by a regeneratively derived rf signal. As the c-axis of the rod is aligned coplanar with the polarization of the electric field within the cavity with birefringent Ti:sapphire rod, an uninterrupted tuning is achieved. Here the Ti:sapphire rod and the birefringent filter plates or prism surfaces consist of a total of ten Brewster's angle surfaces. Eventually, the polarization and the cavity losses are largely determined by the orientation of those surfaces. The fs Tsunami laser is wavelength tuned using a prism sequence and a slit. By

changing the slit width one can tune the bandwidth (hence the temporal width) of the output beam. Prism pairs are used to introduce a net negative intracavity GVD in the fs system.

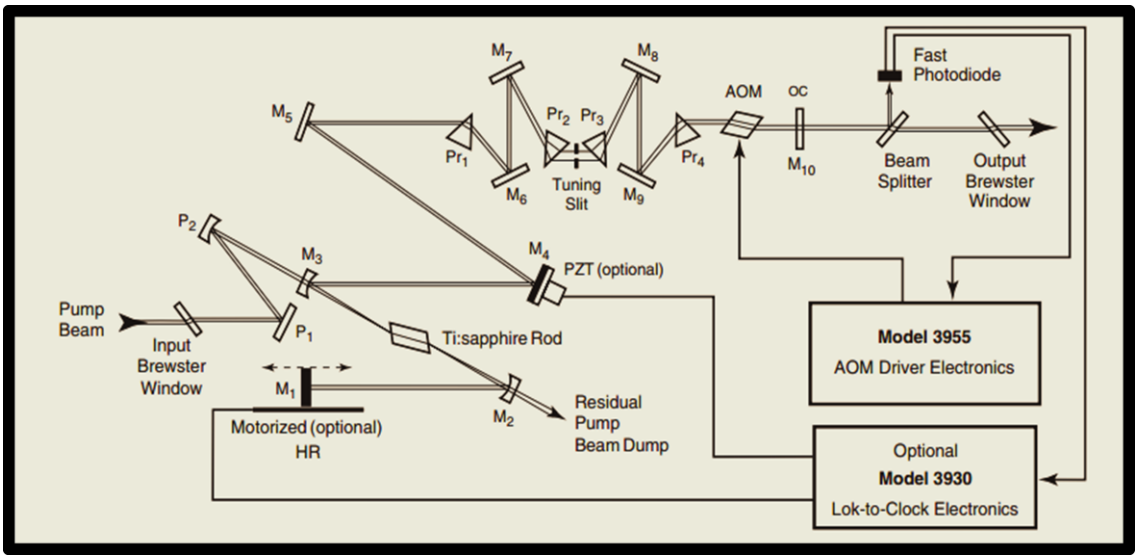

Figure 3.10: Schematic diagram of the Ti:sapphire laser cavity (Tsunami).

3.4.1.3 Second harmonic generator

The Model 3980 of second harmonic generator (SHG) from Spectra-Physics is designed accordingly which can act as a frequency doubler (and/or pulse selector) having the fundamental beam emitted from Tsunami as input [23]. The working principle of this frequency-doubler unit is described below:

Polarization of light in the dielectric material is not only proportional to the electric field but also can be expanded to higher order non-linear terms. Second harmonic generation is a coherent optical process of radiation of dipoles in the material and it depends on the second term of the expansion of polarization. The dipoles oscillate with the applied electric field of frequency ω. Then it radiates electric field of 2ω as well as ω. This is possible in a non-centrosymmetric material. β-Barium borate (β-BaB_2O_4 or BBO) is an efficient non-linear optical crystal which is used to produce the second harmonic of the fundamental pulse in this mechanism though it is also capable of generating third, and higher harmonics of laser. So the near-IR input light comes out as near-UV light. The key features of this crystal are, wide transmission region starting from 190 nm to 3500

nm, large effective SHG coefficient, broad phase-matching range from 409.6 nm to 3500 nm, wide temperature-bandwidth of about 55° C, high damage threshold, high optical homogeneity with $\delta n \approx 10^{-6}$/cm and good mechanical and physical properties, while it does not need any heating arrangement. BBO is much more efficient than LBO in terms of conversion efficiency. The efficiency is inversely proportional to the cross-sectional area of the beam. Thus, the beam waist is reduced before incidence on the crystal by using a telescopic arrangement made by a couple of lenses. To minimize pulse width broadening due to GVD of the fundamental pulse, it is necessary to use a thin SHG crystal to obtain short output pulses without employing another compensating crystal. This crystal is hygroscopic, and thus, kept inside a sealed cylinder with AR-coated windows and filled with an index-matching fluid. There are mirrors which have control over both horizontal and vertical movement of the input beam and to focus the beam at the centre of the SHG crystal so that maximum power can be achieved at the output. The orientation of the crystal can be tuned externally. Traversing through the crystal, the diverging residual fundamental beam and its frequency doubled counterpart travel collinearly. The fundamental beam is vertically polarized whereas the frequency-doubled part is horizontally polarized. Those beams are again collimated and are steered to the beam splitter prism which separates the second harmonic from the fundamental part. The coated surface of prism reflects the fundamental beam to routing mirror. The frequency doubled component diffracts through the two Littrow prisms which correct the horizontal displacement and beam shape distortion of the output beam caused by SHG crystal. Finally, the residual fundamental beam and its second harmonic exit through two different output windows.

3.4.1.4 Description of the two-color pump-probe setup in collinear geometry

The S-polarized fundamental beam from the output of Tsunami is split in to two parts using a 70:30 beam splitter (see Fig. 3.11). The most intense part of the beam is fed into the SHG and after frequency doubling we obtain the pump beam. The other part is attenuated as per requirement and is guided to the retro-reflector (RR) by using a set of three mirrors. After the optical alignment of the probe beam before the RR, a couple of mirrors are used to guide the beam towards the MO. In the middle of this path the collimation is retrieved and beam diameter is slightly expanded with a telescopic arrangement. A pair of lenses (L1 and L2) of focal lengths 75 mm and 200 mm is

arranged to make the beam diameter ~ 5 mm so that it fills the back-aperture of the MO. A GT polarizer is placed in the path to confirm the polarization of the probe beam. Then another mirror steers the beam towards the beam combiner which is a 50:50 beam splitter. The pump beam is guided to the beam combiner after necessary attenuation of the beam intensity. A specified filter is used to exclude the part of the fundamental beam mixed in the pump beam. The linearly polarized beam is then chopped at about 2 kHz frequency by a chopper controlled by a controller unit. The combined beam falls collinearly on the MO and is tightly focused on the sample surface maintaining perfect overlap. The sample is mounted on a holder placed on the top of a computer controlled piezo-electric scanning x-y-z stage. With the help of the MO (40X, N.A. = 0.65) and the z-travel of the piezoelectric stage, the probe beam is tightly focused to a diffraction limited spot size (~ 800 nm) at the sample. The pump beam is spatially overlapped with the probe beam after traversing through the same MO in a collinear fashion. The probe beam is placed at the middle of the pump beam, where the latter is slightly defocused with a spot size of ~1 μm due to the chromatic aberration. A viewing arrangement is made using a white light which is focused on the sample via the same MO. A CCD camera is used to visualize the sample part and the position of pump-probe on the sample.

The beams reflect back through the same MO. A fraction of the beam is fed into the camera. A filter is used to block the pump beam and allow the probe to be incident on the OBD. The working principle of the OBD is already described in section 3.3.7. The signal (A – B) from the OBD is calibrated to obtain the precise value of the Kerr rotation. On the other hand, the sum (A + B) gives the total reflectivity signal showing the dynamics of the electronic state of the sample as well as the acoustic modes.

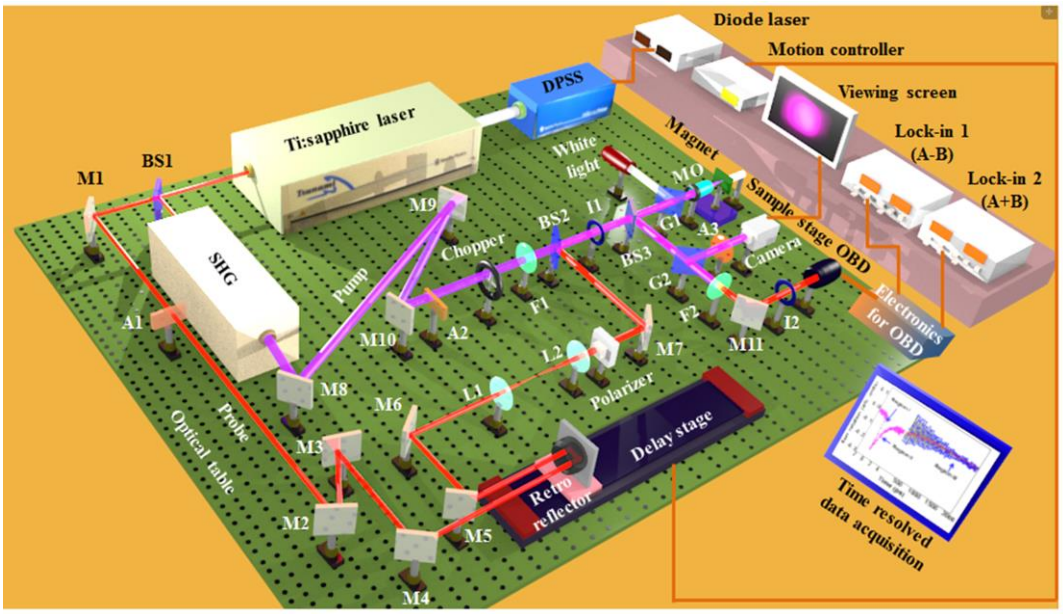

Figure 3.11: Schematic diagram of custom-build TR-MOKE microscope setup with collinear pump and probe geometry. M-mirror, BS-beam splitter, L-lens, OBD-optical bridge detector, F-filter, A-attenuator, G-glass slide.

3.4.1.5 Routine alignments

The stability and path of output beam depend very much on the temperature, humidity, and dust level in the ambience. Some times within few weeks interval a significant walk out of the fundamental beam within the cavity of Tsunami might be observed, resulting in a change in the entire optical path and the pump-probe overlap. In this setup, there are few places where regular care should be taken to align the individual pump-probe beams.

(1) Stability of fundamental laser and optimization of Tsunami – The power, wavelength, and FWHM of the fundamental beam is monitored on daily basis. To check the stability of the cavity, there is a controller with LED indicator where number of bars indicates the extent of cavity alignment. If any deviation from the standard reading is observed there are respective knobs in Tsunami by tweaking which the wavelength, FWHM and power can be adjusted.

(2) Alignment before RR – If the incident beam is not parallel to the axis of the RR then the reflected beam does not maintain the constant height and shifts from the desired path. Three mirrors are placed by adjusting which the probe beam can be made parallel

to the horizontal plane, while maintaining the vertical height of the beam before entering and after exiting the RR. The RR is moved to and fro to check whether the probe spot is shifting its lateral and vertical positions with respect to a reference point on the beam height.

(3) Alignment after RR – After the RR, the overlap of the pump and probe beams is checked on the beam combiner. There are mirrors to adjust their vertical and horizontal positions of the beams on the combiner. If the alignment is correct, both the beams will follow the same path after being combined.

(4) Making the beam collinear through MO – The beam positions at the back aperture of MO is very important. Any misalignment of the beams is adjusted by changing the tilts of the respective mirrors. Monitoring the pump and probe spots falling on to a substrate by a camera, the alignment can be recovered. Also, one can place a screen in front of the MO and by moving the MO back and forth and by monitoring the positions and shapes of the two beams it can be checked whether the beams are coaxial with the MO and with each other.

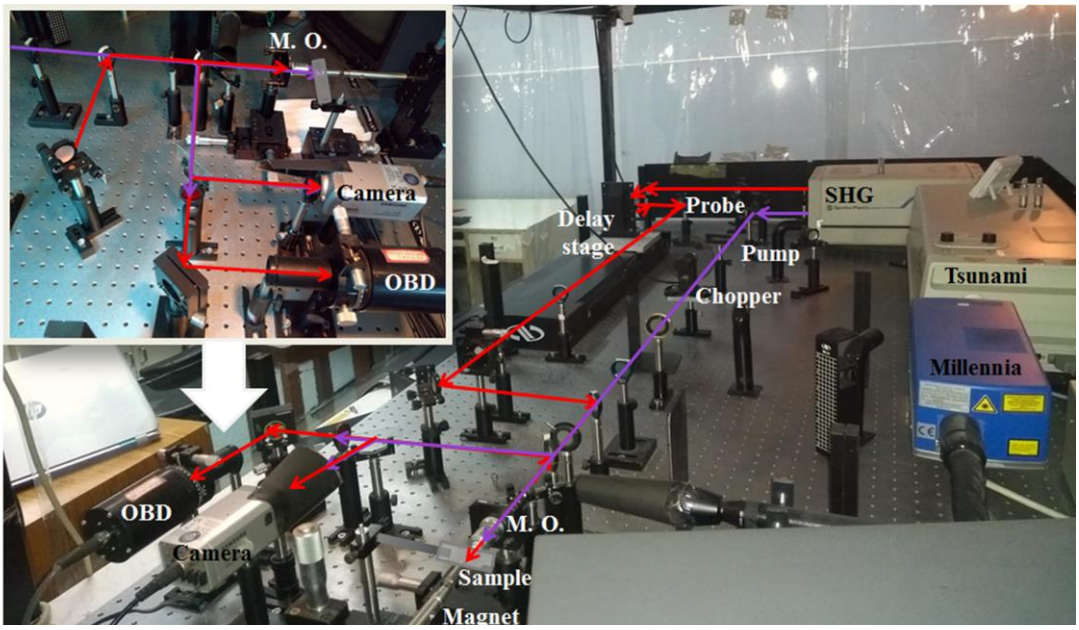

Figure 3.12: A photograph of TR-MOKE microscope in the laboratory of Prof. Anjan Barman at the S.N. Bose National Centre for Basic Sciences, Kolkata, India.

(5) Alignment of the OBD - This alignment is adjusted by superposing the back reflected beam from OBD with the incident beam with the help of a mirror.

After adjusting the optical components, the time-resolved reflectivity data from a test Si-substrate is recorded and its relaxation rate is compared with the standard data to verify the alignment condition. A photograph of the setup is shown at Fig. 3.12.

3.4.2 Non-Collinear Time-Resolved Magneto-Optical Kerr Effect Magnetometry

This setup is based on an amplified femtosecond laser system where fundamental beam having wavelength of 800 nm and pulse width of about 40 fs is generated by using a regenerative amplification method. The laser pulse is again split using beam splitter. One part of this fundamental laser beam is attenuated and collimated to use as the probe beam. Another part is frequency doubled using a second harmonic generator and is used as a pump beam to excite the electron and spin dynamics in the sample. The pump and probe beams and made to incident non-collinearly on the sample surface using wavelength specific lens arrangements. The probe is incident normally on the sample plane and so that the reflected probe beam can be used to detect the time-resolved Kerr rotation in the polar geometry in addition to the simultaneous detection of time-resolved reflectivity signal.

The procedure of generation of amplified femtosecond laser pulse is extremely sophisticated and complicated. The entire amplifier (Libra) system from Coherent consists of the following units: ultrafast oscillator (Vitesse), diode-pumped solid state pump laser (DPSS, Evolution), regenerative cavity, stretcher and compressor grating arrangements, synchronization and delay generator etc. In the following subsections we will discuss those units briefly.

3.4.2.1 Vitesse

Vitesse is a compact DPSS (Verdi)-pumped ultrafast oscillator that produces modelocked sub -100 fs pulses at 80 MHz repetition rate with an output power of about 200 mW at 800 nm wavelength [24]. Three main units are associated with it: the laser diode system, Verdi and the Verdi-pumped ultrafast laser unit (VPUF).

(A) Laser diode system - The Verdi is pumped by the continuous output produced by laser diodes. Power supply box for laser diode contains commercial power supply, two

laser diodes, electrical circuits, monitors and cooling fan. Light generated by laser diode assembly is transported by fiber array package (FAP) and is used to pump the gain medium of Verdi. The main component of diode laser assembly is FAP I and FAP II, each of which contains a laser diode bar capable of efficiently converting the electrical energy to optical energy. It is desirable to operate the FAPs at low temperature and sufficient drive currents. The wavelength of emitted light is temperature dependent. Proper heat sink and cooling fans are there to maintain the optimum temperature.

(B) Verdi- This resonator consists of unidirectional single-frequency ring cavity with the facility of intra-cavity second harmonic generation to produce multi-watt level green (532 nm) output. Intra-cavity etalon enables the single frequency selectivity. This pump resonator is 'end-pump design' where light travel along the optical axis of Nd:YVO4 (Vanadate) gain medium. Verdi absorbs energy from 808 nm input and produce strong single line emission of 1064 nm which is later frequency doubled. As it is known that an optically pumped laser rod can act as a lens, it is important to maintain the temperature of Vanadate to minimize the thermal focusing and hence the astigmatism. The LBO crystal which is also used here for frequency doubling can act as an output coupler. The tower temperature for this crystal is maintained at 150°C in order to have 90° phase matching between fundamental beam (1064 nm) and second harmonic (532 nm). After exiting the resonator, the 532-nm-beam is steered by a mirror towards the VPUF. A Piezoelectric transducer driven lever controls the tilt for maintaining optimum pump beam alignment into VPUF, and hence, this system is known as power track mirror arrangement.

(C) VPUF - Ti:sapphire is the active medium in this laser unit and multiple negative dispersion mirrors (NDMs) provide negative dispersion for producing sub-100 fs pulses. Mode locking is automatically achieved using Kerr lensing. For suitable material, irradiation of high intensity laser beam can create distortion of the atoms due to high electric field. This effect is known as optical Kerr effect which can affect the refractive index of the material. Thus, for a laser beam having higher intensity at the central part actually can set a gradient of refractive index in the material. This lensing narrows the beam waist and a slit is used to allow only narrow mode-locked beams after blocking the CW laser and finally it provides the real driving force for further and continuous mode locking. Depending upon the wavelength of laser and refractive index of optical

components, different portion of a beam can travel with different velocities. This causes group velocity dispersion (GVD) which introduces reshaping of pulse or spectral chirp (either positive or negative). Also, due to Kerr lensing, frequency components of a pulse get phase-shifted differently. This is called self-phase modulation (SPM) which causes temporal chirping leading towards pulse broadening. To compensate these GVD and chirping, multiple NDMs (which are basically Febry-Perot etalons) are employed to bring the net GVD of the cavity down to zero.

3.4.2.2 Evolution

Evolution-30 is a diode-pumped Q-switched Nd:YLF laser capable of producing average energy more than 20 mJ for 527-nm-beam having 1 kHz repetition rate [25]. The components are described below:

(A) Power supply and laser diode – Evolution employed laser diode pumping to excite the laser gain medium. High efficiency results in low power electrical and cooling utility requirement with promising 1000s of hr lifetime.

(B) Nd:YLF gain medium – Nd:YLF or Nd:LiYF4 is used because of long upper-state lifetime (470 microsecond). It provides efficient energy storage for high-pulse energy operation at low repetition rates. Its low thermal lensing and natural birefringence avoid loss of beam quality. An intra-cavity polarizer gives freedom to select 1047 nm or 1053 nm transitions during pumping. The output beam of Evolution is frequency doubled part of 1053 nm laser.

(C) Acousto-optic Q-switching – If a transparent material (here silica) is subjected to ultrasonic vibration, the photo-elastic effect couples the strain field of ultrasonic wave to the refractive index of the material. Now if laser falls on the grating created by this effect, then a part of the light is diffracted in different directions. This energy loss is sufficient to destroy the Q of the cavity. Generally a PZT is used to convert electrical signal to ultrasonic sound. The laser can be returned to the high Q state after switching off the voltage applied of the transducer. If the ultrasonic vibration is stopped, then fused silica block emits Q switched laser pulse.

(D) Frequency doubling component – A nonlinear crystal, *e.g.* LBO, is used as output coupler to frequency double the Q switched beam. A heater maintains the tower temperature usually at 327.5°F (164°C). Though this crystal can efficiently work at the

temperature range between 157°C and 171°C range for noncritical phase matching with 1053 nm laser and it emits about 527 nm in the output.

3.4.2.3 Working principle of Libra

The physical phenomena that are associated with the regenerative amplification of femtosecond laser within Libra [26] are described briefly in the following section:

(A) Chirped pulse amplification (CPA) – This is a technique for amplifying an ultrashort laser pulse up to extremely high pulse energy with the laser pulse being stretched out temporally and spectrally prior to amplification. Sometimes highly intense laser beam can lose its energy within a very short path length due to unwanted self-focusing. CPA can avoid this obstacle. Initially a weak but short duration pulse is generated. The peak power is reduced significantly after stretching. The pulse is then amplified without any self-focusing. Finally, the amplified pulse is compressed to its original pulse duration. Libra employs CPA to stretch a weak pulse by 10,000 times with the help of a grating and amplifies by a factor of 10^6 by using Ti:sapphire crystal.

(B) Pulse stretching and compressing – A diffraction grating which reflects different wavelength of a beam at different angles can introduce varying delay for varying wavelengths. This stretches or compresses the pulse temporally. In a stretcher grating the in-build configuration is such that the higher frequency components (blue side of the spectrum) have to travel far and are time delayed with respect to redder components. The pulse thus has a positive GVD due to this stretching and is known as a positively chirped pulse. In a compressor grating the scenario is just opposite. The bluer frequency components are made to travel faster in order to compensate the delay with respect to the redder part and thus the pulse achieves its desired temporal width again.

(C) Regenerative amplification (RGA) – For a Ti:sapphire crystal absorptive transition takes place between 400-600 nm. However, the short wavelength side of the fluroscence spectrum merges with this transition wavelength. Thus, the actual range of lasing becomes limited in the IR range. This crystal has large gain bandwidth, which is exploited for pulse amplification. In the RGA cavity of Libra, Ti:sapphire crystal rod is used to amplify a single nJ pulse (selected from mode-locked train of seed laser emitted from Vitesse) to mJ pulse. This amplification for single pass within the crystal is very

small. RGA cavity offers a multipass travel to the seed laser so that a very high overall gain can be achieved.

Here, we have described the operation of several optical components involved during the amplification process:

(1) Stretching operation – The entire path traversed by the beam starting from Vitesse output up to RGA cavity is described below,

SM1 - SBS - FI - SM2 - SG - SM3 - SM4 - SM3 - SG - SM5 - SM6 - SG - SM3 - SM4 - SM3 - SG - SM7 - SM8 - SM9 - SM10 - RGA cavity.

There will be four points of reflected light visible on the grating surface after completion of this path. See Fig. 3.13 for the beam path.

(2) RGA operation – RGA cavity employs a Z-fold configuration as follows:

RM1 - PC1 - RWP - RI1 - RM2 - RTS - RM3 - RP - RI2 - PC2 - RM4.

Here, RM2 and RM3 pass the pump beam (green) but reflect the seed laser. RP reflects and transmits the beam depending upon the polarization. The repetition rate of amplified laser is generally much lower than that of the seed laser. In the RGA cavity the injection and ejection of pulses are controlled by manipulating their polarization. The output of Vitesse is an 'S' polarized pulse. RTS (the crystal) and RP transmit only 'P' polarized light. It allows the pump beam to pass. Thus RWP, a quarter wave plate, which is employed with an end-pumped mirror to double pass the beam making it 'S' to 'P' polarized or vice-versa. There are two Pockels cells (PCs) which rely on Pockels electro-optic effect and changes or produces birefringence in an optical medium in application of the electric field. When voltage is applied in PC, it acts as a quarter wave plate. Then again the double-pass mechanism is used to rotate the polarization of the beam by 90°.

The detailed operating procedure is described below.

A. When the PC is 'off'- The 'S' polarized beam is reflected by RTS surface to RM2 and the cavity (see Fig. 3.13). The pulse then double passes the RWP and becomes 'P' polarized. The pulse execute one round trip without being amplified (or with slight amplification) through the RWP and polarization is again rotated to 'S'. Finally, this pulse reflects from the surface of RTS in Brewster angle, out of the RGA cavity.

B. When the PC is ‘on’- The ‘S’ polarized beam is reflected by RTS surface to RM2 and the cavity. The pulse then double passes the RWP and becomes ‘P’ polarized. Immediately PC is ‘on’. Thus double passing PC1 and RWP results no net change in polarization. This ‘P’ polarized light becomes amplified after completing the multipass through the RTS. After appropriate number of round trips, voltage is applied to PC2. This makes the pulse ‘S’ polarized which reflects from the RTS surface and leave the cavity.

(3) Compressing operation – The path of the beam in the compressor part is summarized below:

CM1 – CDI – CG - CM2 - CM3 – CG - CM4 - CM5 – CG - CM3 - CM2 – CG – CDI – Output.

Again there will be four points of reflected light visible on the grating surface after completion of this path.

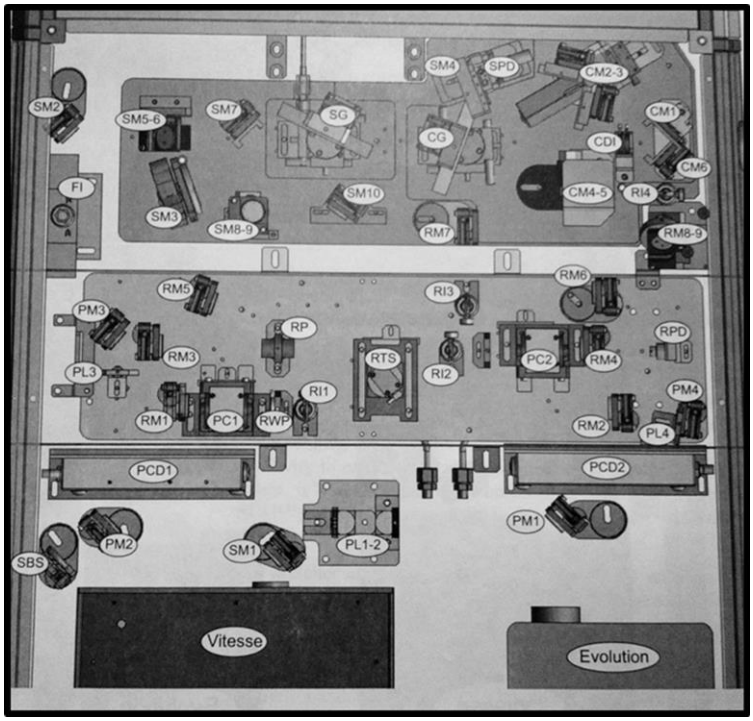

Figure 3.13: Schematic diagram of top view of Libra having separate stages: CPA unit including seed laser, RGA with pump laser and compressor unit.

3.4.2.4 Optimization of the amplified pulse

Efficient amplification depends on precise coordination of timing of seed source, amplifier pump source and amplifier PCs. Synchronization and delay generator (SDG Elite) [27] provides digital control of the timing signal and required voltages to operate the RGA cavity. It accepts input from the seed laser and pump laser, whereas it supplies a trigger signal for each PC at an adjustable delay. Additional delay signals are also provided for other experiments as per user's requirement. All delays can operate at the pump laser frequency or an integral divisor. The system includes a Gate input which is addressable to each channel individually.

Except the timing between the stimuli, bandwidth of the seed laser is extremely important parameter to monitor. Seeding the RGA cavity with the beam having insufficient bandwidth may cause permanent optical damage. Strong signal from a pair of photodiodes located at the stretcher compartment indicates that the seed laser has sufficient bandwidth. SDG monitors these parameters and shows error message once any fault occurs. After efficient generation of amplified pulse the pulse width of the beam can be optimized by user externally. A fine tuning of the compressor delay stage, containing mirrors (CM2-3), can be performed by remote control. For drastic change in pulse width, angle of both the gratings can be tuned manually (especially by the engineer or service person). A photograph of the laser system is shown in Fig. 3.14.

3.4.2.5 Second harmonic generator

The SHG is used with the amplified laser system (Model: Harmonic, HGS-T) to generate the pump beam of 400 nm wavelength for our pump-probe experiment. The working principle is similar to SHG (model: 3980) described in section 3.3.1.3. This model can also generate the third harmonic with wavelength in deep UV regime, from the fundamental beam.

Next, we have compared the specifications of the lasers generated by the fs oscillator and amplifier laser systems in Table 3.1. Usually these systems offer a range of these parameters depending upon the model number and their internal configurations. However, we are currently using the laser systems with the following optimized values as output.

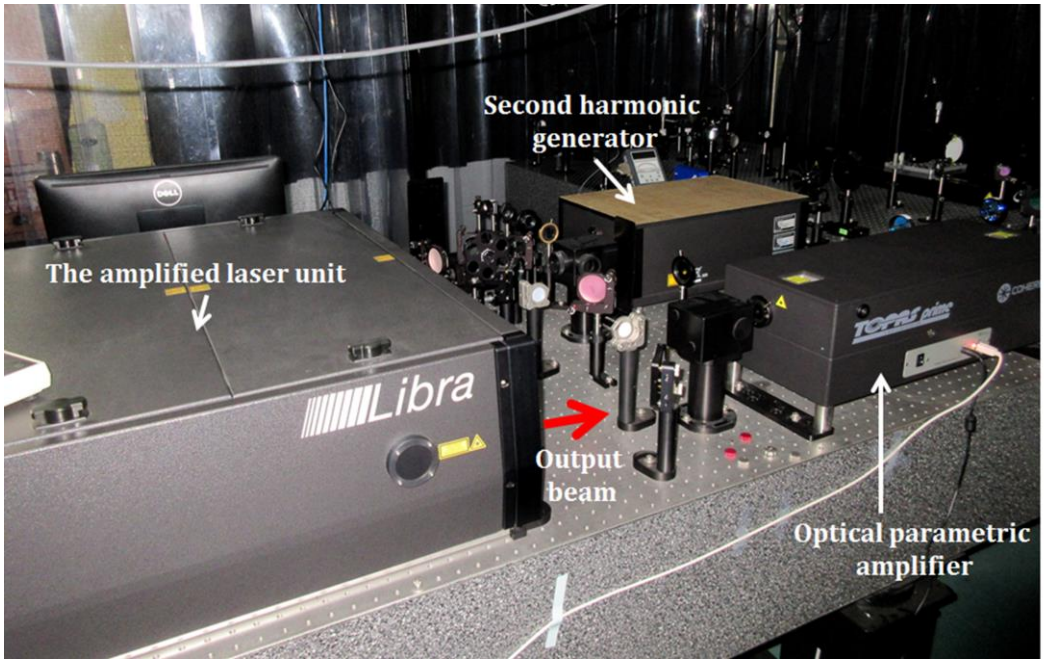

Figure 3.14: A photograph of amplified laser system installed in the laboratory of Prof. Anjan Barman at the S. N. Bose National Centre for Basic Sciences, Kolkata, India.

Table 3.1 Important features of the lasers optimized for our systems are described here.

Specification	Oscillator-based laser	Amplifier-based laser
Wavelength (nm)	~800	~800
FWHM of power spectra (nm)	~12	~30
Pulse width (fs)	~80	~40
Repetition rate	80 MHz	1 kHz
Pulse energy	25 nJ	4 mJ
Average output power	~2 W	~4 W

3.4.2.7 Description of the two color optical pump-probe setup in noncollinear geometry

The S-polarized fundamental laser beam from the output of the amplifier (Libra) is guided by a set of five mirrors before being split into two equal parts using a 50:50 beam splitter (see Fig. 3.15). A portion of this fundamental laser beam is fed into the SHG and after frequency doubling (λ = 400 nm) we obtain the pump beam. The other part of the fundamental laser beam (λ = 800 nm) is heavily attenuated and a very weak part is used as the probe beam. This beam is steered by a number of mirrors into a motorized scanning delay stage (Newport, with motion controller: model number-EPS301) with retro-reflector (RR) for introduction of a variable time delay. Before entering into the RR the probe beam is collimated using a pair of plano-convex lenses of focal lengths 10 cm and 15 cm and its beam-waist is reduced to ~5 mm. The probe beam coming out from the RR is guided to the sample using few mirrors before being focused on to the sample surface by using a plano-convex lens of focal length. A GT polarizer (GTH5M, Thorlabs) with extinction ratio of 100000:1, is placed in the path of the probe beam to ensure high degree of polarization of the incident probe beam. Three iris are kept in the path of the probe beam to monitor the vertical and lateral shift of the probe beam on a regular basis.

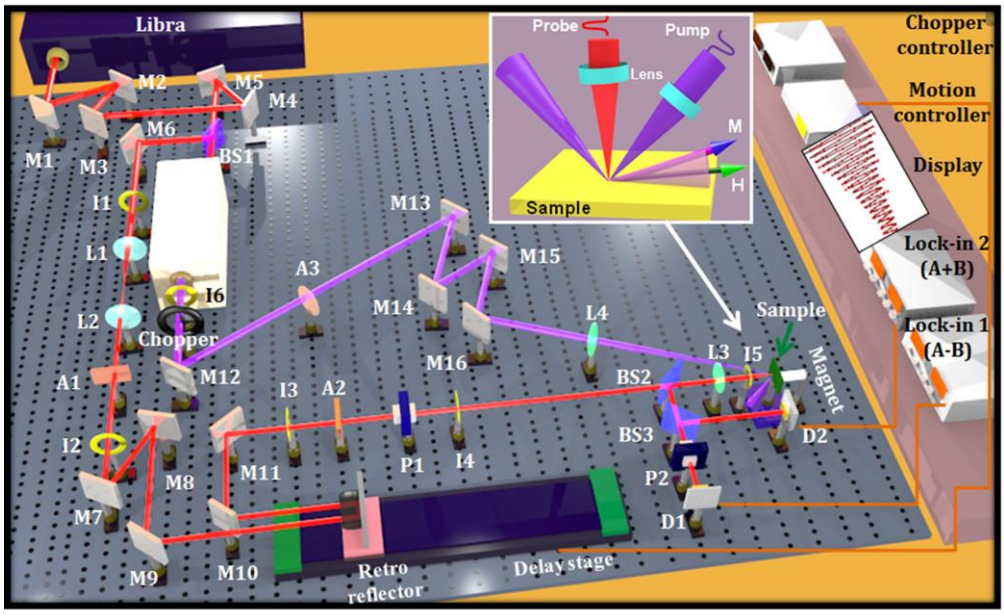

Figure 3.15: Schematic diagram of the optical pump-probe setup with amplified fs laser unit. The experimental geometry is shown in the inset.

The pump beam is guided on to the sample by using a set of five mirrors which are adjusted to compensate the optical path length *w.r.t.* the probe path. A variable attenuator is used for adjusting the probe power falling on to the sample. The pump and probe beams are made to incident non-collinearly on to the sample surface. The pump beam is kept slightly defocused on the sample surface to avoid any damage of the sample by the high irradiation by the pump power. The probe beam is tightly focused on the sample surface and placed carefully at the centre of the pump beam so that the dynamics is probed from the uniformly excited part of the sample. The pump and probe beam have spot sizes of 200 μm and 100 μm. The sample is mounted on a holder placed on the top of a translational x-y-z stage. A viewing arrangement is made using a white light source and a CCD camera for monitoring the overlap of the pump andprobe beams as well as their locations on the sample surface. The pump beam is blocked after reflection. The reflected probe beam is split into two parts with a beam splitter. One part is fed directly into a Si detector which measures the total reflectivity. The other part is fed into another GT polarizer (analyzer) and a Si detector, which measures the Kerr rotation of the probe beam. The analyzer is set at a very small from the extinction so that it measures the Kerr rotation on a minimal background of reflectivity. The bias magnetic field is applied by using permanent magnets in the desired configuration. The pump beam is the chopped by using an optical chopper (Thorlabs, MC2000B) and the detector signals for measuring reflectivity and Kerr rotation are measured by two lock-in amplifiers (SR830, Stanford Research System) in a phase sensitive manner using reference beam from the optical chopper output. The temperature and humidity is the pump-probe laboratory are maintained at 22°C and 30% respectively.

3.4.2.8 Routine alignments

The regenerative cavity remains stable if the temperature, humidity and dust level in the air is maintained carefully. However, after few months a significant movement of the laser path at the output of Libra is generally observed resulting in a change in the entire optical path. In this setup, there are few crucial places where special care is taken to align the pump and probe beams on a regular basis.

(1) Monitoring of the parameters at the output of Libra – The power, wavelength, and FWHM of the fundamental laser beam (800 nm) is monitored on a daily basis. There is no external control provided for the user to align the cavity on a daily basis. If any

significant deviation from the standard values is observed then involved alignment of the cavity is necessary.

(2) Alignment before RR – The beam-shift from the output of Libra can be checked by monitoring the position of the beam in the couple of irises before RR. Any unwanted shift can be adjusted by tweaking the tilt of mirrors placed before these irises. The RR is moved to and fro by the delay stage to check any shift of horizontal and vertical position of the probe spot. By moving the RR in between two extreme ends on the delay stage the beam position can be checked using a height tool or the iris placed after RR. The Beam movement can be stopped by using the set of mirrors placed before the RR.

(3) Alignment after RR – There are three iris through which the probe beam can pass maintaining the desired horizontal and vertical positions. Any unwanted deviation of the probe beam in the path can be adjusted by the set of mirrors placed after RR.

(4) Alignment of the pump beam – There is no external control of the SHG unit and usually the pump beam remains stable. Any slight misalignment of the pump beam is adjusted by changing the tilts of the respective mirrors placed in the pump path. The coarse overlap of the pump and the probe spots on the sample surface is achieved by monitoring them on a CCD camera, whereas the fine adjustment is done by maximizing the reflectivity signal at the zero delay position of RR on delay stage.

(5) Finally, the alignments of the two detectors are checked by viewing the probe spot position at the centre of the sensor by using an IR viewer. After adjusting the optical components, the time-resolved reflectivity data from a test Si-substrate is recorded and its relaxation rate is compared with the standard data to verify the alignment condition and pump-probe overlap.

A photograph of the TR-MOKE setup is shown in Fig. 3.16.

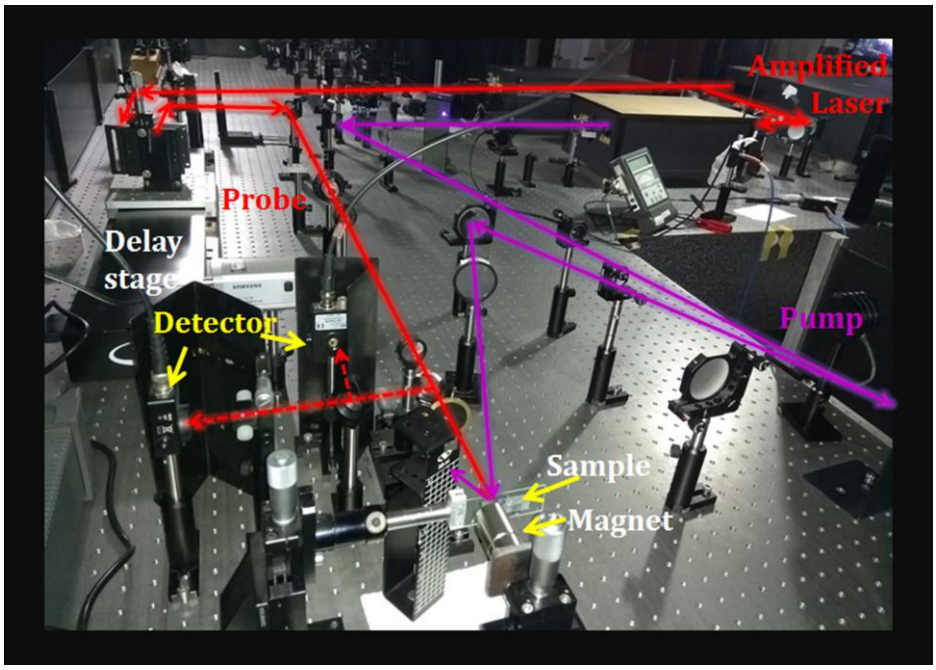

Figure 3.16: A photograph of the optical pump-probe setup based on an amplified fs laser system in the laboratory of Prof. Anjan Barman at the S. N. Bose National Centre for Basic Sciences, Kolkata, India.

3.4.2.9 Measurement of time-resolved dynamics

A fine tuning is required before starting the measurement. The reflectivity signal from a reference sample (*i.e.* Si (100) substrate) is usually monitored. The pump and probe fluences are chosen to be about 10 mJ/cm^2 and 2 mJ/cm^2 by adjusting average power with the help of attenuators. By moving the stage to the position from negative delay towards positive delay, a sharp rise of the reflectivity signal is observed. A careful monitoring helps to find this zero delay position (when the RR is moved with smaller steps) where the pump and probe pulse gets temporally overlapped causing enhancement of the transient signal. Further movement of the RR in the direction of positive delay causes an exponential decay of the signal. Nature of this decay provides us information about the pump-probe alignment with the movement of the delay stage. If necessary, the overlap of pump and probe beams on the sample surface can be improved by adjusting the mirrors in the pump path. Sometimes a faster decay indicates movement of probe beam with RR, which is not desirable. Then the optical alignment of the probe beam before entering into the RR should be improved by following the steps described in section 3.3.2.7. The full time-resolved reflectivity signal is measured again to check the decay constant.

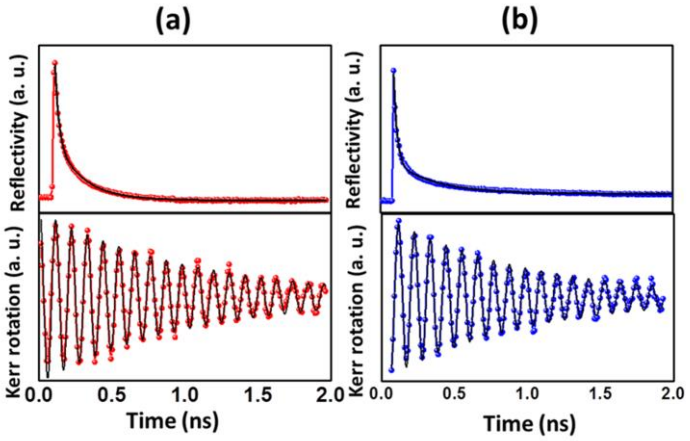

Figure 3.17: The representative data for time-resolved reflectivity of Si and time-resolve Kerr rotation for a $Ni_{80}Fe_{20}$ thin film obtained from the two different setups: (a) TR-MOKE microscope using the fs oscillator and the (b) noncollinear optical pump-probe setup based on amplified fs laser.

Figure 3.17 shows the representative time-resolved reflectivity data for Si(100) samples obtained with decent alignment using two different setups taken for 2 ns. We have fitted the decaying portion of the curve with an exponential function to extract the decay time to be slightly greater than 200 ps. In this condition we have measured time-resolved Kerr rotation data from a reference 20-nm-thick $Ni_{80}Fe_{20}$ (Py) thin film deposited using e-beam evaporation technique. We fitted the data with a damped sinusoidal function. The decay constant of time varying amplitude of Kerr rotation is about 1.0 ns and the precession frequency is obtained around 9.0 GHz for the applied bias magnetic field of ~1.0 kOe. The extracted damping coefficients for both the films are found to be ~0.009.

3.5 Numerical Methods

The macrospin theories developed for continuous magnetic medium based on the macrospin formalism, consider the magnetization throughout the sample to be uniform. The magnetization dynamics is studied by solving the non-linear differential equation, *i.e.* Landau-Lifshitz-Gilbert (LLG) equation, after linearizing it under small angle approximation. However, the real physics is much more nontrivial. In case of confined magnetic structures, the demagnetizing field arising from the unsaturated magnetic dipoles at the finite boundaries play a crucial role in controlling the static magnetic texture and the ensuing magnetization dynamics. The situation becomes more complex with the samples having non-ellipsoidal geometries when analytical solution becomes even more nontrivial. Several numerical and analytical methods have been developed to provide deep insight about the experimental results obtained from these nanoscale magnetic systems in all three dimensions. However, experiments encounter severe challenges due to various limitations in the available fabrication and characterization techniques. Consequently, theory faces stern challenges to reproduce (or predict) the real situation due to the lack of appropriate approximations and boundary conditions used for nanoscale magnetic systems having both short- and long-range interactions. Thus, the development of micromagnetic modelling and computer-based numerical simulation have become necessary. In micromagnetic simulations, the sample is discretized into a number of cells, each of which consists of a macrospin. Those macrospins experience short-range exchange and long-range dipolar interactions as well as the effect of other existing fields. With proper modeling strategies, numerical simulations can have several advantages over the experimental and theoretical approaches. Choice of proper evolver to solve the differential equations, sample discretization method and consideration of all the relevant energies, can lead to a successful numerical solutions. In the following sections, we will discuss few of these important aspects before describing the micromagnetic simulators (*i.e.* OOMMF, LLG, MuMax3 etc.) used for the numerical calculations presented in this thesis.

3.5.1 Free Energies of Ferromagnetic Material in Micromagnetics

The total energy of a micromagnetic system can be represented by the Gibbs free energy (E_{tot}). This depends on the magnetization, external field and some other material parameters. E_{tot} contains all the macroscopic (*i.e.* Zeeman and magnetostatic energies)

and microscopic (*i.e.* exchange and magnetocrystalline energies) energy terms and thus can be expressed as:

$$E_{total} = E_Z + E_d + E_e + E_K \tag{3.4}$$

E_z, E_d, E_e and E_k are Zeeman energy, demagnetization energy, exchange energy and anisotropic energy, respectively. In micromagnetism this expression can be written as [28],

$$E_{total} = \int_V [-\boldsymbol{M}.\boldsymbol{H}_Z - \frac{1}{2}\boldsymbol{M}.\boldsymbol{H}_d + A\left((\nabla \boldsymbol{u}_x)^2 + \left(\nabla \boldsymbol{u}_y\right)^2 + (\nabla \boldsymbol{u}_z)^2\right) + K_1(1 - (\boldsymbol{a}.\boldsymbol{u}))]\, dv \tag{3.5}$$

where $\boldsymbol{H}_Z$ is the Zeeman field, $\boldsymbol{H}_d$ is the demagnetizing field, A is the exchange stiffness constant and K_1 is the first order magnetocrystalline anisotropy constant. $\boldsymbol{a}$ is the unit vector parallel to the easy axis and $\boldsymbol{u}$ is the space and time dependent unit vector of magnetization. The aim of micromagnetic theory is to find the magnetization in equilibrium:

$$\boldsymbol{M}(x,t) = M_s(x).\boldsymbol{u}(x,t) \tag{3.6}$$

Brown proposed an equilibrium condition based on the calculation of variational derivative of free energy with respect to the magnetization:

$$\frac{\partial E_{total}}{\partial \boldsymbol{u}} = 0 \tag{3.7}$$

$$\boldsymbol{u} \times \left(M_s \boldsymbol{H}_Z + M_s \boldsymbol{H}_d + 2A\Delta \boldsymbol{u} + 2K_1 \boldsymbol{a}(\boldsymbol{u}.\boldsymbol{a})\right) = 0 \tag{3.8}$$

In equilibrium the magnetization lies parallel to $\boldsymbol{H}_{\text{eff}}$, which can be expressed as:

$$\boldsymbol{H}_{eff} = \frac{2A}{M_s}\Delta \boldsymbol{u} + \frac{2K_1}{M_s}\boldsymbol{a}(\boldsymbol{u}.\boldsymbol{a}) + \boldsymbol{H}_Z + \boldsymbol{H}_d \tag{3.9}$$

The torque $\left(\boldsymbol{M} \times \boldsymbol{H}_{eff}\right)$becomes zero.

The energy landscape of micromagnetic systems may contain many local maxima, minima as well as saddle points. Sometimes the equilibrium in local minimum is achieved by a dynamic description of the path via energy landscapes. The form of LLG equation found to yield an accurate description of the time evolution of a magnetization of fixed magnitude in presence of $\boldsymbol{H}_{\text{eff}}$:

$$\frac{d\boldsymbol{M}}{dt} = -\gamma\left(\boldsymbol{M} \times \boldsymbol{H}_{eff}\right) + \frac{\alpha}{M_s}\left(\boldsymbol{M} \times \frac{d\boldsymbol{M}}{dt}\right) \tag{3.10}$$

In micromagnetics, when a system is discretized into a finite number of cells the material parameters, *i.e.* A, K, and M_s are assumed to be constant within a single element. However the spatial variation in the magnetization is expressed in terms of node based discrete approximation:

$$\boldsymbol{M}(x) \approx M_s(x)\sum_i \boldsymbol{u}_i\eta_i M_s \approx \sum_i \boldsymbol{u}_i\eta_i M_{s,i} = \sum_i \boldsymbol{M}_i \tag{3.11}$$

where η_i denotes the basis function of the i^{th} cell. Further, the effective fields are calculated from the derivative of the total energy with respect to the local magnetization.

Zeeman energy can be expressed as:

$$E_Z = \int_V (-\boldsymbol{M}.\boldsymbol{H}_Z)dv = \int_V \sum_j \boldsymbol{u}_j\eta_j M_{s,j} \sum_k \boldsymbol{u}_{j,k}\eta_j\, H_{Z,k}dv \tag{3.12}$$

Anisotropy energy can be expressed as:

$$E_k = \int_V \sum_j K_1(1 - (\boldsymbol{a}.\boldsymbol{u}_j\eta_j)^2)\, dv \tag{3.13}$$

Exchange energy can be expressed as:

$$E_e = \int_V \sum_j (A(\nabla \boldsymbol{u}_j\eta_j)^2)\, dv \tag{3.14}$$

Magnetostatic self-energy energy can be expressed as:

$$E_d = \int_V \nabla.\boldsymbol{M}dv = E_e = \int_V \sum_j \sum_k u_{j,k}\,(\nabla_k\eta_j)\, dv \tag{3.15}$$

3.5.2 Different LLG Solvers and Evolvers

For the vast majority of geometries and problems, differential equations cannot be solved with analytical methods. However, it becomes easier with the help of discretization methods to approximate the equations which can be solved numerically. There are two popular approaches to compute such approximations and to solve LLG equation in micromagnetics: finite difference method (FDM) and finite element method

(FEM). In FDM, differential equations are approximated with difference equations. There 'finite differences' approximates the derivatives and finally the equations are solved by matrix algebra techniques. The domain is divided in space and time and the approximations of the solution are calculated at the space or time points. In the simulation, the system is discretized into certain number of cuboidal cells (N) with fixed dimensions due to which sometimes the edges and corners of the nano-object cannot be replicated properly. The FEM requires the discretization of the spatial domain with 'finite elements' of regular triangulation. To solve the problem, initially some simple equations model these finite elements and then assembled into a larger system of equations that helps in modeling of the entire problem. In 2D problems triangles and rectangles, while in 3D problems tetrahedral and hexahedral elements are generally used. Moreover, a mixture of elements having different types is possible which helps to the reproduce the exact size and shape of the micro- and nano-objects. This affects the computational storage capacity and time which are proportional to the N^2 while computing the demagnetizing field from the magnetic volume and surface charges. Fast adaptive algorithms can speed up the process on regular grids for FDM using FFT or multipole expansion, which is inapplicable for FEM with irregular mesh structure. Based on these two approaches there are several codes or packages available [29]. Some of the FDM based codes are OOMMF, LLG, MuMax3, MicroMagus and Boris etc. On the other hand, NMag and Magpar are popular FEM based codes.

For solving numerical problems presented in this thesis we have used: OOMMF, LLG and MuMax3. Before proceeding for the simulation, it is extremely important to gain knowledge about the proper choice of 'Evolvers'. Those are responsible for updating the magnetization configuration from one step to the other. The following table shows the evolvers, which these micromagnetic simulators offer:

Table 3.2 The evolvers for three FDM based simulators are listed.

Name of the code	Method	Evolver
OOMMF	FDM	Euler, Runge-Kutta, SpinXfer and CG Evolver
LLG	FDM	Euler, Rotation matrices, Predictor-Corrector, Gauss-Seidel stable method
MuMax3	FDM	Runge-Kutta (*i.e.* RK45, RK32, RK12, RK1)

All the above mentioned codes utilize the LLG equation according to continuum micromagnetics. Thus, calculated results are valid for time scales > 1 ps and dimensions > 1 nm. Appropriate modeling strategies are imperative for performing reliable numerical experiments. The choice of evolver also depends on the nature of problem, which is discussed in the following sections with an overview of the simulators mentioning their features and functionalities.

3.5.2.1 OOMMF

OOMMF is a public domain micromagnetics program developed at the National Institute of Standards and Technology (NIST) by M. J. Donahue and D. G. Porter [3]. The code is written in C++ and Tcl/Tk language. It covers a wide range of platform: Unix platforms and various versions of Windows. It utilizes an ODE solver to relax 3D spins on a 2D mesh of square cells while using FFT to compute the self-magnetostatic field. Anisotropy, applied field, and initial magnetization can be varied point wise and arbitrarily shaped elements can be modeled. The system can also be discretized in all three dimensions. For being FDM software, it has less flexibility than the FEM software in replicating exact geometries for the objects with curved surface. All the calculations performed in OOMMF are at T = 0 K. The problem is specified with all the necessary input parameters and initial conditions in a file with '.mif' extension. The sample geometry is given in terms of an image or by defining its geometry in terms of set of equations and the sample dimensions are provided in the script. The intrinsic energies such as exchange energy, magnetocrystalline energy can be specified by providing the numerical values of exchange constant, anisotropy constant and its direction of

anisotropy field in the Cartesian coordinate. All the material parameters, *i.e.* damping, saturation magnetization and gyromagnetic ratio are provided in SI unit. It is extremely important to set the proper evolver in the script. There are two types of evolvers: time evolvers to take care of LLG dynamics and minimization evolvers to locate the local minimum in the energy surface by using direct minimization techniques. Evolvers are mainly controlled by their compatible drivers (*i.e.* time and minimization drivers). The drivers provide a magnetization configuration to the evolvers with an indication of advancing the configuration by one step (also called 'iteration'). The drivers determine when a simulation stage (or run) is completed using specified stopping criterion in the input MIF file. For preparing magnetic ground state the minimization evolver is generally used to obtain reliable results. The convergence criterion in the simulation is created by setting the stopping value of d$\boldsymbol{m}$/dt or time. At the stopping time the maximum value of d$\boldsymbol{m}$/dt across all spins reduces below the set value. The maximum torque should go well below 10^{-6} A/m then. The finial magnetization state obtained as the 'ground state' is then specified as the initial magnetization in the dynamic simulation file. Providing an external perturbation in terms of additional field the magnetization dynamics is simulated. The time dependent components of magnetization, magnetic field and energies can be extracted in the output file with '.omf', '.ohf' or '.ovf' formats. OOMMF also offers the user to set a periodic boundary condition (PBC) in different dimensions for simulating realistic systems with finite and smaller sample geometry.

3.5.2.2 LLG Simulator

M. R. Scheinfein is the designer and licensor of this commercial simulator [4]. It has three modules of functionality which are specified in terms of defining the solution. Those maintain consistency with the Windows event-driven programming interface. These modules are described below,

• Input phase: This is the control interface which helps the user to define the parameters and designing customized simulation. Though it increases the risk of input errors, the process is user friendly. As a counter measure LLG performs exhaustive error checking. Since the program solves the LLG equations using finite differences for exchange energies and fields, as well as boundary elements for magnetostatic self-energies and fields, the object must be defined as a grid. This simulator uses rectangular

pixels on a Cartesian grid. After setting up the environment, LLG initializes all of the arrays to start computing the demagnetization field coupling tensors. It calculates the field for any boundary conditions. As the simulation phase begins the user is prompted to store the simulation parameters in several files.

• Simulation phase: In this phase the desired simulation is performed based on the solution of the differential equations (LLG Simulation Sheet).

• Review phase: This phase helps in reviewing the results by re-playing them through a graphically animated movie (LLG Movie Viewer) or the user can view a domain or field file in the viewer control.

As mentioned earlier, LLG supports four integrators to solve ODE. The most primitive one is an Euler Cartesian method, which is the fastest but least accurate. The 'Rotation Matrices method is the integrator of choice for solutions where damping is greater than 0.5. This is used to study the magnetic ground state configurations in our systems. The Cartesian Predictor-Corrector integrator is the most accurate and also faster when damping is about 0.01. The Gauss-Seidel Stable method is a semi-implicit first-order integration scheme. The integration time steps can be much larger on fine grids using this method.

Interestingly, the temperature effects can be introduced in the LLG simulation, which is internally provided in terms of a random field. Study of quasistatic magnetization reversal is more authentic here. In LLG, the effect of spin polarized current, charge current, and several other effects on the magnetization dynamics can be incorporated easily for single layered or multilayered structures. In this thesis the results are obtained using the 2.50 version of LLG simulator which works with a single processor and currently unable to perform parallel computation.

3.5.2.3 MuMax3

MuMax3 is another open source, GPU accelerated micromagnetic simulation program, which requires high performance graphics card such as GTX series. GPU-based acceleration provides speeding up by one to two orders of magnitude as opposed to CPU-based micromagnetic simulation. With explicit help of NVIDIA GPU this program can be run in Linux, Windows and Mac platform. A Vansteenkiste *et al.* have published the design and verification of this code in 2014 [6]. It is written in dedicated scripting

languages Go and CUDA. The simulation is performed in web-based user interface and the output is obtained in form of 'OVF' data format similar to OOMMF.

In this simulator, an object is specified in terms of shape and dimension within the script or can be provided externally in form of an image. Being FDM software, it discretizes the objects into 2D or 3D grids of orthorhombic cells of equal size. Volumetric quantities (M, K etc.) are defined at the middle of the cells, whereas coupling quantities are specified at the faces of the cells. Some of the material parameters and external stimuli can be set space- and time-wise. Their magnitudes can be varied with an extra term of $f(t)\times g(x,y,z)$, *i.e.* time dependent function multiplied by continuously varying spatial profile. The geometry, once defined in terms of x, y, z coordinate, can be rotated, translated, scaled with Boolean operation like AND, OR, XOR, etc. MuMax3 offers several types of Runge-Kutta methods to solve the LLG equation with different convergence criteria and error estimation. Out of those, RK45, RK23 and RK12 give freedom to choose automatic time steps to keep error per step close to preset value. Importantly, MuMax3 provides a 'relax' function that can find the energy minimum of the system. This function prevents the precession term in LLG equation to act upon the system and effective field points only towards decreasing energy. However, the system may often reach a saddle point of the energy landscape. The evolver RK23 is more efficient to set a ground state while using the relaxation condition. MuMax3 can determine the evolution of the reduced magnetization $\boldsymbol{m}(r, t)$, which has unit of length. Any physical phenomena can be represented in terms of effective field, effective magnetization and torque in the program. For example, time derivative of $\boldsymbol{m}(r, t)$ becomes, $\partial\boldsymbol{m}/\partial t=\boldsymbol{\tau}$. $\boldsymbol{\tau}$ has contributions from: LL torque, Zhang-Li spin-transfer torque and Slonczewski spin-transfer torque. This simulator can deal with numerous problems related to magnetic anisotropy, complex interactions (such as, Heisenberg exchange interaction, DM interaction etc.), temperature dependent variations and many more. To make the numerical experiments more realistic, a system with finite geometry can be repeated with the help of periodic boundary condition (PBC) and simulation can be performed using macro-geometry approach. This is different from what is generally being used in OOMMF. The user can actually set the number of repetition in which the image can be copied in each side of the simulation box.

Figure 3.18. shows different 2D and 3D magnetic nanostructures simulated using Mumax3 software and visualized using Muview.

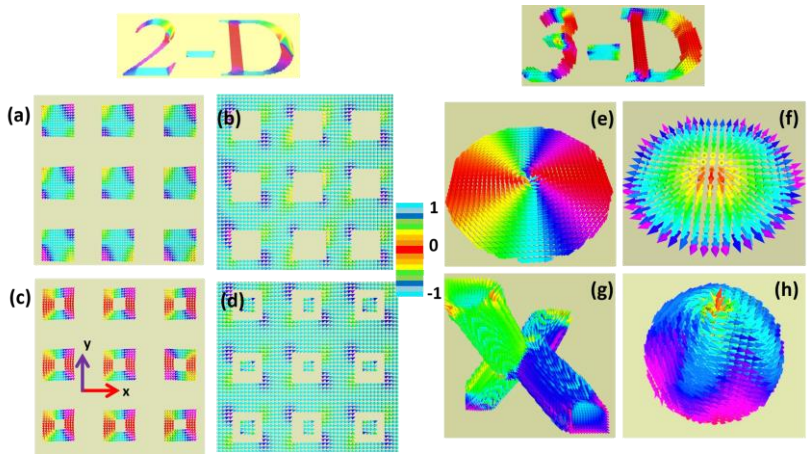

Figure 3.18: Ground state magnetization configuration of 2D structures - (a) dot, (b) antidot, (c) nanoring, (d) antinanoring and 3-D structures- (e) vortex, (f) skyrmion, (g) tetrapod and (h) sphere, simulated using MuMax3 and visualized using Muview software.

3.5.2.4 DotMag

Study of magnetization dynamics and nature of spin wave is incomplete without the spatial mapping of the power and phase profiles of the resonant modes inside a nanostructure. This mapping gives an explicit idea about comparison between relative spin precession amplitudes and phases of different SW modes and helps to visualize their spatial variation throughout the system. The above commercial and non-commercial codes do not readiliy offers to calculate the SW mode profiles. Hence, our research group have developed a code, DotMag, to investigate these features [5]. After simulating the magnetization dynamics using the above-mentioned simulators, one can obtain the output files in terms of time varying magnetization ($\boldsymbol{m}(x, y, z, t)$). The oscillations may correspond to a number of modes superposed on each other having definite powers and phases. Thus, it is not trivial to extract the spatial information of any individual resonant mode from only the dynamic magnetic images of the system. The FFT of such time-resolved spatially averaged magnetization curve gives the frequency spectrum, which may show several well resolved resonant modes. DotMag takes the lead here. It performs a discrete Fourier transform of the time dependent magnetization by fixing one of the spatial co-ordinates with respect to time. Generally,

the simulations performed without discretizing the z dimension, consider an average demagnetizing effect and all other possible effects on spatial distribution of SWs in the entire cell. If there is discretization along z-direction, then after fixing the z-coordinate at a particular value (z = z_m), a discrete Fourier transform of $M(x,y,z,t)|_{z=z_m}$ with respect to time is performed to yield $[\widetilde{M}^{z_m}(f,x,y) = FFT[M(x,y,z,t)\big|_{z=z_m}]$. The fixed value of the z-coordinate can be chosen to at any point from the top to bottom surface of the system. Finally, the program plots the (x, y) spatial distribution of the power $P^{z_m,f_n}(x,y)$ and phase $\phi^{z_m,f_n}(x,y)$ of the SWs at chosen frequencies on that surface according to the following relations:

$$P^{z_m,f_n}(x,y) = 20log_{10}FFT[\widetilde{M}^{z_m}(f_n,x,y)] \tag{3.16}$$

$$\phi^{z_m,f_n}(x,y) = \tan^{-1}\left(\frac{\widetilde{M}^{z_m}(f_n,x,y)}{\widetilde{M}^{z_m}(f_n,x,y)}\right) \tag{3.17}$$

where f_n is the frequency of a resonant mode. The power is presented usually in terms of dB and phase in radian. MATLAB is used to run and control this code, and the output is obtained with the plot of space dependent power and phase at discrete frequencies. The frequency resolution necessarily depends upon the total simulation time and the spatial resolution of calculated power and phase maps depends upon the discretization of sample (or number of cells) during micromagnetic simulation.

References

1. A. Barman and A. Haldar, *Time-domain study of magnetization dynamics in magnetic thin films and micro-and nanostructures.* Solid State Phys, vol **65**. (Elsevier Inc., Burlington, 2014).
2. A. Barman and J. Sinha, *Spin Dynamics and Damping in Ferromagnetic Thin Films and Nanostructures* (Springer Publishing AG, Switzerland, 2017).
3. M. Donahue, D.G. Porter, 1999, OOMMF User's Guide Version 1.0, Interagency Report NISTIR 6376, MD: National Institute of Standard and Technology, Gaithersburg, (<http://math.nist.gov/oommf>)
4. M. R. Scheinfein, E. A. Price, 2003, LLG User Manual v2.50, <http://llgmicro. home.mindspring.com>.

5. A. Vansteenkiste, J. Leliaert, A. Dvorkik, M. Helsen, F. GarciaSanchez, B. van Waeyenberge, AIP Adv. **4**, 107133 (2014).
6. D. Kumar, O. Dmytriiev, S. Ponraj, and A. Barman, J. Phys. D: Appl. Phys. **45**, 015001 (2012).
7. Sputtering by Particle Bombardment, Springer, (2007).
8. Electron Beam Evaporation, Vacuum Deposition onto Webs, Films and Foils (Second Edition), Elsevier (2011).
9. G. R. Sune, Electron beam lithography for nanofabrication, PhD thesis, Universitat Autònoma de Barcelona (2008).
10. D. Mcmullan, Scanning Electron Microscopy 1928–1965, Scanning. **17**, 175 (1995).
11. M. A. Moram and M. E. Vickers, Rep. Prog. Phys. **72**, 036502 (2009).
12. G. Binnig, C. F. Quate, and C. Gerber, Phys. Rev. Lett. **56**, 930 (1986).
13. S. Foner, Rev. Sci. Instrum. **30**, 548 (1959).
14. B. Rana, A. Barman, SPIN **3**, 1330001 (2013).
15. B. Rana, D. Kumar, S. Barman, S. Pal, Y. Fukuma, Y. Otani, and A. Barman, ACS Nano **5**, 9559 (2011).
16. S. Saha, R. Mandal, S. Barman, D. Kumar, B. Rana, Y. Fukuma, S. Sugimoto, Y. Otani, and A. Barman, Adv. Funct. Mater. 23, 2378 (2013).
17. S. Pal, J. W. Klos, K. Das, O. Hellwig, P. Gruszecki, M. Krawczyk, and A. Barman, Appl. Phys. Lett. **105**, 162408 (2014).
18. S. Mondal and A. Barman, Phys. Rev. Appl. **10**, 054037 (2018).
19. S. Pan, S. Mondal, T. Seki, K. Takanashi, and A. Barman, Phys. Rev. B **94**, 184417 (2016).
20. S. Pan, O. Hellwig, and A. Barman, Phys. Rev. B **98**, 214436 (2018).
21. User's Manual, Millenia Pro s-Series: Diode-Pumped, CW Visible Laser System, (Spectra-Physics, California, USA, 2007).
22. User's Manual, Tsunami: Mode-locked Ti:sapphire Laser, (Spectra-Physics, California, USA, 2002).
23. User's Manual, Model 3980: Frequency Doubler and Pulse Selector, (Spectra-Physics, California, USA, 2002).
24. Operator's Manual, Vitesse-Diode Pumped Modelocked Ti:sapphire Laser, (Coherent, USA).

25. Operator's Manual, Evolution-15/30 High Energy High Average Power Q Switched Laser System, (Coherent, USA).
26. Operator's Manual, Libra-Ultrafast Amplifier Laser System, (Coherent, USA).
27. Operator's Manual, SDG Elite-Synchronization and Delay Generator, (Coherent, USA).
28. W. Scholz, J. Fidler, T. Schrefl, D. Suess, R. Dittrich, H. Forster, and V. Tsiantos, Comp. Mater. Sci. **28**, 366 (2003).
29. S. K. Kim, J. Phys. D: Appl. Phys. **43**, 264004 (2010).

Chapter 4

4 Laser Controlled Spin Dynamics of Ferromagnetic Thin Film from Femtosecond to Nanosecond Time scale

4.1 Introduction

Recent developments in magnetic storage [1] and memory [2] devices heavily rely on increasing switching speed and coherent switching of magnetic states in ferromagnetic thin films and patterned structures. Operating speeds of information storage devices have progressed into the subgigahertz regime and controlled switching in individual layers of magnetic multilayers and heterostructures has become important. The relaxation processes involved in magnetization dynamics set natural limits for these switching times and data transfer rates. In the context of precessional magnetization dynamics, the natural relaxation rate against a small perturbation is expressed as Gilbert damping (α) according to the Landau-Liftshiz-Gilbert (LLG) equation [3,4]. This is analogous to the viscous damping of mechanical-frictional torque and leads to the direct dissipation of energy from the uniform precessional mode to a thermal bath in the case of zero wavevector excitation. Gilbert damping originates from spin-orbit coupling and depends on the coupling strength and band width of the 3d ferromagnet [5]. The damping can be varied by various intrinsic and extrinsic mechanisms including phonon drag [6], eddy current [7], doping [8] or capping [9] with another material, injection of spin current [10], magnon-magnon scattering [11], and controlling the temperature of the system [12]. The intrinsic and extrinsic natures of Gilbert damping are primarily studied by using ferromagnetic resonance (FMR) technique. When the magnetization is aligned with either the inplane or out-of-plane applied magnetic field, the linewidth is proportional to the frequency with a slope determined by the damping coefficient. This is the homogeneous or intrinsic contribution to the FMR linewidth. However, experiments show an additional frequency-independent contribution to the linewidth that corresponds to inhomogeneous line broadening [13,14]. A state-of-the-art technique based on pump-probe geometry has been developed and rigorously

exploited for measuring the ultrafast magnetization dynamics of ferromagnetic thin films during the last few decades [15,16]. Using the time-resolved magneto-optical Kerr effect (TR-MOKE) technique, one can directly address the processes which are responsible for the excitation and relaxation of a magnetic system on their characteristic time scales [17–19]. Generally, during the pump-probe measurements, pump fluence is kept low to avoid nonlinear effects and sample surface degradation. Some recent experiments reveal that nonlinear spin waves play a crucial role in high-power thin-film precessional dynamics by introducing spin-wave (SW) instability [20] similar to FMR experiments by the application of a high-rf power [21]. The coercivity and anisotropy of the ferromagnetic thin films can also be lowered by pump fluence, which may have potential applications in heat-assisted magnetic recording (HAMR) [22]. Recent reports reveal that the damping coefficient can be increased or decreased noticeably in the higher excitation regime due to the opening of further energy dissipation channels beyond a threshold pump power [23–25]. Not only relaxation parameters, but also a frequency shift due to enhancement in the pump power has been observed [20]. However, experimental evidence for a large modulation of Gilbert damping along with the frequency shift and temporal chirping of the uniform precessional motion is absent in the literature. This investigation requires a suitable choice material be chosen, and here we have chosen Permalloy ($Ni_{80}Fe_{20}$ or Py hereafter) because of its high permeability, negligible magneto-crystalline anisotropy, very low coercivity, and large anisotropic magnetoresistance with reasonably low damping. Also, due to its negligible magnetostriction, Py is less sensitive to strain and stress exerted during the thermal treatment in HAMR [22].

In this chapter, we use femtosecond amplified laser pulses for excitation and detection of ultrafast magnetization dynamics in a Py thin film. Pump fluence-dependent ultrafast demagnetization is investigated along with fast and slow remagnetization. Our comprehensive study of the picosecond dynamics reveals the transient nature of enhanced Gilbert damping in the presence of high pump fluence. Also, the time-varying precession is subject to temporal chirping, which occurs due to enhancement of the temperature of the probed volume within a very short time scale followed by successive heat dissipation. This fluence-dependent modulation of magnetization dynamics will undoubtedly find suitable applications in spintronic and magnonic devices.

4.2 Experimental Details

20-nm-thick Py film was deposited by using electron-beam evaporation technique (SVT Associates, model: Smart Nano Tool AVD-E01) (base pressure = 3 × 10^{-8} Torr, deposition rate = 0.2 Å/S) on 8 × 8 mm^2 silicon (001) wafer coated with 300-nm-thick SiO_2. Subsequently, 5-nm-thick SiO_2 is deposited over the Py using rf sputter-deposition technique (base pressure = 4.5 × 10^{-7} Torr, Ar pressure = 0.5 mTorr, deposition rate = 0.2 Å/S, rf power = 60 W). This capping layer protects the surface from environmental degradation, oxidation and laser ablation during the pump-probe experiment using femtosecond laser pulses. From the vibrating sample magnetometry (VSM) we have obtained the saturation magnetization (M_s) and Curie temperature (T_c) to be 850 emu/cc and 863 K, respectively [26].

To study the ultrafast magnetization dynamics of this sample, we have used a custom-built TR-MOKE magnetometer based on optical pump-probe technique as shown in Fig. 4.1 (a). Here, the second harmonic (λ = 400 nm, repetition rate = 1 kHz, pulse width > 40 fs) of amplified femtosecond laser pulse generated from a regenerative amplifier system (Libra, Coherent) is used to excite the dynamics while the fundamental laser pulse (λ = 800 nm, repetition rate = 1 kHz, pulse width ≈ 40 fs) is used as probe to detect the time-resolved polar Kerr signal from the sample. The temporal resolution of the measurement is limited by the cross-correlation between the pump and probe pulses (≈ 120 fs). The probe beam having diameter of about 100 μm is normally incident on the sample whereas the pump beam is kept slightly defocused (spot size is about 300 μm) and is obliquely (≈ 30° with normal to the sample plane) incident on the sample maintaining an excellent spatial overlap with the probe spot. Time-resolved Kerr signal is collected from the uniformly excited part of the sample and slight misalignment during the course of the experiment does not affect the pump-probe signal significantly. A large magnetic field of 3.5 kOe is first applied at a small angle of about 10° to the sample plane to saturate its magnetization. This is followed by reduction of the magnetic field to the bias field value (H = in-plane component of the bias field), which ensures that the magnetization remains saturated along the bias field direction. The tilt of magnetization from the sample plane ensures a finite demagnetizing field along the direction of the pump pulse, which is further modified by the pump pulse to induce a precessional dynamics within the sample [17]. In our experiment a 2-ns time window is

used, which gives a damped uniform precession of magnetization. The pump beam is chopped at 373 Hz frequency and the dynamic signal in the probe pulse is detected by using a lock-in amplifier in a phase sensitive manner. Simultaneous time-resolved reflectivity and Kerr rotation data were measured and no significant breakthrough of one into another has been found. The probe fluence is kept constant at 2 mJ/cm^2 during the measurement to avoid additional contribution to the modulation of spin dynamics via laser heating. Pump fluence (F) was varied from 10 to 55 mJ/cm^2 to study the fluence dependent modulation in magnetization dynamics. All the experiments were performed under ambient condition and room temperature.

4.3 Results and Discussions

When a femtosecond laser pulse interacts with a ferromagnetic thin film in its saturation condition, the magnetization of the system is partially or fully lost within hundreds of femtosecond as measured by the time-resolved Kerr rotation or ellipticity. This is known as ultrafast demagnetization of the ferromagnet and was first observed by Beaurepaire *et al*. in 1996 [27]. This is generally followed by a fast recovery of the magnetization within sub-picosecond to few picoseconds and a slower recovery within tens to hundreds of picoseconds, known as the fast and slow remagnetization. In many cases the slower recovery is accompanied by a coherent magnetization precession and damping [17]. In our pump-probe experiment, the sample magnetization is maintained in the saturated state by application of a magnetic field H = 2.4 kOe before zero delay. Right after the zero-delay and the interaction of the pump pulse with the electrons in the ferromagnetic metal, ultrafast demagnetization takes place. The local magnetization is immediately quenched within first few hundreds of fs followed by a subsequent fast remagnetization in next few ps [27]. Figure 4.1(b) shows ultrafast demagnetization obtained for different pump fluences. Several models have been proposed over two decades to explain the ultrafast demagnetization [16, 28-31]. Out of those a phenomenological thermodynamic model, called three temperature model [27, 32, 33] has been most widely used, where the dynamics of these spin fluctuations can be describes as:

$$\Delta M = \Theta(t)[-A_1 + \frac{A_2\tau_{el-lat} - A_1\tau_{el-sp}}{\tau_{el-lat} - \tau_{el-sp}} e^{-\frac{t}{\tau_{el-sp}}} + \frac{A_1 - A_2}{\tau_{el-lat} - \tau_{el-sp}} \tau_{el-lat}\, e^{-\frac{t}{\tau_{el-lat}}}] \times M_0 \otimes \Gamma(t) \quad (4.1)$$

This is an approximated form based on the assumption that the electron temperature rises instantaneously upon laser excitation and can be applied to fit time-resolved Kerr rotation data taken within few picoseconds time scale. The whole system is divided into three subsystems: electron, spin and lattice system. On laser excitation the hot electrons are created above Fermi level. Then during energy rebalancing between the subsystems, quenched magnetization relaxes back to the initial state. The two exponential functions in the above equation mirror the demagnetization given by demagnetization time ($\tau_{\text{el-sp}}$) for energy transfer between electron-spin and the decay of electron temperature ($\tau_{\text{el-lat}}$) owing to the transfer of energy to the lattice. In addition to these characteristics time constants, the spin-lattice relaxation time also can be extracted by including another exponential term in the above equation if the spin specific heat is taken into account [34]. Θ is the Heaviside step function and $\Gamma(t)$ stands for the Gaussian function to be convoluted with the laser pulse envelope determining the temporal resolution (showing the cross correlation between the probe and pump pulse). The constant, A_1 indicates the ratio between amount of magnetization after equilibrium between electrons, spins, and lattice is restored and the initial magnetization. A_2 is proportional to the initial electronic temperature rise. The magnitude of both parameters increases with laser fluence. We have observed that with increasing fluence the demagnetization time has been negligibly varied within a range of 250±40 fs. The weak or no correlation between the pump fluence and the demagnetization rate describes the intrinsic nature of the spin scattering, governed by various mechanisms including Elliott-Yafet mechanism [35]. Another important observation here is that the delay of demagnetization processes which is the time delay between pump pulse (full width at half maxima, FWHM ≈ 130±20 fs) and starting point of the ultrafast demagnetization, becomes shorter due to increase in pump fluences. A plausible explanation for this is the dependence of delay of demagnetization on the electron-thermalization time which is eventually proportional to electron density or pump fluences [36]. On the other hand, fast remagnetization time has been found to be increased noticeably from 0.40 ± 0.05 ps to 0.80 ± 0.05 ps within the experimental fluence range of 10-55 mJ/cm^2. The larger is the pump fluence, the higher is the electron temperature or further the spin temperature. Therefore, it is reasonable that magnetization recovery time increases with the pump fluence.

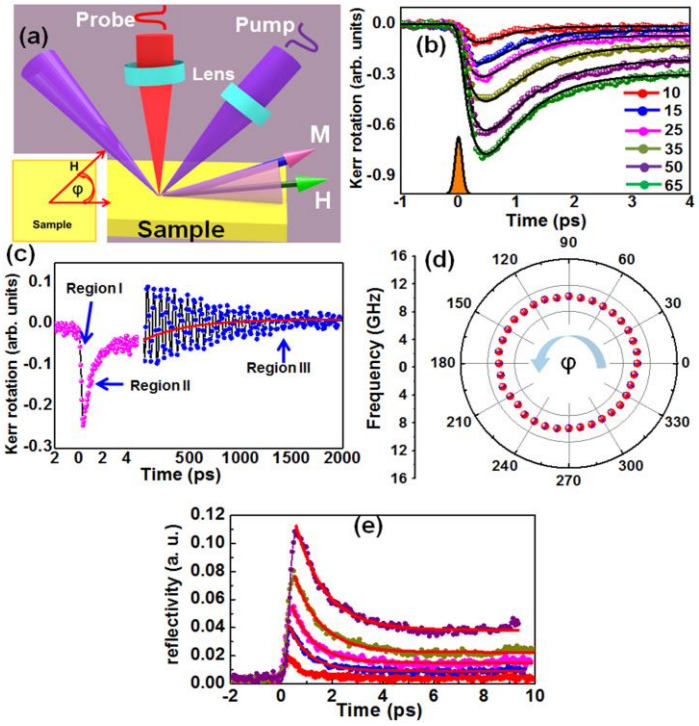

Figure 4.1: (a) Schematic of experimental geometry. In the inset, φ is shown as in-plane rotational angle of H, (b) pump fluence dependence of ultrafast demagnetization; Solid lines are fitting lines. Pump fluences (F) having unit of mJ/cm^2 are mentioned in numerical figure. The Gaussian envelope of laser pulse is presented to describe the convolution. (c) Representative time resolved Kerr rotation data with three distinguished temporal regions for F = 25 mJ/cm^2. (d) Angular variation of precessional frequency at H = 1.1 kOe for 20-nm-thick Py film. φ is presented in degree. (e) Representative time-resolved reflectivity data with varying pump fluence. The solid red lines indicate the exponential fit.

Figure 4.1 (c) shows the representative Kerr rotation data for F = 25 mJ/cm^2 consisting of three temporal regions, *i.e.* ultrafast demagnetization, fast remagnetization and slow remagnetization superposed with damped precession within the time window of 2 ns. We process the magnetization precession part after subtracting a bi-exponential background to estimate the damping and its modulation. The slower remagnetization is mainly due to heat diffusion from the lattice to the substrate and surrounding. Within our experimental fluence range the slow remagnetization time has increased from ≈ 0.4 ns to ≈ 1.0 ns. The precessional dynamics is described by phenomenological LLG equation,

$$\frac{d\boldsymbol{M}}{dt} = -\gamma\,(\boldsymbol{M} \times \boldsymbol{H}_{eff}) + \frac{\alpha}{M_s}\,(\boldsymbol{M} \times \frac{d\boldsymbol{M}}{dt}) \qquad (4.2)$$

where γ is the gyromagnetic ratio, M is magnetization, α is Gilbert damping constant and H_{eff} is the effective magnetic field consisting of several field components. The variation of precessional frequency with the angle between sample plane and bias magnetic field direction is plotted in Fig. 4.1 (d), which reveals that there is no uniaxial anisotropy present in this sample.

The decay of the reflectivity signal is fitted with an exponential function as shown in Fig. 4.1 (e). The decay time is found to vary from 0.55 ps to 1 ps within the experimental fluence range. This characteristic time scale represents the relaxation time of the electron temperature. The energy deposited by the pump pulse, in terms of heat within the probed volume, plays a very crucial role in modification of local magnetic properties, *i.e.* magnetic moment, anisotropy, coercivity, magnetic susceptibility, etc. With increasing fluence the precessional frequency experienced a red shift [20, 25]. Thus, at the onset of the precessional dynamics (about 10 ps from zero delay), for relatively high fluence, the initial frequency (f_i) will be smaller than its intrinsic value (in absence of any significant heat dissipation). As time progresses and the sample magnetization gradually attain its equilibrium value, the precessional frequency continuously changes, causing a temporal chirping of the damped oscillatory Kerr signal. The frequency shift can be estimated from the amount of temporal chirping [37]. Figure 4.2 (a) shows the background subtracted time-resolved Kerr rotation data (precessional part) for different pump fluences fitted with a damped sinusoidal function with added temporal chirping, $\theta_K = Ae^{-\frac{t}{\tau}}\sin[(2\pi f_i + bt)t + \Phi]$, where A, τ, f_i, b and Φ are the amplitude of the magnetization precession, the relaxation time, the initial precessional frequency, chirp parameter and initial phase, respectively. At this point, we are unsure of the exact nature of the damping, *i.e.* it may consist of both intrinsic and extrinsic mechanisms and hence we term it as effective damping parameter (α_{eff}) which can be extracted using the following formula [38],

$$\alpha_{eff} = \frac{1}{\gamma\tau(H + \frac{4\pi M_{eff}}{2})} \tag{4.3}$$

γ = 1.83 ×10^7 Hz/Oe for Py and M_{eff} is the effective magnetization including pump-induced changes at H = 2.4 kOe. This formula is exploited to extract effective damping parameter precisely in the moderate bias field regime.

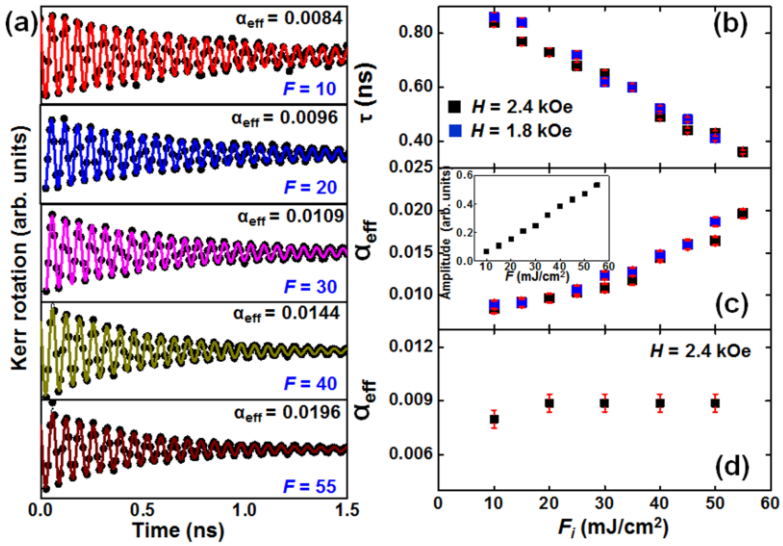

Figure 4.2: (a) Background subtracted time-resolved Kerr rotation data for different pump fluences at H = 2.4 kOe. F having unit of mJ/cm^2 is mentioned in numerical figure. Solid lines are fitting lines. Pump fluence dependence of (b) relaxation time (τ) and (c) effective damping (α_{eff}). Black and blue symbols represent the variation of these parameters at two different field values, H = 2.4 and 1.8 kOe, respectively. Amplitude of precession is also plotted with pump fluence for H = 2.4 kOe, (d) Variation of effective damping with irradiation fluence (F_i) at H = 2.4 kOe. In order to check the possible damage in the sample as high fluence values the pump fluence was taken up to the targeted value of F_i for several minutes followed by reduction of the pump fluence to a constant value of 10 mJ/cm^2 and the pump-probe measurement was performed. The damping coefficient is found to be unaffected by the irradiation fluence as shown in (d).

The variation of relaxation time and effective damping are plotted with pump fluence in Fig. 4.2 (b) and (c). Here, τ decreases with fluence while damping increases significantly with respect to its intrinsic value within this fluence range. We have repeated the experiment for two different field values (2.4 and 1.8 kOe). The slope of fluence dependent damping remains unaltered for both the field values. We have also observed increase in relative amplitudes of precession with pump fluence as shown in the inset of Fig. 4.2 (c). To verify the transient nature of damping we have performed another set of experiment where the probed area is exposed to different pump fluences (F_i) for several

minutes. After the irradiation, the precessioanl dynamics is measured from that area with fixed probe and pump fluences 2 and 10 mJ/cm^2, respectively. We found that damping remains almost constant for all the measurements (as shown in Fig. 4.2 (d)). These results demonstrate that the enhancement of damping is transient and only exists in the presence of high pump fluence but dropped to its original value when the pump laser is set to initial fluence.

The bias field dependence of precessional dynamics at four different pump fluences is studied to gain more insight about the origin of fluence dependent damping. First, we plotted the average frequency (f_{FFT}) with bias field which is obtained from the fast Fourier transformation (FFT) of the precessional data in Fig. 4.3 (a). The experimental data points are fitted with the Kittel formula,

$$f_{FFT} = \frac{\gamma}{2\pi}\sqrt{H(H + 4\pi M_{eff})} \tag{4.4}$$

M_{eff} is the effective magnetization of the sample. Figure 4.3 (b) shows that effective magnetization does not vary much within the applied fluence range. So, we infer that with increasing fluence there is no induced anisotropy developed in the system which can modify the effective damping up to this extent [23]. The variation of relaxation time with bias field for four different pump fluences are plotted in Fig. 4.3 (c). Relaxation time is increased with decreasing field for each case but for the higher fluence regime, those values seem to be fluctuating. This dependence of τ on field was fitted with Eq. (4.3) to extract damping coefficient at different fluence values. The damping coefficient in our sample does not vary with frequency. Thus within the experimental field and fluence regime it shows intrinsic nature and hence, we may now term it as the intrinsic damping coefficient α_0 [39,40]. The extrinsic contributions to damping mainly come from magnetic anisotropy field, two-magnon scattering, multimodal dephasing for excitation of several SW modes, etc., which are negligible in our present case.

Figure 4.3(d) shows the variation of α_0 with pump fluence, which shows that even the intrinsic damping is significantly increasing with pump fluence [20,41]. For generation of perpendicular standing SW modes the film needs to be thick enough. Though the film thickness is 20 nm here, but within the applied bias field range we have not found any other magnetic mode appearing with the uniform Kittel mode within the frequency window of our interest. Also, for 20-nm-thick Py film, the effect of eddy current will be

negligible [42]. The overlap between spatial profile of focused probe and pump laser spot may lead to the generation of magnons that propagate away from the region that is being probed. Generally, enhancement of nonlocal damping by SW emission becomes significant when the excitation area is less than 1 μm. Recently J. Wu *et al.* showed that propagation of magnetostatic spin waves could be significant even for probed regions of tens of microns in size [43].

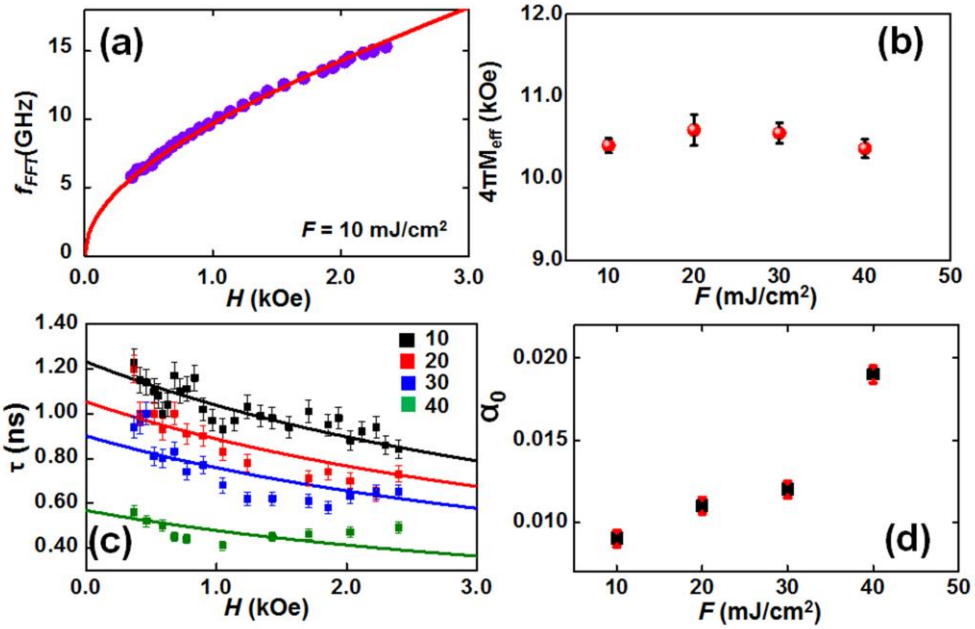

Figure 4.3: (a) Bias field dependence of precessional frequency for F = 10 mJ/cm². The red solid line indicates the Kittel fit. (b) Pump fluence dependence of effective magnetization (M_{eff}) of the probed volume. (c) Bias field dependence of relaxation time (τ) for four different fluences. F having unit of mJ/cm² is mentioned in numerical figures. Solid lines are the fitted data. (d) Variation of intrinsic Gilbert damping (α_0) with pump fluence.

Also, by generating SW trap in the pump-probe experiment modification of precessional frequency in ferromagnetic thin film due to accumulation and dissipation of thermal energy within the probed volume has been reported [44]. During our experiment the overlap between probe and pump spot is maintained carefully and Kerr signal is collected from the uniformly excited part of the sample so that slight misalignment during the course of experiment does not introduce any nonlocal effects. We will now substantiate our results with some theoretical arguments which involve the calculation of electronic temperature rise in the system due to application of higher pump fluence.

The electronic temperature (T_e) is related to absorbed laser energy per unit volume (E_a) according to the following equation [45],

$$E_a = \frac{\xi(T_e^2 - T_0^2)}{2} \tag{4.5}$$

where, ξ is the electronic specific heat of the system and T_0 is the initial electronic temperature (room temperature here). Here we have used ξ as 0.99 mJ/cc.K^2 for Py, considering the contribution from Ni as 80% and from Fe as 20%. First, we have estimated E_a according to the optical parameters of the sample by using the following equation,

$$E_a = \left[\frac{\left(1 - e^{-\frac{d}{\Psi}}\right) F(1-R)}{d}\right] \tag{4.6}$$

where, d is sample thickness, Ψ is optical penetration depth (~17 nm for 400-nm pump laser in 20-nm-thick Py film), R is the reflectivity of the sample (0.5 measured for the Py film) and F is applied pump fluence. By solving Eqs. (4.5) and (4.6) we have observed that amount of deposited energy is 1.72×10^6 mJ/cc to 8.64×10^6 mJ/cc within our experimental fluence range of 10 to 50 mJ/cm^2. Initial T_e increases from ≈ 1800 to 4500 K. Even after 10 ps, T_e (460-1660 K for fluence applied from 10 to 55 mJ/cm^2) remains well above T_c as estimated from the decay of reflectivity signal as shown in Fig. 4.1 (e). In this experiment the precession has been initiated after almost 10 ps and the time-resolved data has been recorded for 2 ns time window. We believe that the substantial increment first in electronic and then lattice temperature and its gradual decay during the precessioanl period play important role in modulation of damping [45-48]. The sample remains in its magnetized state even if the electronic temperature exceeds the Curie temperature. Importantly, ratio of the system temperature, T (as decay of electronic temperature is strongly correlated with rise of lattice temperature) to T_c is affecting the magnetization relaxation time which fundamentally depends on susceptibility. Accordingly damping should be proportional to susceptibility which is strongly temperature dependent [42]. Various procedures for exciting precessional dynamics in ferromagnets show the different mechanisms to be responsible for exploration of different energy dissipation channels. The spin-phonon interaction

mechanism, which historically has been thought to be the main contribution to magnetization damping, is important for picosecond-nanosecond applications at high temperatures such as spin caloritronics. But for laser-induced magnetization dynamics, where spin-flips occur mainly due to electron scattering, quantum Landau-Lifshitz-Bloch equation is sometimes exploited to explain the temperature dependence of damping by considering a simple spin-electron interaction as a source for magnetic relaxation [49]. This approach suggests that increasing ratio between system temperature and Curie temperature induces electron-impurity led spin-dependent scattering. Even slightly below T_c a pure change in the magnetization magnitude occurs which causes the enhancement of damping. Also our experimental results reveal that the precession amplitude and damping have been subjected to a sudden change for $F >$ 30 mJ/cm^2. Energy density deposited in the probed volume is proportional to pump fluence. For higher fluence, the temperature dependence of the electronic specific heat plays major role. The increase in the electronic specific heat value with temperature may lead to longer thermal-relaxation time. We infer that relative balance between the energy deposited into the lattice and electron system is also different for higher fluence regime compared to that in the lower fluence regime. Thus, the system temperature remains well above Curie temperature for $F >$ 30 mJ/cm^2, during the onset of precession for $t \geq$ 10 ps. This may open up additional energy dissipation channel for the magnetization relaxation process over nanoseconds time scale. Sometimes within very short time scale the spin temperature can go beyond the Curie temperature leading towards formation of paramagnetic state but that is a highly non-equilibrium case [50]. However we believe that in our experiment, even for the high fluence limit and in local thermal equilibrium the ferromagnetic to paramagnetic transition is not observed. Repetitive measurements established the reversibility of the damping parameter and bias-magnetic-field dependence of precessional frequency confirms ferromagnetic nature of the sample.

Pump fluence also eventually modulates the precessional frequency by introducing temporal chirping in the uniform precession. After immediate arrival of pump pulse, due to enhancement of the surface temperature, the net magnetization is reduced in picosecond time scale which results in chirping of the precessional oscillation. The initial frequency (f_i) is reduced with respect to its intrinsic value at a constant field. But when the probed volume cools with time, the spins try to retain their original

precessional frequency. Thus, within a fixed time window, the average frequency (f_{FFT}) also undergoes slight modification. In the high fluence regime, significant red shift is observed in both f_{FFT} and f_i. For H = 2.4 and 1.8 kOe, modulation of frequency is found to be 0.020 GHz.cm^2/mJ for f_{FFT} and 0.028 GHz.cm^2/mJ for f_i, from the slope of linear fit (as shown in Fig. 4.4(a)). The f_{FFT} is reduced by 7.2% of the extrapolated value at zero pump fluence for both the fields.

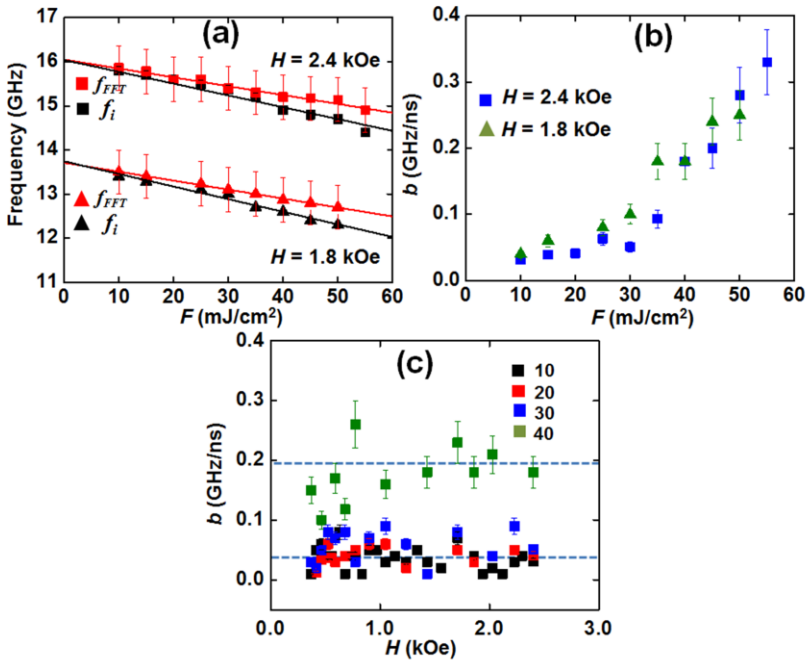

Figure 4.4: (a) Pump-fluence dependence of precessional frequencies for H = 2.4 and 1.8 kOe. Red and black symbols represent the variation of average frequency (f_{FFT}) and initial frequency (f_i) respectively. (b) Variation of temporal chirp parameter 'b' with pump fluence for two different magnetic field values. (c) Variation of temporal chirp parameter with bias field for four different pump fluences. F having unit of mJ/cm^2 is mentioned in numerical figure. Dotted lines are guide to eye.

On the other hand, f_i is decreased by 8.7% of its zero pump value for the highest pump fluence. The temporal chirp parameter, b shows giant enhancement within the experimental fluence range (Fig. 4.4(b)). For H = 2.4 kOe, b has increased up to ten times (from 0.03 GHz/ns to 0.33 GHz/ns) in this fluence limit which implies an increase in frequency of 0.66 GHz. Within our experimental scan window (2 ns), the maximum frequency shift is found to be 4.5% for F = 55 mJ/cm^2. For another bias field (H = 1.8 kOe), the enhancement of chirp parameter follows the similar trend. This ultrafast

modulation is attributed to the thermal effect on the local magnetic properties within the probed volume and is inferred to be reversible [37]. We have also plotted the variation of b with applied bias field for four different pump fluencies. It seems to be almost constant for all the field values in moderate fluence regime (as shown in Fig. 4.4 (c)). But for F = 40 mJ/cm^2, data points are relatively scattered and large errors have been considered to take care of those fluctuations.

Similar experiment is performed for 50-nm-thick Py film where another SW mode is observed with the uniform precessional mode. In order to extract the decay time and Gilbert damping of the precessional oscillations quantitatively, the sum of multiple damped sinusoidal functions is applied and the time variation of Kerr rotation angle ($\Delta\theta_K$) can be expressed as:

$$\theta_K = Ae^{-\frac{t}{\tau_1}}\sin[2\pi f_1 t + \Phi_1] + Be^{-\frac{t}{\tau_2}}\sin[2\pi f_2 t + \Phi_2] \quad (4.7)$$

Here the symbols have usual meaning.

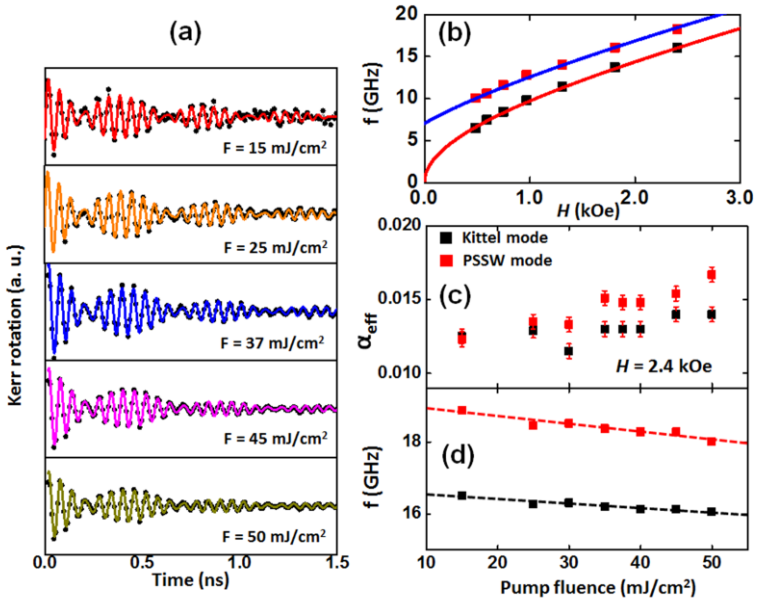

Figure 4.5: (a) Background subtracted time-resolved Kerr rotation data for different pump fluences at H = 2.4 kOe. Solid lines are fitting lines. (b) Bias field dependence of precessional frequency for both Kittel and PSSW modes are shown. Pump fluence dependence of (c) effective damping (α_{eff}) and (d) precessional frequencies. Dotted lines are guide to the eye.

This is used to fit the transient magnetization curves shown in Fig. 4.5 (a). The field dispersion of precessional frequencies reveals that the low frequency mode (f_1) is the uniform Kittel mode whereas higher frequency mode (f_2) is perpendicular standing spin-wave (PSSW) mode (Fig. 4.5 (b)). Experimental data points are fitted using the following form of the Kittel formula;

$$f = \frac{\gamma}{2\pi}\sqrt{(H + \frac{2A_{ex}}{M_{eff}}\left(\frac{n\pi}{d}\right)^2)(H + \frac{2A_{ex}}{M_{eff}}(\frac{n\pi}{d})^2 + 4\pi M_{eff})} \quad (4.8)$$

where A_{ex} is the exchange stiffness constant of Py. From the fitting we obtain the order of PSSW mode, n = 1. The decay times (τ_1 and τ_2) for both the mode decrease gradually as the pump fluence increases. Thus the effective damping show clear increment in the applied fluence range (Fig. 4.5 (c)). However, the slope is higher for Kittel mode with respect to PSSW mode. It is previously discusses in this section that the deposited energy within the probed volume is inversely proportional to the film thickness. Thus at a constant fluence the rise in electronic temperature and hence system temperature for 50-nm-thick film will not be as high as for 20-nm-thick film. This may be the reason of moderate enhancement in the effective damping observed in 50-nm-thick film. The precessional frequency decreases slightly with increase in fluence and the maximum modulation is found about 0.5 GHz.

4.4 Conclusions

In essence, a fluence-dependent study of ultrafast magnetization dynamics in Py thin film reveals very weak correlation between ultrafast demagnetization time and Gilbert damping within our experimental fluence range. We obtain large enhancement of damping with pump fluence. From the bias field as well as pump fluence dependence of experimentally obtained dynamical parameters we have excluded all the possible extrinsic contributions and observed a pump-induced modulation of intrinsic Gilbert damping. Also, from repetitive measurements with different pump irradiation we have shown that the pump-induced changes are reversible in nature. Enhancement of the system temperature to Curie temperature ratio is believed to be responsible for increment in remagnetization times and damping. The temporal chirp parameter has been found to be increased by up to ten times within the experimental fluence range,

while the frequency experiences a significant red shift. From application point of view, as increasing demand for faster and efficient magnetic memory devices, has led the scientific community in the extensive research field of ultrafast magnetization dynamics.

Our results will further enlighten the understanding of the modulation of magnetization dynamics in ferromagnetic systems in the presence of higher pump fluences. Low damping materials are preferred because it is easier to switch their magnetization in expense of smaller energy, lower write current in spin transfer torque magnetic random-access memories devices and longer propagation length of spin waves in magnonic devices. On the other hand, higher damping is also required to stop the post switching ringing of the signal. The results also have important implications in the emergent field of all-optical helicity-dependent switching [51–53]. In this context, the transient modulation of Gilbert damping and other dynamical parameters in ferromagnetic materials are of fundamental interest for characterizing and controlling ultrafast responses in magnetic structures.

References

1. O. Hellwig, A. Berger, T. Thomson, E. Dobisz, Z. Z. Bandic, H. Yang, D. S. Kercher, and E. E. Fullerton, Appl. Phys. Lett. **90**, 162516 (2007).
2. S. Tehrani, E. Chen, M. Durlam, M. DeHerrera, J. M. Slaughter, J. Shi, and G. Kerszykowski, J. Appl. Phys. **85**, 5822 (1999).
3. L. Landau and E. Lifshitz, Phys. Zeitsch. der Sow. **8**, 153 (1935).
4. T. L. Gilbert, IEEE Trans. Magn. **40**, 6 (2004).
5. P. He, X. Ma, J. W. Zhang, H. B. Zhao, G. Lupke, Z. Shi, and S. M. Zhou, Phys. Rev. Lett. **110**, 077203 (2013).
6. B. Heinrich, J. F. Cochran, and K. Myrtle, J. Appl. Phys. **53**, 2092 (1982).
7. P. Krivosik, N. Mo, S. Kalarickal, and C. E. Patton, J. Appl. Phys. **101**, 083901 (2007).
8. J. O. Rantschler, R. D. McMichael, A. Castillo, A. J. Shapiro, W. F. Egelhoff, B. B. Maranville, D. Pulugurtha, A. P. Chen, and L. M. Connors, J. Appl. Phys. **101**, 033911 (2007).
9. Y. Tserkovnyak, A. Brataas, and G. E. W. Bauer, Phys. Rev. B **66**, 224403 (2002).
10. A. Ganguly, R. M. Rowan-Robinson, A. Haldar, S. Jaiswal, J. Sinha, A. T. Hindmarch, D. A. Atkinson, and A. Barman, Appl. Phys. Lett. **105**, 112409 (2014).

11. K. Lenz, H. Wende, W. Kuch, K. Baberschke, K. Nagy, and A. Jánossy, Phys. Rev. B **73**, 144424 (2006).
12. Y. Zhao, Q. Song, S. H. Yang, T. Su, W. Yuan, S. S. P. Parkin, J. Shi, and W. Han, Sci. Rep. **6**, 22890 (2016).
13. V. Kamberský, Czech J. Phys. B **34**, 1111 (1984).
14. J. M. Beaujour, D. Ravelosona, I. Tudosa, E. E. Fullerton, and A. D. Kent, Phys. Rev. B **80**, 180415R (2009).
15. M. R. Freeman, R. R. Ruf and R. J. Gambino, IEEE Trans. Magn. **27**, 4840 (1991).
16. G. P. Zhang and W. Hübner, Phys. Rev. Lett. **85**, 3025 (2000).
17. M. van Kampen, C. Jozsa, J. T. Kohlhepp, P. LeClair, L. Lagae, W. J. M. de Jonge and B. Koopmans, Phys. Rev. Lett. **88**, 227201 (2002).
18. A. Barman, S. Wang, J. D. Maas, A. R. Hawkins, S. Kwon, A. Liddle, J. Bokor and H. Schmidt, Nano Lett. 6, 2939 (2006).
19. A. Barman and J. Sinha, Spin dynamics and damping in ferromagnetic thin films and nanostructures, (Springer, Switzerland, 2018).
20. G. M. Muller, M. Munzenberg, G.-X Miao and A. Gupta, Phys. Rev. B **77**, 020412(R) (2008).
21. S. Y. An, P. Krivosik, M. A. Kraemer, H. M. Olson, A. V. Nazarov and C. E. Patton, J. Appl. Phys. **96**, 1572 (2004).
22. W. Peng, Y. T. Hsia, K. Sendur and T. McDaniel, Tribol. Int. **38**, 588 (2005).
23. B. Liu, X. Ruan, Z. Wu, H. Tu, J. Du, J. Wu, X. Lu, L. He, R. Zhang and Y. Xu, Appl. Phys. Lett. **109**, 042401 (2016).
24. Z. Chen, M. Yi, M. Chen, S. Li, S. Zhou and T. Lai, Appl. Phys. Lett. **101**, 222402 (2012).
25. S. Mizukami, H. Abe, D. Watanabe, M. Oogane, Y. Ando and T. Miyazaki, Appl. Phys. Exp. **1**, 121301 (2008).
26. P. Yu, X. F. Jin, J. Kudrnovský, D. S. Wang and P. Bruno, Phys. Rev. B **77**, 054431 (2008).
27. E. Beaurepaire, J. C. Merle, A. Daunois and J. Y. Bigot, Phys. Rev. Lett. **76**, 4250 (1996).
28. S. I. Anisimov, B. L. Kapeliovich and T. L. Perelman, Sov. Phys. JETP **39**, 2 (1974).
29. M. Krauß, T. Roth, S. Alebrand, D. Steil, M. Cinchetti, M. Aeschlimann and H. C. Schneider, Phys. Rev. B **80,** 180407 (2009).

30. G. Malinowski, F. Dalla Longa, J. H. H. Rietjens, P. V. Paluskar, R. Huijink, H. J. M. Swagten and B. Koopmans, Nat. Phys. **4,** 855–858 (2008).
31. D. Rudolf, C. La-O-Vorakiat, M. Battiato, R. Adam, J. M. Shaw, E. Turgut, P. Maldonado, S. Mathias, P. Grychtol, H. T. Nembach, T. J. Silva, M. Aeschlimann, H. C. Kapteyn, M. M. Murnane, C. M. Schneider and P. M. Oppeneer, Nat. Comm. **3**, 1037 (2012).
32. F. Dalla Longa, J. T. Kohlhepp, W. J. M. de Jonge, and B. Koopmans, Phys. Rev. B **75**, 224431 (2007).
33. J. Walowski, G. Muller, M. Djordjevic, M. Munzenberg, M. Klaui, A. F. Vaz and J. A. C. Bland, Phys. Rev. Lett. **101**, 237401 (2008).
34. U. Atxitia, O. Chubykalo-Fesenko, J. Walowski, A. Mann, and M. Münzenberg, Phys. Rev. B, **81**,174401 (2010).
35. B. Koopmans, J. J. M. Ruigrok, F. Dalla Longa, and W. J. M. de Jonge, Phys. Rev. Lett. **95,** 267207 (2005).
36. X. Liu, Z. Xu, R. Gao, H. Hu, Z. Chen, Z. Wang, J. Du, S. Zhou and T. Lai, Appl. Phys. Lett. **92**, 232501 (2008).
37. Y. Liu, L. R. Shelford, V. V. Kruglyak, R. J. Hicken, Y. Sakuraba, M. Oogane and Y. Ando, Phys. Rev. B, **81**, 094402 (2010).
38. J. Walowski, M. Djordjevic Kaufmann, B. Lenk, C. Hamann, J. McCord and M. Munzenberg, J. Phys. D: Appl. Phys. **41,** 164016 (2008).
39. G. Woltersdorf, M. Buess, B. Heinrich, and C. H. Back, Phys. Rev. Lett. 95, 037401 (2005).
40. J. A. King, A. Ganguly, D. M. Burn, S. Pal, E. A. Sallabank, T. P. A. Hase, A. T. Hindmarch, A. Barman, and D. Atkinson, Appl. Phys. Lett. 104, 242410 (2014).
41. A. Capua, S. H. Yang, T. Phung and S. S. P. Parkin, Phys. Rev. B **92**, 224402 (2015).
42. B. Heinrich and J. A. C. Bland, Spin relaxation in magnetic metallic layers and multilayers, in Ultrathin magnetic structures: fundamentals of nanomagnetism, edited byBland J. A. C. (Springer, New York, 2005), Vol. 3.
43. J. Wu, N. D. Hughes, J. R. Moore and R. J. Hicken, J. Magn. Magn. Mater. **241**, 96 (2002).
44. F. Busse, M. Mansurova, B. Lenk, M. von der. Ehe and M. Münzenberg, Sci. Rep. **5**, 12824 (2015).
45. E. Carpene, E. Mancini, C. Dallera, M. Brenna, E. Puppin and S. De Silvestri, Phys. Rev. B **78**, 174422 (2008).

46. J. Mendil, P. Nieves, O. Chubykalo-Fesenko, J. Walowski, T. Santos, S. Pisana, and M. Munzenberg, Sci. Rep. **4**, 3980 (2014).
47. R. W. Schoenlein, W. Z. Lin, J. G. Fujimoto, and G. L. Eesley, Phys. Rev. Lett. **58**, 1680 (1987).
48. Z. Lin, Leonid V. Zhigilei, and V. Celli, Phys. Rev. B **77**, 075133 (2008).
49. P. Nieves, D. Serantes, U. Atxitia, and O. ChubykaloFesenko, Phys. Rev. B **90**, 104428 (2014).
50. N. Kazantseva, U. Nowak, R. W. Chantrell, J. Hohlfeld, and A. Rebei, EPL **81**, 27004 (2008).
51. G. M. Choi, A. Schleife, and D. G. Cahill, Nat. Comm. **8**, 15085 (2017).
52. T. D. Cornelissen, R. Córdoba, and B. Koopmans, Appl. Phys. Lett. **108**, 142405 (2016).
53. Md. S El Hadri, M. Hehn, G. Malinowski, and S. Mangin, J. Phys. D: Appl. Phys. **50**, 133002 (2017).

Chapter 5

5 Role of magnetic anisotropy on the ultrafast magnetization dynamics of Gd-Fe thin films with different thicknesses

5.1 Introduction

The possibilities of manipulating magnetic system without applying external magnetic field have gained considerable research interest during last two decades due to their potential applications in magnetic storage devices. The familiar examples include spin polarized current induced spin-transfer torque (STT) switching [1], electric field controlled magnetic devices [2] and all-optical switching (AOS) of magnetization in ultrafast time scale using ultra-short laser pulses [3]. Optical control of magnetic order by femtosecond (fs) laser pulses has developed an exciting and expanding research field as it explores faster way for magnetization reversal in sub-picosecond (ps) time scale. This was not achieved from the precessional switching of the magnetization in presence of an orthogonal external magnetic field. A realistic switching time, which can be achieved in such process, is in the order of 100 ps and is determined by the strength and duration of the magnetic field pulse [4-6]. There are three fundamental effects of ultrafast stimuli on a magnetic system, namely, ultrafast demagnetization, AOS and laser-induced spin precession and damping. Since the first report on the ultrafast demagnetization in Ni films by Beaurepaire *et al.*, the mechanism behind this has become a topic of intense debate [7]. Unlike the transient change in magnetization described by ultrafast demagnetization, Stanciu *et al.* demonstrated a complete reversal of magnetization in rare-earth (RE) and transition-metal (TM) alloys employing optical stimuli in absence of an external magnetic field [8]. All-optical helicity dependent switching (AO-HDS) thus promises rapid increase in writing speed for magnetic recording devices [3]. This has widely been studied in the last decade for various magnetic thin films including perpendicularly magnetized multilayers, synthetic antiferromagnets and different ferromagnetic alloys [9, 10]. The dynamics of the magnetization precession gives a direct access to study the magnetic anisotropy,

damping and precessional frequency of different dynamic modes, such as uniform Kittel mode, perpendicular standing spin-wave (PSSW) mode and other dispersive modes in a continuous thin film [11, 12] and patterned nanostructures [13]. Control of Gilbert damping by various external stimuli has been demonstrated [14-19] which promises their applications in spintronic and magnonic devices. The magnetization dynamics becomes further intriguing in case of multi-sublattice magnets, where an important role is played by the exchange of angular momentum between the non-equivalent sublattices after being stimulated. Alloys of 3d TM and 4f RE metals are at the center of attraction because they exhibit tunable magnetic properties with the change in stoichiometry [20-24]. This behavior with a strong magneto-optic effect makes them particularly interesting for magneto-optical recording when they exhibit perpendicular magnetic anisotropy (PMA) [25, 26]. Another aspect of technological interest is higher magnetostriction with IP anisotropy which makes them applicable in magnetostrictive memory [27, 28], sensors and actuators. Among such RE-TM alloy systems, it is observed that the time scale of magnetization dynamics is dependent on the exchange interaction and the balance of angular momentum between the RE and TM sublattices, particularly when they display antiferromagnetic coupling [20]. This gives an excellent opportunity to study element-specific response of the materials using X-ray probes [21]. Gd-Fe based ferrimagnetic alloys are potential candidate for magneto-optic media, bubble memories and those are scientifically rich due to the antiferromagnetic coupling between the Gd and Fe sublattices. Thus, substantial efforts have been made to explore the composition dependent nature of ultrafast demagnetization and remagnetization in this system aiming towards the decrease in switching time [22]. On the other hand, role of higher magnetic field in the study of magnetization dynamics has been explicitly observed by Becker and colleagues in the context of RE-TM alloys [29]. The role of RE concentration and pump fluence on the Gilbert damping have also been reported for these alloys [30, 31]. Substantial research work has been performed to study the magnetic domains [32] and spin re-orientation transition with external perturbations [33, 34] for amorphous Gd-Fe thin films. However, a systematic investigation of magnetization dynamics as a function of film thickness with special emphasis towards understanding of the dynamic modes and their damping behavior has not been reported so far for Gd-Fe system.

This paper aims at systematic investigation of ultrafast magnetization dynamics in Gd-Fe thin films with different thicknesses *viz.,* 20, 50 and 100 nm employing time-resolved magneto-optical Kerr effect (TR-MOKE) technique with two color pump-probe geometry. Here, we report the overall ultrafast demagnetization time and remagnetization times of Gd-Fe system. The bias magnetic field dependence of precessional frequency of the Kittel mode for lower thickness and several standing SW modes in the higher thickness regime is studied for different field orientation. The frequency dependence of damping of the Kittel mode and decay constants, for both Kittel and PSSW modes has been explicitly demonstrated. The OOP magnetic anisotropy is found to be developed in these films with increasing thickness, which influences the magnetization dynamics significantly. Importantly, the tunability of the orientations of magnetization with applied field for different thicknesses of Gd-Fe films has also been shown from the field-dispersion relations. It should be noted that, all the experiments are performed at room temperature which is below the compensation point of the considered Gd-Fe films and hence we essentially probe the net ferromagnetic moment of the system instead of considering the magnetization of the individual sublattice and the antiferromagnetic coupling between them. The mutual energy transfer mechanism between the PSSW modes and the uniform Kittel mode is reported for Gd-Fe thin films showing evolution with magnetic field strength.

5.2 Experimental Details

Gd-Fe thin films of thicknesses d = 20, 50 and 100 nm were deposited by electron-beam (e-beam) evaporation at room temperature on Si (100) substrates with background pressure better than 2×10^{-6} Torr. The growth rate of the films was set at around 0.3 nm/sec employing an alloy target of equi-atomic elemental composition Gd and Fe. The substrate was rotated at a constant speed of 10 rpm in order to ensure the uniformity in thickness. 3-nm-thin layer of Cr was deposited as a capping layer.

The e-beam evaporated Gd-Fe films are amorphous in nature [33] and the stoichiometry (using energy dispersive X-ray spectroscopy) has been recorded in Table 5.1, which shows that the films are Fe-rich irrespective of their thickness. The roughness of the films was measured by atomic force microscopy (AFM) and found to

be about 1 nm for all three films. The IP and OOP hysteresis loops for the Gd-Fe films measured from vibrating sample magnetometry (VSM) are shown in Fig. 5.1 (a) [35].

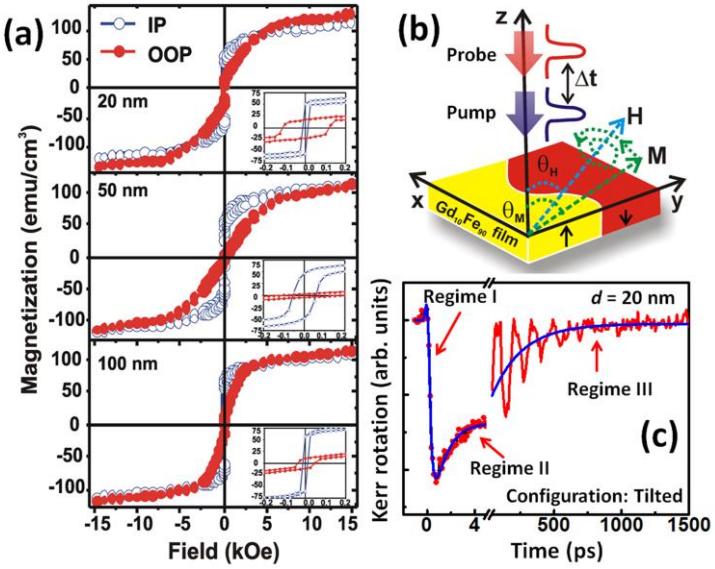

Figure 5.1: (a) Hysteresis loops measured by using VSM in OOP and IP configuration for film thickness, d = 20 nm, 50 nm and 100 nm. The nature of magnetization reversal is more prominently shown in the plots provided at insets. (b) Schematic of experimental geometry used in TR-MOKE microscopy. (c) Time-resolved Kerr rotation data showing three different temporal regimes for 20-nm-thick Gd-Fe film for tilted configuration of magnetic field. Blue solid lines are fitting.

The values for the extracted magnetic properties have also been recorded in Table 5.1. Lesser coercivity (H_C) indicates the soft magnetic characteristic of the samples, which reverse the magnetization at a low field (listed in Table 5.1). It is worthy to mention that the lower values of H_C essentially confirm the state of saturation with uniform magnetization for the magnetic field values applied in the dynamic measurements.

The remanent magnetization (M_R) measured in the IP geometry is greater than that in the OOP geometry which confirms that all the films show a predominant IP magnetization and hence easier to saturate along the plane. The saturation magnetization (M_s) calculated from the initial curves shows increasing trend with the increase in film thickness which is in agreement with the previous results obtained from ferrimagnetic thin films [35, 36]. The effective anisotropy constant (K_{eff}) is calculated by

subtracting the area under the OOP initial curve from the IP initial curve. Hence, positive values of K_{eff} quantitatively indicate the presence of weak IP anisotropies in the films. Surprisingly, the evolution of stripe domains and development of weak OOP anisotropy with increasing film thickness were reported previously for Gd-Fe thin films [37]. This is unusual for magnetic films with relatively higher thickness. Though such domain feature was not observed from magnetic force microscopy (MFM) in the present films with the specified stoichiometry but the decrease in K_{eff} hints about a change in the orientation of magnetization for the thicker films. The quantitative confirmation about the anisotropy and the direction of magnetization will be discussed further in the light of magnetization dynamics.

TABLE 5.1. Stoichiometry, average roughness, H_C, M_R, M_S and K_{eff} for Gd-Fe thin films with different thicknesses are shown.

Film thickness (nm)	Stoichiometry (atomic %)	Average Rough-ness (nm)	H_C (Oe)		M_R (emu/cm^3)		M_S (emu/cm^3)	K_{eff} (erg/cm^3)
			IP	OOP	IP	OOP		
20	$Gd_{12.7}Fe_{87.3}$	0.7	13	114	53	20	129	1.87×10^5
50	$Gd_{10.2}Fe_{89.8}$	1.0	55	144	48	4	131	1.45×10^5
100	$Gd_{12.1}Fe_{87.9}$	0.8	12	59	59	11	148	0.49×10^5

We have used a two-color pump-probe technique in the time-resolved MOKE experiment. Here the fundamental laser beam generated from a (Tsunami: Spectra Physics, λ = 800 nm, pulse width ≈ 80 fs, spot size ≈ 800 nm) femtosecond laser cavity is exploited to probe the polar Kerr rotation of the sample and the second harmonic of the fundamental beam (λ = 400 nm, pulse width ≈ 100 fs, spot size ≈ 1 μm) excites the magnetization dynamics [12]. The time delay between the pump and probe pulse is indicated by Δt. For all experiments, the probe fluence is kept fixed at ≈ 2 mJ/cm^2 and the pump fluence is fixed at ≈ 15 mJ/cm^2. A large static field is applied to saturate the samples along the direction of the field (> 5 kOe) and then its magnitude (H) is varied according to the experimental requirement. During this experiment the orientation of

the H (θ_H) is varied from OOP to IP (as shown in Fig. 5.1(b)). Here, we have considered θ_H = 21°, 50° and 88° as OOP, tilted and IP configuration. The probe beam falls collinearly with the pump beam through the same microscope objective (N. A. = 0.65) and measure the magnetization dynamics from a uniformly excited region from the sample. The detection assembly allows the measurement of Kerr rotation and reflectivity simultaneously by avoiding breakthrough of one signal to another. The time-resolved Kerr rotation data for 20-nm-thick Gd-Fe thin film is presented in Fig. 5.1 (c). Initially the magnetization of the entire Gd-Fe sublattice system is aligned by the combination of anisotropy field and bias magnetic field and its orientation is indicated by θ_M in Fig. 5.1 (b). The rapid quenching of magnetization just after arrival of the pump pulse is known as the ultrafast demagnetization [7] (regime I, Fig. 5.1 (c)). The thermalization between electron and lattice results fast remagnetization within few picoseconds (regime II). The heat-induced changes in saturation magnetization and anisotropy compel the magnetization to move to a new equilibrium direction. During the cooling process, laser induced demagnetization field exerts a toque in the magnetization and triggers damped precessional motion of the magnetization towards the previous equilibrium directions [11]. The energy dissipation from lattice to surrounding results in slow remagnetization and introduces a bi-exponential background with the magnetization precession (regime III). The time scales for ultrafast demagnetization and fast remagnetization for 20-nm-thick film were obtained as about 300 fs and 1 ps, respectively from the fitting of experimental data by using a simplified expression of 'Three temperature model' [38]. Earlier reports show that the TM demagnetizes faster than the RE element and forms a ferromagnetic like state for a short period of time due to the antiferromagnetic interaction between Gd and Fe atoms [22, 39], which justifies the demagnetization time obtained in our system. The slow remagnetization time is obtained about 220 ps. From the background subtracted precessional data we obtain both the precession frequency and decay time of precessional amplitude.

5.3 Results and Discussions

The magnitude and orientation of bias magnetic field is varied to obtain field dispersion of precessional frequency which is equivalent to ferromagnetic resonance in the magnetic system. We perform fast Fourier transformation (FFT) of the precessional

data to obtain the spin-wave (SW) spectra in frequency domain, for d = 20 and 100 nm (as shown in Figs. 5.2 and 5.3). For IP configuration the reduction in precessional amplitude leads to poor signal to noise ratio for both the samples. As the bias magnetic field is tilted in the OOP direction the precessional amplitude increases and we observed time-resolved Kerr rotation showing superposition of multiple SW modes. The number of peaks varies for different magnitude and orientations of bias magnetic field.

For d = 20 nm, mostly single mode with reasonable power is observed in the spectra whose frequency decreases with decreasing H for OOP configuration. Another lesser intensity mode with different slope in the field-dispersion curve appears in the low field regime for tilted configuration (see Fig. 5.2). At IP configuration the dominance of nonmagnetic noise has suppressed the features of magnetic peaks. For d = 100 nm, there appear three, two and single modes within our experimental field regime for IP, tilted and OOP configurations respectively (Fig. 5.3). Presence of few spurious peaks in the spectra is found in IP configuration which disappears as the field is rotated towards OOP direction. Mode 3 in the IP configuration and mode 2 in the tilted configuration disappears in the low field regime.

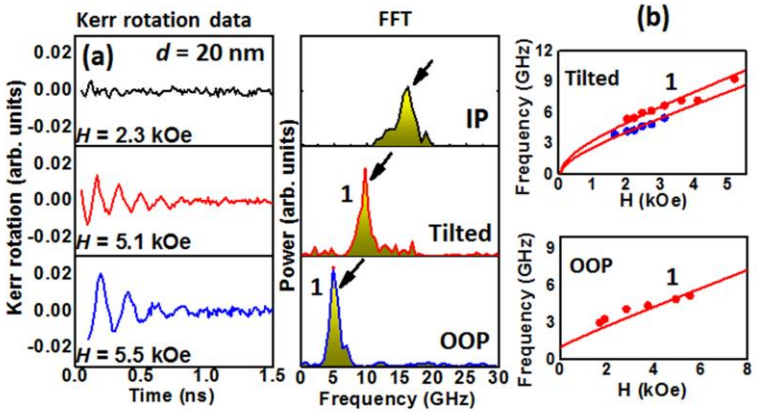

Figure 5.2: Background subtracted time-resolved Kerr rotation data and corresponding FFT spectra for (a) d = 20 nm for IP, tilted and OOP configuration. The magnetic modes are marked with black arrows and also are numbered subsequently. The magnitudes of bias magnetic field are indicated at the corner of the figures. Bias magnetic field dependence of precessional frequency is presented for (b) d = 20 nm for tilted and OOP configuration. Solid lines correspond to the Kittel fit.

To investigate the anisotropic behavior of these modes, we have fitted our experimental data points using the following form of Kittel formula [40],

$$f = \frac{\gamma}{2\pi}\sqrt{H_1 \times H_2} \tag{5.1}$$

$$H_1 = Hcos(\theta_H - \theta_M) - 4\pi M_{eff} cos^2(\theta_M) \tag{5.2}$$

$$H_2 = Hcos(\theta_H - \theta_M) - 4\pi M_{eff} cos(2\theta_M) \tag{5.3}$$

Here, f is the precessional frequency, $\gamma = \frac{g\mu_B}{\hbar}$ is gyromagnetic ratio and g is Lande-g-factor. H, θ_H and θ_M are the parameters, already described before. M_{eff} is the effective magnetization, which can be expressed also as,

$$4\pi M_{eff} = 4\pi M_s - H_\perp \tag{5.4}$$

where $H_\perp = \frac{2K_\perp}{M_s}$ is the OOP anisotropy field and $K_\perp$ is the anisotropy constant. M_s is the saturation magnetization of the samples at room temperature obtained from VSM measurement. θ_M during onset of dynamics can be found, by solving the following equation numerically;

$$\sin(2\theta_M) = \frac{2Hsin(\theta_M - \theta_H)}{4\pi M_{eff}} \tag{5.5}$$

where the IP azimuthal angle for bias magnetic field and magnetization should be same with respect to the IP coordinates.

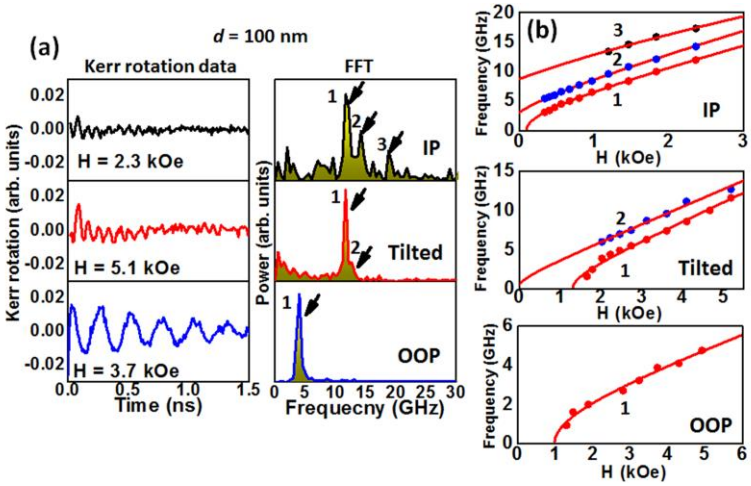

Figure 5.3: Background subtracted time-resolved Kerr rotation data and corresponding FFT spectra for (a) d = 100 nm for IP, tilted and OOP configuration. The magnetic modes are marked with black arrows and also are numbered subsequently. The magnitudes of bias magnetic field are indicated at the corner of the figures. Field dispersion of precessional frequency is presented for (b) d = 100 nm. Solid lines correspond to the Kittel fit.

Combining the above mentioned equations, we have fitted the Kittel mode for different field orientations of both the samples and the fitting parameters have been recorded in Table 5.2.

TABLE 5.2: Parameters corresponding to field dispersion of uniform Kittel modes in the frequency spectra of Gd-Fe samples having thickness 20 and 100 nm, are presented.

Film thickness (nm)	Parameters obtained from fitting				
	θ_H (°)	θ_M (°)	g	M_S (emu/cm^3)	$K_\perp$ (erg/cm^3)
20	21	73	2.0	127	0.9×10^5
	50	73	2.0	137	0.9×10^5
100	21	67	2.0	152	1.6×10^5
	50	70	2.0	152	1.6×10^5
	88	86	2.0	160	1.3×10^5

The M_S values obtained from fitting differ with the saturation magnetization within ±10%. The magnetization follows mostly the orientation of bias magnetic field, though the combined effect of anisotropy and external field controls the tilt of magnetization. The positive sign of the anisotropy constant demonstrate an evolution of OOP anisotropy although its magnitude is comparatively lower than the conventional PMA systems, such as, Co/Pd multilayers, etc. [41]. Although the sources of OOP anisotropy in amorphous RE-TM films are a topic of debate, previous studies on Gd-Fe thin films explained the development of PMA in thicker Gd-Fe films with the presence of labyrinth-like magnetic domains, width of which increases with the increase in film thickness along with the simultaneous reduction in domain wall width. The energetics, derived from micromagnetic simulations elucidated the dominant role of dipolar coupling behind the development of this anisotropy in thicker films [37].

We fitted the higher frequency modes appeared for 100-nm-thick film using the following formula of PSSW modes [42, 43],

$$f = \frac{\gamma}{2\pi}\sqrt{\begin{matrix}(Hcos(\theta_H - \theta_M) - 4\pi M_{eff}cos^2(\theta_M) \\ +\frac{2A}{M_s}(\frac{n\pi}{d})^2)((Hcos(\theta_H - \theta_M) - 4\pi M_{eff}(2\theta_M) + \frac{2A}{M_s}(\frac{n\pi}{d})^2)\end{matrix}} \quad (5.6)$$

Here *A, n* and *d,* are the exchange stiffness constant, order of PSSW mode and thickness of the film, respectively. The other parameters have their usual meaning. This formula holds good for the experimental configuration with $\theta_H \approx \theta_M \approx 90°$. From the fit we have confirmed that mode 2 for IP and tilted configuration is the 1st order PSSW mode (n =1) for this thick film. Mode 3 for IP configuration is the 2nd order PSSW with n = 2. The exchange stiffness constant is found to be, A = 2.6×10^{-7} erg/cm which agrees well with the reported values for Gd-Fe thin films [32]. It is worthy to mention here that we also observed a lower frequency mode in the close vicinity of the Kittel modes in the 20-nm-thick film. This mode is of magnetic origin as confirmed from its field dispersion. However, the field dispersion of these modes could not be fitted well with reasonable parameters. It may arise from the magnetic inhomogeneity developed in the system. Slight change in anisotropy sometimes along the thickness of the film cannot be ruled out. Kittel fit of this mode with M_S = 111 emu/cm^3 and $K_\perp$ = 0.8×10^5 erg/cm^3, justifies the above speculation. There is possibility of inhomogeneous growth of the films with nonuniformity in the elemental composition along the thickness [34] which can cause appearance of modes other than Kittel mode. Moreover, the strength of the dipolar field is more at the surface of the film due to the closure of magnetic lines of force through the top and the bottom of the sample. This may result in non-uniformity in magnetization along the thickness, where the net magnetization at the surface is less compared to the middle layers and hence may display weaker domain contrast.

The bias-field dependent precessional magnetization dynamics for 50-nm-thick film in tilted and OOP configuration are presented Fig. 5.4. In IP configuration the signal to noise ratio is poor in the time-resolved data. The precessional data is noisy and damps very quickly after few tens of picoseconds, making a precise determination of the precessional frequency from FFT spectra very difficult. In tilted configuration, we are able to identify splitting of a peak where the higher frequency mode may have PSSW

nature. In OOP configuration, the picosecond precession shows a single frequency oscillation. The precessional frequencies are plotted as a function of bias magnetic field magnitude. For tilted and OOP configuration, the experimental data points are fitted well with Kittel formula and the extracted values of M_S is about 130 emu/cm^3 and $K_\perp$ is about 1.15×10^5 erg/cm^3, which indicates systematic development of OOP anisotropy. All the modes cannot be fitted with the Kittel formula.

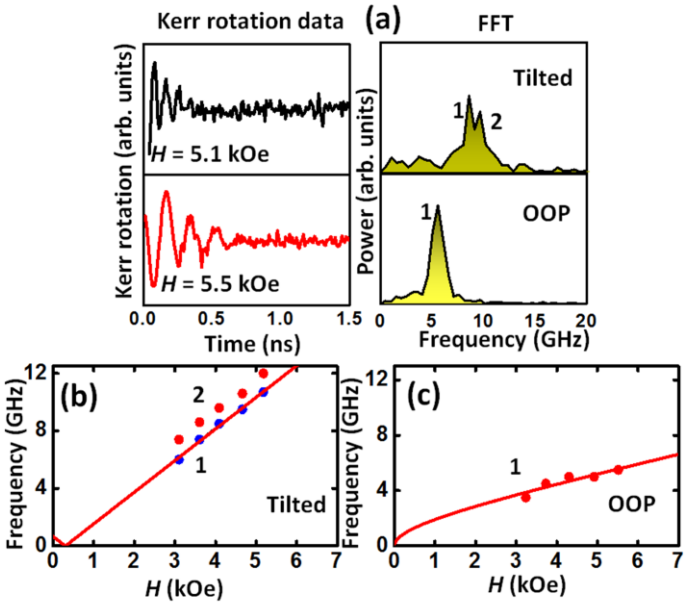

Figure 5.4: (a) Time resolved Kerr rotation data and corresponding FFT spectra for tilted and OOP configuration at H > 5 kOe for 50-nm-thick Gd-Fe film. Bias field dependence of precessional frequency at (b) tilted and (c) OOP configuration. Red and blue dots represent two different modes. The red solid line is Kittel fit.

In order to extract the decay time and Gilbert damping of the precessional oscillations quantitatively, the sum of multiple damped sinusoidal functions is applied [44] and the time variation of Kerr rotation angle ($\Delta\theta_K$) can be expressed as:

$$\Delta\theta_K \propto \sum_{i=1}^{m} A_i\, e^{\frac{-t}{\tau_i}} \sin(2\pi f_i t + \phi_i) \qquad (5.7)$$

where A_i, τ_i, f_i, ϕ_i are the precessional amplitude, decay time, frequency and initial phase of oscillation of the i^{th} mode, and m is the mode number. This is used to fit the transient magnetization curves if there is clear existence of more than one SW modes ($1 \leq m \leq 3$). In

other cases, a single damped sinusoidal function is applied to give a good fit to the curves. For example, in the 20-nm-thick film, the intensity of a low frequency mode (mode 2) observed for tilted configuration may not have any significant contribution to the dephasing of precessional amplitude of the Kittel mode (mode1). Thus for, both OOP and tilted configurations time-resolved data are fitted with single damped sinusoidal function (Fig. 5.5 (a)). We have plotted the variation of decay time (τ) with precessional frequency in order to understand the bias magnetic field dependence of damping for this system in Fig. 5.7. In OOP, the decay time is found to be almost constant at 0.3 ns, whereas in tilted configuration, decay time shows a random variation about 0.3 ns. We have extracted the damping of these modes from the following expression [43],

$$\alpha_{eff} = \frac{1}{\gamma\tau(H - \frac{k_{\perp}}{\mu_0 M_s} + \frac{4\pi M_s}{2})} \tag{5.8}$$

Here, α_{eff} is the effective damping of the system which consists of intrinsic and extrinsic contribution. Other parameters have their usual meaning. In Fig. 5.5 (b), the variation of damping with precessional frequency is plotted corresponding to each field orientation. For tilted and OOP configuration, effective damping increases rapidly with decreasing frequency and the enhancement is almost three times from their intrinsic values. Here, we believe that for f > 5 GHz, the bias magnetic field is high enough to suppress any additional effects present in the sample which can extrinsically modulate the damping [44]. Thus for tilted configuration, damping shows constant value for f > 5 GHz. As the saturation magnetization for this sample is quite less (~130 emu/cm^3) the field values of about 4 kOe can be considered to be sufficiently high.

The damping of the Kittel mode in OOP configuration for 50-nm-thick film also increases with decrease in frequency. For 100-nm-thick Gd-Fe film, time-resolved data are fitted with damped sinusoidal function consisting of multiple frequencies (see Fig. 5.6 (a)) and Eq. (5.7) has been exploited to fit the precessional oscillations. The decay times for Kittel as well as PSSW modes for IP are in the order of 0.4 to 0.8 ns. The extracted damping values are significantly high (α_{eff} increased up to 0.2) (as shown in Fig. 5.6 (b)). However for tilted and OOP configuration, the decay time of Kittel mode has been increased from 0.5 ns to almost 1.0 ns within the experimental frequency range. For the 1st order PSSW mode at tilted configuration, the trend is opposite (shown in Fig. 5.6) where decay time decreased with the decrease in frequency. For IP

configuration, we would like to mention that the decay times extracted from the 'three-frequency' fitting (at higher field) may contain relatively large error due to non-trivial fitting conditions adopted with multiple fitting parameters and smaller precessional amplitude of the higher frequency modes. Effective damping extracted for the Kittel modes shows increasing nature with decreasing frequency and attains a constant value at the higher field regime.

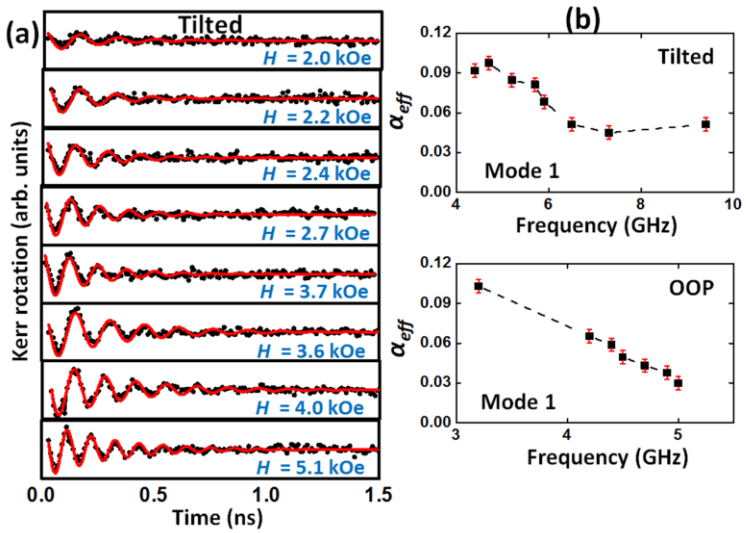

Figure 5.5: (a) Background subtracted time-resolved Kerr rotation data and corresponding fitting with damped sine function for d = 20 nm for tilted configuration. (b) The variation of effective damping with precessional frequency IP and tilted configuration. The solid lines are fits. Dotted lines are guide to eye.

The Gilbert damping parameter is mainly responsible for bringing the system into an equilibrium state. The effective damping parameter depends on several extrinsic factors, including composition of the RE and TM in the sample. Due to the presence of half-filled 4*f* shell in Gd, the direct spin-lattice excitation is absent and the damping occurs only through the interaction with the conduction band electrons. Hence, the damping of Gd sublattice is found to be very low. Natural damping of Fe sublattice lies in the vicinity of α_{Fe} = 0.02. In our experiments the extracted effective damping parameters lie in the range of 0.02 to 0.15 ($0.02 \leq \alpha_{eff} \leq 0.15$) within our experimental field regime [8,31]. As the samples are Fe rich, the higher values of damping of the Kittel mode in some field orientation indicate the presence of extrinsic contribution other than the intrinsic Gilbert damping in these films. We discuss the possibilities below.

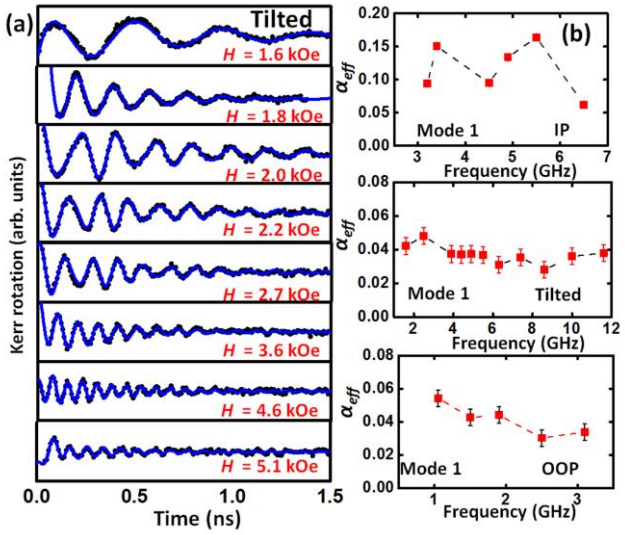

Figure 5.6: (a) Background subtracted time-resolved Kerr rotation data and corresponding fitting with damped sine function for d = 100 nm for tilted configuration. (b) The variation of effective damping with precessional frequency for IP, tilted and OOP configuration. The solid lines are fits. Dotted lines are guide to eye. Some of the error bars may not be visible as those are merged within the size of points indicated in the plot.

We obtained that in the high frequency regime the damping is similar for both the films and is in the order of 0.15. As the films show roughness below 1 nm (Table 5.1) with no identifiable feature or ripple in the surface, the contribution of roughness to the higher damping values can probably be ruled out. Sometimes the TM film with RE doping can contain specific regions with nonuniform RE concentration. Magnetic inhomogeneity can sometimes cause two-magnon scattering (TMS) where the resonant FMR mode (usually $k \sim 0$) scatters into other magnons having the same frequency. In the presence of magnetic defects, magnon momentum is not generally conserved and the relaxation parameter becomes strongly frequency dependent. Thus, the TMS causes enhancement of damping in the lower frequency regime [44, 14]. Specifically, TMS is a bulk effect and also its magnitude depends on the angle of the magnetization with respect to IP crystallographic axis (if any). In our experiments we have found that effective damping increases as frequency decreases and with different bias magnetic field orientation the slopes are different. This qualitatively indicates that the contribution from TMS can be present in the damping values. Here, the natural damping of Kittel mode for Gd-Fe system is expected to be less compared to the highest intensity mode. But the presence of other modes in the system is causing additional dephasing and effectively increases the intrinsic damping. Figure 5.7 shows that the decay time of the Kittel mode for 20-nm-thick film does not vary much with precessional frequency [44]. However in IP and

tilted configuration the corresponding decrease in τ of the Kittel mode (mode 1) for the 100-nm-thick film indicates an energy transfer from the uniform Kittel mode to the PSSW mode [15]. Thus, τ of the PSSW mode increases with increasing frequency. The absence of PSSW modes in the lower field regime could be due to the presence of TMS, caused by the magnetic inhomogeneities in the film [34, 45]. Higher value of damping can suppress the unwanted ringing after a precessional switching. On the other hand, lower damping is advantageous for long distance SW propagation and smaller write-current in STT-MRAM devices. The observed tunability of damping in the Gd-Fe system over a broad range by bias magnetic field variation can thus be important for the above possible applications.

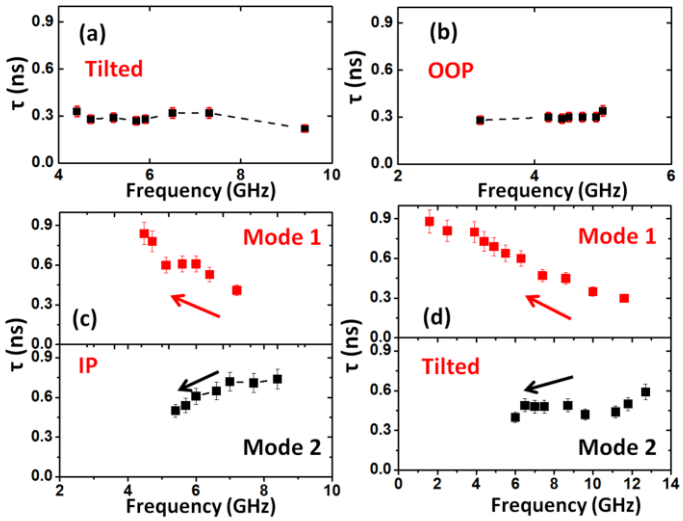

Figure 5.7: The variation of decay time (τ) with precessional frequency of mode 1 (Kittel mode) for the Gd-Fe film with thickness, d = 20 nm in (a) tilted and (b) OOP configuration. Variation of τ for mode 1 and mode 2 for the Gd-Fe film with thickness, d = 100 nm in (c) IP and (d) tilted configuration is shown. The arrow indicates an opposite trend in the variation of τ. The dotted lines are guide to eye.

5.4 Conclusions

A systematic investigation of ultrafast magnetization dynamics has been presented for Gd-Fe thin films of different thicknesses. The demagnetization time was found to be about 300 fs for these thin films. A special emphasis has been provided to the study of precessional magnetization dynamics as a function of magnitude and orientation of the bias magnetic field. Our time-resolved results show a development of weak OOP

anisotropy with increasing film thickness which is complemented by static magnetization measurements. A large tunability of effective damping of the system has been obtained with the variation in bias magnetic field which could be due to extrinsic effects such as, TMS, magnetic inhomogeneity, impurity scattering and multimodal dephasing. The presence of higher order PSSW modes along with the uniform Kittel mode was evidenced for the 100-nm-thick film. Inter-mode energy transfer from PSSW modes to uniform Kittel mode is found to be a possible mechanism behind the modification of decay times for the thicker film. The extensive study of magnetization dynamics presented here may lead to development of magnonic and spintronic devices based on RE-TM thin films.

References

1. J. A. Katine, F. J. Albert, R. A. Buhrman, E. B. Myers, and D. C. Ralph, Phys. Rev. Lett. **84**, 3149 (2000).
2. H. Ohno, D. Chiba, F. Matsukura, T. Omiya, E. Abe, T. Dieti, Y. Ohno, and K. Ohtani, Nature **408**, 944 (2000).
3. C. D. Stanciu, F. Hansteen, A. Kimel, A. Kirilyuk, A. Tsukamoto, A. Itoh and Th. Rasing, Phys. Rev. Lett. **99**, 047601 (2007).
4. T. Gerrits, H. A. M. van den Berg, J. Hohlfeld, L. Bär, and Th. Rasing, Nature **418**, 509 (2002).
5. S. Kaka and S. E. Russek, Appl. Phys. Lett. **80**, 2958 (2002).
6. H. Schumacher, C. Chappert, P. Crozat, R. C. Sousa, P. P. Freitas, J. Miltat, J. Fassbender, and B. Hillerbrands, Phys. Rev. Lett. **90**, 017201 (2003).
7. E. Beaurepaire, J.-C. Merle, A. Daunois, and J.-Y. Bigot, Phys. Rev. Lett. **76**, 4250 (1996).
8. C. D. Stanciu, A. V. Kimel, F. Hansteen, A. Tsukamoto, A. Itoh, A. Kirilyuk, and Th. Rasing, Phys. Rev. B **73,** 220402 (R) (2006).
9. C.-H. Lambert, S. Mangin, B. S. D. Ch. S. Varaprasad, Y. K. Takahashi, M. Hehn, M. Cinchetti, G. Malinowski, K. Hono, Y. Fainman, M. Aeschilmann, and E. E. Fullerton, Science **345**, 1337 (2014).
10. S. Mangin, M. Gottwald, C.-H. Lambert, D. Steli, V. Uhlíř, L. Pang, M. Hehn, S. Alebrand, M. Cinchetti, G. Malinowski, Y. Fainman, M. Aeschilmann, and E. E. Fullerton, Nat. Mater. **13**, 286 (2014).

11. M. van Kampen, C. Jozsa, J. T. Kohlhepp, P. LeClair, L. Lagae, W. J. M. de Jonge, and B. Koopmans, Phys. Rev. Lett. **88**, 227201 (2002).
12. A. Barman and J. Sinha, *Spin dynamics and damping in ferromagnetic thin films and nanostructures* (Springer, Switzerland, 2018).
13. A. Barman, and A. Haldar, *Time-domain study of magnetization dynamics in magnetic thin films and micro-and nanostructures.* Solid State Phys, vol **65**. (Elsevier Inc., Burlington, 2014).
14. G. Woltersdorf, M. Buess, B. Heinrich, and C. H. Back, Phys. Rev. Lett. **95**, 037401 (2005).
15. S. N. Panda, S. Mondal, J. Sinha, S. Choudhury, and A. Barman, Sci. Adv. **5**, eaav7200 (2019).
16. Y. Zhao, Q. Song, S. H. Yang, T. Su, W. Yuan, S. S. P. Parkin, J. Shi, and W. Han, Sci. Rep. **6**, 22890 (2016).
17. S. Mondal, S. Choudhury, N. Jha, A. Ganguly, J. Sinha, and A. Barman, Phys. Rev. B **96**, 054414 (2017).
18. G. M. Muller, M. Munzenberg, G.-X. Miao, and A. Gupta, Phys. Rev. B **77**, 020412(R) (2008).
19. S. Mondal, and A. Barman, Phys. Rev. Appl. **10**, 054037 (2018).
20. A. Kirilyuk, A. V. Kimel, and Th. Rasing, Rep. Prog. Phys. **76**, 026501 (2013).
21. A. R. Khorsand, M. Savoini, A. Kirilyuk, A. V. Kimel, A. Tsukamoto, A. Itoh, and Th. Rasing, Phys. Rev. Lett. **110**, 107205 (2013).
22. I. Radu, K. Vahaplar, C. Stamm, T. Kachel, N. Pontius, H. A. Durr, T. A. Ostler, J. Barker, R. F. L. Evans, R. W. Chantrell, A. Tsukamoto, A. Itoh, A. Kirilyuk, Th. Rasing, and A. V. Kimel, Nature **472**, 205-208 (2011).
23. J. Sizeland, Ph.D Thesis, *Crystallographic and magneto-dynamic characterization of thin film spintronic materials*, University of York, U.K, 2015.
24. J. Miguel, Ph.D Thesis, *Static and dynamic X-ray resonant magnetic scattering studies on magnetic domains*, University of Amsterdam, The Netherlands, 2015.
25. J. C. Suits, R. D. Rugar, and C. J. Lin, J. Appl. Phys. **64**, 252 (1988).
26. W. H. Meiklejohn, Magnetooptics: a thermomagnetic recording technology, Proc. IEEE **74**, 1570 (1986).
27. A. K. Biswas, H. Ahmad, J. Atulasimha, and S. Bandyopadhyay, Nano Lett. **17**, 6, 3478 (2017).

28. S. Mondal, M. A. Abeed, K. Dutta, A. De, S. Sahoo, A. Barman, and S. Bandyopadhyay, ACS Appl. Mater. Interfaces **10**, 50, 43970 (2018).
29. J. Becker, A. Tsukamoto, A. Kirilyuk, J. C. Maan, Th. Rasing, P. C. M. Christianen, and A. V. Kimel, Phys. Rev. B **92**, 180407 (R) (2015).
30. R. Salikhov, A. Alekhin, T. Parpiiev, T. Pezeril, D. Makarov, R. Abrudan, R. Meckenstock, F. Radu, M. Farle, H. Zabel, and V. V. Temnov, Phys. Rev. B **99**, 104412 (2019).
31. K. Nishibayashi, K. Kuga, and H. Munekata, AIP Adv. **3**, 032107 (2013)
32. J. Miguel, J. F. Peters, O. M. Toulemonde, S. S. Dhesi, N. B. Brookes, and J. B. Goedkoop, Phys. Rev. B **74,** 094437 (2006).
33. A. Talapatra, J. Arout Chelvane, and J. Mohanty, J. Magn. Magn. Mater. **448**, 360-366 (2018).
34. A. Talapatra, J. Arout Chelvane, B. Satpati, S. Kumar, and J. Mohanty, J. Alloy. Comp. **774**, 1059-1068 (2019).
35. A. Talapatra, J. Arout Chelvane and J. Mohanty, J. Magn. Magn. Mater. 489, 165469 (2019).
36. B. Hebler, A. Hassdenteufel, P. Reinhardt, H. Karl, and M. Albrecht, Front. Mater. **3**, 8 (2016).
37. A. Talapatra, J. Arout Chelvane, and J. Mohanty, AIP Conf. Proc. **1832**, 130044 (2017).
38. F. Dalla Longa, J. T. Kohlhepp, W. J. M. de Jonge, and B. Koopmans, Phys. Rev. B **75**, 224431 (2007).
39. I. Radu, C. Stamm, A. Eschenlohr, F. Radu, R. Abrudan, K. Vahaplar, T. Kachel, N. Pontius, R. Mitzner, K. Holldack, A. Fohlisch, T. A. Ostler, J. H. Mentink, R. F. L. Evans, R. W. Chantrell, A. Tsukamoto, A. Itoh, A. Kirilyuk, A. V. Kimel, and Th. Rasing, Spin **5**, 1550004 (2015).
40. S. Mizukami, H. Abe, D. Watanabe, M. Oogane, Y. Ando, and T. Miyazaki, Appl. Phys. Exp. **1**, 121301 (2008).
41. S. Pal, B. Rana, O. Hellwig, T. Thompson, and A. Barman, Appl. Phys. Lett. **98**, 082501 (2011).
42. B. Samantaray, A. K. Singh, C. Banerjee, A. Barman, A. Perumal, and P. Mandal, IEEE. Trans. Magn. **52**, 2003104 (2016)

43. J. Walowski, M. D. Kaufmann, B. Lenk, C. Hamann, J. McCord, and M. Münzenberg, J. Phys. D: Appl. Phys. **41**, 164016 (2008).
44. Z. Chen, Y. Yan, S. Li, X. Xu, Y. Jiang, and T. Lai, Sci. Rep. **7**, 42513 (2017).
45. X. Lu, L. J. Atkinson, B. Kuerbanjiang, B. Liu, G. Li, Y. Wang, J. Wang, X. Ruan, J. Wu, R. F. L. Evans, V. K. Lazarov, R. W. Chantrell, and Y. Xu, Appl. Phys. Lett. **114**, 192406 (2019).

Chapter 6

6 Transition from strongly collective to completely isolated ultrafast magnetization dynamics in two dimensional hexagonal arrays of nanodots with varying inter-dot separation

6.1 Introduction

Magnonics is a young research field which deals with the generation and manipulation of spin waves (SWs) in periodically modulated ferromagnetic materials. Magnonic Crystals [1-6] (MCs) are the magnetic analogue of photonic and phononic crystals, which possess interesting properties arising from the frequency band structure of SWs. The use of SWs may offer high energy efficiency, reconfigurability [7] and higher storage density of magnetic storage device [8]. Recent advancements in nanoscience have opened up new possibilities to tune the SWs through miniaturization and manipulation of MCs. Various sophisticated techniques for patterning and tailoring of ferromagnetic materials from two-dimensional thin films to zero-dimensional nanocrystals [9] and nanomagnets [10], have been nurtured. Ferromagnetic nanodot arrays are potential candidates for magnonic crystals as well as magnetic bit patterned media (BPM) [11,12]. For construction of BPM, an essential criterion is to eliminate cross-talk or temporal overlapping of information between the bits. For that purpose, the magnetic islands where the bits are supposed to be stored, must be non-interactive. However, in SW filters or logic devices [13], long wavelength collective SWs must be guided through the patterned nanostructures where individual nanoelements maintain constant phase and amplitude relationships with their neighbours. Both of these purposes can be solved by perceptive usage of patterned nanodot arrays with different inter-dot separations. Nanodots are capable of making some uncoupled resonators while one can couple them through magnetostatic interactions by varying their inter-dot separations. In general, in a ferromagnetic material, spins are exchange coupled. But for the nanodot

arrays, as the inter-dot separation is much larger compared to the exchange length of the material, the spins near the edges of the nanodots are exchange decoupled. The dots experience magnetic coupling via magnetostatic stray fields and one can observe collective behavior of the SWs through the whole array [14-16]. Further increase in separation between the dots will cease the collective behavior and individual dynamics of each dot get exposed. To explore the potentiality of these multitasking nanodots in novel computing devices, studies of their static and dynamic magnetization properties have become extremely popular in the scientific community. A new term 'photo-magnonics' related to the excitation and detection of SWs using light, has been disseminated. Static magnetization properties of nanomagnets with different configurations have been studied using static magneto-optical Kerr effect (MOKE) microscopy [17,18]. On the other hand study of magnetization dynamics of nanomagnet arrays have also been reported by time-resolved magneto optical Kerr effect microscopy (TR-MOKE) [6,14,16,19-22] ferromagnetic resonance (FMR) [18,23,24] and Brillouin light scattering (BLS) [25-27] techniques. Beside these experimental techniques, numerical simulations have been used for the development of nanomagnet based computing [28,29]. A detailed study on ferromagnetic nanodot arrays revealed that the response of the nanomagnets to the external pulsed magnetic field becomes non-uniform for the dot size smaller than 220 nm [30]. This may cause degradation of signal to noise ratio in future nanomagnet based devices. The quest to overcome the problem of miniaturization of nanomagnet based devices has motivated us to study the precessional dynamics of the systems which consist of circular permalloy ($Ni_{80}Fe_{20}$) nanodots of 100 nm in diameter, arranged in close packed hexagonal lattice symmetry with varying inter-dot separation. Here, all-optical TR-MOKE microscopy is used to excite and detect the magnetization dynamics including SWs. The time-resolved magnetization dynamics contains ultrafast demagnetization followed by two step relaxation processes with damped precession. Though the magnetization dynamics of nanodots having different sizes and shapes arranged in different lattice symmetries have already been reported [6,31-33] but the effect of variation of areal density on SW spectra in hexagonal arrays of nanodots has hitherto not been investigated. We observe a clear variation in the SW dynamics associated with a gradual transition from a strongly collective to a completely isolated dynamical behavior with the variation of the inter-dot separation, which is clearly different from what was observed in square lattice

symmetry [16,32]. Finally, when the inter-dot separation becomes 290 nm or greater, the magnetostatic interaction becomes negligible, which enabled us to probe the magnetization dynamics of a single circular nanodot of 100 nm in diameter by using an all-optical technique. Our experimental findings, along with the numerical analyses, can promote this kind of systems to be promising candidates for construction of magnetic storage, memory and magnonic devices.

6.2 Experimental Details

Two-dimensional $Ni_{80}Fe_{20}$ (permalloy) dot arrays (each with total area of 10 μm × 10 μm) with dot diameter of 100 nm, dot thickness of 20 nm and with varying lattice constants arranged in hexagonal symmetry were prepared by a combination of electron-beam evaporation and electron-beam lithography. The beam current used during electron-beam lithography is 100 pA for a dose time of 1.0 μs. A bilayer MMA/PMMA (methyl methacrylate/poly methyl methacrylate) resist pattern was first prepared on self-oxidized Si(100) substrate by using electron-beam lithography and permalloy was deposited on the resist pattern by electron-beam evaporation at a base pressure of about 1.3×10^{-7} Torr. A 5-nm-thick Al_2O_3 capping layer was deposited on top of the permalloy layer to protect the dots from external contamination in the environment as well as degradation with time. Besides that, the capping layer secures the permalloy surface from exposure to the femtosecond laser during optical pump-probe experiments in air. This was followed by the lifting off of the sacrificial material and oxygen plasma cleaning of the residual resists that remained after the lift-off process. The lattice parameters a and b are varied while γ is kept constant at 120^0 for the hexagonal lattice as shown in Fig. 6.1 (a) and the unit cell is also marked in that figure. The lattice constant a, is related to the interdot separation S by $a = d + S$. From the scanning electron micrographs, we obtained the values of (a, b) as (130, 120), (180, 200), (220, 240), (260, 290), (310, 315), (390, 420), and (490, 520) while γ is obtained as 120 ± 2°, as S is varied from 30 to 390 nm. About ±5% deviation in dot diameter and lattice constant is observed in the micrographs. The size of the dot is chosen so that it can accommodate the characteristic edge and centre modes precession [6,32]. Considering the measured values of a, b and γ from the micrographs, we found that the number of unit cells vary from about 72 × 72 for a = 130 nm to about 20 × 20 for a = 490

nm. For convenience, the arrays will be described only by the lattice constant *a*, from here on.

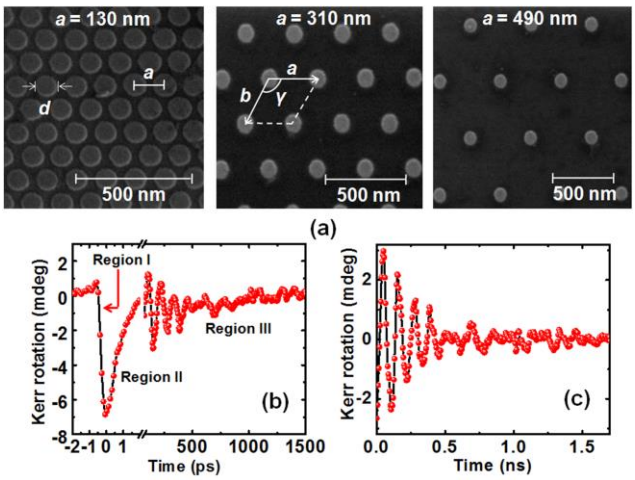

Figure 6.1: (a) Scanning electron micrographs of the permalloy dot arrays with dot diameter (*d*) = 100 nm, thickness = 20 nm, arranged in hexagonal lattice with varying lattice constants, *a* = 130 nm, *b* = 120 nm; *a* = 310 nm, *b* = 315 nm; and *a* = 490 nm, *b* = 520 nm. The dot diameter and lattice constants are shown in the micrographs along with the length scales. The unit cell is marked inside the lattice. (b) Typical time-resolved Kerr rotation data for the array with *a* = 180 nm for *H* = 1.3 kOe. (c) Background subtracted time-resolved data.

To study the time-resolved magnetization dynamics of these nanodot arrays we used a custom-build TR-MOKE microscope [32,34]. This technique is based upon a two-colour collinear optical pump-probe geometry. Here, the second harmonic (λ_b = 400 nm, power = 10 mW, pulse width = 100 fs) of the fundamental laser beam from a mode-locked Ti:sapphire laser (Tsunami, Spectra physics) is used to pump the sample by creating a population of hot electrons. This causes a modification of spin population by spin dependent electron scattering process. The fundamental beam (λ_a = 800 nm, power = 2mW, pulse width = 80 fs) is used to probe the time varying polar Kerr rotation from the samples. A delay stage situated at the probe path is used to create the necessary time delay with temporal resolution of about 100 fs limited by the cross-correlation of the pump and the probe beams. Finally, both the beams are combined together and focused at the centre of the array by a microscope objective (N.A. = 0.65) in a collinear fashion. The probe beam with spot diameter of about 800 nm is tightly focused and overlapped with the pump having a larger diameter (≈ 1 μm), at the centre of the array. Under this condition the probe can collect information from the uniformly excited part

of the sample. This allows us to measure upto a maximum of 65 elements for the array with smallest lattice constant, whereas a single element was probed for the largest lattice constant. The sample is scanned under the focused pump and probe beams by mounting it on a piezoelectric scanning stage (x-y-z), which gives high stability to the sample in presence of feedback loops. A static magnetic field is applied at a small angle (~15°) to the sample plane, the in-plane component of which is defined as the bias field H. The time varying polar Kerr rotation is measured at room temperature by using an optical bridge detector and a lock-in amplifier in a phase sensitive manner. The pump beam is modulated at 2 kHz frequency, which is used as the reference frequency of the lock-in amplifier. This detection technique completely isolates the Kerr rotation and reflectivity signals. Figure 6.1 (b) shows a typical raw data of time-resolved Kerr rotation from the array with a = 180 nm. Here, the ultrafast demagnetization (region l) occurs within first 500 fs from the zero delay, followed by fast (region II) and slow (region III) relaxation processes having relaxation time of 1.3 ps and 700 ps, respectively. The precessional magnetization dynamics is observed as an oscillatory signal on the slowly decaying part of the time-resolved data. Figure 6.1 (c) shows the time-resolved data after removing the negative delay and ultrafast demagnetization and subtracting a bi-exponential background. Fast Fourier transform (FFT) is performed over this background subtracted data to obtain the power vs. frequency plot. The measurement time window of 1.7 ns is found to be sufficient for resolving the SW spectra in these systems. Although the number of nanodots probed under the focused laser spot varied from about 65 to 1 with increasing areal density, we have improved the sensitivity of our equipment to the extent that even the single dot dynamics is measured with good signal/noise ratio.

6.3 Results and Discussions

Figures 6.2 (a) and (b) show the background subtracted experimental time-resolved Kerr rotation data with corresponding FFT power spectra for nanodot arrays with different lattice constants. From the experimental data, a clear variation in the magnetization dynamics is observed with varying lattice constant. Damped nonuniform oscillations consisting of multiple frequency precessional modes are observed for all lattice constants. The corresponding power spectra (Fig. 6.2 (b)) show the presence of three clear SW modes for 130 nm ≤ a ≤ 310 nm. However, there is a sudden downshift

in frequencies of all three modes as a changes from 130 to 180 nm, indicating a change in the collective nature of the dynamics. Beyond this, the mode frequencies remain nearly unaltered while the relative intensities and linewidths of the modes change with the increase in lattice constant, indicating a change in the relative powers of the modes. For $a \geq 390$ nm, another drastic change occurs and instead of three modes, only two modes are observed. While mode 1 retains its position, mode 2 merges with mode 3 to form a single mode. Consequently, we observe a clear transition from a collective dynamical regime to an isolated regime of dynamics with the variation of lattice constant.

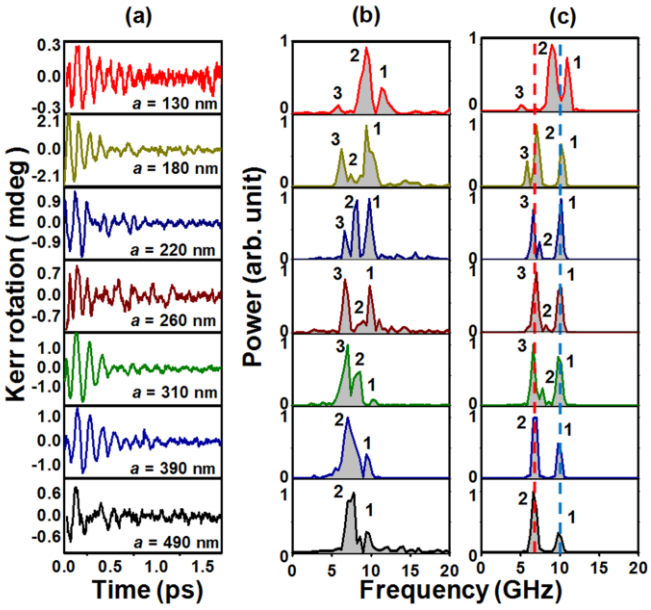

Figure 6.2: (a) Experimental time-resolved Kerr rotation data and (b) corresponding FFT power spectra are shown for the permalloy nanodot lattices arranged in hexagonal symmetry with lattice constant (a) varying from 130 nm to 490 nm at H = 1.3 kOe. (c) FFT power spectra of simulated time-domain magnetization. Mode numbers are shown in both experimental and simulated power spectra. The red and blue dashed vertical lines indicate the positions of edge and centre modes of a single permalloy dot with diameter (d) = 100 nm and thickness = 20 nm.

We further reproduce our experimental data by micromagnetic simulations using OOMMF software [35]. The experimental technique is based on optical excitation of magnetization but in the simulation this is achieved by applying a pulsed magnetic field, which reproduces the experimental conditions successfully. The details of simulation can be found elsewhere [21]. The samples were discretized into rectangular prisms of dimensions 2 × 2 × 20 nm^3 where the lateral cell size is well below the exchange length of permalloy (~5.2 nm). Material parameters used for permalloy were gyromagnetic

ratio γ' = 18.5 MHz/Oe, anisotropy field H_k = 0, saturation magnetization M_s = 860 emu/cc, and exchange stiffness constant $A = 1.3 \times 10^{-6}$ erg/cm. The material parameters were extracted by measuring the variation of precessional frequency (f) with bias field for a permalloy thin film and by fitting them using Kittel formula,

$$f = \frac{\gamma'}{2\pi}\sqrt{(H + H_k)(H + H_k + 4\pi M)} \tag{6.1}$$

The exchange stiffness constant A is obtained from literature [36]. In OOMMF simulation, at first the static magnetic configuration was obtained by applying a large magnetic field to saturate the sample magnetization and then by reducing the magnetic field to bias field value. The system was allowed to reach the equilibrium (maximum torque $\boldsymbol{m} \times \boldsymbol{H}$, where $m = M/M_s$ goes well below 10^6 A/m). The magnetization dynamics was simulated by applying a pulsed magnetic field. Calculation of the spatial maps of magnetization at time steps of 10 ps was done for a total duration of 4 ns.

Although the simulation reproduced the main observed features qualitatively (Fig. 6.2 (c)), the quantitative disagreement appears due to some limitations in the simulation such as edge roughness and statistical differences in sizes and shapes between the experimental and simulated nanodots. The average disagreement between the simulated and experimental SW frequencies is maximum (12%) for arrays with higher lattice constants due to the reduction in the amount of magnetic materials, which reduces the signal/noise ratio. Finally, for $a \geq 390$ nm, dynamics of a single nanodot of diameter 100 nm is probed. The magnetization in the dot edges gets randomized and affect the stray field distribution around the dot. This leads to the modification of some conventional SW modes in the experimental power spectra and appearance of some other localized modes due to the pinning in magnetization. As a reference, we have also simulated the magnetization dynamics of a single circular nanodot of diameter 100 nm and thickness 20 nm, which reveals two distinct precessional modes. The positions of those two modes are shown by the dotted lines in Fig. 6.2 (c). It is clearly visible from the figure that at higher lattice constants ($a \geq 390$ nm) the frequency values of SW modes of the nanodot array are nearly identical to those for a the single circular nanodot of diameter 100 nm.

Figures 6.3 (a), (b) show the bias field dependences of SW frequencies extracted from the experimental and simulated results for a = 180 and 390 nm, respectively. The

simulated data points corresponding to modes 1, 2 and 3 in Fig. 6.3 (a) are well fitted with Kittel formula. The simulated frequencies are quantitatively slightly different as compared to the experimental frequencies. This is probably due to the unavoidable contribution from the randomized magnetization at the rough edges of the dots, which could not be incorporated in the simulation. The extracted magnetic parameters from the fits are similar to those found earlier for the permalloy thin film except for the saturation magnetization. For the array with a = 180 nm, we obtained M_s values as 700 emu/cc, 274 emu/cc and 153 emu/cc for modes 1, 2 and 3, respectively (Fig. 6.3 (a)). As a is increased to 390 nm, we obtain M_s values as 655 emu/cc and 226 emu/cc for modes 1 and 2, respectively.

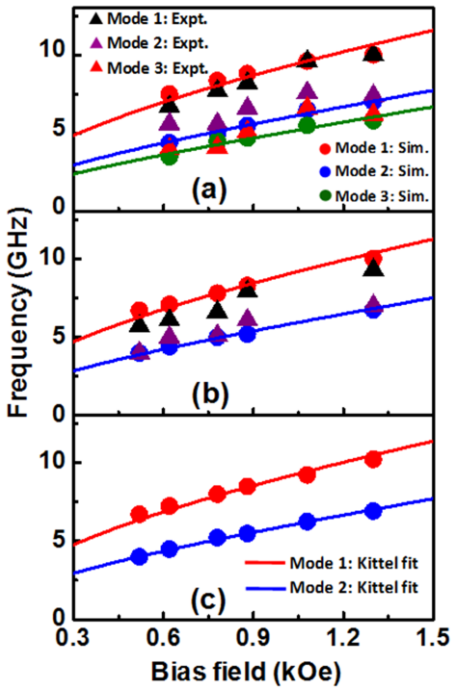

Figure 6.3: Bias field dependence of precessional frequencies of different SW modes for permalloy nanodot lattices arranged in hexagonal symmetry with (a) a = 180 nm, (b) a = 390 nm and (c) single permalloy dot with diameter = 100 nm and thickness 20 nm (triangular symbols: experimental data, circular symbols: micromagnetic simulation results, solid line: Kittel fit) are plotted as a function of H.

In ref. 6 we already showed that for the array with a = 130 nm, M_s values were obtained as 860 emu/cc and 560 emu/cc for modes 1 and 2, respectively. For a comparison, we simulated the dynamics of single circular permalloy nanodot with 100 nm diameter and 20 nm thickness and the field dependences of its precession frequencies are shown in Fig. 6.3 (c). The extracted M_s values from the Kittel fit of the field variation of the centre

and edge modes of the single nanodot are 672 emu/cc and 243 emu/cc, respectively. From the above results, we understand that when the nanodots are densely packed in an array (a = 130 nm), they show a strongly collective magnetization dynamics and the uniform mode (mode 1) is showing a behavior similar to the precessional mode of a continuous thin film (M_s = 860 emu/cc). As we increase the inter-dot separation, we enter into weakly collective dynamics and the effective saturation magnetization for the resonant modes reduces due to the reduction in the inter-dot interaction field, and as we increase the inter-dot separation further to $a \geq 390$ nm, we enter into a regime of dynamics of isolated dots with effective M_s values similar to that of a single nanodot. The degradation in precessional signal quality with decrease in areal density introduces line broadening in the FFT spectra. So the simulated data points in Fig. 6.3 (b) qualitatively follow the trend of experimental results but there is quantitative disagreement between the two.

We have further simulated the power and phase maps of various observed SW modes by using a home built code [37] as shown in Fig. 6.4. The spatial profiles of the power and phase information for various modes are obtained by fixing one of the spatial coordinates in the space and time-dependent magnetization and then by performing a discrete Fourier transform with respect to time domain [37]. It is well known that for the single circular nanodot the higher and lower frequency modes correspond to the centre and edge modes [6,32]. The SW spectra for array with a = 180 nm showed a drastic change from that for a = 130 nm, indicating a change in the collective nature of the mode. This was further confirmed from the bias field dependence of the mode frequencies.

Figure 6.4 (a) shows although the natures of mode 1 is similar to that for a = 130 nm, there are indeed some changes in modes 2 and 3. Instead of a backward volume-like collective mode of the array, mode 2 here corresponds to a nearly uniform distribution of the edge modes of the dots in the array. On the other hand, the bow-tie like mode (mode 3) as observed in a = 130 nm [6] is now transformed to a collective edge mode of the array for a = 180 nm. With increasing lattice constant (a), the strength of collective nature of SW spectra reduces further causing a sudden change in the nature of modes. A new collective SW mode (mode 2) appears with its frequency in between that of the uniform distribution of conventional edge mode (mode 3) and centre mode (mode 1)

over the array as shown for a = 310 nm in Fig. 6.4 (b). Here, mode 2 corresponds to a non-uniform collective mode with power of the SW mode concentrated along each alternative column as shown by the dotted boxes. The phase profile shows that the spins precess in phase within the dotted boxes but the spins of two consecutive columns are out of phase with each other.

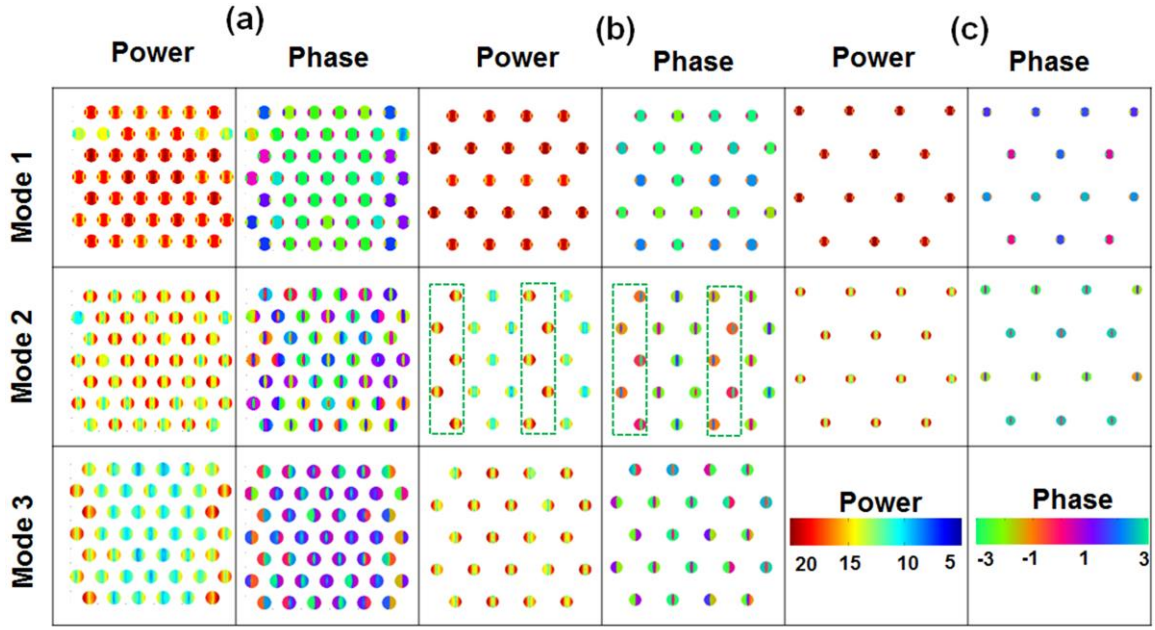

Figure 6.4: The power and phase maps for different collective SW modes of permalloy dot lattices arranged in hexagonal symmetry with lattice constants (a) a = 180 nm, (b) a = 310 nm and (c) a = 490 nm at a bias field of H = 1.3 kOe. The colour bars of power and phase maps are shown at the bottom right corner of the image. Sizes of the dots are not in scale.

Thus, it forms collective backward volume like standing SW mode directed along the applied bias field. With further increase in lattice constant the dynamics enters into an isolated regime, which is also clear from the SW mode profiles. For the sample with a = 490 nm (Fig. 6.4 (c)) modes 1 and 2 correspond to the centre and edge modes, respectively which are distributed uniformly over entire lattice. These modes have same frequencies and mode profiles as a single nanodot.

We further simulated the SW mode profiles for samples with a = 180 and 310 nm at two different magnetic fields to understand how the collective behavior is affected by the bias field.

Figures 6.5 (a) and (b) show that for the array with a = 180 nm, the nature of all three modes remain qualitatively same when the bias field is reduced from 1.3 kOe to 0.62 kOe. Only the power in the edges of the dots gets stronger for mode 2 for the lower field value as the contribution from stray field becomes more prominent when the bias field is weaker. Similarly, Figs. 6.5 (c) and (d) show that for a = 390 nm, two distinct modes remain same as centre mode and edge mode of the whole array with the reduction of bias magnetic field. Hence, a variation of bias magnetic field does not cause a transition between different collective regimes but only causes small changes in the relative powers of the modes.

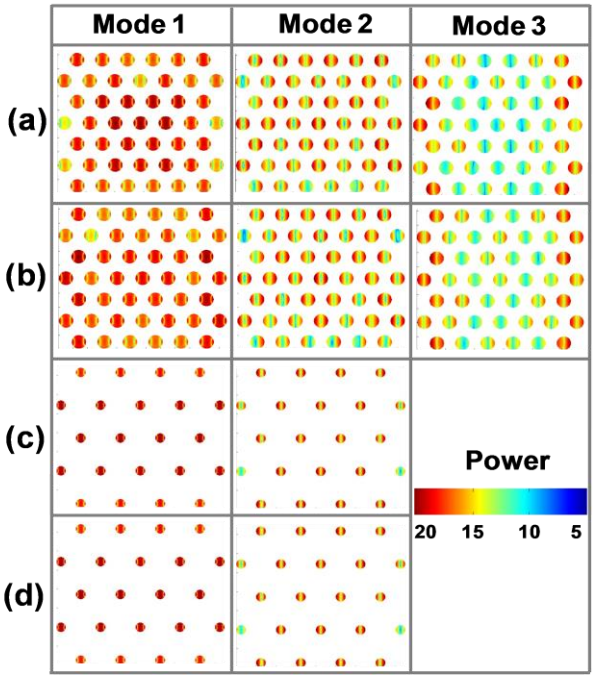

Figure 6.5: The power maps of collective SW modes in permalloy nanodot arrays with lattice constants (a), (b) a = 180 nm and (c), (d) a = 390 nm. The applied bias fields are H = 0.78 kOe ((a), (c)), 0.62 kOe (b) and 0.52 kOe (d). The colour bar of power profile is shown at the bottom right corner of the image. Sizes of the dots are not in scale.

To gain more insight into the dynamics, we have simulated the magnetostatic field distribution of the arrays by using LLG micromagnetic simulator as shown in Fig. 6.6. The contour plots of the magnetostatic fields show that dipolar contribution from the magnetostatic stray field dominates for all arrays but the density of the interacting field lines reduces significantly with the increase in lattice constant and nearly vanishes for higher lattice constants (Figure 6.6 (c)). Consequently, the dynamics of arrays of higher lattice constants are similar to that of a single circular nanodot of diameter 100 nm.

To quantify the inter-dot interaction, we took line scans along the solid red lines as shown in Figs 6.6 (a) – (c) plotted in Fig. 6.7 (a). For a = 130 nm, the magnitude of stray field between two consecutive dots is maximum (~3500 Oe), which sharply decreases with the increase in the lattice constant and becomes negligibly small for a > 310 nm. The inter-dot interactions across the arrays are modelled simply by considering arrays of nanomagnets behaving like parallely placed magnetic dipoles. Considering the center to center distance (r) between two consecutive nanomagnets (as shown in the inset of Fig. 6.7 (b)) as the lattice constant (a) of the array, the magnetic field (B) of a coupled dipole system orienting in same direction can be expressed as,

$$B \propto \frac{1}{r^3} \tag{6.2}$$

Fig. 6.7 (b) shows a good fit of the variation of simulated magnetostaic stray field with lattice constant using equation (6.2).

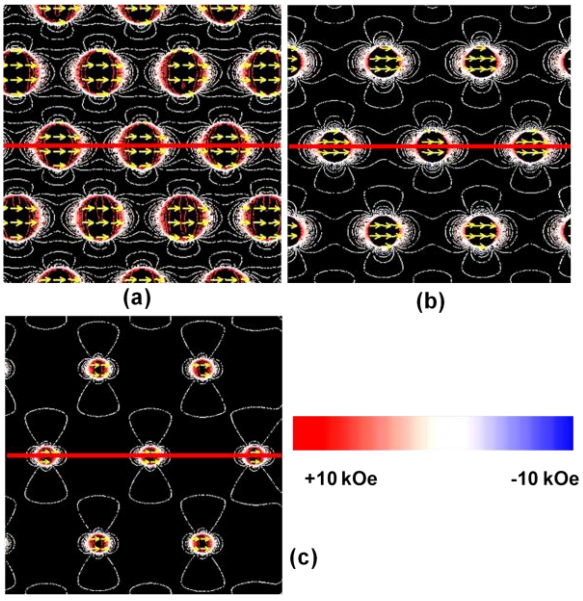

Figure 6.6: The contour maps of simulated magnetostatic field distribution (x component) are shown for permalloy nanodot arrays arranged in hexagonal symmetry with lattice constants of (a) a = 180 nm, (b) a = 310 nm and (c) a = 490 nm. The arrows inside the dots represent the magnetization states of the dots and the strength of magnetostatic field is represented by the colour bar given at the bottom right corner of the figure. The red horizontal lines represent the position of the lattice from where the line scans have been taken. Sizes of the dots are not in scale.

This indicates that the inter-dot interaction is of purely dipolar in nature as opposed to square nanodots, which showed quadrupolar interaction to be dominant [21]. From Fig. 6.6 (b), it is clear that at a = 130 nm, the system is strongly coupled via magnetostatic interaction which can guide a broad spectrum of long wavelength SW to carry and process information. Hence, they can be considered as promising candidate for magnonics applications, whereas for a > 310 nm, the arrays behave like magnetostatically isolated dots, which can be used to store bits, free from any external disturbances.

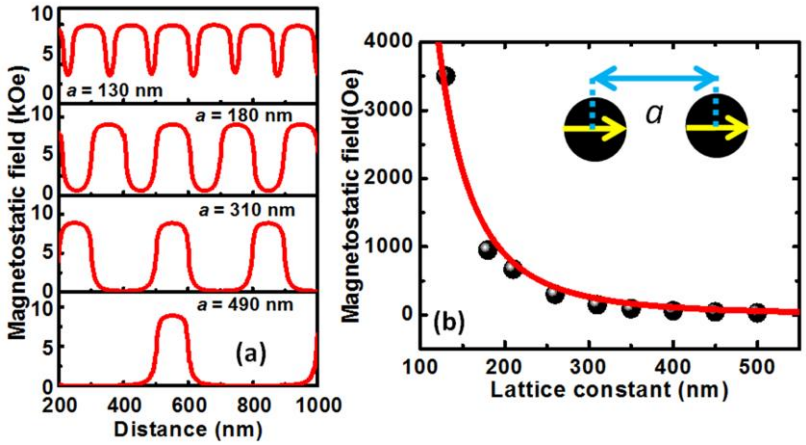

Figure 6.7: (a) Line scans of simulated magnetostatic fields from the arrays with different lattice constants (a) as obtained from the positions indicated by horizontal solid lines (as shown in Fig. 6.6). (b) The variation of magnetostatic stray field with the lattice constant (circular symbols: micromagnetic simulation, solid line: fitted curve). The schematic of the dipolar coupled dots is shown in the inset.

6.4 Conclusions

In essence, we have investigated the variation in collective magnetization dynamics in permalloy circular nanodot arrays arranged in hexagonal symmetry with systematic variation of inter-dot separation, by using time-resolved Kerr microscopy. The experimental results along with the numerical analysis, reveal that the nature of magnetization dynamics gets modified significantly with inter-dot separation. For smaller separation, the dots in the array strongly interact with each other leading towards a strongly collective dynamics with modes different from the modes of the individual nanodots. With the increase in inter-dot separation the dynamics goes

through weakly collective regimes with the appearance of new modes in addition to the uniform distribution of the centre and edge modes of the individual dots in the array. At larger separation the system enters into an isolated regime with only the modes of the individual nanodots. Further, the bias field dependence of the SW modes reveals that the modes are robust enough to sustain the variation in external bias field. No qualitative changes are observed with the decreasing bias field values barring a variation in relative powers of the modes. These salient features of dot arrays with hexagonal lattice symmetry can make them viable for construction of various nanomagnet based devices. For smaller separations the arrays can be used as SW band-pass filter in GHz regime whereas for higher lattice constants, reduction in magnetostatic coupling strength makes these nanodot arrays suitable for storing information within them. Besides these, the dots in the arrays, are arranged in hexagonal lattice symmetry which is the most closely packed structure. Consequently, they will be capable of maintaining reasonable signal to noise ratio for much smaller nanodots leading towards their potential applications. The above experimental findings along with circumstantial numerical analyses have a pragmatic approach towards the development of nanomagnonic devices and patterned magnetic media.

References

1. V. V. Kruglyak, S. O. Demokritov and D. Grundler, J. Phys. D: Appl. Phys., 2010, **43**, 264001.
2. B. Lenk, H. Ulrichs, F. Grabs and M. Munzenberg, Phys. Rep., 2011, **507**, 107.
3. S. A. Nikitov, Ph. Tailhades and C. S. Tsai, J. Magn. Magn. Mater., 2001, **236**, 320.
4. A. V. Chumak, A. A. Segra, B. Hillebrands and M.P. Kostylev, Appl. Phys. Lett., 2008, **93**, 022508.
5. Z. K. Wang, V. L. Zhang, H. S. Lim, S. C. Ng, M. H. Kuok, S. Jain and A. O. Adeyeye, ACS Nano, 2010, **4**, 643.
6. S. Saha, R. Mandal, S. Barman, D. Kumar, B. Rana, Y. Fukuma, S. Sugimoto, Y. Otani and A. Barman, Adv. Funct. Mater., 2013, **23**, 2378.
7. J. Topp, D. Heitmann, M.P. Kostylev and D. Grundler, Phys. Rev. Lett., 2010, **104**, 207205.
8. M. Krawczyk and D. Grundler, J. Phys.: Condens. Matter, 2014, **26**, 123202.
9. C. T. Black, C. B. Murray, R. L. Sandstrom and S. Sun, Science, 2000, **290**, 1131.

10. J. Shen and J. Krischner, Surf. Sci., 2002, **500**, 300.
11. M. Todorovic, S. Schultz, J. Wong and A. Scherer, Appl. Phys. Lett., 1999, **74**, 2516.
12. T. W. McDaniel, J. Appl. Phys., 2012, **112**, 093920.
13. A. Haldar and A. O. Adeyeye, ACS Nano, 2016, **10**, 1690.
14. V. V. Kruglyak, P. S. Keatley, A. Neudert, R. J. Hicken, J. R. Childress and J. A. Katine, Phys. Rev. Lett., 2010, **104**, 027201.
15. G. Gubbiotti, M. Madami, S. Tacchi, G. Socino, G. Carlotti and T. Okuno, Surf. Sci., 2006, **600**, 4143.
16. B. Rana, S. Pal, S. Barman, Y. Fukuma, Y. Otani and A. Barman, Appl. Phys. Express, 2011, **4**, 113003.
17. R. P. Cowburn, D. K. Koltsov, A. O. Adeyeye, M. E. Welland and D. M. Tricker, Phys. Rev. Lett., 1999, **83**, 1042.
18. J. Ding and A. O. Adeyeye, Adv. Funct. Mater., 2012, **23**, 1684.
19. V. V. Kruglyak, A. Barman, R. J. Hicken, J. R. Childress and J. A. Katine, J. Appl. Phys., 2005, **97**, 10A706.
20. A. Barman, S. Wang, J. D. Maas, A. R. Hawkins, S. Kwon, A. Liddle, J. Bokor and H. Schmidt, Nano Lett., 2006, **6**, 2939.
21. B. Rana, D. Kumar, S. Barman, S. Pal, Y. Fukuma, Y. Otani and A. Barman, ACS Nano, 2011, **5**, 9559.
22. S. Saha, S. Barman, Y. Otani and A. Barman, Nanoscale, 2015, **7**, 18312.
23. S. Jung, B. Watkins, L. DeLong, J. B. Ketterson and V. Chandrasekhar, Phys. Rev. B, 2002, **66**, 132401.
24. O. N. Martyanov, V. F. Yudanov, R. N. Lee, S. A. Nepijko, H. J. Elmers, C. M. Schneider and G. Schonhense, Appl. Phys. A, 2005, **81**, 679.
25. G. Gubbiotti, G. Carlotti, T. Okuno, M. Grimsditch, L. Giovannini, F. Montoncello and F. Nizzoli, Phys. Rev. B, 2005, **72**, 184419.
26. S. Tacchi, M. Madami, G. Gubbiotti, G. Carlotti, H. Tanigawa, T. Ono and M. P. Kostylev, Phys. Rev. B, 2010, **82**, 024401.
27. A. Haldar, D. Kumar, and A. O. Adeyeye, Nat. Nanotech., 2016, **11**, 437.
28. S. K. Kim, J. Phys. D: Appl. Phys., 2010, **43**, 264004.
29. D. Kumar, S. Barman and A. Barman, Sci. Rep., 2014, **4**, 4108.
30. V. V. Kruglyak, A. Barman, R. J. Hicken, J. R. Childress and J. A. Katine, Phys. Rev. B, 2005, **71**, 220409.

31. B. K. Mahato, B. Rana, D. Kumar, S, Barman, S. Sugimoto, Y. Otani and A. Barman, Appl. Phys. Lett., 2014, **105**, 012406.
32. B. Rana and A. Barman, SPIN, 2013, **3**, 1330001.
33. S. Saha, S. Barman, S. Sugimoto, Y. Otani and A. Barman, RSC. Adv., 2015, **5**, 34027.
34. A. Barman and A. Haldar, *Time-domain study of magnetization dynamics in magnetic thin films and micro-and nanostructures.* Solid State Phys, vol **65**. (Elsevier Inc., Burlington, 2014).
35. M. Donahue and D. G. Porter, OOMMF User's guide, Version 1.0, NIST Interagency Report no. 6376, National Institute of Standard and Technology, Gaithersburg, MD, 1999, http://math.nist.gov/oommf.
36. K. H. J. Buschow, J.: Handbook of Magnetic Materials (North Holland, Amsterdam, 2009) vol. **18**, p. 168.
37. D. Kumar, O. Dmytriiev, S. Ponraj and A. Barman, J. Phys. D, 2012, **45**, 015001.

Chapter 7

7 Influence of Anisotropic Dipolar Interaction on the Spin Dynamics of $Ni_{80}Fe_{20}$ Nanodot Arrays Arranged in Honeycomb and Octagonal Lattices

7.1 Introduction

Magnetically coupled ferromagnetic nanodots are systems of profound interest because of their potential application in high density magnetic storage [1, 2], logic device [3], magnonic crystal [4-7], spin torque nano-oscillator [8] and various other sensor applications. Information stored inside the dot relies on its strength and orientation of magnetization. Static magnetization of coupled nanodots can be reversed [9, 10] and their spin-wave (SW) dynamics [11, 12] can be modulated due to the influence of dipolar and multipolar coupling of the neighboring dots. When the dots are closely packed the magnetic coupling is strong and with the increase in dot separation the effect of this coupling gradually decreases and disappears. The influences of magnetostatic field on the magnetization distribution, domain formation and magnetization dynamics of the nanomagnets have been subject of interest for long time [13-15]. The initial static configurations of the spins within the nanodot array are found to be responsible for the generation of multiple resonant modes with various phases and amplitudes. The aspect ratio of the individual dot as well as the lattice configuration of the whole array influences the intrinsic and extrinsic configurational anisotropies arising from the internal magnetic field and the inter-dot magnetostatic coupling. These eventually modify the dynamic field distribution and SW spectra [16, 17].

The collective behavior in the nanodot array is well studied using various static characterization techniques [18] including static magneto-optical Kerr effect (SMOKE) microscopy [19]. Dynamics of the array have been investigated using time-resolved magneto-optical Kerr effect (TR-MOKE) microscopy [20-23], ferromagnetic resonance (FMR) [24, 25] and Brillouin light scattering [26-28] technique. The effects of

magnetostatic coupling on the collective precessional mode and damping of nanodot arrays with varying inter-dot separation down to the single dot regime have been investigated in details [22, 29]. Few reports are also available on the dipolar coupled binary nanodots [10, 30, 31]. Dvornik *et al*. used micromagnetic simulation to study the dipolar interaction between a pair of rectangular nanomagnets [32]. Keatley *et al.* exploited time-resolved scanning Kerr microscopy (TRSKM) to isolate the dynamic dipolar interaction between a pair of nominally-shaped ferromagnetic disks [33]. Using cavity enhanced TR-MOKE technique, Liu *et al.* quantified the effect of magnetostatic interaction on single magnet dynamics while the inter-dot separation is varied [34]. G. Shimon *et al*. [35] used a micro-focused Brillouin light scattering (BLS) technique to selectively probe the SW mode of coupled nanodots due to anisotropic dipolar interactions. However, the investigation of variation of collective SW dynamics of coupled nanodots arranged in honeycomb and octagonal lattice symmetries by varying the inter-dot separation has hitherto not been tried.

Here we have explored the collective SW dynamics of $Ni_{80}Fe_{20}$ (Permalloy, Py hereon) nanodot arrays arranged in honeycomb and octagonal lattice symmetries with varying inter-dot separations. Honeycomb lattice can be considered as a Bravais lattice with two-atom basis where each pair of nanodots is horizontally coupled. On the other hand, in octagonal lattice, paired nanodots with horizontal as well as vertical coupling construct the unit cell with complex basis structure providing more control points. This dipolar interaction is highly anisotropic in nature depending on the relative orientation between the inter-dot coupling and applied bias field. TR-MOKE microscopy has been used to probe the precessional magnetization dynamics of the arrays which reveal rich SW spectra for both the lattices. Experimentally and numerically we have studied the effect of the anisotropic dipolar interaction between nanodot pairs present through the entire array. The existence of two self-standing centre modes (CMs) of octagonal lattice and their frequency shift with inter-dot separation are completely different from the dynamics of honeycomb lattice. The SW dynamics of the arrays show transition from strongly collective to noncollective regime via weakly collective regime with varying inter-dot separations. In the collective regime, bias field variation of precessional frequencies establishes the SW mode stability within the experimental field regime. The salient features of these dot arrays can make them viable for construction of various nanomagnet based devices.

7.2 Experimental Details

Cylindrical Py nanodots having diameter (d) of 100 nm and thickness (t) of 20 nm are fabricated in 10 ×10 μm^2 arrays on top of self-oxidized Si (100) substrate. The dots are arranged in honeycomb and octagonal lattice symmetries with different inter-dot separations (S) varying from 30 nm to 300 nm. The number of unit cells present in the array vary from about 30×30 for S = 30 nm to about 12×12 for S = 300 nm. A combination of electron-beam evaporation and electron-beam lithography is used for the fabrication of the nanodots.

Bilayer MMA/PMMA (methyl methacrylate/polymethyl methacrylate) resist pattern was prepared on the Si substrate by using electron beam lithography with 100 pA beam current for a dose time of 1.0 ms. Subsequently, Py was deposited on the resist pattern by electron-beam evaporation at a base pressure of about 1.3×10^{-7} Torr. The final structure is coated with 5-nm-thick Al_2O_3 for preventing the possible degradation during direct exposure to femtosecond laser or environmental deterioration of sample due to oxidation. Finally, the residual resist was lifted off and oxygen plasma cleaning was done to remove the sacrificial material after lift-off.

Figure 7.1 (a) shows the scanning electron micrograph (SEM) of the nanodot arrays with honeycomb symmetry having S = 30, 100 and 300 nm. This lattice symmetry can be considered as a Bravais lattice with two-atom basis. The unit cell is marked with white dotted line in the images where a and b are considered as lattice constants. θ is the angle between two consecutive arms of a unit cell and for honeycomb it is measured as 60 ± 2°. Figure 7.1 (b) shows the SEM images of the arrays with octagonal lattice symmetry which belongs to non-Bravais class with lattice constant (a) and the angle θ = 135 ± 3° (as shown in the Fig. 7.1).

In Fig. 7.1 (c), a schematic of the experimental setup with polar Kerr geometry [21] is shown. In this two-color pump-probe technique, the fundamental laser beam generated from Tsunami (Spectra Physics, λ = 800 nm, pulse width ≈ 80 fs) is exploited to probe the magnetization dynamics of the sample. Some part of this fundamental beam is frequency doubled (λ = 400 nm) and used as pump beam. The pump beam travels with a time delay (Δt) relative to the probe beam and they collinearly fall upon the sample through a microscope objective (MO) with N.A. = 0.65 to excite and probe the sample.

The spot size of the probe beam is about 800 nm, while the pump beam is slightly defocused at the focal plane of the probe beam with a spot size of about 1μm.

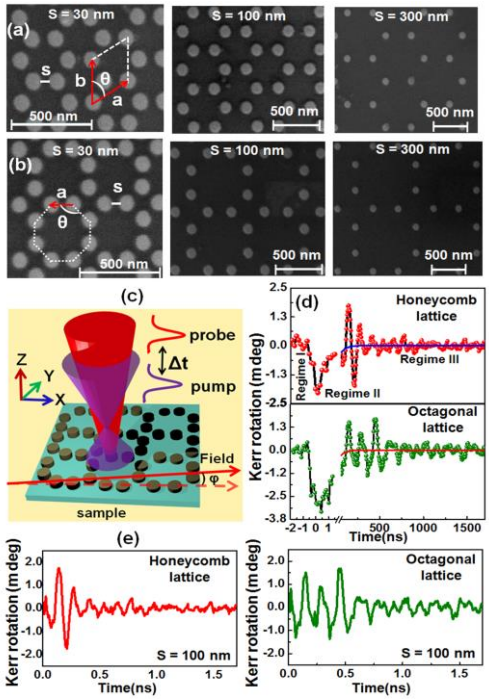

Figure 7.1: Scanning electron micrograph images of the Py nanodot array arranged in (a) honeycomb and (b) octagonal lattices. Inter-dot separations (*S*) and corresponding length scales are mentioned in numerical figures on the top and bottom of each image, respectively. Unit cells of the honeycomb and octagonal lattices are marked in dotted line in the figure. (c) Schematic of experimental arrangement used in pump-probe technique. (d) Raw and (e) background subtracted time-resolved Kerr rotation data for honeycomb and octagonal lattices with *S* = 100 nm. The red and blue solid lines are bi-exponential fits.

The probe beam is carefully placed at the centre of the pump beam to ensure uniform excitation of the probed area. A bias magnetic field is applied at a small angle (φ) of about 10°-15° *w.r.t.* the sample plane (as shown in Fig. 7.1(c)). The magnitude of the in-plane bias magnetic field (*H*) is 1.3 kOe in our case. The pump pulse results in ultrafast demagnetization followed by two-step relaxation and a damped precession of magnetization. Here, we used 1.7 ns time window which captures the full time-domain spin dynamics including the damping. The probe beam detects the time varying out-of-plane magnetization component from the sample using the optical bridge detector (OBD), and lock-in-amplifiers in a phase sensitive manner. The probe beam covers up to about 26 elements from the array when *S* = 30 nm for honeycomb lattice, which gradually decreases with increasing *S* and single-dot-like behavior is obtained at *S* = 300 nm. For octagonal lattice, as *S* varies from 30 nm to 300 nm, the number of probed dots

varies from 24 to 1. Figure 7.1 (d) shows the raw time-resolved Kerr trace which shows three different temporal regimes. The regime I corresponds to ultrafast demagnetization (~ 500 fs) due to incoherent interaction right after the pump pulse excites the electrons and spins [36]. In regimes II and III, a fast relaxation (τ_1) followed by a slow relaxation (τ_2) take place due to the relaxation of electron and spin energies to the lattice (τ_1) and then relaxation of lattice energy to the substrate and the surroundings (τ_2) [37, 38]. The damped precessional oscillation is superposed on the top of slow relaxation as shown in this figure. For honeycomb and octagonal lattices with S = 100 nm, τ_1 = 9, 11 ps and τ_2 = 58, 65 ps, respectively. Figure 7.1 (e) shows the background subtracted time-resolved Kerr rotation data for the lattices with S = 100 nm, which show multimodal oscillations in both cases.

The experimental data was further reproduced by micromagnetic simulations using OOMMF software [39]. Here, at first the static magnetic configuration was obtained by applying a large magnetic field to saturate the sample. Then the field was reduced to the required field value and allowed to reach the equilibrium (maximum torque $\mathbf{m} \times \boldsymbol{H}$, where $\mathbf{m} = \mathbf{M}/M_S$ goes well below 10^{-6} A/m). The spatial distribution of magnetization at time steps of 10 ps was recorded for a total duration of 4 ns. The optical excitation in the experiment was mimicked by a pulsed magnetic field excitation in the simulation, which reproduced the experimental results successfully. The samples were discretized into rectangular prisms of dimensions 2 × 2 × 20 nm^3 where the lateral cell size is well below the exchange length of Py (≈ 5.2 nm). Material parameters for Py used in the dynamic simulations were gyromagnetic ratio γ'= 18.5 MHz/Oe, anisotropy field H_k = 0, saturation magnetization M_s = 860 emu/cc, and exchange stiffness constant A = 1.3×10^6 erg/cm. The exchange stiffness constant A is obtained from literature [40]. The other parameters were obtained from the Kittel fit of bias field dependence of precessional frequency for a Py blanket film with 20-nm thickness.

7.3 Results and Discussions

Figure 7.2 shows the fast Fourier transform (FFT) spectra of background subtracted time-resolved Kerr rotation data for the nanodot arrays. The experimental FFT spectra (Fig. 7.2(a)) for the honeycomb lattice with S = 30 nm shows a rich band of SW frequencies starting from 3.5 to 11.5 GHz, indicating a strongly collective behavior of the array. Out of the five modes, the lower frequency modes have relatively higher

intensities. For S = 75 nm, the SW spectra is narrowed with only three modes and a sudden downshift of the highest frequency mode (mode 1) is observed. With increasing S, mode 2 and 3, slowly merge together and the collective behavior reduces. Finally, for $S \geq 250$ nm, only two modes appear, which are identical to the two distinct modes of a single nanodot (mode 1: 9.9 GHz, mode 2: 6.7 GHz) [29]. Micromagnetic simulation results for all samples are shown at the right-hand panel of Fig. 7.2 (a). Simulated modes show decent agreement with the experimental modes except for the broadening of peaks and relative mode intensities. The average disagreement between the peak frequencies for experiment and simulation is found to be about 10%. This can be attributed to the difficulty in precise accounting for the detailed roughness and edge deformation of the real samples in the finite difference method based micromagnetic simulation. Further, the reduction in signal to noise ratio for the arrays with lower areal densities may cause in appearance of some spurious modes in the experimental spectra. Also the disagreement may arise due to the limitation in total time window of less than 2 ns taken during the measurement where as simulated spectra are obtained for 4 ns. The line width broadening is more in experimental FFT than simulation and peak positions for different SW modes can be determined less accurately.

For octagonal lattice, the experimental and simulated SW spectra are shown in Fig. 7.2(b). Clearly three modes are present for the array with smallest inter-dot separation S = 30 nm, forming a narrow band, which evolves into rich spectra at S = 75 nm. Mode 1 for S = 30 nm splits into two modes and two additional lower frequency modes appear. Mode 1 also experiences a red shift. This SW spectra remain nearly unchanged for S = 100 nm except for the relative mode intensities. For S = 150 nm, two high frequency modes merge together and three other modes persist in the spectra. However, only two distinct SW modes appear for $S \geq 200$ nm both in the experimental and simulated spectra. This observation indicates transition of the dynamics from strongly collective to completely isolated regime via a weakly collective regime with increasing inter-dot separation for the octagonal lattice. The red and blue dotted lines indicate two precessional modes of a single nanodot having diameter of 100 nm and thickness of 20 nm, obtained from micomagnetic simulation [29]. The three collective regimes have been represented by three different color bands in the FFT spectra.

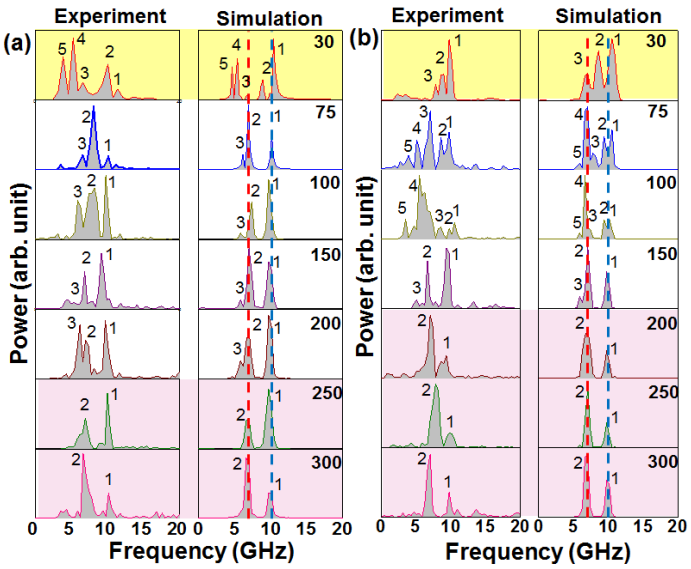

Figure 7.2: The experimental and simulated FFT power spectra of background subtracted experimental time-resolved Kerr rotation data along with simulated spectra obtained from Py nanodot arrays with (a) honeycomb and (b) octagonal lattice symmetries. Inter-dot separations are mentioned in numerical figures on the right-hand side of each panel. The number of peak corresponds to each SW mode is indicated at the top of the peak for all the spectra. The red and blue dotted lines shown in the simulated FFT spectra indicate the peak position of two SW modes of a single nanodot. Different color shades indicate different magnetostatic interaction regimes.

For S = 30 nm of the octagonal lattice, no mode splitting is observed for the highest frequency mode but for S = 75 and 100 nm, clear splitting is observed in the experimental and simulated FFT spectra (as shown in Fig. 7.2 (b)). Figure 7.3 (a) shows the simulated mode frequencies (mode 1 for honeycomb and mode 1, 2 for octagonal lattice) as a function of S. While mode 1 shows a sharp decrease for 30 nm ≤ S ≤ 100 nm followed by saturation for S ≥ 150 nm for both lattice, mode 2 for the octagonal lattice shows an opposite trend, i.e. it increases sharply for 75 nm ≤ S ≤ 150 nm followed by a saturation at 9.7 GHz, where mode 1 and mode 2 of the octagonal lattice merge to form a single mode.

To understand it further we have studied bias-field dependence of precessional frequency by varying the in-plane bias magnetic field in the range 0.62 kOe ≤ H ≤ 1.30 kOe as shown in Fig. 7.3 (b) for honeycomb and octagonal lattice at S = 75 nm.

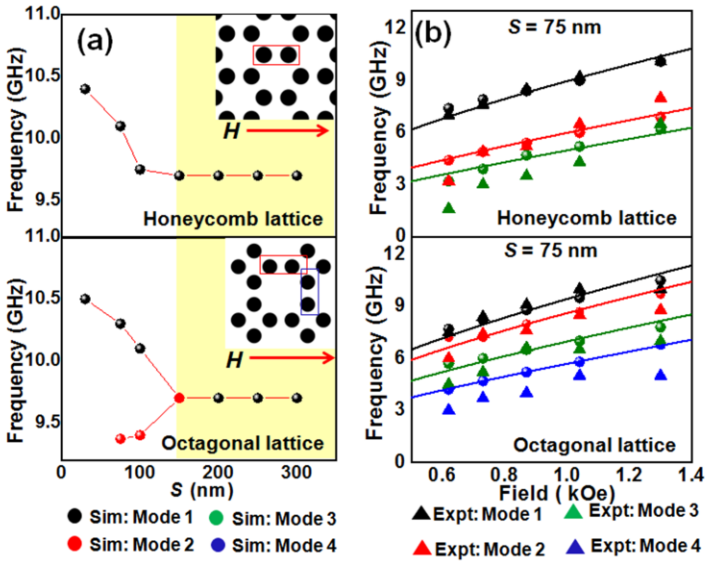

Figure 7.3: (a) Variation of precessional frequencies of mode 1 obtained from simulated FFT spectra of honeycomb lattice and mode 1, 2 for octagonal lattice with *S.* Constant field (*H*) of 1.3 kOe is applied as shown in the insets. Precessional frequencies of different SW modes for Py nanodot array with inter-dot separation, S = 75 nm, arranged in (b) honeycomb and octagonal lattice symmetries, are plotted as a function of bias field H. Triangular symbols: experimental data, circular symbols: micromagnetic simulation results, solid line: Kittel fit.

The Kittel formula has been used to fit the high frequency modes after including an additional uniaxial anisotropy field originating from the dipolar field as given below:

$$f = \frac{\gamma'}{2\pi}\sqrt{(H + H_{dx} + H_k)(H + H_{dx} + H_k + 4\pi M_x)} \qquad (7.1)$$

where f is the precession frequency, H_k is the magnetocrystalline anisotropy field, which is negligible in Py, H_{dx} is the inter-dot interaction field along x-direction and M_x is effective magnetization of the sample along x-direction. Other parameters are described earlier. For horizontally coupled nanodots, the effective field along x-direction responsible for frequencyof the spins precessing at the centre of the dots can be represented as,

$$H_x = H + H_{dx} \qquad (7.2)$$

Fitting the frequency variation of mode 1 of honeycomb lattice we have found that M_x = 646 ± 13 emu/cc and H_{dx} = 37 Oe. On the other hand, the fitting parameters found from equation 7.1, for mode 1 of octagonal lattice are M_x (mode 1) = 657 ± 16 emu/cc and H_{dx} (mode 1) = 97 Oe. For mode 2, these parameters are found to be, M_x (mode 2) = 657 ± 16 emu/cc and H_{dx} (mode 2) = -57 Oe. Earlier reports reveal that for single nanodot (d = 100 nm, thickness 20 nm) the effective M_s value obtained for highest frequency mode

was 672 emu/cc [29]. The weaker inter-dot interaction field results in a splitting of the uniform centre mode of a single dot, which is absent for S = 30 nm, where strong collective dynamics of the array dominate (as shown in Fig. 7.2 (b). The negative value of H_{dx} indicates that it opposes the bias field due to complex coupling between the vertically situated nanodot pairs [35]. The lower frequency branches for both the lattices are fitted with a simple Kittel formula by excluding the interaction field H_{dx} from eq. 1 to avoid additional complications:

$$f = \frac{\gamma'}{2\pi}\sqrt{(H + H_k)(H + H_k + 4\pi M_x)} \tag{7.3}$$

The M_x values obtained for mode 2 and 3 of honeycomb lattice are 236 ± 2 emu/cc and 147 ± 11 emu/cc. For octagonal lattice, mode 3 and 4 yielded M_x values as 367 ± 17 and 217 ± 2 emu/cc, respectively. The other magnetic parameters are found to be similar to the 20-nm-thick Py film values. Relatively smaller effective magnetization values for lower frequency modes indicate the effect of nonuniform internal field due to unsaturated spins near the edges of the dots. These modes have similarity with the edge mode of a single nanodot studied earlier [29]. For octagonal lattice, mode 5 (Fig. 7.2 (b)) is hardly identified at the low field regime due to overlap with the low frequency noise (around 1-2 GHz) in the time-resolved data. Hence, even in their most strongly coupled regime, the honeycomb and octagonal lattices do not show a continuous thin-film-like coupled dynamical behavior as observed for the hexagonal lattice [29]. In addition, the opposite trend of variation of frequency with inter-dot separation in mode 1 and mode 2 of the octagonal lattice is a consequence of complex coupling between the horizontal and vertically paired nanodots. These two modes are found to be stable with bias field.

Figure 7.4 shows the power and phase maps of the SW modes for the honeycomb lattice having three different inter-dot separations (S = 30, 75 and 250 nm). For mode 1, the power of the SW is mainly concentrated at the central part of the individual dots. The phase of a dot is shown in the inset which confirms that the mode is centre mode [29] of the dot distributed uniformly through the whole array. Mode 2 is the backward volume (BV) like mode of the nanodots distributed uniformly through the entire array. For mode 3, the shaded area indicates the region where magnetostatic interaction along the field is less causing appearance of the asymmetric edge modes between the dots along each column. Mode 4 has similar nature as asymmetric edge mode. Mode 5 is edge mode

of the array where power of SWs is mainly concentrated along two vertical edges of the array.

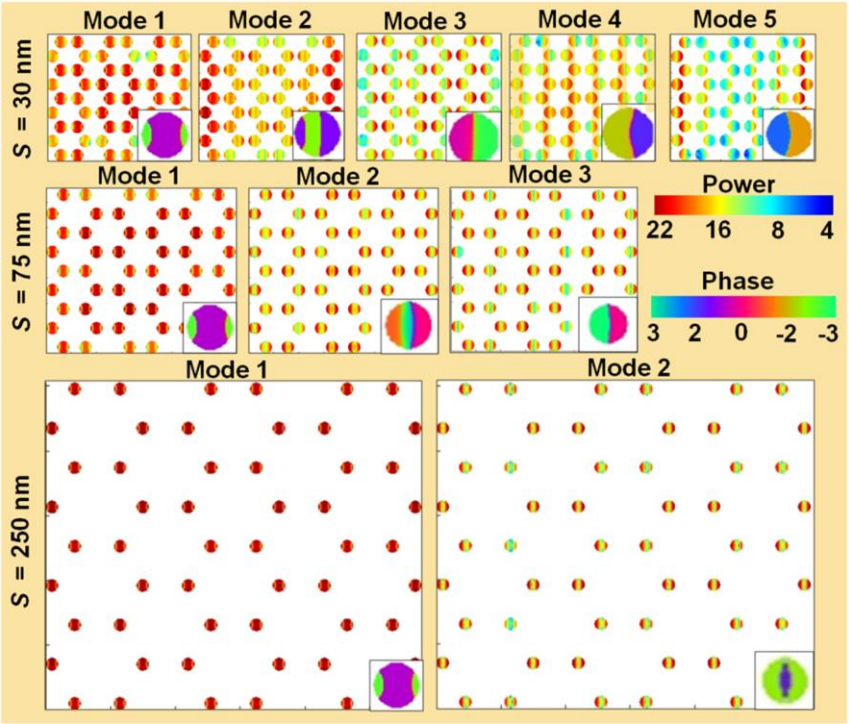

Figure 7.4: Simulated SW power-phase maps of Py nanodot arrays with honeycomb lattice symmetry. Inter-dot separations are mentioned in numerical figures on the left-hand side of each panel. The mode numbers are indicated at the top of the images. Phase map for individual dots correspond to each SW mode profile is shown in the inset of each image. The color bars corresponding to power and phase profiles are indicated with respective scales.

For S = 75 nm, mode 1 is again the centre mode of the dots distributed over the entire array. Mode 2 is the modified BV-like mode of the dots. Mode 3 is an edge mode of individual dot uniformly distributed through the whole array. Finally, for S > 200 nm, the collective behavior of the whole array disappears and the SW modes of single nanodot come up individually. Consequently, at S = 250 nm, only centre and edged modes of the dots persist.

Figure 7.5 shows the power and phase profiles of the nanodot arrays arranged in octagonal symmetry with different inter-dot separations. For S = 30 nm, mode 1 corresponds to center mode of each dot distributed through the array. Mode 2 is the BV like mode of the dot placed at each denser row shown in dotted area. Appearance of this mode is a consequence of strong collective interaction between the spins of the edges of the dot placed very closely with each other. But the dots located in sparser rows have negligible power. Mode 3 is purely the edge mode of nanodot placed in the vertical

column as indicated by the shaded regions. This mode is not uniformly distributed through the whole array because presence of strong interaction has destroyed the edge modes of two consecutive nanodots placed in denser row.

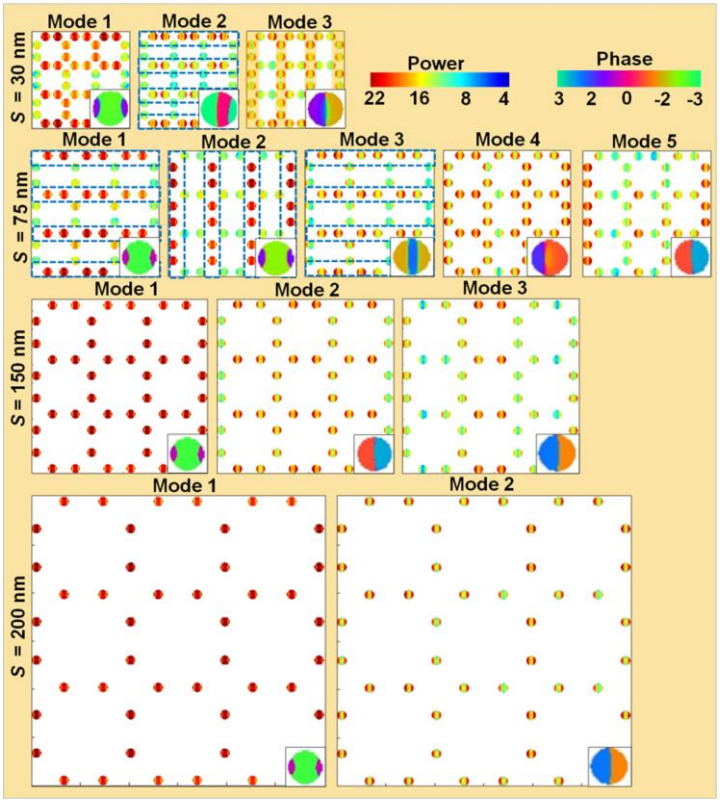

Figure 7.5: Simulated SW power-phase maps of Py nanodot arrays with octagonal lattice symmetry. Inter-dot separations are mentioned in numerical figures on the left-hand side of each panel. The mode numbers are indicated at the top of the images. Phase map for individual dot corresponding to each SW mode profile is shown in the inset of each image. The color bars corresponding to power and phase profiles are indicated with respective scales.

For S = 75 nm, the highest frequency mode of S = 30 nm splits into two complementary modes. Mode 1 is the centre mode of the dots placed in denser rows. Mode 2 is center mode of the dots placed in the sparser rows. Mode 3 shows that within each dot the nature of SW is BV like and the power mainly lies in each alternate row as shown in the figure.

The phase shown in the inset of the corresponding power supports the BV-like nature of SW. For mode 4, edge mode of the dots is uniformly distributed through the whole array. Mode 5 is edge mode of the array. However, these five modes converge into three modes as the inter-dot separation increases. As shown in Fig. 7.5, for S = 150 nm, mode 1 is the centre mode of the dots distributed through the whole array. Mode 2 is edge mode of the individual dot which is supported by phase shown in the inset of the image.

Mode 3 is clearly a driven mode appeared in the vicinity of mode 2 with relatively lesser intensity. For S > 200 nm, two low frequency modes merge together similar to honeycomb lattice and forms distinct edge mode. The high frequency mode is the centre mode which remains at the same position. Undoubtedly the collective behavior of the whole array disappears here and magnetostatic interaction among the dots is reduced drastically.

To gain more insight about the collective dynamics for honeycomb and octagonal lattice symmetries with varying inter-dot separations, we have calculated magnetostatic field distribution for the dot arrays using LLG micromagnetic simulator [41]. Solving Landau-Lifshitz-Gilbert equation, this solver calculates the static field distribution of the system. From this we can get a qualitative idea about the dipolar coupling strength as well as magnetization distribution across the dot array. At first the whole system is saturated along x-direction with a high magnetic field followed by reduction of the field to desirable bias field value, mimicking the experimental geometry. We have observed that for H = 1.3 kOe, in the static configuration, the magnetizations remain aligned along the field direction (x-axis) forming a quasi-single domain inside each dot. Due to the presence of unsaturated charges near the dot edges the demagnetizing field (H_{dx}) comes into the picture. This field is known to be the dipolar field acting in between two magnetic dipoles situated at finite distance. To analyze the x-component of the field (as shown in Fig. 7.6(a), (b)) for the honeycomb lattice, linescan has been taken along the white line shown in the inset of Fig. 7.6(c), for S = 30, 75, 200 nm representing the strongly collective, weakly collective and isolated regime, respectively. The variation of stray field with distance shows that there are two different positions, P1 and P2, where stray field exhibits local minima. Here the centre-to-centre distance between two dots along x direction is represented by r. In Fig. 7.6 (c) the trend of stray field value is found to be decreasing and then saturating with increasing r. Similarly, for octagonal lattice we have taken linescan along the row, but this time for two different rows, denser (as shown in white dotted line in Fig. 7.6 (d) inset) and sparser (yellow dotted line) row. Figure 7.6 (b) shows the variation of stray field with distance for S = 30, 75 and 200 nm. Interestingly in this case, we find three different positions (P1, P2, P3) where the stray field exhibits local minima. We have plotted those values with respect to r in Fig. 7.6 (d) which showed similar trend like honeycomb lattice. We have considered a simple model to explain the behavior of this field variation. Considering each dot as a single dipole

oriented along x-direction in a row [29], the magnetic field (B) in between two parallel dipoles can be expressed as:

$$B \propto \frac{1}{r^3} \tag{7.4}$$

and the two curves in Figs. 7.6 (c) and (d) are fitted with this equation.

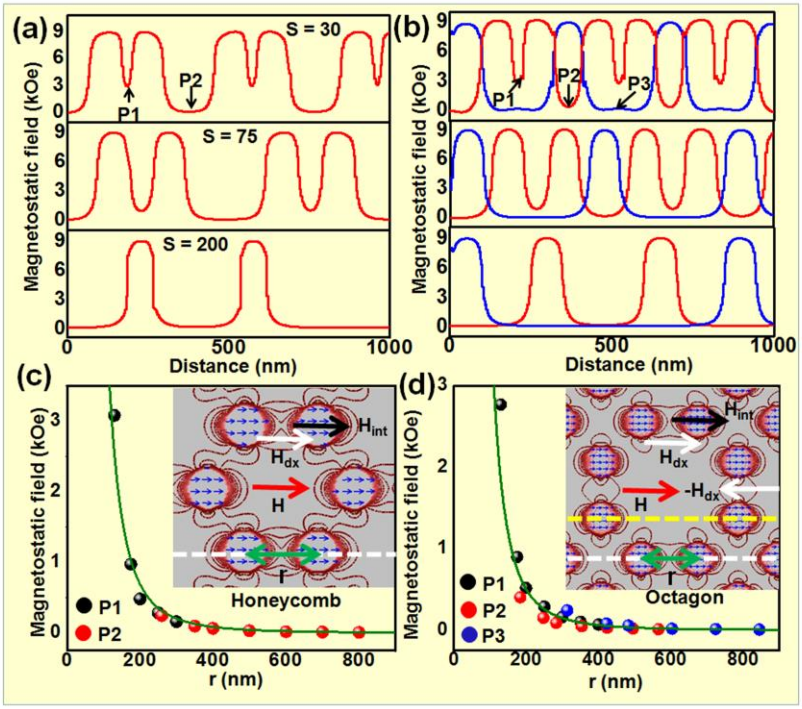

Figure 7.6: Distribution of x-component of magnetostatic interaction field with distance along the row in the Py nanodot arrays having (a) honeycomb and (b) octagonal lattice symmetries with different *S.* The red linescans are taken along the white dotted line for the honeycomb lattice. The red and blue linescans are taken along white (denser row) and yellow (sparser row) dotted lines for octagonal lattice respectively. P1, P2, P3 indicates the position of the linescan where the magnetostatic field value experiences local minima. Variation of magnetostatic field values for different positions, with distance between the corresponding nanodots for all the arrays having (c) honeycomb and (d) octagonal lattice symmetries. The magnetostatic field distribution is shown at the inset of each figure.

The fitting shows that the stray fields in between the dots placed at denser row or sparser row of these lattices are dipolar in nature.

The dipolar interaction is highly anisotropic depending on the relative orientation between the inter-dot coupling direction and the applied field (H). When the dots are in

single domain state the effective field inside the dot governs the frequency (f) of centre mode. For horizontally coupled dots, the dipolar field along x-direction (H_{dx}) is added to the applied field. However, for vertically coupled dots the effective field is reduced due to this anisotropic dipolar field.

With increasing inter-dot separation (S) the strength of the dipolar interaction decreases (as shown in Fig. 7.6 (c), (d)), so the contribution to the effective field modifies accordingly. The honeycomb lattice can be thought as assembly of horizontally coupled paired nanodots having inter-dot separation $r = S+d$, placed along the rows. So, the applied magnetic field will act parallel to this pair (see Fig. 7.6 (c) inset). For, S = 30 nm, the magnetostatic coupling is strongest in our case and the dipolar interaction solely contributes to the enhancement of H_x. So, the peak frequency of the centre mode was found to be highest (see Fig. 7.3 (a)). With increasing separation, the collective behavior becomes weaker and the peak frequency experiences a red shift. When the dots become almost isolated, then the frequency of the center mode attains a constant value and the whole array shows the nature of isolated dots.

Interestingly we have found that for octagonal symmetry the lattice is an assembly of horizontally as well as vertically coupled paired nanodots. Hence, when bias field is applied along x-direction, the magnetization inside the dots in the horizontal arms starts to precess with slightly higher frequency than the other nanodots according to equation 7.3. So, for S = 75 nm mode spitting appear at the higher frequency which cannot be seen for honeycomb lattice. As S increases from 75 nm to 100 nm, the gap between mode 1 and mode 2 reduces. For higher separations (S > 150 nm) those two modes merge. Figure 7.6, shows that, the stray field distribution among the dots forming the diamond structure is different than other separations. The connecting stray fields between the dots placed at the vertical apex of the diamond strongly dominate over the features of dipolar interaction of the neighboring pairs. Due to strongly collective behavior of the whole array the mode splitting does not appear. The asymmetric edge modes of the dots (mode 3, 4 of honeycomb and mode 3 of octagonal lattice), arise due to the dipolar coupling among the neighbors.

If the dipolar interaction is weak and is not directed along bias field, the effect of unsaturated spins of those edges cannot be ruled out by the strong internal field.

In the context of appearance of BV-like mode for octagonal lattice at S = 30 nm, the contribution from diamond shaped region again comes into the scenario. In this region,

stray fields are vertically distributed and flux density is very high. This is responsible for increasing the demagnetization at the corresponding edges of the dots and uniform BV-like nature of mode 2 is affected by the field distribution of this region. For S = 75 nm, the field distribution undergoes a drastic change. The dots forming diamond shaped region are no longer connected by the vertically interacting fields. So, the unsaturated spins of one edge of each dot along the denser row have strong magnetostatic coupling with another dot whereas the other three edges form closed flux structure. Thus, the BV-like nature of the SW inside each dot does not appear for $S \geq 75$ nm.

The other modes in the collective and non-collective regimes originate from the resultant dipolar interactions of different positions as shown in Figs. 7.6 (a), (b) for both the lattices. For higher separation, the dots are free from neighboring magnetostatic interaction and they flaunt their individual character being in the same array. For these completely isolated dots the dipolar interaction becomes negligibly small.

7.4 Conclusions

In essence, we have systematically studied the magnetization dynamics of Py nanodot arrays having two different lattice configuration, honeycomb and octagon. All-optical time-resolved MOKE technique is used for excitation and detection of collective magnetization dynamics and to probe various features of anisotropic dipolar interaction among the nanodots. The purpose of studying these Bravais and non-Bravais lattices is two-fold. Firstly, the effect of anisotropic dipolar interaction can be prominently observed within the octagonal lattice having horizontally as well as vertically coupled paired nanodots. Consequently, splitting of highest frequency mode and their variation with inter-dot separation are explored. On the contrary, the honeycomb lattice does not contain this unique feature with the paired nanodots placed only parallel with the field. This exclusive feature obtained in our experiment will intensify the interest of scientific community to study the field driven SW modes in magnonic crystal. From the time-resolved Kerr traces we have obtained damped sinusoidal precession involving multiple frequency modes for the nanodot arrays. The FFT spectra for honeycomb lattice contain three separate regimes within increasing inter-dot separation from 30 nm to 300 nm. A strongly collective behavior was observed for the array with highest areal density. Rich SW spectra experience a transition to weakly collective regime and reach a completely isolated regime. For octagonal lattice the evolution of SW modes with strongly collective

nature, is noticeably different. Here only three modes observed for the array with highest areal density which is spread to a rich frequency band with increasing separation. Most interestingly the highest frequency mode splits into two modes. The bias field dependence of precessional frequency shows that these modes are stable within our experimental field regime. Gradually this rich SW band emerges to the isolated regime for $S \geq 200$ nm. The simulated mode profiles enhance our knowledge about the spatial distribution of power and phase in these arrays as well as identification of each mode. The numerically calculated stray field distribution of the ground state for honeycomb and octagonal lattices having different inter-dot separations helps our understanding about the anisotropic dipolar coupling of the magnetic dipoles. Our findings will promote the understanding of complex interactions in magnonic crystals for application as GHz frequency filter and attenuator. For smaller areal density, reduction in magnetostatic coupling strength makes these nanodot arrays suitable for storing information within them. Thus, the signal overlapping, cross talk in the microwave communication devices can be avoided.

References

1. O. Hellwig, A. Berger, T. Thomson, E. Dobisz, Z. Bandic, H. Yang, D. S. Kercher and E. E. Fullerton, Appl. Phys. Lett.**90** 162516 (2007).
2. T. Thomson, G. Hu and B. D. Terris, Phys. Rev. Lett.**96** 257204 (2006).
3. A. Haldar and A. O. Adeyeye, ACS Nano **10** 1690 (2016).
4. B. Lenk, H. Ulrichs, F. Garbs and M. Münzenberg, Phys. Rep. **507** 107–136 (2011).
5. S. A. Nikitov, Ph. Tailhades and C. S. Tsai, J. Magn. Magn. Mater. **236** 320 (2001).
6. M. Krawczyk and D. Grundler, J. Phys.: Condens. Matter **26** 123202 (2014).
7. V. V. Kruglyak, S. O. Demokritov and D. Grundler, J. Phys. D: Appl. Phys. **43** 264001 (2010).
8. A. D. Belanovsky, N. Locatelli, P. N. Skirdkov, F. A. Araujo, J. Grollier, K. A. Zvezdin, V. Cros, and A. K . Zvezdin, Phys. Rev. B **85** 100409 (2012).
9. R. P. Cowbarn, Phys. D: Appl. Phys. **33** R1-R16 (2000).
10. J. Ding and A. O. Adeyeye, Adv. Funct. Mater. **23** 1684 (2013).
11. V. V. Kruglyak, A. Barman, R. J. Hicken, J. R. Childress and J. A. Katine Phys. Rev. B **71** 220409 (2005).

12. S. Saha, R. Mandal, S. Barman, D. Kumar, B. Rana, Y. Fukuma, S. Sugimoto, Y. Otani and A. Barman, Adv. Funct. Mater. **23** 2378 (2013).
13. J. M. Shaw, W. H. Rippard, S. E. Russek, T. Reith and C. M. Falco, J. App. Phys. **101** 023909(2007).
14. B. Rana, S. Pal, S. Barman, Y. Fukuma, Y. Otani and A. Barman, Appl. Phys. Express **4** 113003 (2011).
15. A. Barman, S. Wang, J. Maas, A. R. Hawkins, S. Kwon, J. Bokor, A. Liddle and H. Schmidt, Appl. Phys. Lett. **90** 202504 (2007).
16. J. M. Shaw, T. J. Silva, M. L. Schneider and R. D. Schneider, Phys. Rev. B **79** 184404 (2009).
17. S. Saha, S. Barman, S. Sugimoto, Y. Otani and A. Barman, RSC Adv. **5** 34027 (2015).
18. J. Chang, V. L. Mironov, B. A. Gribkov, A. A. Fraerman, S. A. Gusev and S. N. Vdovichev, J. App. Phys.**100** 104304 (2006).
19. F. Nasirpouri, A. Nogaret and S. J. Bending, IEEE Trans. Magn.**47** 4695 (2011).
20. B. Rana and A. Barman, SPIN **3** 1330001 (2013).
21. A. Barman, and A. Haldar, *Time-domain study of magnetization dynamics in magnetic thin films and micro-and nanostructures.* Solid State Phys, vol **65**. (Elsevier Inc., Burlington, 2014).
22. B. Rana, D. Kumar, S. Barman, S. Pal, Y. Fukuma, Y. Otani and A. Barman, ACS Nano. **5** 9559 (2011).
23. B. K. Mahato, B. Rana, D. Kumar, S. Barman, S. Sugimoto, Y. Otani and A. Barman App. Phys. Lett. **105** 012406 (2014).
24. O. N. Martyanov, V. F. Yudanov, R. N. Lee, S. A. Nepijko, H. J. Elmers, C. M. Schneider and G. Schonhense, Appl. Phys. A **81** 679–683 (2005).
25. X. M. Liu, J. Ding, G. N. Kakazei and A. O. Adeyeye, Appl. Phys. Lett.**103** 062401 (2013).
26. G. Gubbiotti, G. Carlotti, T. Okuno, M. Grimsditch, L. Giovannini, F. Montoncello and F. Nizzoli, Phys. Rev. B **72** 184419 (2005).
27. R. Zivieri, F. Montoncello, L. Giovannini, F. Nizzoli, S. Tacchi, M. Madami, G. Gubbiotti, G. Carlotti and A. O. Adeyeye, Phys. Rev. B **83** 054431 (2011).
28. S. Tacchi, M. Madami, G. Gubbiotti, G. Carlotti, H. Tanigawa, T. Ono and M. P. Kostylev, Phys. Rev. B **82** 024401 (2010).

29. S. Mondal, S. Choudhury, S. Barman, Y. Otani and A. Barman, RSC Adv. **6** 110393 (2016).
30. S. Saha, S. Barman, J. Ding, A. O. Adeyeye and A. Barman, Appl. Phys. Lett. **102** 242409 (2013).
31. A. De, S. Mondal, C. Banerjee, A. K. Chaurasiya, R. Mandal, Y. Otani, R. K. Mitra and A. Barman, J. Phys. D: Appl. Phys. **50** 385002 (2017).
32. M. Dvornik, P. V. Bondarenko, B. A. Ivanov and V. V. Kruglyak, J. Appl. Phys. **109** 07B912 (2011).
33. P. S. Keatley, P. Gangmei, M. Dvornik and R. J. Hicken, Phys. Rev. Lett. **110** 187202 (2013).
34. Z. Liu, R. Brandt, Y. Yahagi, B. Hansen, B. Harteneck, J. Bokor, A. R. Hawkins and H. Schmidt, Appl. Phys. Lett. **98** 052502 (2011).
35. G. Shimon and A. O. Adeyeye, Adv. Elec. Mater.1500074 (2015).
36. E. Beaurepaire, J. C. Merle, A. Daunois and J. Y. Bigot, Phys. Rev. Lett.**76** 22 (1996).
37. A. Laraoui, J. Venuat, V. Halte, M. Albrecht, E. Beaurepaire and J. Y. Bigot, J. Appl. Phys. **101** 09C105 (2007).
38. A. Barman and J. Sinha, Spin Dynamics and Damping in Ferromagnetic Thin Films and Nanostructures, Springer (doi: 10.1007/978-3-319-66296-1), 2018.
39. M. Donahue and D. G. Porter, OOMMF User's Guide Version 1.0 *Interagency Report NISTIR* 6376 (Gaithersburg, MD: National Institute of Standard and Technology), (http://math.nist.gov/oommf), 1999.
40. K. H. J. Buschow, *Handbook of Magnetic Materials*, vol **18** (Amsterdam: Elsevier) p 168, 2009.
41. M. R. Scheinfein and E. A. Price, *LLG User Manual* v2.50 http://llgmicro.home.mindspring.com, 2003.

Chapter 8

8 Hybrid Magneto-Dynamical Modes in A Single Magnetostrictive Nanomagnet on A Piezoelectric Substrate Arising from Magneto-Elastic Modulation of Precessional Dynamics

8.1 Introduction

Nanomagnetic switches are potential replacements for the celebrated transistor in computing and signal processing hardware because they are energy-efficient switches that are also non-volatile. Nanomagnets exhibit interesting spin configurations such as quasi-single domain configurations, vortices, skyrmions, and magnetic monopole defects [1-3]. A wide variety of dynamics can occur in them over a broad time scale, e. g. ultrafast demagnetization, re-magnetization, precession, damping, motion, and domain wall movement [4] all of which have their own intriguing applications [5,6]. A nanomagnet's magnetization can be switched with an external agent in a variety of ways, among which an extremely energy-efficient approach is "straintronics" [7-9]. Here, the magnetization of a magnetostrictive nanomagnet is switched with mechanical strain (Villari effect) via elastic coupling to an underlying piezoelectric substrate that is activated by a voltage [7-11]. While this methodology has attracted attention because of its excellent energy-efficiency, to our knowledge, there has been no experimental study of the ultrafast magnetization dynamics associated with straintronic switching, even though non-straintronic magnetization reversal and dynamics of large arrays of nanomagnets [12], or even single nanomagnets, have been extensively studied [13-15]. Here, we report the study of ultrafast strain-modulated magnetization dynamics in a single magnetostrictive Co nanomagnet fabricated on a (001) PMN-PT piezoelectric substrate, performed using time-resolved magneto-optical Kerr effect (TR-MOKE) measurements. These studies elucidate the temporal dynamics of strain-induced magnetization rotation and reveal the time-scales associated with switching. In our study, we chose Co as the magnetostrictive nanomagnet, despite its relatively weak magnetostriction, since it is a single element and not an alloy. Alloys such as GaFe and

Terfenol-D have much higher magnetostriction than Co, but they have multiple phases (not all of which produce high magnetostriction) and also pinning sites that pin the magnetization and inhibit magnetization dynamics [16]. For these reasons, Co is better suited to this study.

In our TR-MOKE setup, a femtosecond laser pump beam excites the magnetization of the Co nanomagnet to precess about an applied bias magnetic field. At the same time, the alternating electric field in that same beam also generates periodic (compressive and tensile) strain in the PMN-PT substrate from d_{33} and/or d_{31} coupling. This happens because the laser electric field periodically reconfigures the charge distribution on the surface of the PMN-PT substrate and that, in turn, modulates the electric field within the substrate via the Poisson equation. Since PMN-PT is piezoelectric and has been poled, the periodically modulated electric field within the substrate will produce a periodic strain due to d_{33} and d_{31} coupling. The strain will alternate between tensile and compressive (strain is tensile if the electric field in the substrate is in the same direction as poling and compressive if the electric field is opposite to the direction of poling). Additional periodic strain is generated in the substrate (underneath the nanomagnet) from the differential thermal expansions of the nanomagnet and the substrate due to periodic heating by the pulsed pump beam [16-18]. This thermally generated strain is however always tensile in the substrate in our experiment (its magnitude varies periodically, but the sign does not change) because the thermal coefficient of expansion of Co (13×10^{-6}/K) is greater than that of PMN-PT (9.5×10^{-6}/K). Note that the former mechanism requires a piezoelectric substrate while the latter does not. The latter mechanism has been studied in some earlier work [17-20], but the former has not. In our system, the former is expected to be dominant and hence, to our knowledge, this is the first study of this effect. The total periodic strain produced in the substrate generates surface acoustic waves (SAWs) [17-20] which periodically expand and contract the nanomagnet sitting on the substrate and change its magnetization owing to the Villari effect [21,22]. Thus, two distinct sources induce oscillations in the out-of-plane component of the nanomagnet's magnetization: the Villari effect associated with the SAW and the Larmor precession about the bias magnetic field that can be set off by the laser-induced optical pumping. The interaction of these two oscillations gives rise to multiple hybrid oscillation modes (each with its own characteristic frequency) in the out-of-plane component of the magnetization, which then induce corresponding

oscillations in the nanomagnet's reflectivity and polarization of the reflected light (Kerr signal). The periods of these oscillations are found to be 70-200 ps, which suggest that the magnetization of the nanomagnet can respond to SAW-induced strain in time scales on the order of 100 ps. This is an important insight since SAW-based magnetization switching has attracted significant interest owing to its many applications [23-38].

Our study also revealed that the spin waves which are excited in the nanomagnet in the form of hybrid magneto-dynamical modes exhibit complex power and phase profiles owing to the mixing of the precessional magneto-dynamics and SAW-induced magneto-dynamics.

8.2 Experimental Details

The nanomagnets were fabricated with electron-beam lithography and electron beam evaporation of Co, followed by lift-off. Two different electron-beam resists of different molecular weights were used to facilitate lift off. Prior to fabrication, the PMN-PT substrate was poled with a high electric field in the direction of the major axes of the elliptical nanomagnets. To investigate the hybrid modes experimentally, we fabricated an array of slightly elliptical (eccentricity ≈ 1) Co nanomagnets (magnetostriction χ = 40-60 ppm) on a piezoelectric (001) PMN-PT substrate (d_{33}>2000 pC/N). The thickness of the nanomagnets is nominally 15 nm. Figures 8.1(a) and (b) show a scanning electron micrograph (SEM) of the nanomagnets and their magnetic force microscope (MFM) images. The nanomagnets are almost circular with major axis of 190 nm and minor axis of 186 nm. Because of this small aspect ratio, they do not show good phase contrast in the MFM images or single domain behavior, but because their shape anisotropy is small, the magnetic anisotropy is dominated by strain anisotropy in the presence of the SAWs. The spacing between neighboring nanomagnets (~1 μm) is large enough for the dipole interaction between them to be negligible, which means that magnetically isolated single nanomagnets are probed.

A two-color pump-probe technique (pump wavelength = 400 nm, pulse width = 100 fs, repetition rate = 80 MHz; probe wavelength = 800 nm, pulse width = 80 fs, repetition rate = 80 MHz) was used to measure the Kerr rotation and reflectivity signals as a function of time. The spot size of the probe beam was about 800 nm, while the pump beam was slightly defocused at the focal plane of the probe beam to obtain a spot size of

about 1μm. It is very important to make the center of the pump beam coincide with that of the probe beam in order to collect the signal corresponding to uniform excitation (Fig. 8.1(c)). Since the diameter of a nanomagnet is about 190 nm and the pitch of the array is ~1 μm in a row, the probe beam can be carefully placed and maintained on top of a single nanomagnet using a high-precision x-y-z piezoelectric scanning stage with feedback loop. We were able to obtain signal from a single nanomagnet without cavity enhancement.

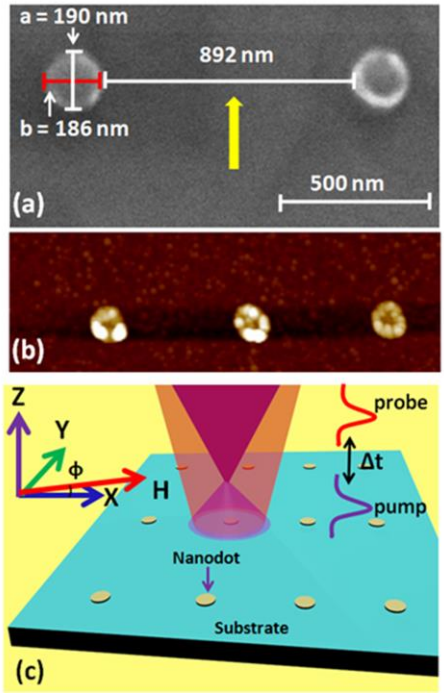

Figure 8.1: (a) Scanning electron micrograph of the Co nanomagnets deposited on a PMN-PT substrate. The edge-to-edge separation between two neighboring nanomagnets in a row [along the line collinear with their minor axis (x-direction)] is about 892 nm, which shows that the pitch of the array is about 1 μm. The separation between two adjacent rows is ~4 μm along the y-direction. Major and minor axes are denoted as a (≈ 190 nm) and b (≈ 186 nm), respectively. The yellow arrow indicates the poling direction of the substrate. (b) Magnetic force micrograph of the nanomagnets which do not show good phase contrast because of insufficient shape anisotropy. (c) The experimental geometry is shown with the bias magnetic field (H) applied along the array in the direction of the nanomagnets' minor axes (x-direction) with a slight out-of-plane tilt (ϕ) of few degrees.

To ascertain that the pump beam indeed generates SAWs in the PMN-PT substrate, we first measured the polarization and intensity of light reflected from the bare PMN-PT

substrate as a function of the delay between the pump and the probe by focusing both pump and probe beams on to the bare substrate. Clear oscillations are observed in both polarization and intensity of the light reflected from the bare substrate and they can only originate from the SAWs. In Fig. 8.2(a), we show the intensity (reflectivity) oscillation for 15 mJ/cm^2 pump fluence (wavelength = 400 nm). As expected, there are multiple oscillation modes in both reflectivity and polarization because of the excitation of SAWs with multiple frequencies. Their frequencies at any given fluence were found to be independent of the bias magnetic field, showing that these oscillations are not of magnetic origin. They arise from the SAWs which cause periodic atomic displacements on the substrate's surface thereby changing the surface charge polarization periodically (PMN-PT is a polar material) and giving rise to polar phonons. The fast Fourier transformation (FFT) of these oscillations reveals the dominance of two peaks (2 GHz and 8 GHz) in the spectra (see Fig. 8.2(b)), which we conclude are the two dominant SAW frequencies excited in the PMN-PT substrate by the pulsed pump beam. There is also a small peak in the spectrum at ~16 GHz, which we ignore (it may be a second harmonic of the 8 GHz oscillation). The SAW wavelength λ associated with the 2 GHz frequency is ascertained from the relation $v = \lambda f$ where v is the phase velocity of the SAW and f is the frequency. The phase velocity of SAW in a (001) PMN-PT crystal depends on the propagation direction, but it is on the order of 2000 m/sec [39]. The 2 GHz mode therefore corresponds to a wavelength of roughly 1 μm, which happens to be the pitch of the array. It therefore appears that this mode is a resonant mode determined by the geometry of the array, as in refs. [17-19]. The 8 GHz mode cannot be related to any obvious geometric feature of the nanomagnet array and may be intrinsic to the substrate.

We next probe the out-of-plane magnetization dynamics (temporal variation in the spatially averaged out-of-plane component of the magnetization) of a single Co nanomagnet on the PMN-PT substrate in the presence of both a bias magnetic field and SAWs by focusing the pump and probe beams (probe beam wavelength = 800 nm and fluence = 2 mJ/cm^2) on a single nanomagnet and measuring the Kerr oscillations as well as oscillations in the reflectivity. We were able to obtain signals from a single nanomagnet without cavity enhancement. In Figs. 8.3 (a) and (b), we show the background-subtracted time-resolved Kerr oscillations in time as a function of bias magnetic field along with their Fourier transforms. The pump fluence was 15 mJ/cm^2.

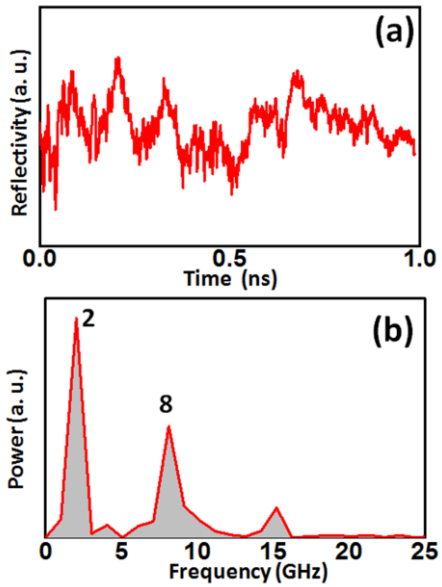

Figure 8.2: (a) Background subtracted time-resolved data for reflectivity of the bare PMN-PT substrate as a function of the delay between the pump and the probe, obtained at 15 mJ/cm^2 pump fluence. (b) Also shown are the fast Fourier transforms of the oscillations. Frequencies of the two most intense peaks are indicated in GHz.

Multiple modes (corresponding to peaks in the Fourier spectra) are observed in both Kerr and reflectivity oscillations at all bias magnetic fields used, with all peaks shifting to lower frequencies with decreasing bias field. This magnetic field dependence shows that these modes have a magnetic component mixed in. The most intense peak (at all bias fields except 700 Oe) is denoted as 'F' in Fig. 8.3(b). Two other prominent peaks that appear at higher and lower frequencies with respect to F are indicated as 'F_H' and 'F_L', respectively. All modes associated with these three peaks in the Fourier spectra are hybrid magneto-dynamical modes arising from the interaction between the magnetic (precession of the magnetization about the bias magnetic field) and the non-magnetic (periodic change in the magnetization due to the periodic strain generated by the SAWs) dynamics. The former dynamics depends on the bias magnetic field while the latter does not. We observed that in all cases, the amplitudes of the reflectivity oscillations are much smaller than those of the Kerr oscillations.

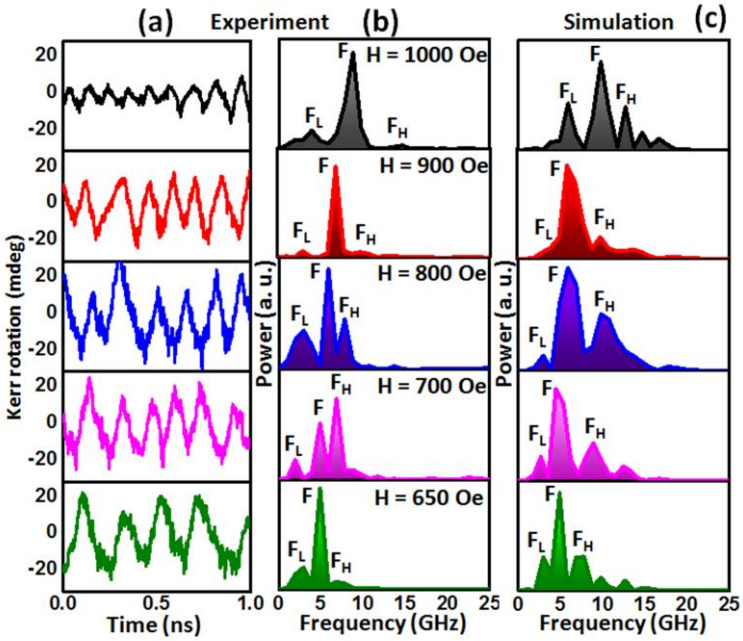

Figure 8.3: Bias magnetic field dependence of the (background-subtracted) time-resolved Kerr oscillations from a single Co nanomagnet on a PMN-PT substrate. The pump fluence is 15 mJ/cm^2. (a) The measured Kerr oscillations in time and (b) the fast Fourier transforms of the oscillations. The Fourier transform peaks shift to lower frequencies with decreasing bias magnetic field strength. There are multiple oscillation modes of various Fourier amplitudes. Out of those, the dominant mode (at all bias fields except 700 Oe) is denoted by F and its nearest modes F_H and F_L. (c) Fourier transforms of the temporal evolution of the out-of-plane magnetization component at various bias magnetic fields simulated with MuMax3 where the amplitude of the periodically varying strain anisotropy energy density K_0 is assumed to be 22,500 J/m^3. The simulation has additional (weak) higher frequency peaks not observed in the experiment. The spectra in the two right panels are used to compare simulation with experiment.

8.3 Results and Discussions

The Kerr and reflectivity oscillations are due to the temporal variation of the spatially-averaged out-of-plane component of the magnetization in the nanomagnet. Therefore, in order to understand the origin of the modes observed in the Kerr and reflectivity oscillations, we have modeled the magnetization dynamics in the Co nanomagnet in the presence of the bias magnetic field and the periodic strain due to the SAWs using the MuMax3 package [40]. The SAW-induced periodic strain anisotropy in the nanomagnet is included in the simulation by making the oscillating strain anisotropy energy density, $K_1(t) = K_0[\sin(2\pi f_1 t) + \sin(2\pi f_2 t)]$,where $K_0 = \frac{3}{2}\chi\sigma$ and f_1, f_2 are the frequencies of the two dominant SAW modes (2 GHz and 8 GHz) observed for the pump fluence of 15

mJ/cm^2. Note that the Kerr and reflectivity signals were obtained at the same fluence, which is why we consider the dominant SAW modes at that fluence. We include only two frequency components in the periodic strain anisotropy (f_1 = 2 GHz and f_2 = 8 GHz) since these two frequency components are dominant and have much higher amplitude than other components in the SAW signal (as shown in Fig. 8.2). Here χ is the magnetostriction coefficient of the nanomagnet (40 ppm) and σ is the maximum stress generated in it by the SAW (stress amplitude). There are also some additional contributions to the periodic stress because of the differential thermal expansions of Co and PMN-PT due to periodic heating by the pump beam, which we neglect in this first-order analysis.

Micromagnetic simulations are carried out with the MuMax3 and Dotmag software. We first run the MuMax3 simulation with the bias magnetic field present, but strain absent, for 1 ns to allow the micromagnetic distribution to settle to steady state. It is verified that running the simulation for a longer time does not change the distribution perceptibly. This distribution is then used as the initial state of the nanomagnet when the oscillating strain and out-of-plane tickle field are turned on in the simulation. The simulation provides the time variation of the (spatially averaged) out-of-plane component of the magnetization $\bar{M}_z(t)$ for any given bias field and oscillating strain anisotropy energy density amplitude K_0. Its Fourier transform spectrum corresponds to that of the Kerr oscillations at that bias field and strain amplitude. The peaks in this spectrum correspond to the (theoretically calculated) frequencies of the hybrid magneto-dynamical modes at that bias field and strain amplitude. The points in the dotted lines of Fig. 8.4 are found by this procedure. Note that only the points in the dotted lines at bias fields of 650, 700, 800, 900 and 1000 Oe have been computed and are meaningful. The rest of the points are extrapolations and are a guide to the eye.

We treat K_0 as a fitting parameter. In the MuMax3 modeling, we generate the time-varying components of the nanomagnet's magnetization $\left[M_x(x,y,z,t), M_y(x,y,z,t), M_z(x,y,z,t)\right]$ for different values of K_0. The minor axis of the nanomagnet is in the x-direction, the major axis is along the y-direction and the z-direction is the out-of-plane direction. We first generate the micromagnetic distribution within the nanomagnet in the presence of the bias magnetic field applied along the x-

direction (but with no strain present) from MuMax3. Then, with this distribution as the initial state, we turn on the two-frequency oscillating strain and a small out-of-plane (square-wave) tickle pulse of amplitude 30 Oe, rise time 10 ps, and duration 100 ps to set the magneto-dynamics in motion. We find $M_x(x,y,z,t), M_y(x,y,z,t), M_z(x,y,z,t)$ for different bias magnetic fields and different values of K_0. We then perform fast Fourier transform of the spatially averaged value of $M_z(x,y,z,t)$, which we call $\bar{M}_z(t)$, and the spectra obtained from this transform (for different bias magnetic fields) are shown in Fig. 8.3 (c). They are compared with the spectra of the Kerr oscillations found experimentally and shown in Fig. 8.3 (b). This comparison leads us to the best fit value of K_0. We find reasonably good agreement between the three dominant peaks F_L, F and F_H of the simulated Kerr spectra and the experimentally measured Kerr spectra for a value K_0 = 22,500 J/m^3 at low bias fields, as shown in Fig. 8.4(a). The agreement deteriorates slightly at high bias fields, showing that perhaps a single fitting parameter K_0 is not adequate to model the entire range of bias fields used in the experiments.

From the value K_0 = 22,500 J/m^3, we can also find the effective stress σ generated in the nanomagnet. Since, $K_0 = \frac{3}{2}\chi\sigma$ we find σ = 375 MPa. We can then find the strain amplitude generated in the nanomagnet from Hooke's law: $\sigma = Y\epsilon$, where Y is the Young's modulus of Co (209 GPa) [41] and ε is the strain amplitude generated by the (polychromatic) SAW. This yields ε = 0.18%. Here, we treat the stress and strain as scalars since we are interested not so much in the accurate stress distribution, but rather the maximum uniaxial strain that is generated in any direction. There are reports of strain > 0.6% generated in PMN-PT [42], so, this large value of strain is not unusual. We can then calculate the effective electric field that would be required to produce the strain of 0.18% in PMN-PT. The reported d_{33} values in PMN-PT are on the order of 2800 pC/N [43]. Hence the effective electric field E in the PMN-PT substrate (calculated from $\epsilon = d_{33}E$) is ~6.4× 10^5 V/m.

In Fig. 8.4(b), we show the pump fluence dependences of the three peak frequencies F_L, F and F_H in the Kerr oscillation spectra (frequencies of the hybrid magneto-dynamical modes) for a bias magnetic field strength of 900 Oe. We expect that the frequency of the magnetic (precessional) component of the mode should depend primarily on the bias magnetic field and hence should be independent of fluence.

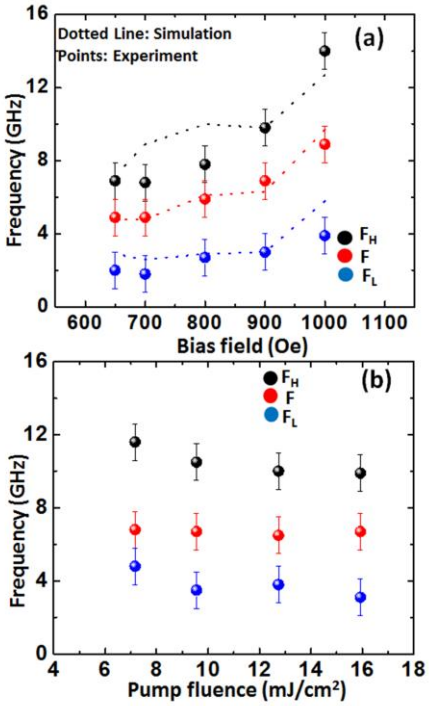

Figure 8.4: (a) Bias field (H) dependence of the observed three dominant frequencies in the Kerr oscillations F_L, F and F_H (frequencies of hybrid magneto-dynamical modes) at 15 mJ/cm^2 pump fluence. We also show alongside (with a dotted line) the Kerr oscillation frequencies obtained from the MuMax3 modeling based on the assumption K_0 = 22,500 J/m^3. The intermediate points in the dotted line are a guide to the eye and are extrapolated. The simulated data points are, for the most part, within the error bars of the experimentally measured data points. (b) Fluence dependence of the frequencies at H = 900 Oe.

Since the frequency of the dominant hybrid mode, F (the one with the largest Fourier component at most bias fields) is almost fluence-independent, and the frequencies of the other two modes are weakly fluence-dependent, it appears that the magnetic component of the hybrid mode (the one associated with precessional dynamics) dominates over the non-magnetic one (the one associated with SAWs) in the hybridization process. This is further supported by the observation that the mode frequencies have a pronounced bias magnetic field dependence, which would not have happened if the non-magnetic component was dominant. Note, however, that the magnetic field dependence of none of the three dominant mode frequencies (F_L, F or F_H) could be fitted with the Kittel formula [44] showing that none is a pure Kittel mode because of the hybridization. In the presence of the SAWs, the total field (resultant of bias magnetic field and the periodic effective magnetic field due to strain) periodically changes the orientation of the magnetization, giving rise to spin waves. This will happen

even if we ignore the precession around the bias field caused by the femtosecond pump beam excitation.

To gain more insight into the nature of the hybrid magneto-dynamical modes associated with the three dominant frequencies in the Kerr oscillations, F_L, F and F_H, we have calculated the power and phase distributions of the spin waves associated with these modes, using a home-built code Dotmag [45].

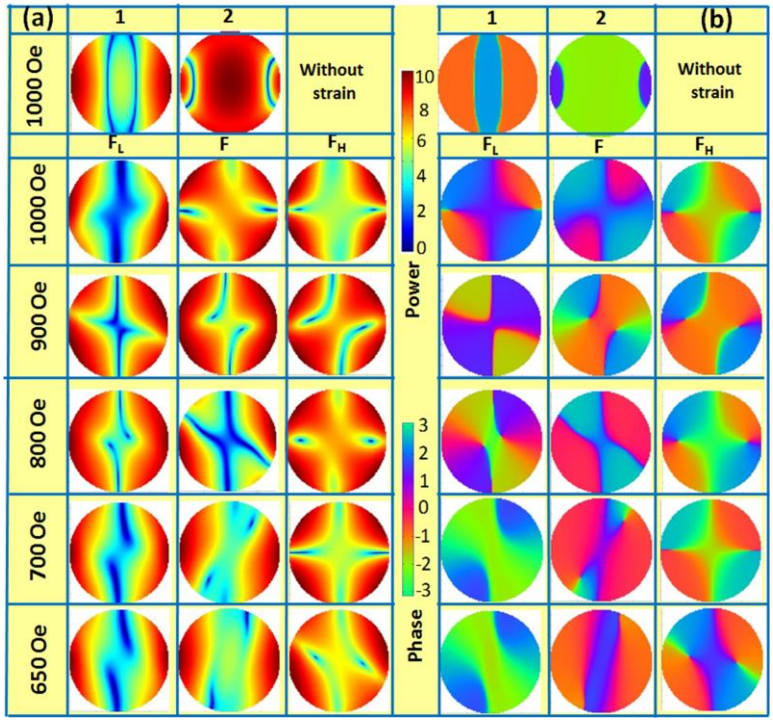

Figure 8.5: (a) Simulated power and (b) phase profiles of the spin waves associated with the three dominant frequencies F_L, F and F_H in the Kerr oscillations at any given bias field. The top most row shows edge and center modes at the two dominant frequencies in the Kerr oscillations in the absence of strain at 1000 Oe bias field. The units of power and phase are dB and radians, respectively.

We first theoretically examine the unstrained nanomagnet that is not subjected to SAWs and hence experiences pure precessional dynamics because of the bias magnetic field. In this case, the fast Fourier transform of $\bar{M}_z(t)$ reveals two (bias-dependent) dominant frequencies at any given bias magnetic field. The power and phase distributions of the spin wave modes associated with these two frequencies are shown in the first row of Fig. 8.5 for a bias magnetic field of 1000 Oe applied along the ellipse's minor axis. These distributions reveal that one of the spin wave modes in the unstrained nanomagnet is a

center mode (mode 2), with power concentrated in the center, and the other is an edge mode (mode 1) with power concentrated at two vertical edges which are perpendicular to the bias field [46].

When the periodic strain anisotropy due to the SAWs (with frequencies of 2 and 8 GHz and energy density amplitude K_0 = 22,500 J/m^3) is introduced, the nature of the spin waves associated with the dominant frequencies F_L, F and F_H in the Kerr oscillations becomes very different. Instead of center and edge mode behavior, the hybrid magneto-dynamical modes of frequencies F_L, F and F_H display complex spin wave profiles with their unique characteristics. The most intense mode F at 1000 Oe field contains power throughout the nanomagnet, while the phase profile suggests that spins precess alternatively in opposite phases giving rise to the azimuthal contrast with azimuthal mode quantization number n = 5. On the other hand, the spin waves corresponding to the two modes at frequencies F_L and F_H appear as the modified edge mode and quantized mode of the nanomagnet. As the bias field is reduced, the mode with frequency F starts showing some quantization at the intermediate fields and finally transitions to edge mode like behavior in the low field regime. At an intermediate bias field of H = 800 Oe, the higher frequency mode (F_H) shows azimuthal character with n = 5. An important feature is that spin wave power is no longer concentrated along the vertical edges of the nanomagnet like in the conventional edge mode (perpendicular to the applied field) but gets slightly rotated. This is a consequence of having the SAW induced time-varying strain field present, along with the constant bias field in the system, and their competition. The component of the effective magnetic field due to strain in the i-th direction (i = x, y, z) is approximately, $H_{strain}^{i}(t) = \frac{3\chi\sigma(t)m_i(t)}{\mu_0 M_s} = \frac{2K_1(t)m_i(t)}{\mu_0 M_s}$, where $m_i(t)$ is the i-th component of the (spatially averaged) normalized magnetization of the nanomagnet at time t [47]. The amplitude of this field is 409 Oe when K_0 = 22,500 J/m^3. Hence, it is of the same order as the bias field when it is at its maximum. The spin wave profiles in Fig. 8.5 reveal the rich physics of the interaction between the bias field and SAW that produces the hybrid magneto-dynamical modes.

8.4 Conclusions

In conclusion, we have observed hybrid magneto-dynamical modes in a single quasi-elliptical nanomagnet of Co fabricated on top of a poled (001) PMN-PT substrate due to magneto-elastic modulation of the precessional dynamics. The frequencies of these modes are in the neighborhood of 10 GHz, corresponding to ~100 ps time scale dynamics. This shows that strain can affect the magnetization state of even a weakly magnetostrictive nanomagnet in time scales far shorter than 1 ns. The spin wave textures of these modes display rich variation with the applied bias field.

Magneto-electrically generated spin waves have important applications, such as in magneto-electric spin wave amplifier for logic [48, 49]. This work sheds light on the practical operating speeds of such devices. This work also has implications for magnetic nano-oscillators which are used as nanoscale microwave generator [50], spin wave emitters, and in artificial neural networks [51]. They are usually actuated by a spin-polarized current delivering a spin-transfer-torque. One can actuate them with strain, instead of a spin -polarized current, if they are fashioned out of a magnetostrictive nanomagnet elastically coupled to an underlying piezoelectric substrate [52]. Since strain-induced switching is far more energy-efficient than spin-transfer-torque (STT) switching, such nano-oscillators will dissipate far less energy than their STT-counterparts. This work shows that the frequency range of operation of straintronic nano-oscillators can be ~10 GHz, which makes them an attractive alternative for the more common spin-torque based nano-oscillators.

Finally, there are other mechanisms at the interface of a ferromagnet and a ferroelectric that can affect the magnetic moments in the ferromagnet. One such mechanism is associated with charge screening at the interface that can affect the magnetic moments or magnetic anisotropy [53]. These mechanisms usually require an epitaxially grown thin ferromagnetic film that has strong bonding at the interface with the ferroelectric substrate. Our structures are not thin films and not epitaxially grown on the PMN-PT substrate. They are amorphous or polycrystalline Co nanostructure deposited (not epitaxially grown) on a ferroelectric substrate by electron-beam evaporation of Co through lithographically delineated windows in a resist. It is therefore very unlikely that these other mechanisms can play any significant role.

References

1. S. D. Bader, Rev. Mod. Phys. **78**, 1-15 (2006).
2. A. Fert, V. Cros, J. Sampaio, **8**, 152-156 (2013).
3. S. Ladak, D. E. Read, W. R. Branford, L. F. Cohen, Nat. Phys. **6**, 359-363 (2010).
4. A. Barman and J. Sinha, *Spin Dynamics and Damping in Ferromagnetic Thin Films and Nanostructures*, (Springer, Switzerland, 2018).
5. S. S. P. Parkin, M. Hayashi, L. Thomas, **320**, 190-194 (2008).
6. A. Fernández-Pacheco, R. Struebel, O. Fruchart, R. Hertel, P. Fischer, and R. P. Cowburn, Nat. Commun. **8**, 15756 (2017).
7. K. Roy, S. Bandyopadhyay, and J. Atulasimha, Appl. Phys. Lett. **99**, 063108 (2011).
8. N. D'Souza, M. Salehi-Fashami, S. Bandyopadhyay, and J. Atulasimha, Nano Lett., **16**, 1069-1075 (2016).
9. N. D'Souza, A. Biswas, H. Ahmad, M. Salehi-Fashami, M. M. Al-Rashid, V. Sampath, D. Bhattacharya, M. A. Abeed, J. Atulasimha, and S. Bandyopadhyay, Nanotechnology **29**, 442001 (2018).
10. Y. Yang, H. Huang, Z. Luo, C. Gao, X. Li, and C. F. Tao, J. Appl. Phys. **122**, 134105 (2017).
11. S-W. Yang, R-C. Peng, T. Jiang, Y-K. Liu, L. Feng, J-J. Wang, L-Q. Chen, X-G. Li, and C-W. Nan, Adv. Mater. **26**, 7091-7095 (2014).
12. A. Barman, and A. Haldar, *Time-domain study of magnetization dynamics in magnetic thin films and micro-and nanostructures.* Solid State Phys, vol **65**. (Elsevier Inc., Burlington, 2014).
13. A. Barman, S. Wang, J. D. Maas, A. R. Hawkins, S. Kwon, A. Liddle, J. Bokor, H. Schmidt, Nano Lett. **6**, 2939-2944 (2006).
14. A. Barman, and S. Wang, Appl. Phys. Lett. **90**, 202504 (2007).
15. B. Rana, D. Kumar, S. Barman, S. Pal, Y. Fukuma, Y. Otani, and A. Barman, ACS Nano **5**, 9559-9565 (2011).
16. H. Ahmad, J. Atulasimha, and S. Bandyopadhyay, Nanotechnology **26**, 401001 (2015).
17. Y. Yahagi, B. Hartenek, S. Cabrini, H. Schmidt, Phys. Rev. B. **90**, 140405(R) (2014).
18. Y. Yahagi, C. Berk, B. Hebler, S. Dhuey, S. Cabrinia, M. Albrecht, and H. Schmidt, J. Phys. D: Appl. Phys. **50**, 17LT01 (2017).

19. Y. Yahagi, B. Hartenek, S. Cabrini, H. Schmidt, Control of Magnetization Dynamics in Patterned Nanostructures with Magneto-elastic Coupling, Photonic and Phononic Properties of Engineered Nanostructures V, Eds. A. Adibi, S-Y Lin, and A. Scherer, Proc. SPIE 9371 (2015).
20. H. F. Yang, F. Garcia-Sanchez, X. K. Hu, S. Sievers, T. Bohnert, J. D. Costa, M. Tarequzzaman, R. Ferreira, M. Bieler, and H. W. Schumacher, Appl. Phys. Lett. **113**, 072403 (2018).
21. V. Sampath, N. D'Souza, D. Bhattacharya, G. M. Atkinson, S. Bandyopadhyay, and J. Atulasimha, Nano Lett. **16**, 5681-5687 (2016).
22. V. Sampath, N. D'Souza, G. M. Atkinson, S. Bandyopadhyay, and J. Atulasimha, Appl. Phys. Lett. **109**, 102403 (2016).
23. K. Roy, S. Bandyopadhyay, and J. Atulasimha, arXiv:1012.0819, (2012)**.**
24. A. K. Biswas, S. Bandyopadhyay, and J. Atulasimha, Appl. Phys. Lett. **103**, 232401 (2013).
25. S. Davis, A. Baruth, and S. Adenwalla, Appl. Phys. Lett. **97**, 232507 (2010).
26. W. Li, B. Buford, A. Jander, P. Dhagat, IEEE Trans. Magn. **50**, 2285018 (2014).
27. W. Li, B. Buford, A. Jander, and P. Dhagat, J. Appl. Phys. **115**, 17E307 (2014).
28. O. Kovalenko, T. Pezeril, and V. V. Temnov, Phys. Rev. Lett. **110**, 266602 (2013).
29. M. Foerster, F. Macià. N. Statuto, S. Finizio, A. Hernández-Mínguez, S. Lendínez, P. V. Santos, J. Fontcuberta, J. M. Manel Hernàndez, M. Kläui, and L. Aballe, Nat. Commun. **8**, 407 (2017).
30. M. Bombeck, A. S. Salasyuk, B. A. Glavin, A. V. Scherbakov, C. Brüggemann, D. R. Yakovlev, V. F. Sapega, X. Liu, J. K. Furdyna, A. V. Akimov, M. Bayer, Phys. Rev. B **85,** 195324 (2012).
31. A. V. Scherbakov, A. S. Salasyuk, A. V. Akimov, X. Liu, M. Bombeck, C. Brüggemann, D. R. Yakovlev, V. F. Sapega, J. K. Furdyna, and M. Bayer, Phys. Rev. Lett. **105**, 117204 (2010).
32. L. Thevenard, I. S. Camara, S. Majrab, M. Bernard, P. Rovillain, A. Lemaître, C. Gourdon, and J.-Y. Duquesne, Phys. Rev. B **93**, 134430 (2016).
33. M. Weiler, L. Dreher, C. Heeg, H. Huebl, R. Gross, M. S. Brandt, and S. T. B. Goennenwein, Phys. Rev. Lett. **106,** 117601 (2011).
34. J. Janusonis, C. L. Chang, P. H. M. van Loosdrecht, and R. I. Tobey, Appl. Phys. Lett. **106**, 181601 (2015).

35. U. Singh, and S. Adenwalla, Nanotechnology **26**, 255707 (2015).
36. L. Thevenard, J.-Y Duquesne, E. Peronne, H. J. von Bardeleben, H. Jaffres, S. Ruttala, J-M. George, A. Lemaître, and C. Gourdon, Phys. Rev. B **87**, 144402 (2013).
37. E. M. Chudnovsky, and R. Jaafar, Phys. Rev. Appl. **5**, 031002 (2016).
38. J. Tejada, E. M. Chudnovsky, R. Zarzuela, N. Statuto, J. Calvo-de la Rosa, P. V. Santos, and A. Hernández-Mínguez, Europhys. Lett. **118**, 37005 (2017).
39. K. H. Choi, J. H. Oh, H. J. Kim, J. Y. Kim, S. G. Lee, Rhim, S. M. Proc. 2001 IEEE Ultrasonics Symp. **161** (2001).
40. A. Vansteenkiste, J. Leliaert, M. Dvorkik, M. Helsen, F. Garcia-Sanchez, and B. van Waeyenberge, AIP Adv. **4**, 107133 (2014).
41. A. M. James, and M. P. Lord, Macmillan's Chemical and Physical Data, Macmillan, London, UK, 1992.
42. S-E. Park, and T. R. Shrout, J. Appl. Phys. **82**, 1804-1811 (1997).
43. R. Zhang, B. Jiang, and W. Cao, Elastic, J. Appl. Phys. **90**, 3471-3475 (2001).
44. C. Kittel, Phys. Rev. **73**, 155-161 (1984).
45. D. Kumar, O. Dmytriiev, S. Ponraj, and A. Barman, J. Phys. D: Appl. Phys. **45**, 015001 (2012).
46. A. Barman, V. V. Kruglyak, R. J. Hicken, J. M. Rowe, A. Kundrotaite, J. Scott, and M. Rahman, Phys. Rev. B **69**, 174426 (2004).
47. M. Salehi-Fashami, K. Roy, J. Atulasimha, and S. Bandyopadhyay, Nanotechnology **22**, 155201 (2011).
48. A. Khitun, D. E. Nikonov, and K. L. Wang, J. Appl. Phys. **106**, 123909 (2009).
49. S. Cherepov, P. K. Amiri, J. G. Alzate, K. Wong, M. Lewis, P. Upadhyaya, J. Nath, M. Bao, A. Bur, T. Wu, G. P. Carman, A. Khitun, K. L. Wang, Appl. Phys. Lett. **104**, 082403 (2014).
50. T. Chen, R. K. Dumas, A. Eklund, P. K. Muduli, A. Houshang, A. A. Awad, P. Dürrenfeld, B. Gunnar Malm, A. Rusu, and J. Akerman, Proc. IEEE **104**, 1919-1945 (2016).
51. K. Yogendra, D. Fan, and K. Roy, IEEE Trans. Magn. **51**, 4003939 (2015).
52. M. G. A. Park; S-H. C. Baek, B. G. Park, and S. H. Lee, Appl. Phys. Lett. **108**, 023504 (2016).
53. C. G. Duan, S. S. Jaswal, and E. Y. Tsymbal, Phys. Rev. Lett. **97**, 047201 (2006).

Chapter 9

9 All-optical Detection of Spin Hall Angle in W/CoFeB/SiO_2 Heterostructures by Varying Tungsten Layer Thickness

9.1 Introduction

The exciting new frontier of spintronics [1, 2] and magnonics [3, 4] research is driven by the need of utilizing spin-orbit (SO) effect for obtaining pure spin current [5, 6]. An important aspect of improving the performance of the device is to minimize Joule heating, which requires fundamentally pure spin current [5, 6, 7]. It is quite non-trivial to generate and transport the spin current. Some of the earlier studies have used non-local spin-injection (NLSI) techniques [8, 9, 10], spin pumping [11, 12, 13], and Rashba effect [14] for generating spin currents. Moreover, utilization of pure spin current for magnetization manipulation poses additional challenges. Recent finding of spin Hall effect (SHE) [15] has opened up the possibility of utilizing pure spin current for manipulation of magnetic moments [5, 16, 17]. To quantify the SHE, an important parameter, namely, spin Hall angle (SHA), has been proposed and it is related to the conversion efficiency of charge-to-spin current [18, 19]. Considerable efforts have been devoted for estimating and understanding the value of SHA for various heavy metals (HMs). Particularly, the SHE in HM layers can generate sufficiently large spin current to manipulate magnetic moments of a ferromagnetic layer adjacent to the HM layer as it exerts significant spin torque [16, 20]. Furthermore, the SHE induced spin-orbit torques (SOTs) have been shown to induce the large domain wall velocity [17], excite precessional magnetization dynamics [21, 22, 23] as well as result in magnetization switching [24]. Remarkably, it has been recently demonstrated that by using sophisticated device structuring, SOT induced magnetization switching can be triggered in the absence of any magnetic field [25, 26, 27]. Some key requirements for technological implementation of the above mentioned interesting applications are to search for HMs with reasonably large SHA, investigation of various factors affecting the SHA of HM thin films, and to understand the variation of SHA in such HM thin films by

controlling those factors. An important issue in this research is to establish an accurate and unambiguous measurement technique of SHA. The precise quantification of SHA and its origin in a conventional metal-based system is of technological interest for spintronics based device applications. In general, the techniques used for determining the SHA are the spin torque ferromagnetic resonance (ST-FMR) technique [16, 28, 29] spin torque switching of perpendicularly magnetized films [26] and measurement based on non-local spin valves [7]. All these techniques primarily rely on electrical excitation, detection and extremely delicate micro-fabrication [30]. Recently, it has been demonstrated that by using time resolved magneto-optical Kerr effect (TR-MOKE) [31] technique SHA can be measured more conveniently in a non-invasive manner without the requirement of advanced micro-fabrication and electrical detection, and more precise estimate of SHA may be obtained [32].

The highly resistive β-tungsten (distorted tetragonal phase commonly referred to as A15 structure) is known to be one of the efficient materials for exhibiting large SHA due to strong SO coupling [33]. Also, in ferromagnetic thin film heterostructures, use of tungsten (W) leads to highly stable perpendicular magnetic anisotropy [34] and interfacial Dzyaloshinskii Moriya interaction [35]. Another important characteristics associated with W is the thickness dependent phase transition exhibited by it, usually observed in the thickness range of sub-10 nm [36, 37]. In general, sputter deposited W films with thickness below 5 nm is found to have β phase with resistivity larger than 150 μΩ-cm, whereas the films with thickness above 5 nm possess predominantly α phase (BCC structure) with resistivity of about 40 μΩ-cm [24, 33, 38]. Till date, the SHA for W has been reported in few studies for mostly in β phase. However, a systematic study of SHA in W/ferromagnet (FM)/oxide heterostructure with W layer thickness varying across the structural phase transition is missing. Depending on the deposition condition, SHA values of up to about 0.4 have been reported specifically for β phase of W [24, 39]. Few reports have mentioned relatively small SHA for α phase of W [33]. Therefore, it calls for investigating the systematic dependence of SHA on the structural phase of W which is intricately related to its thickness. Furthermore, few important recent studies have suggested that the transparency of HM/FM interface plays a crucial role in evaluating the SHA of HM layer [40, 41, 42]. Additionally, a theoretical study has classified the bulk and interface SHE and claimed that the interface SHE may be as large as 25 times than the bulk SHE [43]. Recently, by alloying different HM layers, attempts

have been made to achieve large SHA [44]. All these studies relate to the intricate role of spin orbit coupling induced SHE in generating pure spin current that is aimed towards utilization for device applications.

Here, we present the correlation between thickness dependent phase transition in W thin films and large SHE induced modulation of damping (MOD) in technologically important Sub/W(t)/$Co_{20}Fe_{60}B_{20}$(3 nm)/SiO_2(2 nm) heterostructures. All-optical detection technique TR-MOKE is used for investigating the magnetization dynamics [32]. Utilizing the sensitive variation of MOD, we estimate the SHA. We observe a clear variation in the value of estimated SHA with the phase of W underlayer. However, even within the β phase, when the thickness of W is smaller than its spin diffusion length, the value of SHA is found to be significantly low. We correlate this variation of SHA with the SO coupling of the bulk of the HM layer as well as the interfacial electronic effect at the HM/FM interface.

9.2 Experimental Details

The thin film heterostructures Sub/W(t)/$Co_{20}Fe_{60}B_{20}$(3 nm)/SiO_2(2 nm) with t = 2 to 7 nm in the step of 1 nm were deposited by dc/rf magnetron sputtering on Si (100) wafers coated with 100 nm SiO_2. The purpose of varying W underlayer thickness was to choose W thickness across the phase transition regime. The base pressure of the deposition chamber was better than 2 × 10^{-7} Torr. CoFeB and W were grown using dc power of 20 Watt whereas the SiO_2 was grown using rf power of 60 Watt at 13.56 MHz. All thin films were grown in Ar gas atmosphere of 1 mTorr pressure and deposition conditions were carefully optimized [35]. Using a shadow mask, 5-nm-thick chromium/25-nm-thick gold contact electrodes were first prepared, followed by deposition of the sample stack of 3 mm × 1 mm dimension between the contact electrodes using another shadow mask.

The dc charge current was applied along the length of the sample using a standard source-meter [U3606A, Agilent Technologies] and experimental arrangement allowed us to suitably choose the applied bias magnetic field angle with respect to the current flow direction. Time resolved magneto-optical Kerr effect microscopy was exploited to study the magnetization dynamics of the heterostructures. The second harmonic (wavelength: 400 nm, pulse width: 100 fs) of a mode locked Ti:sapphire oscillator

(Tsunami, Spectra Physics) was used as the pump beam to excite the magnetization dynamics in the samples, whereas the fundamental laser beam (wavelength: 800 nm, pulse width: 80 fs, repetition rate: 80 MHz) was used as the probe beam to detect polar Kerr rotation from the sample as a function of the time delay between the pump and the probe beam [31, 32]. The temporal resolution of the measurement is limited by the cross-correlation between the pump and probe pulses. A large magnetic field is first applied at a small angle of about 15° to the sample plane to saturate its magnetization. This is followed by reduction of the magnetic field to the bias field value (H = in-plane component of the bias field), which ensures that the magnetization remains saturated along the bias field direction.The slight tilt of magnetization from the sample plane ensures a finite demagnetizing field along the direction of the pump pulse, which is further modified by the pump pulse to launch a precessional dynamics within the sample. In our experiment 1.7 ns time window has been used, which gave a damped uniform precession of magnetization. The pump and probe beams are made collinear andare focused on the sample through a microscope objective with N.A. = 0.65. At the focal plane of the probe (diameter ≈ 800 nm) the pump beam is slightly defocused and has a larger diameter (≈ 1 μm) than the probe beam. The probebeam is carefully centred on the pump beam so that the Kerr signal can be collected from the uniformly excited part of the sample and slight misalignment duringthe course of the experiment does not affect the pump-probe signals. The pump beam is chopped at 2 kHz frequency and the Kerr rotation in the reflected probe pulse is detected by using a balanced photodiode detector and lock-in amplifier in a phase sensitive manner. The time-resolved reflectivity data is simultaneously recorded to ensure that there is no breakthrough of Kerr rotation and reflectivity data into one another. The pump and probe fluences are chosen to be about 10 mJ/cm^2 and 2 mJ/cm^2 to avoid the transient increment in damping due to laser heating. All the experiments were performed under ambient condition. Atomic force microscope was used to investigate the surface topography, whereas vibrating sample magnetometer was used to characterize the static magnetic properties of these heterostructures. Using standard four probe technique the resistivity of W film was determined and the grazing incidence X-ray diffraction was used for investigating the phase of W.

9.3 Results and Discussions

Figure 9.1 (a) shows the grazing incidence X-ray diffraction (XRD) patterns for Sub/W(t)/$Co_{20}Fe_{60}B_{20}$(3 nm)/SiO_2(2 nm). In these XRD plots, the peaks corresponding to α and β phase of W are marked. The high intensity XRD peak at ~40.5° corresponds primarily to the α phase (BCC structure) of W (~40.5°) (110) orientation. Interestingly, we find that the peak in the vicinity of 40.5° is present for all thicknesses of W but when the W thickness is less than 6 nm, then the peaks (~34.8° and ~42.1°) corresponding to β-W (A15 structure) with (200) and (211) crystal orientations appear [38, 41]. One may note that in close proximity of 40°, β-W peak for (210) crystal orientation could also be present, which is quite difficult to identify. We wish to clarify here that for W thickness below 5 nm the β-rich phase along with small amount of α phase exists while with increasing thickness of the W layer the fraction ofα phase increases and starts to dominate for W thickness above 5 nm. For the sake of simple notation we refer the phase below 5 nm W as β-phase and above this thickness as α-phase. These findings are consistent with some of the existing literature reports, where it is described that W exhibits a transition from β phase (A15 structure) to α phase (BCC structure) with increasing film thickness in the range of about 5 to 6 nm [36, 37]. It has also been shown in some other studies that this transition thickness may be increased or decreased by carefully tuning the deposition conditions of the W thin films [38, 45].

In Fig. 9.1 (b), the atomic force microscope images for all the Sub/W(t)/$Co_{20}Fe_{60}B_{20}$(3 nm)/SiO_2(2 nm) heterostructures, investigated in the present study are shown. We have used WSxM software to process the images [46]. From these images we observe that the average topographical roughness for the samples with t = 2, 3, 4, 5, 6 and 7 nm are listed below,

Table 9.1: The average roughness values obtained using atomic force microscopy for Sub/W(t)/$Co_{20}Fe_{60}B_{20}$(3 nm)/SiO_2(2 nm) samples with different W thicknesses.

W thickness (nm)	2	3	4	5	6	7
Average roughness (nm)	0.21	0.21	0.16	0.19	0.14	0.23

The roughness values vary by about 10% when measured at various regions of space of the same sample. Overall, the topographical roughness in all film stacks is found to be significantly small irrespective of whether the W thickness corresponds to its β or α phase. Due to the small thicknesses of the thin film heterostructures, presumably, the interfacial roughness will clearly show its imprint on the topographical roughness. We thus infer that the interfacial roughness, if any, present in these heterostructures is very small and is similar in all samples.

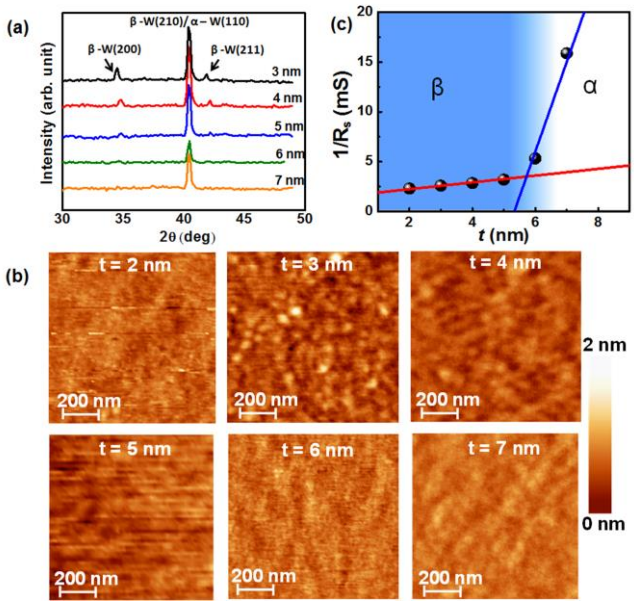

Figure 9.1: (a) X-ray diffraction patterns measured at grazing angle incidence for W films with thickness of 3 nm, 4 nm, 5 nm, 6 nm and 7 nm. Peaks corresponding to β and α phase of W are marked in the plots. (b) Atomic force microscope images showing the surface topography of the Sub/W(t)/$Co_{20}Fe_{60}B_{20}$(3 nm)/SiO_2(2 nm) samples with t = 2 nm to 7 nm. The images are presented with the same scale bar as shown at the right hand side of the figure. (c) Variation of inverse of sheet resistance of Sub/W(t)/$Co_{20}Fe_{60}B_{20}$(3 nm)/SiO_2(2 nm) as a function of W thickness (t) measured using linear four probe technique.

To determine the variation of resistivity of W with its thickness across the two different phases, we performed four probe measurements on all the samples. Charge current was applied along the length of the sample and the experiment was performed in constant current mode. The inverse of sheet resistance (R_S) of the film stack as a function of W thickness is plotted in Fig. 9.1(c). A change of the slope is observed beyond 5 nm, which indicates a change in the W resistivity. We estimate the average resistivity of W in β and α-rich phase to be about 260 μΩ-cm and 105 μΩ-cm, respectively [47].

We next focus on the mechanism involved in the tuning of magnetization dynamics under the influence of spin current. Figures 9.2 (a) and (b) show the schematics of experimental arrangement before and after the approach of pump-probe pulses. The flow of charge current through the W layer and consequent spin current generation due to SHE are shown along x and z directions, respectively. Under the influence of spin current, the CoFeB layer experiences an anti-damping like SOT and the magnetization dynamics is governed by modified Landau-Lifshitz-Gilbert equation [32] as given below:

$$\frac{d\boldsymbol{m}}{dt} = -\gamma\, \boldsymbol{m} \times \boldsymbol{H}_{eff} + \frac{\alpha}{M_s}\, \boldsymbol{m} \times \frac{d\boldsymbol{m}}{dt} + \frac{\hbar}{2e\mu_0 M_s d} J_s\, (\boldsymbol{m} \times \boldsymbol{\sigma} \times \boldsymbol{m}) \tag{9.1}$$

Here, γ is the gyromagnetic ratio, σ is the spin polarization vector, $\hat{m}$ is the magnetization vector, M_s is saturation magnetization, J_s is spin current density, H_{eff} is the effective magnetic field, d is the ferromagnetic layer thickness and α is the Gilbert damping constant [7, 48]. Depending on the polarity of σ, the spin torque [28] acts collinearly against or towards the intrinsic Gilbert damping of the precessing magnetization. Effective damping, in turn, gets modulated depending on the injected spin current density and relative orientation between the magnetic moment (which lies along the direction of magnetic field) and charge current density [28]. The modulation of damping (MOD) under the influence of spin current [32] can be expressed as:

$$\Delta\alpha = \alpha_{eff} - \alpha_0 = \frac{\hbar\gamma\, J_s}{2eM_s d 2\pi f} \tag{9.2}$$

where α_0 and α_{eff} are the damping in the absence and presence of applied charge current, e is electronic charge, f is the precessional frequency and other symbols have the same meaning as described before in the text. This approach is valid in the high field limit and assuming that the the magnetic moment and the direction of the charge current is perpendicular to each other [49, 50]. Thus, the SHA (charge current to spin current conversion efficiency) is given by:

$$\theta_{SH} = \frac{J_s}{J_c} = \frac{2eM_s d 2\pi f \Delta\alpha}{\hbar\gamma\, J_c sin\theta} \tag{9.3}$$

where, charge current density through W layer has been denoted as J_c. θ is the angle between J_c and bias magnetic field direction which is 90° in the present case.

Experimentally, we find the value of $\Delta\alpha/J_c$ and estimate the SHA using the above expression.

In Fig. 9.2(c), the as measured data using TR-MOKE set-up is shown for the Sub/W(4 nm)/$Co_{20}Fe_{60}B_{20}$(3 nm)/SiO_2(2 nm)sample at H = 1.46 kOe without any applied charge current. The femtosecond laser excites the sample thereby triggering the magnetization dynamics. Overall, the dynamics can be divided into three different temporal regimes as shown in the plot. Regime I (sharp drop immediately after negative delay, ~700 fs) corresponds to ultrafast demagnetization [51] and regime II corresponds to the fast relaxation (1.7 ps) due to the spin lattice relaxation. Subsequently, in regime III, we observe a slower relaxation (~ 40 ps) along with magnetization precession, which gets damped in few ns. The slower relaxation is due to heat diffusion from the lattice to the substrate and surrounding. We mainly concentrate in regime III to estimate the damping and its modulation due to the action of spin torque. The blue line in Fig. 9.2(c) corresponds to the bi-exponential background present in the precessional data in regime III. We subtract this background from the raw data and fit the resulting data using standard damped harmonic function. From the fit we estimate the damping α_{eff} using the expression $\alpha_{eff} = \frac{1}{2\pi f\tau}$, where f is the precessional frequency and τ is the relaxation time corresponding to magnetization oscillation.

We further studied the bias field dependent magnetization dynamics and Fig. 9.3(a) shows a representative experimental data of precessional magnetization dynamics along with the theoretical fit using a damped sinusoidal function for Sub/W(4 nm)/$Co_{20}Fe_{60}B_{20}$(3 nm)/SiO_2(2 nm) sample. From the fitting, we extract the relaxation time (τ) as 0.52, 0.59 and 0.70 ns for bias field values of 1.46, 1.05 and 0.65 kOe, respectively. Figure 9.3(b) shows the corresponding fast Fourier transform (FFT, power vs. frequency), from which the precessional mode frequency is extracted. The frequency (f) versus bias magnetic field (H) is plotted in Fig. 9.3(c) for the same film stack. Standard Kittel expression mentioned below is used to fit the f vs. H data:

$$f = \frac{\gamma}{2\pi}\sqrt{H(H + 4\pi M_{eff})} \tag{9.4}$$

where $\gamma = g\mu_B/\hbar$, g is the Lande g factor, H is the applied bias magnetic field and M_{eff} is the effective magnetization.

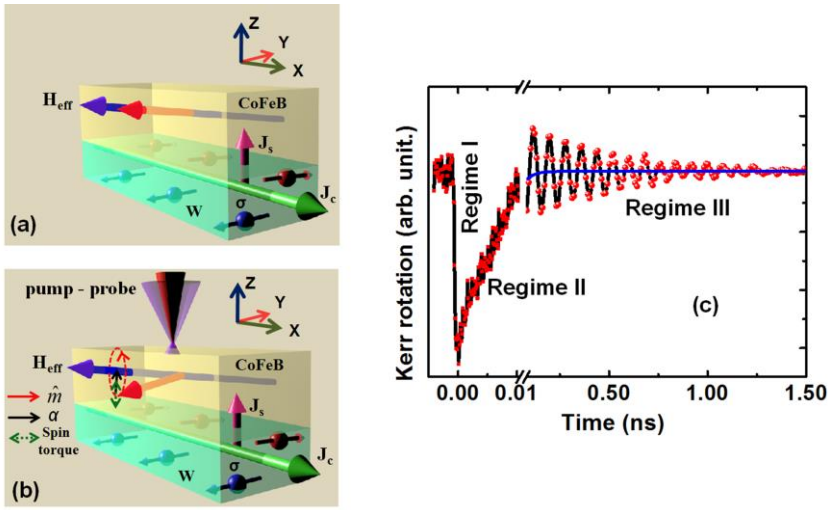

Figure 9.2: Schematic of sample geometry and illustration of experimental geometry (a) before and (b) after the approach of pump and probe laser pulses. Co-ordinate convention as followed is also shown. The blue and red cylindrical arrows indicate the orientation of effective magnetic field and initial magnetization, respectively.(c) Time-resolved Kerr rotation data for Sub/W(4 nm)/$Co_{20}Fe_{60}B_{20}$(3 nm)/SiO_2(2 nm) sample at applied field, H = 1.46 kOe is shown. The three different temporal regimes are indicated in the graph.

From the fit M_{eff} and g are determined as fitting parameters. For these film stacks we obtain $M_{eff} \sim 1000 \pm 30$ emu/cc and $g = 2.0 \pm 0.5$, except for the W thickness of 5 nm, where M_{eff} is found to be lower (770 ± 24 emu/cc). In Fig. 9.3(d), the M_{eff} obtained from the dynamic measurement is plotted as a function of W thickness, t. Interestingly, for all the film stacks investigated in this study, M_{eff} is found to be close to the saturation magnetization M_s obtained using vibrating sample magnetometer. From this we infer that interface anisotropy is negligibly small in these heterostructures [35]. Figure 9.4 shows some typical time-resolved Kerr rotation data after the application of dc charge current through the film stack with different polarities and the MOD as a function of the dc charge current density. The applied charge current through the heterostructure gets distributed into W and CoFeB layers according to the resistivity of each metallic layer. Here, J_c represents the current density through the W underlayer. Figure 9.4(a) shows the magnetization precession data at a bias field H = 1.46 kOe and for positive and negative J_c (θ = 90°) along with the fit using damped sine function to extract the damping. The magnitude and sign of J_c and the corresponding extracted value of effective damping α are mentioned in each panel. A direct comparison of MOD with

applied J_c is shown for three representative thickness of W in Fig. 9.4(b) *i.e.*, t = 3 nm, 4 nm (corresponding to β-rich phase) and 7 nm (corresponding to α-rich phase).

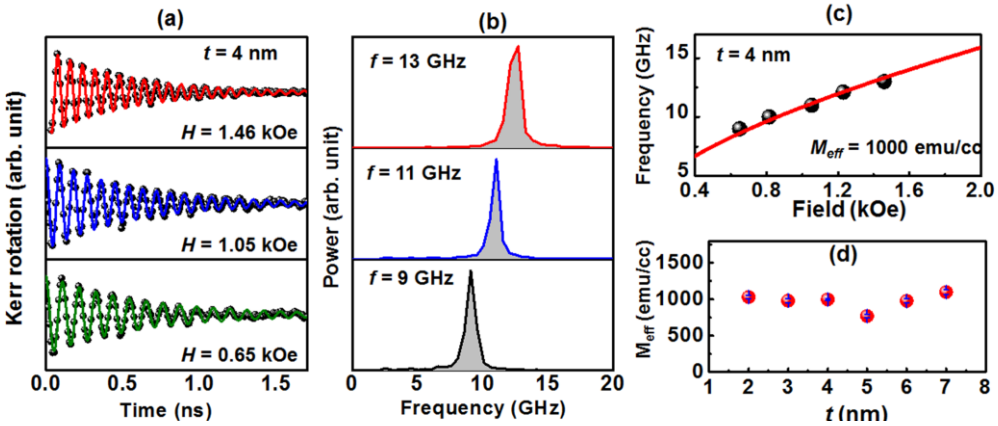

Figure 9.3: (a) Time-resolved precessional magnetization dynamics for Sub/W(4 nm)/$Co_{20}Fe_{60}B_{20}$(3 nm)/SiO_2(2 nm) sample at different bias magnetic field values. (b) The corresponding FFT power spectra to extract the precession frequency. (c) Plot of variation of frequency as a function of bias magnetic field. The solid line is the fit with Kittel formula. (d) Saturation magnetization of the Sub/W(t)/$Co_{20}Fe_{60}B_{20}$(3 nm)/SiO_2(2 nm) samples as a function of W layer thickness.

From these plots, it is evident that the spin current induced spin torque generated by SHE almost linearly modulates the damping consistent with the existing literature [28, 32]. We use a linear fit and extract the slope of MOD ($\Delta\alpha/J_c$) in order to estimate the SHA using Eq. 3 for a given thickness of W. The values of the slope extracted from the fit for 2 nm, 3 nm, 4 nm, 5 nm, 6 nm and 7 nm thick W are tabulated below:

Table 9.2: Experimentally obtained values of modulation of damping for Sub/W(t)/$Co_{20}Fe_{60}B_{20}$(3 nm)/SiO_2(2 nm) samples with different W thicknesses.

W thickness (nm)	Modulation of damping (m^2/A)
2	$(0.47\pm0.04)\times10^{-12}$
3	$(1.29\pm0.10)\times10^{-12}$
4	$(1.20\pm0.06)\times10^{-12}$
5	$(1.02\pm0.04)\times10^{-12}$
6	$(0.39\pm0.06)\times10^{-12}$
7	$(0.11\pm0.01)\times10^{-12}$

Note that the slope of MOD due to the spin current generated by SHE is generally larger for the β phase W (3, 4, 5 nm) in comparison to the α phase W (6, 7 nm). The sample with 2 nm W thickness is an exception and it will be discussed later in this article. With increasing current density, precessional frequency has experienced a down shift for either direction of the charge flow [47] . This may possibly arise either from the Joule heating affecting the local magnetization as well as the frequency [28, 55] or due to the presence of a field-like torque. The limited J_c value for the high resistive β phase W (in Fig. 9.4 (b), for t = 3 and 4 nm) is retained to avoid Joule heating in these films. Nevertheless, damping variation in α up to ±15% is observed for a reasonably small current density of 0.3×10^{10} A/ m^2 for the sample with t = 3 nm. Here we cannot rule out the possibility of small increment in damping values due to heat accumulation following the ultrafast demagnetization by the pump pulse on short time scales but that will not affect the slope of modulation of damping originating due to spin current generated by SHE. The enhancement (if any) will be constant and additive for all the represented damping values.

Figure 9.5(a) shows the plot of SHA as a function of W thickness 2 nm ≤ t ≤ 7 nm in Sub/W(t)/$Co_{20}Fe_{60}B_{20}$(3 nm)/SiO_2(2 nm). Interestingly, in this plot we notice that the SHA is quite small when the W layer thickness is 2 nm, subsequently, SHA increases to a large value for W layer thickness of 3 nm and 4 nm. For t > 4 nm, the SHA decreases monotonically up to t = 7 nm. It is important to emphasize here that we observe a giant value of SHA as large as 0.4 ± 0.04 for t = 3 nm. Within the β phase of W, the SHA decreases as the thickness of W becomes comparable to spin diffusion length of W (λ_{sf}) [45, 52]. The observed dependence of SHA on W thickness from 2 nm to 4 nm can be explained by considering drift diffusion analysis of the spin flow that incorporates spin Hall effect. Earlier, theoretical and experimental studies have proposed that within the spin diffusion length, the counter flowing spin current generated due to vertical gradient in the spin dependent electron chemical potential adjacent to the HM surface (under the assumption that no spin current penetrate out of HM) cancel the spin Hall generated spin current [24, 45, 50, 53, 54]. Due to this, the magnitude of the spin Hall spin current reduces significantly (resulting in smaller MOD and underestimation of SHA) as the thickness of the HM layer becomes comparable to λ_{sf}. From our experimental data we understand that the λ_{sf} of our W thin film is less than 3 nm as it is

difficult to extract this parameter precisely using standard fit with few numbers of data points available in β-W phase.

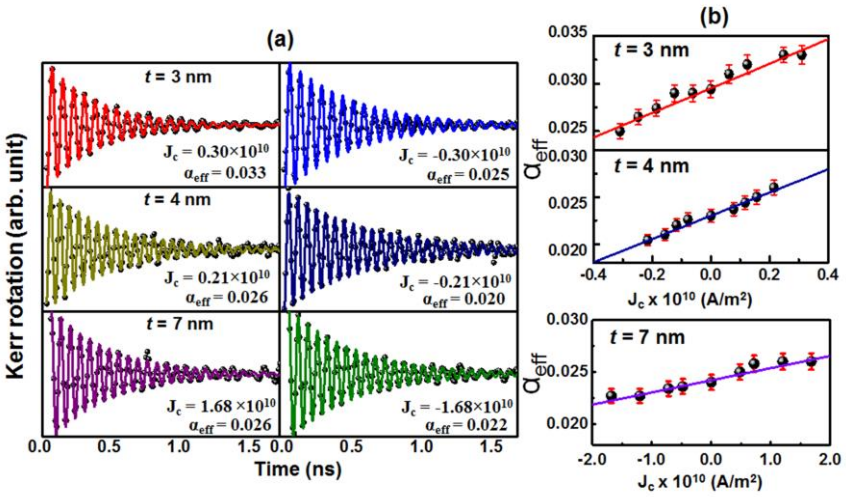

Figure 9.4: (a) Representative TR-MOKE traces for extraction of damping under the influence of positive and negative current densities. Here, W thickness is mentioned in the left panel. The estimated damping values at mentioned current densities (in A/m^2) are also shown. Comparison of left and right panel indicates that the damping value changes with the polarity of charge current. (b) Modulation of damping plot for W thickness of 3 and 4 nm corresponding to the β phase and 7 nm corresponding to the α phase. Solid line is the linear fit to the modulation of damping with current density. Error bars correspond to the fitting error obtained during the estimation of damping.

In order to understand whether the variation of SHA is directly correlated with the variation of resistivity, we plot the W resistivity with its thickness in Fig. 9.5 (b). The significant drop in the resistivity value for t > 5 nm indicates a transition from β-W to α-W phase in the W film used in our experiment. It is important to notice here that the variation in SHA above spin diffusion length is primarily correlated with the thickness dependent β to α phase transition (structural change which is also related to the resistivity change (see Fig. 9.5 (b)) of W [24, 33, 36, 38, 52]. Though from Fig. 9.5 (b), the resistivity of 5 nm thick W film is found to be primarily in β phase, but from the trend of SHA values, it appears that there is probably a mixed β and α phase of W at this thickness. Hence, apart from W thickness of 2 and 5 nm, SHA is found to be in direct correspondence with the resistivity, which is similar to the variation of SHA with conductivity as observed for other HMs [44, 55].

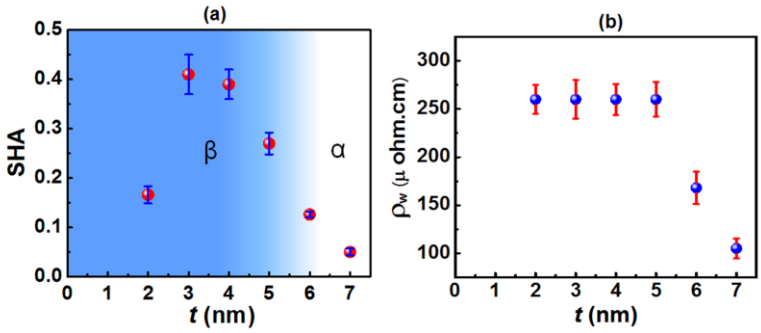

Figure 9.5: (a) Variation of spin Hall angle with W thickness. Error bars are estimated by considering errors in damping, saturation magnetization and resistivity measurements. The color contrast shows the transition from β to α phase of W. (b) Variation of resistivity of W with thickness (t).

In the phase transition regime, the change in crystal structure indicates a change in SO coupling strength of W which may play an important role in modifying the SHA [36]. There is a possibility that in the low resistive regime (for t > 5 nm), the SHA is influenced by the change in SO coupling strength. As the phase transition in W with its thickness and the associated resistivity change predominantly originates from the bulk portion of W, thus, it indicates that the bulk part of W plays dominant role in defining the SHA and thereby the spin current above the spin diffusion length of W. The bulk SHA in the NM layers is theoretically predicted and experimentally found to consist of contributions from the intrinsic, the side-jump, and the skew scattering mechanisms [5, 6, 56]. SHA of W obtained in our experiment qualitatively follows the resistivity of the W layer, which indicates that the intrinsic or side jump mechanism is primarily responsible for conversion of charge current to spin current [55]. However, it requires more elaborate study for full understanding of this phenomenon. The estimated large value of SHA indicates that the W/CoFeB interface is transparent enough to efficiently exert spin torque on the adjacent FM layer. The trend found in the variation of SHA with W thickness (β-W has larger SHA in comparison to α-W) is mostly consistent with earlier reported results [33] while the values of SHA obtained using all-optical detection technique is a new addition in this field. The method employed here is non-invasive and more unambiguous as it helps to eliminate any experimental artifacts involved in the electrical detection schemes [57]. Being a local technique, the all-optical method does

not suffer from the large area averaging, which could have produced spurious effects due to inhomogeneities and defects present in the sample. Further, in the time-domain measurement technique, magnetization damping can be directly extracted from time-resolved precession data, which is more advantageous than other techniques such as FMR line width measurement, where excitation of multiple modes may lead to inhomogeneous line broadening, which could artificially increase the damping.

9.4 Conclusions

In summary, we have used all-optical time-resolved magneto-optical Kerr effect microscopy to investigate the magnetization dynamics in Sub/W(t)/$Co_{20}Fe_{60}B_{20}$(3 nm)/SiO_2(2 nm) with varying W layer thickness under the influence of spin current generated by SHE. The W layer thickness is so chosen that it undergoes a transition from β-rich to α-rich phase at a thickness above 5 nm. For highly resistive β phase W, large modulation of damping of up to ±15% at a modest current density of 0.3×10^{10} A/m^2 and corresponding SHA as large as 0.4 is achieved. The SHA above the spin diffusion length of W follows the thickness dependent phase transition of W. On the other hand, a smaller modulation of damping and underestimation of SHA is observed for W layer thickness smaller than its spin diffusion length. In order to realize the full value of spin current due to SHE, it is thus important to use the HM thickness above its spin diffusion length. The variation of SHA with W thickness (β-W has larger SHA in comparison to α-W) is mostly consistent with the change in resistivity. Though in some of the recent theoretical and experimental studies, direct correspondence of SHA with conductivity has been discussed, however, we believe our investigations will trigger more studies to get further deep insight into the relationship between conductivity and spin Hall angle specifically for materials with mixed phase. Our results of detailed variation of SHA for different values of W thickness, will be beneficial for in-depth understanding of correlation between the thickness dependent phase transition in W and SHA. Furthermore, these studies will be significantly important from the application perspective as the future spintronic devices are expected to use large SHA material and spin current induced magnetization switching.

References

1. A. Hoffmann and S. D. Bader, Phys. Rev. Appl. **4,** 047001 (2015).
2. A. V. Chumak, V. I. Vasyuchka, A. A. Serga and B. Hillebrands, Nat. Phys. **11,** 453 (2015).
3. S. Neusser and D. Grundler, Adv. Mater. **21,** 2927 (2009).
4. S. Choudhury, S. Saha, R. Mandal, S. Barman, Y. Otani and A. Barman, ACS Appl. Mater. Interfaces. **8,** 18339 (2016).
5. A. Hoffmann, IEEE Trans. Magn. **49,** 5172 (2013).
6. J. Sinova, S. O. Valenzuela, J. Wunderlich, C. H. Back and T. Jungwirth, Rev. Mod. Phys. **87,** 1213 (2015).
7. Y. Niimi and Y. Otani, Rep. Prog. Phys. **78,** 124501 (2015).
8. Y. Fukuma, L. Wang, H. Idzuchi, S. Takahashi, S. Maekawa and Y. Otani, Nature Mater. **10,** 527 (2011).
9. H. Idzuchi, Y. Fukuma and Y. Otani, Sci. Rep. **2,** 628 (2012).
10. V. E. Demidov, S. Urazhdin, R. Liu, B. Divinskiy, A. Telegin and S. O. Demokritov, Nat. Commun. **7,** 10446 (2016).
11. H. J. Jiao and G. E. W. Bauer, Phys. Rev. Lett. **110,** 217602 (2013).
12. S. Maekawa, H. Adachi, K. Uchida, J. Ieda and E. Saitoh, J. Phys. Soc. Jpn **82,** 102002 (2013).
13. M. Jamali, J. S. Lee, J. S. Jeong, F. Mahfouzi, Y. Lv, Z. Y. Zhao, B. K. Nikolic, K. A. Mkhoyan, N. Samarth and J. P. Wang, Nano Lett. **15,** 7126 (2015).
14. I. Mihai Miron, G. Gaudin, S. Auffret, B. Rodmacq, A. Schuhl, S. Pizzini, J. Vogel and P. Gambardella, Nature Mater. **9,** 230 (2010).
15. J. E. Hirsch, Phys. Rev. Lett. **83,** 1834 (1999).
16. L. Liu, C.-F. Pai, Y. Li, H. W. Tseng, D. C. Ralph and R. A. Buhrman, Science **336,** 555 (2012).
17. S. Emori, U. Bauer, S.-M. Ahn, E. Martinez and G. S. D. Beach, Nature Mater. **12,** 611 (2013).
18. M. Morota, Y. Niimi, K. Ohnishi, D. H. Wei, T. Tanaka, H. Kontani, T. Kimura and Y. Otani, Phys. Rev. B **83,** 174405 (2011).

19. O. Mosendz, J. E. Pearson, F. Y. Fradin, G. E. W. Bauer, S. D. Bader and A. Hoffmann, Phys. Rev. Lett. **104,** 046601 (2010).
20. J. Kim, J. Sinha, M. Hayashi, M. Yamanouchi, S. Fukami, T. Suzuki, S. Mitani and H. Ohno, Nature Mater. **12,** 240 (2013).
21. L. Liu, C.-F. Pai, D. C. Ralph and R. A. Buhrman, Phys. Rev. Lett. **109,** 186602 (2012).
22. M. Jamali, A. Klemm and J.-P. Wang, Appl. Phys. Lett. **103,** 252409 (2013).
23. M. Evelt, V. E. Demidov, V. Bessonov, S. O. Demokritov, J. L. Prieto, M. Muñoz, J. B. Youssef, V. V. Naletov, G. d. Loubens, O. Klein, M. Collet, K. Garcia-Hernandez, P. Bortolotti, V. Cros and A. Anane, Appl. Phys. Lett. **108,** 172406 (2016).
24. Q. Hao and G. Xiao, Phys. Rev. Appl. **3,** 034009 (2015).
25. D. Bhowmik, L. You and S. Salahuddin, Nature Nanotech. **9,** 59 (2014).
26. J. Torrejon, F. Garcia-Sanchez, T. Taniguchi, J. Sinha, S. Mitani, J. V. Kim and M. Hayashi, Phys. Rev. B **91,** 214434 (2015).
27. G. Q. Yu, P. Upadhyaya, Y. B. Fan, J. G. Alzate, W. J. Jiang, K. L. Wong, S. Takei, S. A. Bender, L. T. Chang, Y. Jiang, M. R. Lang, J. S. Tang, Y. Wang, Y. Tserkovnyak, P. K. Amiri and K. L. Wang, Nature Nanotech. **9,** 548 (2014).
28. S. Kasai, K. Kondou, H. Sukegawa, S. Mitani, K. Tsukagoshi and Y. Otani, Appl. Phys. Lett. **104,** 092408 (2014).
29. A. Ganguly, K. Kondou, H. Sukegawa, S. Mitani, S. Kasai, Y. Niimi, Y. Otani and A. Barman, Appl. Phys. Lett. **104,** 072405 (2014).
30. V. T. Pham, L. Vila, G. Zahnd, A. Marty, W. Savero-Torres, M. Jamet and J. P. Attane, Nano Letters **16,** 6755 (2016).
31. A. Barman and A. Haldar, *Time-domain study of magnetization dynamics in magnetic thin films and micro-and nanostructures.* Solid State Phys, vol **65**. (Elsevier Inc., Burlington, 2014).
32. A. Ganguly, R. M. Rowan-Robinson, A. Haldar, S. Jaiswal, J. Sinha, A. T. Hindmarch, D. A. Atkinson and A. Barman, Appl. Phys. Lett. **105,** 112409 (2014).
33. C.-F. Pai, L. Liu, Y. Li, H. W. Tseng, D. C. Ralph and R. A. Buhrman, Appl. Phys. Lett. **101,** 122404 (2012).
34. G. G. An, J. B. Lee, S. M. Yang, J. H. Kim, W. S. Chung and J. P. Hong, Acta Mater. **87,** 259 (2015).
35. A. K. Chaurasiya, C. Banerjee, S. Pan, S. Sahoo, S. Choudhury, J. Sinha and A. Barman, Sci. Rep. **6,** 32592 (2016).

36. J. Liu, T. Ohkubo, S. Mitani, K. Hono and M. Hayashi, Appl. Phys. Lett. **107,** 232408 (2015).
37. J. Torrejon, J. Kim, J. Sinha, S. Mitani, M. Hayashi, M. Yamanouchi and H. Ohno, Nature Commun. **5,** 4655 (2014).
38. Q. Hao, W. Chen and G. Xiao, Appl. Phys. Lett. **106,** 182403 (2015).
39. C. Zhang, S. Fukami, K. Watanabe, A. Ohkawara, S. DuttaGupta, H. Sato, F. Matsukura and H. Ohno, Appl. Phys. Lett. **109,** 192405 (2016).
40. W. F. Zhang, W. Han, X. Jiang, S. H. Yang and S. S. P. Parkin, Nature Phys. **11,** 496 (2015).
41. K. U. Demasius, T. Phung, W. F. Zhang, B. P. Hughes, S. H. Yang, A. Kellock, W. Han, A. Pushp and S. S. P. Parkin, Nature Commun. **7,** 10644 (2016).
42. C. F. Pai, Y. X. Ou, L. H. Vilela-Leao, D. C. Ralph and R. A. Buhrman, Phys. Rev. B **92,** 064426 (2015).
43. L. Wang, R. J. H. Wesselink, Y. Liu, Z. Yuan, K. Xia and P. J. Kelly, Phys. Rev. Lett. **116,** 196602 (2016).
44. M. Obstbaum, M. Decker, A. K. Greitner, M. Haertinger, T. N. G. Meier, M. Kronseder, K. Chadova, S. Wimmer, D. Ködderitzsch, H. Ebert and C. H. Back, Phys. Rev. Lett. **117,** 167204 (2016).
45. J. W. Yu, X. P. Qiu, W. Legrand and H. Yang, Appl. Phys. Lett. **109,** 042403 (2016).
46. I. Horcas, R. Fernández, J. M. Gómez-Rodríguez, J. Colchero, J. Gómez-Herrero and A. M. Baro, Rev. Sci. Instrum. **78,** 013705 (2007).
47. W. Chen, G. Xiao, Q. Zhang, and X. Zhang, Phys. Rev. B **98**, 134411 (2018).
48. L. Liu, T. Moriyama, D. C. Ralph and R. A. Buhrman, Phys. Rev. Lett. **106,** 036601 (2011).
49. K. Ando, S. Takahashi, K. Harii, K. Sasage, J. Ieda, S. Maekawa and E. Saitoh, Phys. Rev. Lett. **101,** 036601 (2008).
50. L. Liu, R. A. Buhrman and D. C. Ralph, arxiv **1111.3702** (2011).
51. E. Beaurepaire, J. C. Merle, A. Daunois and J. Y. Bigot, Phys. Rev. Lett. **76,** 4250 (1996).
52. S. Cho, S. H. C. Baek, K. D. Lee, Y. Jo and B. G. Park, Sci. Rep. **5,** 14668 (2015).
53. P. C. Vanson, H. Vankempen and P. Wyder, Phys. Rev. Lett. **58,** 2271 (1987).
54. M. H. Nguyen, D. C. Ralph and R. A. Buhrman, Phys. Rev. Lett. **116,** 126601 (2016).

55. E. Sagasta, Y. Omori, M. Isasa, M. Gradhand, L. E. Hueso, Y. Niimi, Y. Otani and F. Casanova, Phys. Rev. B **94,** 060412 (2016).
56. X. Zhou, M. Tang, X. L. Fan, X. P. Qiu and S. M. Zhou, Phys. Rev. B **94,** 144427 (2016).
57. I. Neudecker, G. Woltersdorf, B. Heinrich, T. Okuno, G. Gubbiotti and C. H. Back, J. Mag. Magn. Mater. **307,** 148 (2006).

Chapter 10

10 Conclusions and Future Perspective

10. 1 Conclusions

In essence, the study of ultrafast magnetization dynamics in femtosecond to nanosecond time scales has been conducted in the following systems: ferromagnetic thin films, nanostructures and nonmagnet/ferromagnet heterostructures. For the growth of thin films and fabrication of magnetic nanostructures and magnonic crystals, rf/dc magnetron sputtering, e-beam evaporation and e-beam lithography have been used. To extract the information of elemental composition and crystallinity of the samples EDX and XRD have been used. The surface morphology of the samples has been studied using AFM. The static magnetic properties, such as, magnetic reversal, saturation magnetization, saturation field, coercivity, anisotropy, domain features have been explored by using VSM, static MOKE and MFM. The ultrafast magnetization dynamics in fs to ns time scale has been studied by employing all-optical TRMOKE microscopy based on mode-locked fs oscillator system in a collinear geometry and a two-colour optical pump probe technique based on femtosecond amplifier system in noncollinear geometry. The experimental results have been analyzed with the help of micromagnetic simulations (*i.e.* OOMMF, LLG and MuMax3 simulator).

Laser fluence-dependent study of ultrafast magnetization dynamics in Py thin films with different thicknesses reveals a substantial enhancement of the Gilbert damping for Kittel and PSSW modes. We experimentally show that the pump laser-induced changes in the dynamics are reversible in nature. We found that the enhancement of the system temperature to Curie temperature ratio is responsible for the increment in remagnetization times and Gilbert damping, while a very weak correlation of that is found with the ultrafast demagnetization. The temporal chirping, introduced because of pump-induced changes in the magnetic parameters, is found to be increased up to ten times with fluence. It causes red shift in the precessional frequency with time. The results also have important implications in the several spintronic applications.

We have further studied the precessional magnetization dynamics as a function of magnitude and orientation of the bias magnetic field in Fe-rich Gd-Fe thin films with varying thickness. Our time-resolved dynamics data show the development of a weak out-of-plane anisotropy with increasing film thickness, which is complemented by static magnetization measurements. A large tunability of effective damping of the system has been obtained with the variation in bias field due to various extrinsic effects such as, TMS, magnetic inhomogeneity, impurity scattering and multimodal dephasing. We found an opposite trend in the variation of decay time with the frequency of Kittel mode and PSSW mode, possibly due to inter-mode energy transfer. The extensive study presented here may shed light to the knowledge of magnetization dynamics in RE-TM thin films.

We have investigated the collective magnetization dynamics in $Ni_{80}Fe_{20}$ circular nanodot arrays arranged in hexagonal, octagonal and honeycomb lattice symmetry by systematic variation of inter-dot separation. Measurements of magnetization dynamic by time-resolved magneto-optical Kerr microscopy reveal that the nanodots in the array strongly interact with each other leading towards strongly collective SW modes, which are completely different from the modes of the individual nanodots. With the increase in inter-dot separation, the dynamics passes through weakly collective regimes with the appearance of new modes. The uniformly distributed centre and edge modes of the individual dots through the entire array get modulated. Finally, at higher inter-dot separations the dynamics reach to an isolated regime, where modes of the individual nanodots prevail. Subsequently, we make a comparative study between honeycomb and octagonal lattices. The effect of anisotropic dipolar interaction can be prominently observed within the octagonal lattice having horizontally as well as vertically coupled paired nanodots. Consequently, splitting of highest frequency mode and their variation with inter-dot separation are explored. On the contrary, the honeycomb lattice does not contain this feature as the paired nanodots placed only parallel with the field. The above experimental findings along with the support of numerical analyses will enrich the knowledge of magnetization dynamics in ferromagnetic nanodot arrays and have potential applications in GHz frequency filter, phase shifter and other magnonic devices.

We have observed hybrid magneto-dynamical modes in a single Co nanomagnet fabricated on top of a piezoelectric PMN–PT substrate due to magnetoelastic

modulation of the precessional dynamics. The frequencies of these modes are in the order of 10 GHz which corresponds to ~100 ps time scale dynamics. This shows that strain can affect the magnetization state of even a weak magnetostrictive nanomagnet within ~1 ns. The spatial power and phase maps of SW textures simulated for these modes display quantization and rotation of quantization axis with the applied bias field in the micromagnetic simulation.

We have used all-optical detection technique to determine the spin transfer torque induced modulation of damping in Sub/W(t)/$Co_{20}Fe_{60}B_{20}$(3 nm)/SiO_2(2 nm) with varying W layer thickness under the influence of spin current generated by SHE. The W layer thickness is varied from 2 nm to 7 nm, so that it undergoes a transition from β to α phase at a thickness above 5 nm. For highly resistive β-phase W, large modulation of damping (about 30%) is found at modest current densities and corresponding SHA as large as 0.4 are achieved. The modulation of damping and SHA show nonmonotonic decrease with transition from β to α phase. These studies will be significantly important for the development of the future spintronic devices, which deals with large SHA material and spin-current-induced magnetization switching.

10.2 Future Perspective

The idea of controlling several physical processes those occur within ultrafast time scale can be advantageous in many ways. Storing and processing of information by harnessing the effect of external stimuli on the static and dynamic properties of magnetic material is a very popular area. For example, few years back, heat assisted magnetic recording (HAMR) gained considerable momentum. The working principle of this device relies on laser induced modification of static magnetic properties of the material on magnetic track. For magnetic memory devices it is very important to retain the nonvolatility of the information stored in the magnetic domain. The study of laser induced modification of ultrafast magnetization dynamics in ferromagnetic thin films reveals that not only static but also dynamic parameters can be controlled reversibly with pump induced rapid heating and simultaneous cooling in ultrafast time scale. Similar study in several other technologically important materials may find application in future heat assisted data writing technology. The TR-MOKE set up based on amplified laser system, in which the above mentioned experiments are performed, can even be

extended to perform dynamic measurements at low temperatures. Different magneto-caloric effects, specifically variation of Gilbert damping with temperature can be studied. The formation of 'spin-wave trap' is a recent observation in all-optical experiments. The spatial profile of the pump beam can create its imprint in the sample plane as well as in the bulk due to nonuniform heating effect. By tuning the spatial overlapping between pump and probe pulses the modification of precessional frequency and damping can be studied. Using an additional optical parametric amplifier, lasers of different wavelengths having different penetration depths can be generated. Exploiting those as pump, rich physics related to ultrafast demagnetization, remagnetization and precessional dynamics in thin films and multilayers can be explored. In ferrimagnetic Gd-Fe thin films, varying the elemental composition a Gd rich state can be formed. With increasing system temperature (either by laser fluence or by heating the system) magnetic moment and angular momentum compensation points can be reached where the precessional frequency diverges. Also Gd rich phase is known to exhibit two-step ultrafast demagnetization. Thus the study of ultrafast magnetization dynamics with variation of composition and pump fluence will be further intriguing. Also, formation of stripe domain, labirynth domain and bubble domain are extensively studied in this multi-sublattice system. As a consequence, stabilization of chiral spin texture, such as, skyrmions in thicker films is an emerging topic of research. Study of skyrmion dynamics and skyrmion Hall effect in Gd-Fe thin films can be one of the future goals using some of the existing measurement facilities, *e.g.* MFM, Kerr microscopy etc. Regarding the ferromagnetic nanodot arrays arranged in different Bravais and non-Bravais geometry, collective and noncollective SW dynamics can be more interesting if those are patterned on PZ substrates, or on top of heavy metal with high SOC. To excite and control the unprecedented nature of SWs, application of electric field, periodic strain, spin current generated spin torque in such nanostructures will be interesting. The application potential of pure spin current generated spin transfer torque in controlling the magnetization of ferromagnetic is described in several places of this thesis. The generation of spin current and its effect on adjacent ferromagnetic layer can be studied in various emerging systems, such as, topological insulator, Weyl semimetal, doped heavy metals etc. which may provide exceptionally high charge to spin current conversion efficiency and giant modulation of damping leading towards energy efficient magnetic switching.